NASA Contractor Report 165625

A DESIGN PROCEDURE FOR FAN INFLOW CONTROL STRUCTURES

M. R. Gedge

UNITED TECHNOLOGIES CORPORATION
Pratt & Whitney Aircraft Group
Commercial Products Division

East Hartford, Connecticut 06108

Contract No. NAS1-15085

September 1980

NASA

National Aeronautics and
Space Administration
Langley Research Center
Hampton, Virginia 23665

TABLE OF CONTENTS

PRECEDING PAGE BLANK NOT FILMED

TABLE OF CONTENTS (Cont'd)

LIST OF ILLUSTRATIONS

LIST OF ILLUSTRATIONS (Cont'd)

LIST OF ILLUSTRATIONS (Cont'd)

LIST OF ILLUSTRATIONS (Cont'd)

LIST OF ILLUSTRATIONS (Cont'd)

LIST OF ILLUSTRATIONS (Cont'd)

LIST OF ILLUSTRATIONS (Cont'd)

LIST OF ILLUSTRATIONS (Cont'd)

1.0 SUMMARY

Significant differences exist in the noise generated by engines in flight and engines operating on the test stand. It has been observed that these differences are reduced by the use of an inflow control structure in the static test situation. It is a purpose of this contract (NAS1-15085) to produce a design system for inflow control structures. This report first describes the results of a test program conducted to develop various theoretical models used in the design system. Following this the design system is developed. Finally an assessment of this procedure is made using measured data.

The primary result of this work is a step by step inflow control structure design procedure in terms, for the most part, of parameters quantifiable by the designer. The assessment of this procedure using blade mounted transducer data was inconclusive due to the transducer responding to stimuli other than the engine inflow field. However an assessment made with hot film data was very encouraging.

2 0 INTRODUCTION

Reduction of jet engine noise levels is a continuing evolutionary process and significant noise reduction has been achieved since the advent of the original commercial jet aircraft in the early 1950's. Engine noise reduction features are usually verified by means of static or flight testing. Since the cost of flight testing is much greater than that of static testing, use of the latter technique results in significantly lower costs being accrued to the development of engine noise reduction features. As such, the use of static testing techniques should be fully exploited. The purpose of this contract is to develop, for turbofan engines, static testing techniques that result in measurements of fan noise that are representative of inflight levels.

It has been noted by various observers that the noise produced by the fan of turbofan engines operating statically on the test stand is greater than that produced when the engine is operating under flight conditions. This may be a result of both fan blade passing tone and broadband levels being contaminated by extraneous noise sources present during static testing. As a consequence, predictions of flight noise levels using static data are consistently high. A no less important ramification is that flight noise sources cannot be identified from noise measurements from statically operating engines. Correspondingly, noise reduction techniques cannot be evaluated on the test stand in the presence of a contaminating noise floor. To identify the source of extraneous noise it is necessary to note that, statically, the fan interacts with a more distorted inflow field than it does when in flight. There are several distinct characteristics of the inflow field that are quite different when the engine is operating statically, each of which could produce extraneous noise.

Firstly, the ambient atmospheric turbulence field in the vicinity of the ground is more turbulent than at higher altitudes. In addition, this turbulence field is convected through a very high flow contraction when the engine is operating statically, whereas, in flight, the turbulence field convects through a very small contraction on its way to the fan. This high flow contraction in the static case results in a distortion of the field in which the "eddies" are "stretched", then "chopped" by successive fan blades, producing "bursts" of discrete noise that are virtually absent in the flight operation of the engine.

Secondly, in the static case, there exists stand structure and a ground plane that are sources of flow disturbances. Engine ingested air passes over the stand structure and the ground resulting in vortices and wakes in the inflow field. Engine case protuberances can also generate ingestible distortions. Usually these sources of distortion do not exist inflight since the air ingested into an engine has not passed over any boundaries.

Thirdly, the nacelle boundary layer is different during static operations of the engine. In flight, at takeoff and approach conditions, air is drawn into the engine through a streamtube forward of the engine, which is slightly larger than the fan, causing the locus of the stagnation points to be near the leading edge of the nacelle. In static operation, however, air is ingested from a much wider streamtube causing the stagnation locus to move rearward on the outside of the flight nacelle. The acceleration of the flow from this stagnation locus around the lip region produces higher local velocities than those occuring in flight and consequently, a larger adverse pressure gradient along the nacelle inner wall than that which is encountered in flight. The boundary layer then becomes thicker in this region and may even separate (the use of bellmouth inlets during static testing is an attempt to alleviate this situation). Due to these differences in boundary layers, the area of the fan tip that is affected by the boundary layer during static operation is probably larger. The nacelle boundary layer in static operation is also affected by the presence of free stream flow distortions which can locally perturb it. It seems probable, then, that the nacelle boundary layer generated by static operation of the engine constitutes a larger flow disturbance than its flight counterpart and thus could be a cause of higher noise levels.

Finally, since it is possible for the flow to be drawn from all angles by an engine on the test stand, turbulent flows from the jet plume may be reingested. This distortion source is not present in flight. These disturbances (i.e., atmospheric turbulence, ground plane and stand induced distortions, dissimilar nacelle boundary layer and jet plume reingestion) are considered to be the most important extraneous noise sources in static engine operation. In order to obtain useful static acoustic data, it is therefore necessary to develop techniques which modify the inflow field so that, for all intents and purposes, the fan is operating as it would in flight. In the past, various techniques for accomplishing this simulation have been used, including mounting engines in wind tunnels and using devices upstream of the fan to condition the inflow. Inflow Control Structures (ICS) for conditioning the flow have been mounted upstream of the engine by several investigators. A boundary layer suction system has also been used in conjunction with a screen. Both of these techniques have resulted in reduced radiated noise levels, indicating the reduction of inflow distortion.

In view of the encouraging results achieved by the use of ICS's, the present contract was awarded for the purpose of developing an inflow control screen design procedure and a flight noise prediction procedure using data gathered from the static testing of engines equipped with such a structure. The use of wind tunnels, or other techniques for simulating the flight environment are not considered under this contract. In addition, the problem of nacelle boundary layer modification is not addressed under this contract, but is certainly an important area for future work. The major components of the contract are:

Phase I Definition of Atmospheric Turbulence Characteristics and Engine Sensitivity Study.

Phase II Development of Inflow Control Structure (ICS) Preliminary Design System.

Phase III Interim Procedures Report Development and Coordination.

This report describes a preliminary design system for the inflow control structure (ICS). Specifically Tasks F, G and H are addressed here.

An Interim Phase II report, previously published, contains details of the analytical models used in the design system. The results of a test program designed to assess and/or modify these analytical models are reported here. Subsequently, the models are modified and used to develop an ICS design system. This design system is exercised for the JT9D and JT15D. Finally, the ICS design system was assessed using blade mounted pressure transducer (BMT) data gathered under the P&WA/Boeing Joint Noise Reduction Program.

This report, in conjunction with the Interim Phase II report comprises the final Phase II report. It should be noted, that in this report and the Interim Phase II report, the term "screen" is used in it's general sense, thus, perforated plate, honeycomb and gauze are all types of screen.

3.0 SYMBOLS

a	Characteristic Dimension
a_0	Speed of Sound
B	Fan Blade Number
b	Wake Width
D	Contraction Length
D_0	Inlet Diameter
d	Detail Dimension
F	Velocity PSD
$\tilde{F}$	Normalized Velocity PSD
f	Frequency
ΔH	Total Pressure Loss
K	Pressure Drop Coefficient
KE	Kinetic Energy
$\underline{k}$	Wavenumber Vector
L	Integral Length Scale
ℓ	Thickness
ℓ_1	Contraction Ratio
M	Mach Number
N	Isotropic Turbulence Characteristic
NR	Noise Reduction
P	Pressure PSD
p	Pressure
	Function Defined in 6.4
q	Dynamic Head

R	Radius
Re	Reynolds Number
r	Vortex Radius
SPL	Sound Pressure Level
s	Defined in 6.4
$\underline{U}$	Mean Velocity Vector
ΔU_1	Velocity Deficit
$\underline{u}$	Turbulent Velocity Vector
X	Streamwise Distance
X_0	Virtual Source Distance
$\underline{x}$	Position Vector
z	Engine Height
z_0	Terrain Characteristic Height
z_{REF}	Reference Height
α	Flow Angle Ratio
β	Bias
Γ	Circulation
Γ_{ij}	Velocity Spectrum Tensor
γ	Isotropic Turbulence Characteristic
γ_0	Blade Relative Mean Flow Angle
θ	Angle
λ_{min}	Minimum Sensitive Scale
μ	Mean Square Velocity Component Ratio
ν	Kinematic Viscosity
ρ	Air Density
σ	Open Area Ratio
ϕ	BMT Path Angle
ω	Circular Frequency

Subscripts

A	Pre, Contraction Or Screen Atmosphere
AMB	Ambient
B	Post, Contraction or Screen
c	Core
EFF	Effective
F	Flight
	Final Contraction
H	Honeycomb
I	Initial Contraction
ICS	At ICS
i, j	Indices
L	Lower
m	Microphone
max	Maximum
NS	No Screen
n	Upwash Component
o	Fan Face Conditions
P	Perforated Plate (Gauze)
R	Receiver
REF	Reference
S	Source, Static
SC	Screen
TU	Total Upstream
TD	Total Downstream

4.0 BACKGROUND

It has long been known that the flight and static test environments of an engine are different. For instance, in 1966, Sofrin and McCann (1) recognized the existence of noise generation mechanisms peculiar to ground operation of an engine. They identified "natural atmospheric air currents" and ground vortices as causes of inflow distortion that, upon interaction with a rotor, produce noise. They also surmised that the inflow into a fan in flight was not distortion free, but probably had a different distortion flow field than which existed during static testing.

Subsequently, accumulated evidence (2, 3, 4, 5, 6) showed that not only were static and flight inflow distortions different, but that the static distortion field generated noise levels, especially blade passing tone levels (and possibly its harmonics) that were significantly greater than those generated in flight. However, while the source of the extraneous static noise is generally ascribed to the more disturbed inflow field, the particular distortion type responsible is not clearly defined. For example, Cumpsty and Lowrie (2) produced results that indicated that boundary layer changes were important at relative tip Mach numbers less than .85. In the flow outside the boundary layer, they suggest that distortions produced by the contraction of the ambient atmospheric turbulence field are important. Hanson's (7, 8, 9) measurements of inlet flow fields are explained by that author also as the result of contraction of the atmospheric turbulence, although, in some situations, he also identifies distortions due to flow over the stand structure. Distortions have also been detected that were generated by protuberances on the exterior nacelle casing (10). Earlier work by Povinelli et al (11) identified distortions of the inflow by the installation structure. Hodder (12) examined among other things, the noise generated by a JT15D at two heights from the ground, and found the ground vortex interacting with the rotor to be a significant source. Recent P&WA/Boeing experience under the Joint Noise Reduction Program (JNRP) indicates that on a full size test stand, ground effects, stand structure and possibly atmospheric turbulence contribute to inflow distortions

(13). The above review indicates that any or all of the distortion sources can exist but to a varying degree depending on the details of the test stand configuration.

Significant suppression of these flow distributions has been achieved by the mounting of Inflow Control Structures (ICS) upstream of the inlet. These structures consist of screening materials either supported by a frame or substantially self supporting with the minimum of unnecessary structure.

Published experience with ICSs has been quite varied. The scales of the fans has ranged from model to the large high bypass ratio fan. The ICS has been placed in the inlet duct and externally.

The in-duct ICS has consisted of either a honeycomb panel mounted upstream of the rotor (12, 14, 15) or multiple gauze screens at the inlet entrance (4). All except Leggat and Siddon observed a reduction in tone level, however, these investigators did note a change in blade loading caused by the suppression of transverse velocities in a ground vortex. Suppression of this vortex nearer its stagnation point resulted in noise reductions. In conjunction with the noise reduction, Hodder (12) observed a reduction in axial length scale, as determined by making auto correlations of the hot wire signal obtained at the fan face. Hodder ascribed the noise reduction to a change in length scale caused by the screen. However, Jones, et al, (15) demonstrated that honeycomb screens mounted in the inlet duct have an acoustic transmisssion loss associated with them, so there is some question as to the reason for the noise reductions when the screens are mounted in the inlet.

The externally mounted ICS's do not suffer from this problem of acoustic transmission loss to any great degree (15, 16). In general, all screens of this type (17, 18, 15, 19, 20, 21, 13, 22, 23, 24) produced a significant reduction in tone noise at subsonic relative tip Mach numbers, whether in the anechoic chamber, wind tunnel or on the test stand. The work of Rogers et al (13), Atvars et al (22) and McArdle et al (23) demonstrates conclusively, with the use of blade mounted pressure transducers, the substantial clean up of the inflow field that can be achieved with the ICS. In addition, Rogers and Ganz

(13), by comparing static and flight BMT data show that the ICS goes a long way to reproducing the flight fan face environment. Woodward et al (24), and Kantola et al (21), have also used inflow boundary layer modification in conjunction with an Inflow Control Structure to produce encouraging results.

While universal screen design criteria have not yet been determined, certain desirable characteristics have emerged based on the literature reviewed. These characteristics are summarized below:

- The minimization of acoustic transmission loss is enhanced by use of external ICSs as opposed to use of ICSs mounted in the engine inlet (15, 16).
- Distortion suppression, primarily of transverse velocities, is effected by use of honeycomb. Honeycomb characteristics suggested by Ho, et al, (25) are that a length to diameter ratio of 5 to 10 is necessary. However, Ginder (26) shows that increasing this ratio beyond 2 does not improve disturbance suppression. This latter view is born out, in some degree, by Prandtl (27).
- Axial velocity distortion suppression is effected by use of gauzes or perforated plate because of their relatively high pressure loss coefficients.
- Distortions generated by honeycomb structure can be suppressed by use of gauzes mounted downstream of the honeycomb, as suggested by the work in references (17), (25), (26) and (28).
- Gauzes and perforated plates can be mounted upstream of the honeycomb to protect it from damage by incoming debris.

- Inflow control devices should be designed to avoid large structural members and discontinuities (as noted by Lowrie and Newby (16) and PWA/Boeing experience) since they can give rise to self generated distortions entering the fan. As can be seen from the above review of the literature, the feasibility has been shown of using an inflow control structure during static testing to effect a better simulation of the fan inflight flow field. Certain desirable characteristics of ICS designs have been identified, but as yet, a design procedure does not exist. An ICS design procedure that is generally appplicable is developed in the present work.

5.0 TEST PROGRAM (PHASE II TASK F)

The purpose of this program was to provide data to empirically verify or correct the analytical models for the ICS design procedure identified in the Interim Phase II report (29). The tests conducted were basically of two types, aerodynamic and acoustic.

The aerodynamic tests consisted of determining the effect of flow contraction and screening on inflow distortion elements and turbulence. In addition screen pressure drop coefficients were measured.

The acoustic portion of the program consisted of measuring the effect of structural members and panel corners on the acoustic radiation field. (This was described in part in (29). Acoustic transmission loss measurements across various screens were also made.

In the following subsections the aerodynamic measurements are discussed in Section 5.1 and the acoustic data in Section 5.2.

5.1 The Effect of a Flow Contraction and Screening on Turbulence and Steady Flow Distortion

The tests were carried out at Pratt & Whitney Aircraft's 25.4 cm suction rig facility. Flow through this rig is provided by three 450 hp vacuum pumps. Duct velocities ranging from 18.29 m/s to 121.95 m/s were generated to encompass the range of contraction ratios likely to be experienced by the engine on the test stand. A bellmouth was mounted on the suction duct to ensure a smooth transition of flow from the test room into the 25.4 cm duct. A schematic diagram of the basic configuration is shown in Figure 1.

A turbulence generator was mounted upstream of the test room as shown in Figure 2. This consisted of a plenum which exhausted into the test room through a series of opposing jets (porcupine) (Figure 3). This arrangement

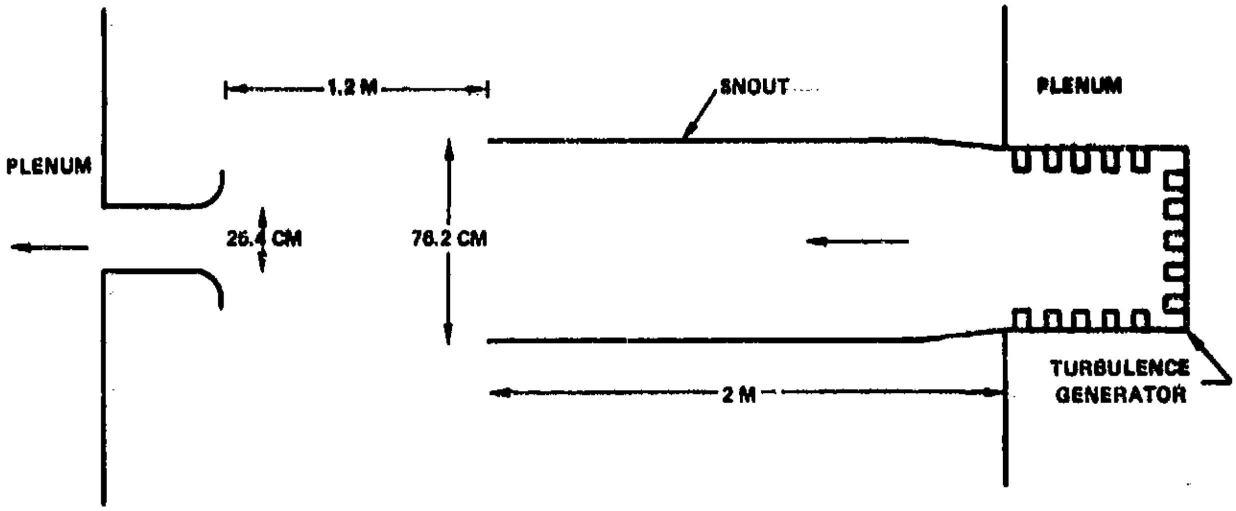

Figure 1 Basic Configuration of Suction Rig

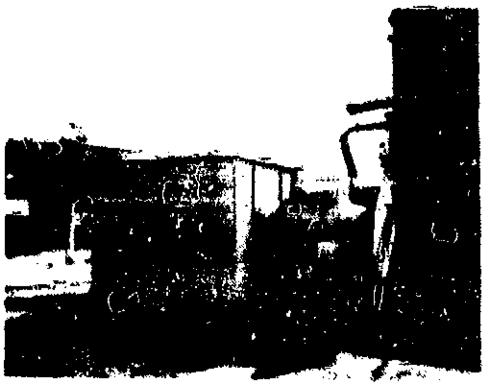

Figure 2 The Plenum Chamber of the Turbulence Generator

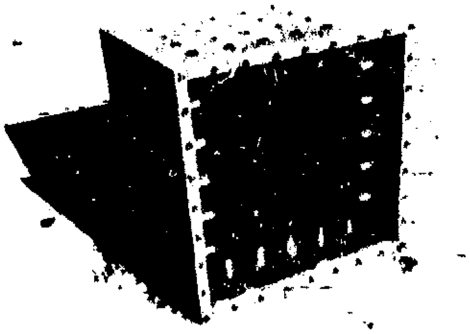

Figure 3 Turbulence Generating Device

Test	Screen Spec.	Wake Gen	Turb. Gen	Axial (cm)	Radial Positions (Range in cm)	Duct Velocities (Range in m/s)	Meas. Type
1A	None	- -	Yes	-20.32	(CL to +10.16)	(24.39 to 121.95)	#2
				25.4	(CL to +412.7)	(30.49 to 121.95)	#4
				55.88		(30.49 to 121.95)	#4
1B	None	3.81 Sq. Rod	No	-20.32	(-10.16 to +10.16)	(30.49 to 121.95)	#1
		5.08 x 7.62 Rod					
		SYM. A/F (NACA Series 6)					
		3.81 Sq. Rod		55.88	(-3.8 to +3.8)	(30.49 to 121.95)	#3
		3.81 Sq. Rod		25.4			
		5.08 x 7.62 Rod			55.88		
		5.08 x 7.62 Rod			25.4		
		SYM. A/F (NACA Series 6)			55.88		
		5.08 x 7.62 Rod			25.4		
1C	.953 cm H/C	- -	Yes	48.26	(CL to +12.7)	(30.49 to 121.95)	#4
	.953 cm H/C	- -		30.48			
	1.27 cm H/C	- -		48.26			
	1.27 cm H/C	- -		30.48			
	2.54 cm H/C	- -		48.26			
	2.54 cm H/C	- -		30.48			
	41% O.A. P.P.	- -		48.26			
	41% O.A. P.P.	- -		30.48			
	66% O.A. P.P.	- -		48.26			
	66% O.A. P.P.	- -		30.48			
1D	.953 cm Honeycomb	3.8 Sq. Rod	No	48.26	(-12.7 to +12.7)	(53.35 to 121.95)	#3
		3.8 Sq. Rod		30.48			
		5.08 x 7.62 Rod		48.26			
		5.08 x 7.62 Rod		30.48			
		Tip Vortex A/F (NACA 0012)		48.26			
		Tip Vortex A/F (NACA 0012)		30.48			
	1.27 cm Honeycomb	3.81 Sq. Rod		48.26			
		3.81 Sq. Rod		30.48			
		5.08 x 7.62 Rod		48.26			
		5.08 x 7.62 Rod		30.48			
		Tip Vortex A/F (NACA 0012)		48.26			
		Tip Vortex A/F (NACA 0012)		30.48			
	2.54 cm Honeycomb	3.81 Sq. Rod	No	48.26	(-12.7 to +12.7)	(53.35 to 121.95)	#3
		3.81 Sq. Rod		30.48			
		5.08 x 7.62 Rod		48.26			
		5.08 x 7.62 Rod		30.48			
		Tip Vortex A/F (NACA 0012)		48.26			
		Tip Vortex A/F (NACA 0012)		30.48			
	41% O.A. Perf. Plate	3.81 Sq. Rod		48.26			
		3.81 Sq. Rod		30.48			
		5.08 x 7.62 Sq. Rod		48.26			
		5.08 x 7.62 Sq. Rod		30.48			
	66% O.A. Perf. Plate	3.81 Sq. Rod	No	48.26	(-12.7 to +12.7)	(53.35 to 121.95)	#3
		3.81 Sq. Rod		30.48			
		5.08 x 7.62 Rod		48.26			
		5.08 x 7.62 Rod		30.48			
		Tip Vortex A/F (NACA 0012)		48.26			
		Tip Vortex A/F (NACA 0012)		30.48			

Figure 4 Configurations and Measurement Locations For Contraction and Screening Tests

is based on a similar design of R. Betchov (30) and produces, to some degree, isotropic turbulence of reasonably high intensity. For the steady distortion part of this program the porcupine was removed and the outlet snout of the generator covered with honeycomb to provide a uniform flow over the distortion generating bodies. Measurements of the velocity fields were made in the duct itself and upstream of the suction duct.

Outside of the duct, measurements were made with traversing hot wire probes. The alignment of the probe traverse mechanism was accomplished by mounting the probes on support rails attached to 2.54 cm thick steel bed plates. The probe positions were set using a laser beam directed along the rig axis. For the turbulence and vortex measurements, 'X' wires were used enabling two components of velocity to be determined. Specifically, these were the streamwise velocity component and the vertical transverse component. A single hot wire was used to measure the steady streamwise velocity distortions.

Inside of the duct, in the high velocity region, the turbulence and mean velocity measurements were made with 'X' hot wires and a wedge probe, respectively. The wedge probe allowed the magnitude and vertical angle of the component of the mean velocity vector in the vertical plane to be determined. Figure 4 contains a table of the measurement types and probe locations for the contraction and screening experiments. All turbulence fields were investigated with two probes to provide information about their transverse nature. A description of the measurement types and their accuracy is presented in Appendix A.

5.1.1 The Contraction of Turbulence and Steady Distortions

The contraction of turbulence was measured with the turbulence generating porcupine in place, in the plenum. The measurements were made at three axial locations through the contraction (55.8 cm, 25.4 cm and -20.32 cm referenced to the bellmouth face with negative distance downstream) as shown in Figure 5. The two probes were separated by incremental amounts at each location in the horizontal transverse plane. The sum and difference of the signals from

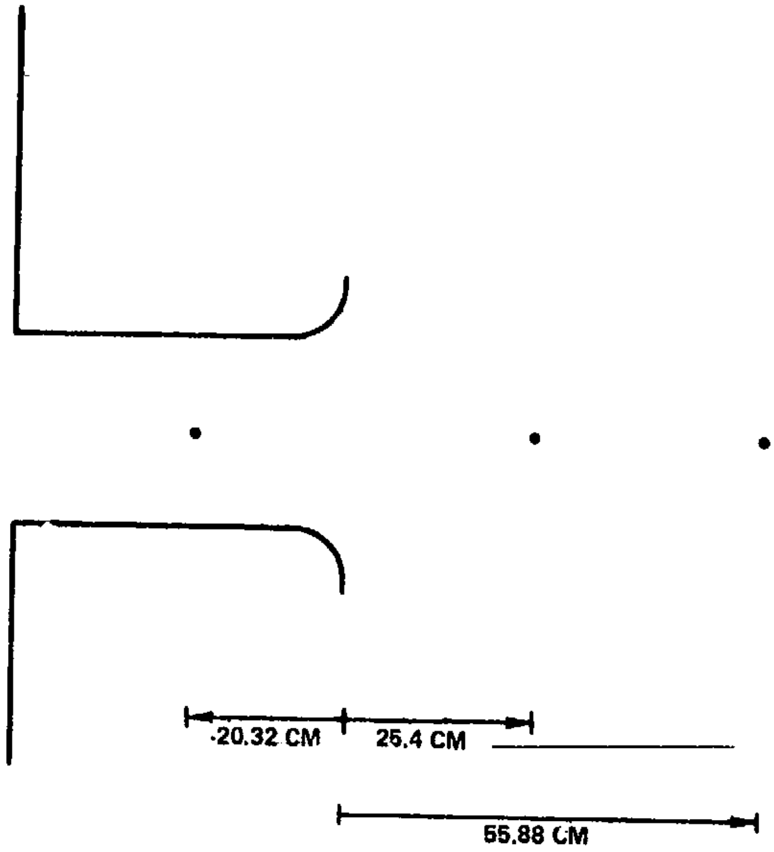

Figure 5 Axial Measurement Locations for Turbulence Contraction Experiment

each hotwire probe were recorded on magnetic tape and subsequently analyzed. The duct velocities examined in the contraction experiments nominally ranged from 30.48 m/s to 121.95 m/s. This allowed contraction ratios from about 1 to 21.3 to be examined.

Auto correlations, cross correlations, PSDs and mean square values were obtained directly from the analysis. Figures 6 and 7 show how the auto correlations of the streamwise and transverse velocity components change as the turbulence is convected through various contractions. It seems that the turbulence deviates somewhat from the isotropic at the initial point since the auto correlation function of the streamwise component becomes negative; however, the turbulent kinetic energy is reasonably evenly distributed at this point. The streamwise component auto correlations at the two highest contraction ratios display somewhat anomalous characteristics as the tendency to narrowing

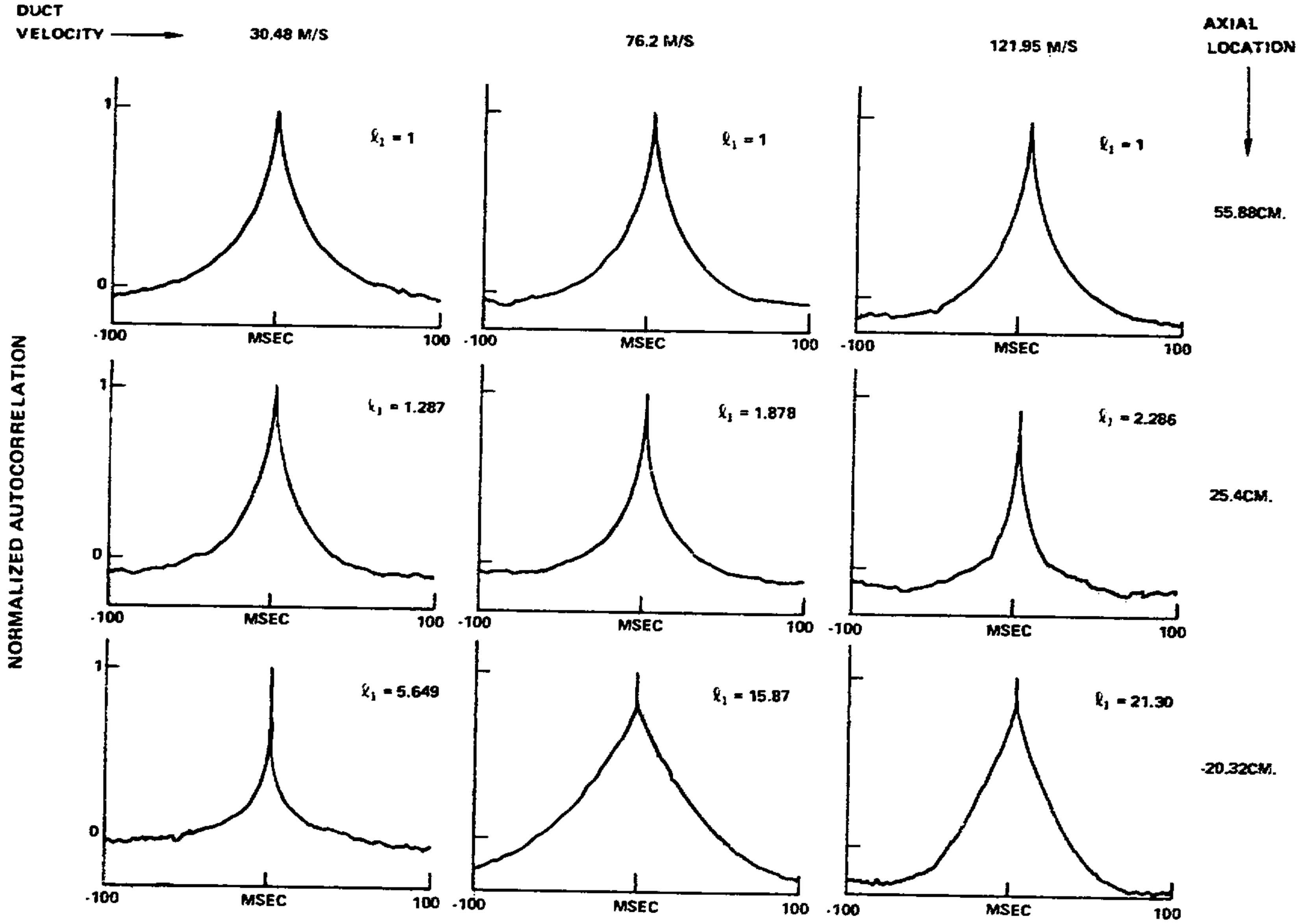

Figure 6 *The Change in the Streamwise Component Auto Correlation on Convection Through the Flow Contraction (Contraction Ratio - ℓ_1)*

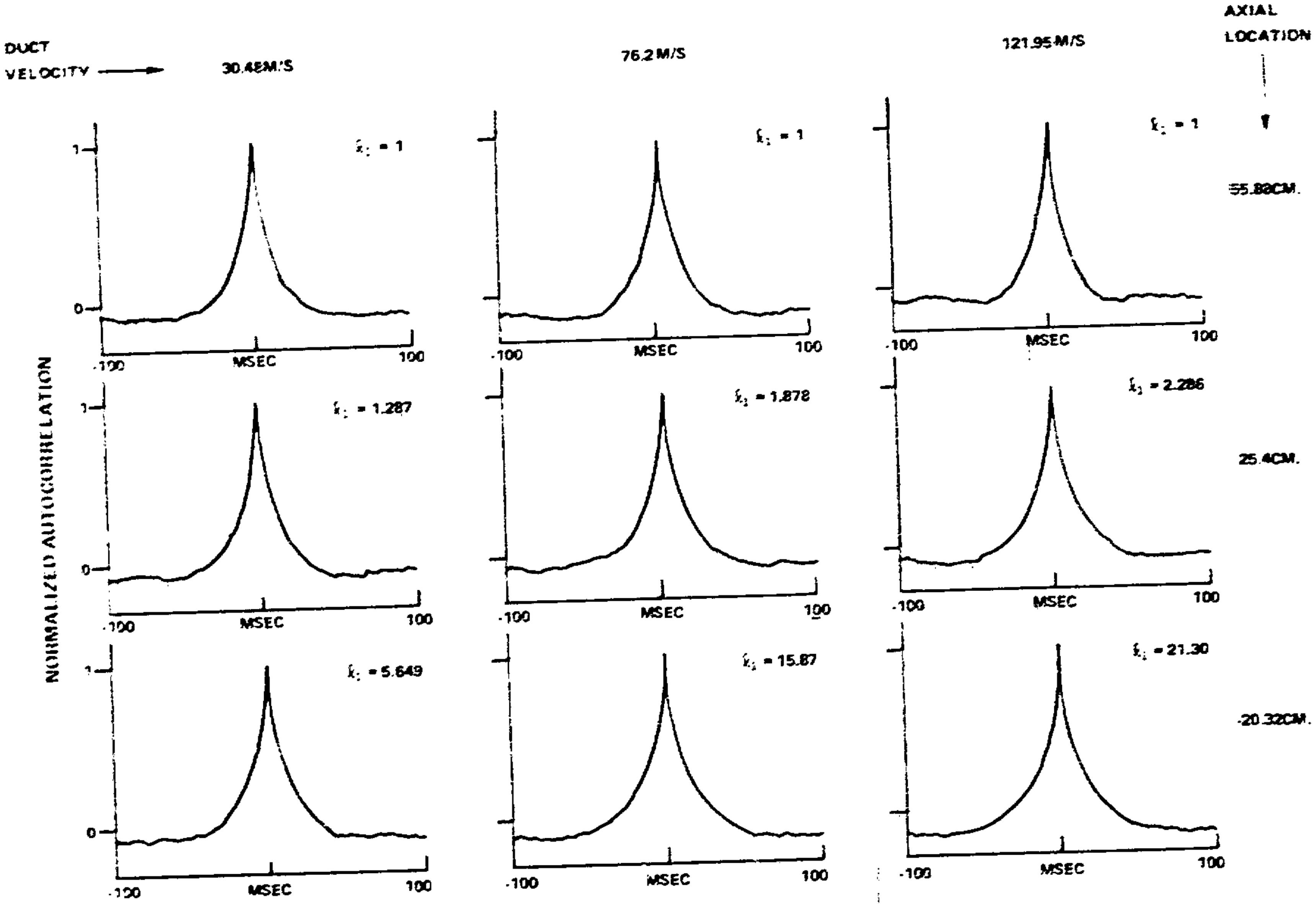

Figure 7 The Change in the Transverse Component Autocorrelation on Convection Through the Flow Contraction (Contraction Ratio - ℓ_1)

of the auto correlation with increasing contraction is reversed in these two cases. This is explained later as due to transfer of turbulent kinetic energy from the transverse velocity component by turbulent inertial effects. From the auto correlations, this energy is transferred into the lower frequencies. The transverse component auto correlations indicate little change in energy distribution as the turbulence is contracted. The corresponding changes in the PSDs are shown in Figures 8 and 9. The change in the transverse structure of the turbulence as it is contracted can be found from the cross correlation, an example of which is shown in Figure 10. From the cross correlations, estimates of the transverse spatial auto correlations can be made by taking the values of the correlation at zero time delay and plotting them against the spatial separation of the probes. Examples of these spatial auto correlations are shown in Figure 11 as the contraction ratio increases, and the decreasing transverse extent of the correlation area is apparent. From these plots, estimates of the integral length scales were made and examined in light of the analytical models in Section 6. The change in the mean square values of the component velocities is shown in Figure 12 and the initial suppression of the streamwise velocity and the amplification of the transverse velocity that is observed by other investigators (31,32) is also seen here.

Turbulence fields are not the only type of distortion to be encountered in static engine operation. Steady and quasi-steady velocity distortions can also be present and the effect of a contraction on this type of distortion was also examined in the suction rig facility. The distortion generating bodies that were considered were a 3.81 cm square rod, a symmetric NACA Series 6 airfoil, and a symmetric NACA 0012 airfoil was used to generate a tip vortex. The axial measurement locations were the same as for the turbulence measurements.

The evolution of a steady axial velocity deficit as it is convected through the contraction is illustrated by the wakes of the airfoil and the rod shown in Figure 13. The airfoil wake is very rapidly and totally suppressed, while that of the bluff body persists somewhat longer. In both cases no trace of the wakes was found at the -20.32 cm (in the suction duct) location, at which the highest contraction ratios occurred.

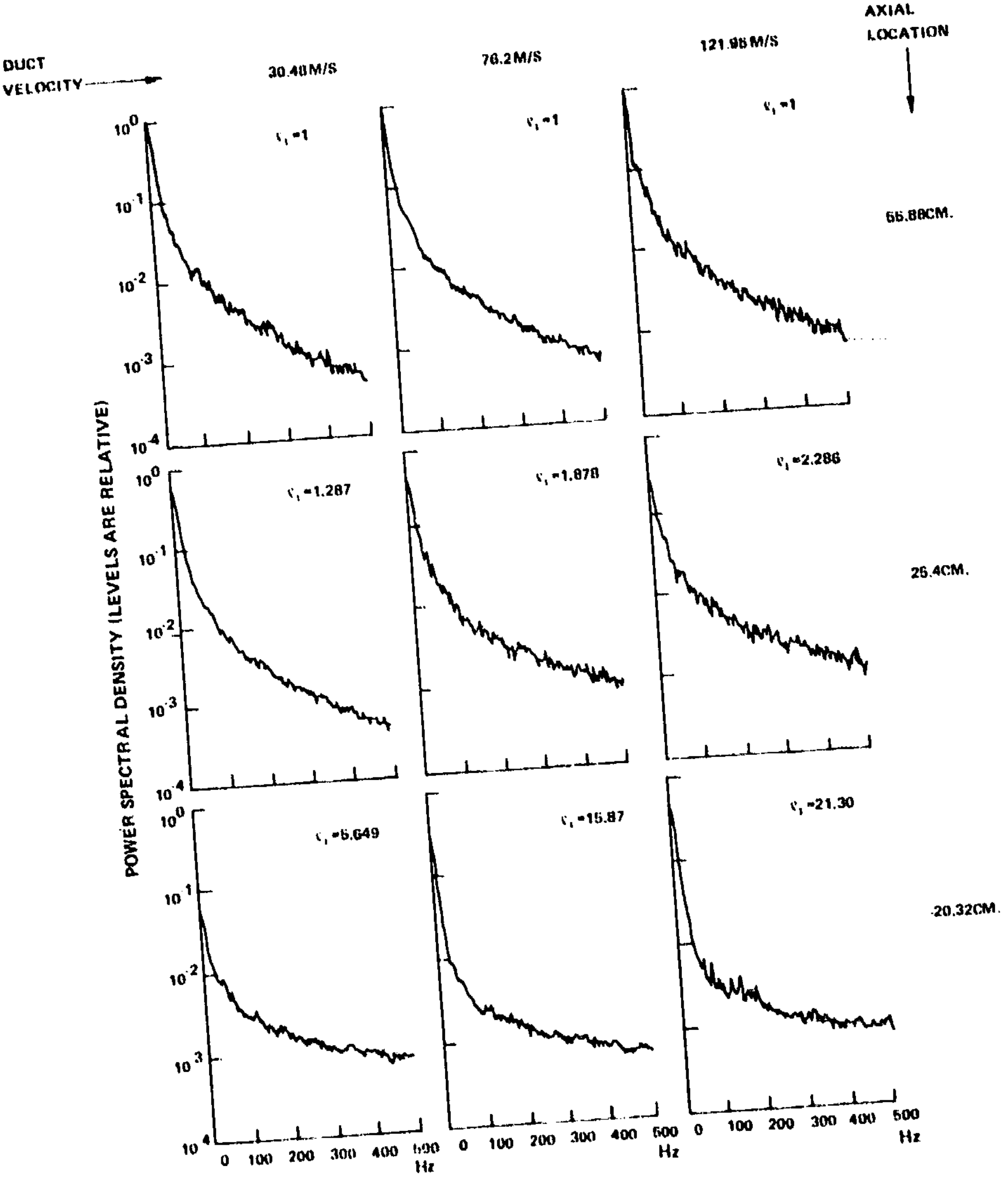

Figure 8 The Change in the Streamwise Component PSD on Convection Through the Contraction (Contraction Ratio - ϵ_1)

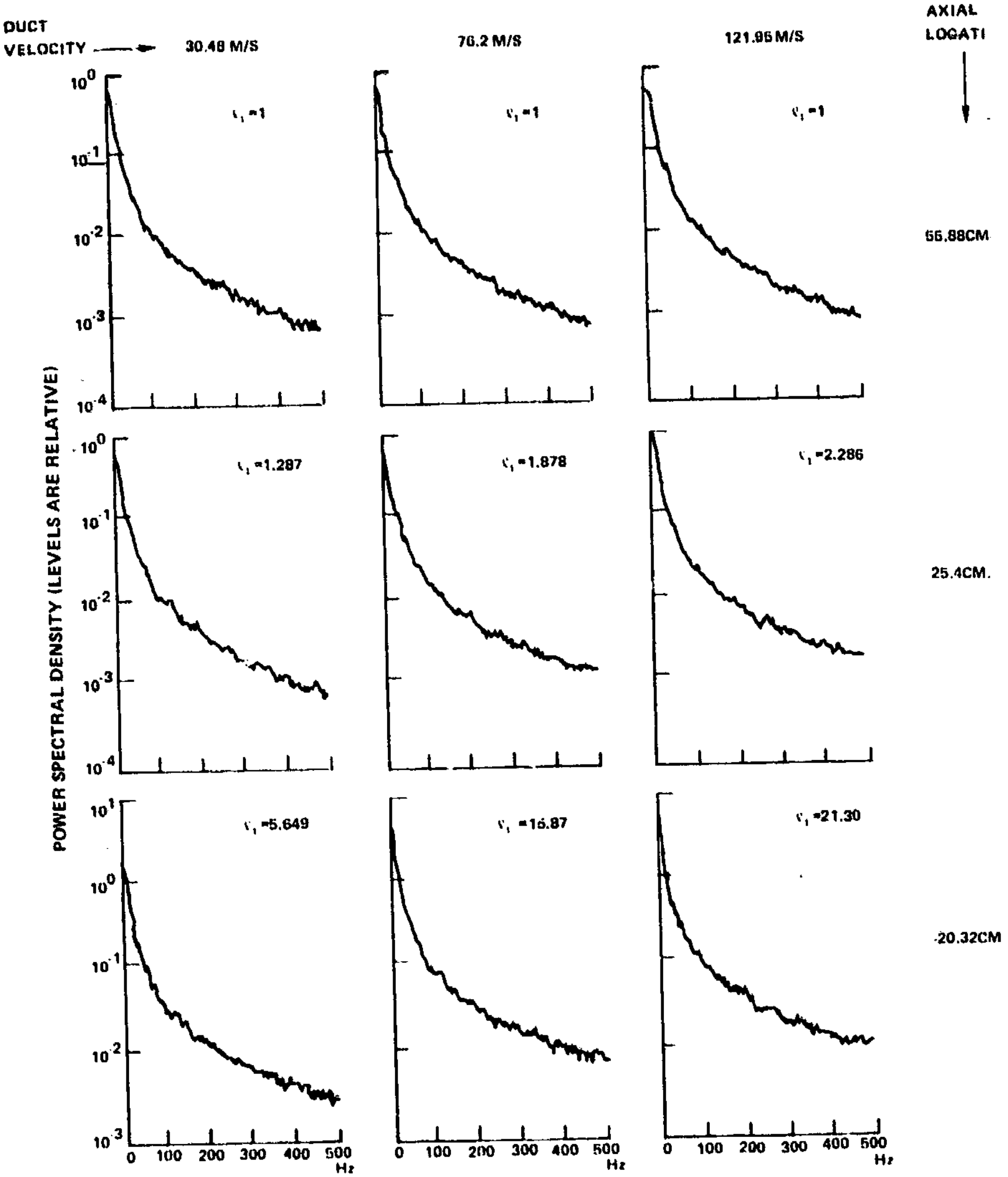

Figure 9 The Change in the Transverse Component PSD on Convection Through the Contraction (Contraction Ratio - ℓ_1)

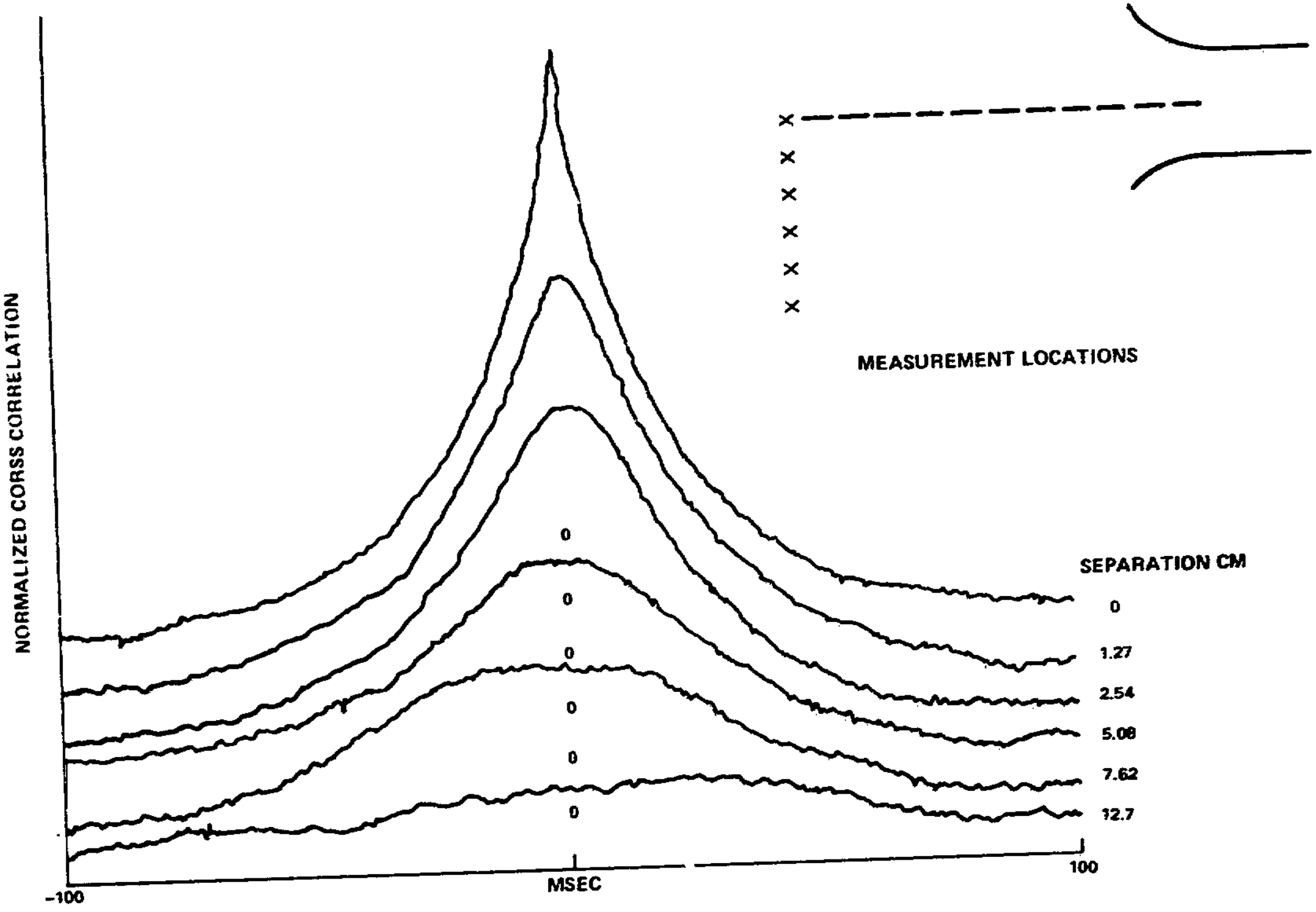

Figure 10 An Example of Cross Correlations of the Streamwise Velocity Component in the Transverse Direction (Axial Location 55.88 cm, Duct Speed 76.2 m/s)

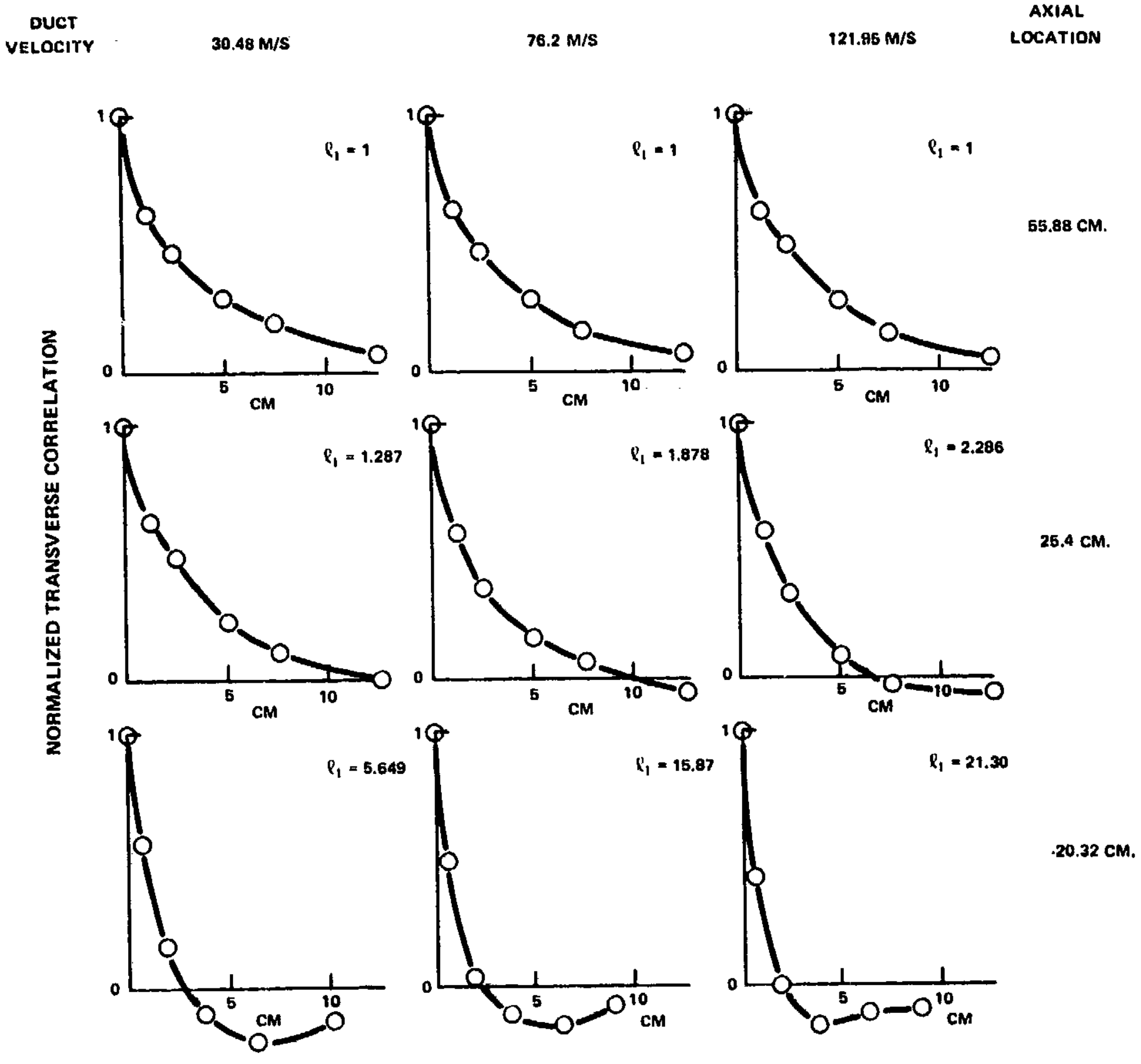

Figure 11 The Change in the Transverse Correlation of the Transverse Component on Convection Through the Flow Contraction (Contraction Ratio - ℓ_1)

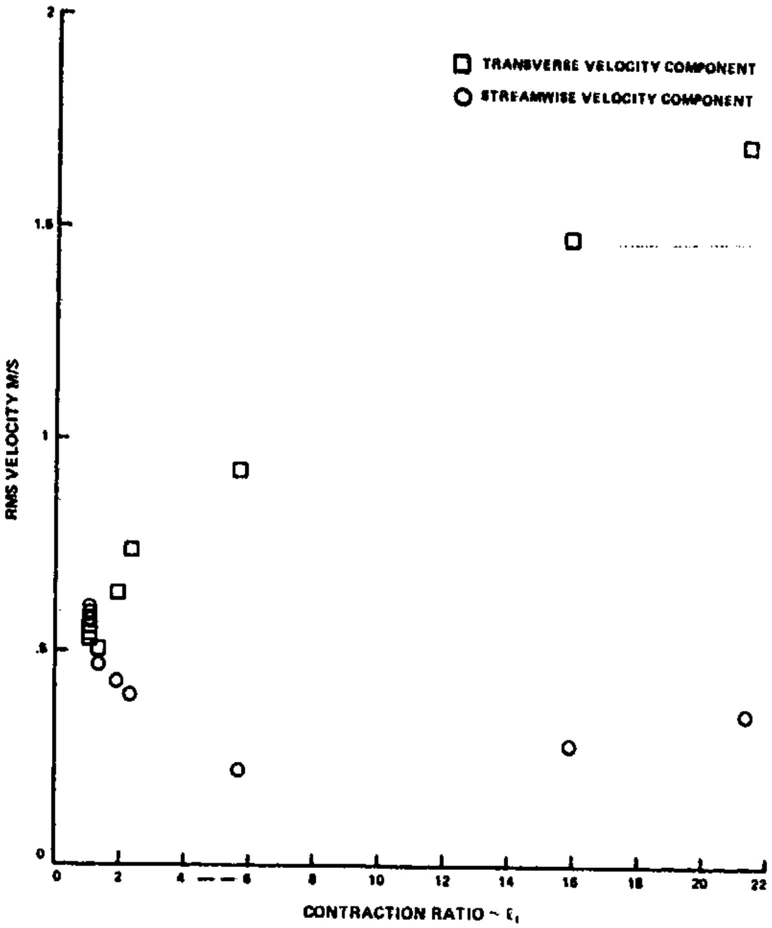

Figure 12 Variation of RMS Velocity Through the Flow Contraction

The NACA 0012 airfoil was set at the highest angle of attack possible without stalling, in order to generate as strong a tip vortex as possible. This was done by observing the flow over it with a cotton thread. The angle of attack was about 14°. The vortex was positioned approximately on the rig axis. Both streamwise and a transverse velocity component were measured in the vortex and the changes in these two aspects of the velocity field as the flow accelerates are shown in Figures 14 and 15. The transverse, or azimuthal, velocity field is substantially unchanged by the flow contraction while the streamwise velocity deficit associated with the vortex increases and broadens. This behavior of the streamwise deficit is completely opposite to that observed for the two dimensional wake and indicates the need for vortex suppression as near to the origin as possible.

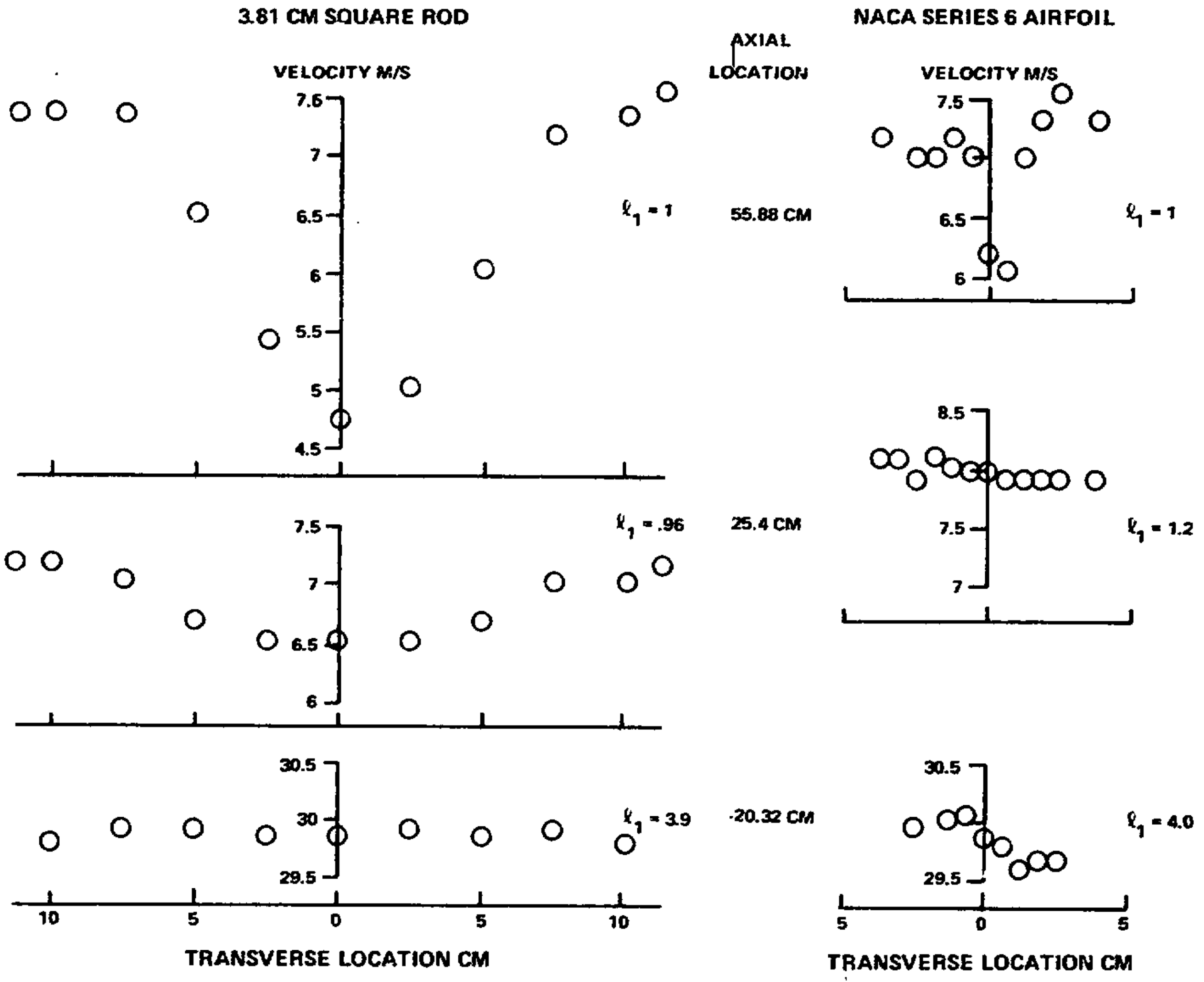

Figure 13 The Evolution of a Wake on Passage Through the Flow Contraction

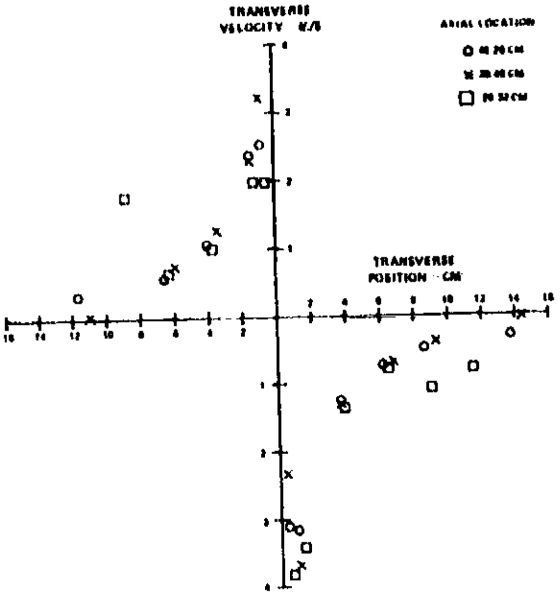

Figure 14 The Invariance of the Azimuthal Velocity Field Through a Contraction

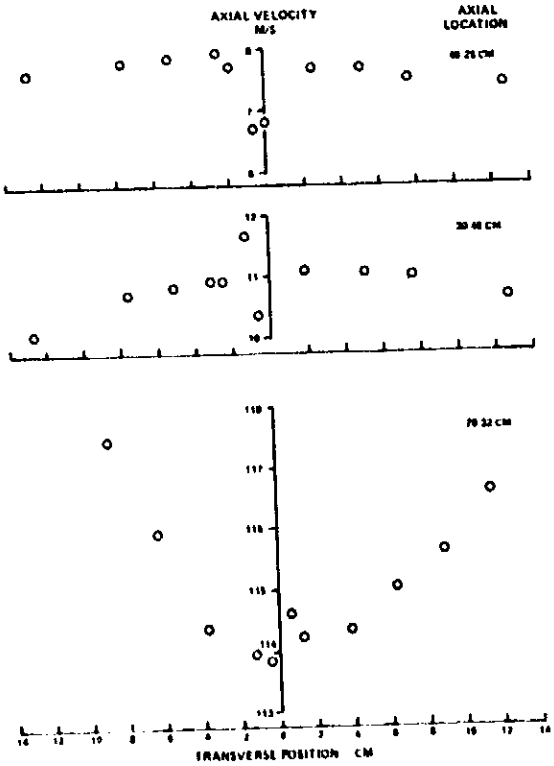

Figure 15 The Streamwise Velocity Field in a Vortex Under Flow Contraction

5.1.2 The Effect of Screens on Turbulence and Steady Distortions

As in the contraction experiment, the turbulence part of this test was conducted with the turbulence generator in place. Five screen types were examined; three were made of honeycomb and two of perforated plate. The honeycomb used had a nominal cell diameter of .3175 cm and the thicknesses (cell lengths) were 0.953 cm, 1.27 cm and 2.54 cm giving thickness to cell diameter ratios of 3, 4 and 8 respectively. The corresponding honeycomb construction material thicknesses were 0.008 cm, 0.005 cm, and 0.01 cm. The perforated plates that were tested had 41 percent and 66 percent open area. The hole diameter of each plate was .0366 cm and the plate thickness was .0126 cm. Each screen was mounted normal to the rig axis, 38.1 cm forward of the bellmouth, by means of a supporting frame and measurement locations were upstream and downstream of the screen at 30.48 cm and 48.26 cm (Figure 16). The duct velocities ranged from 30.49 m/s to 121.95 m/s. This variation allowed a range of screen throughflow velocities to be observed. A summary of test configurations and probe locations is shown in Figure 4.

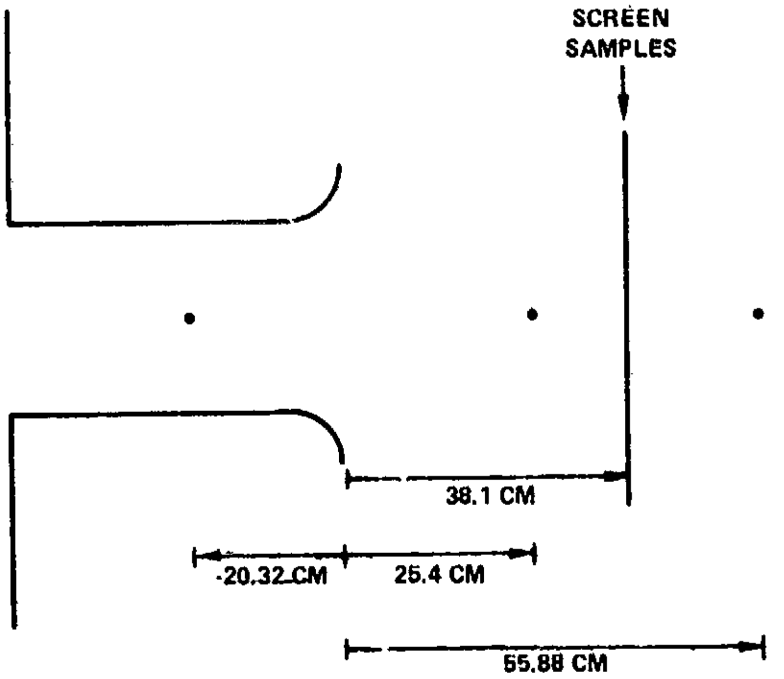

Figure 16 Axial Measurement Locations for Turbulence Screen Experiment

For the turbulence field definition the same techniques were used as in the contraction experiment. Auto correlations PSDs, cross correlations and mean square values of velocity components were determined on either side of the screens. The effect of the various screens on the auto correlations of each velocity component is illustrated in Figures 17, 18, 19 and 20 with the corresponding PSDs shown in Figures 21, 22, 23 and 24. The presence of small scale turbulence downstream of the honeycombs is immediately apparent. While some of this may be residual from the upstream field, the majority is due to turbulence self-generated by the screen. This phenomenon is particularly apparent in the transverse turbulent velocity component which is heavily suppressed by all honeycombs. The auto correlations (which are all normalized) downstream of the perforated plate, however, do not show a distinct bi-modal behavior which indicates that the self generated turbulence spans the whole spectrum rather than being confined to the higher wave numbers. This is borne out by the PSDs downstream of the perforated plate, where the level increases at all frequencies with increasing throughflow speed (Figure 25). The turbulent energy generation at the low frequencies is due to the unbounded nature of the flow and the finiteness of the screen. The high resistance perforated plates probably divert the incident flow over the edges of the plate where it separates and thereby produces turbulent kinetic energy at wave numbers corresponding to the plate dimensions. The PSDs of the velocity components downstream of the honeycomb show the low wave number energy to be constant, with the higher frequency levels increasing with throughflow velocity. The change in the transverse structure of the turbulence across the screen can be determined to some extent by the cross correlations. An example of these for honeycomb and perforated plate is shown in Figures 26 and 27. Estimates of the transverse integral length scale change are made from these which are discussed in Section 6. The streamwise integral length scales determined from the auto correlations are also examined in Section 6. In view of the contamination of the downstream (post screen) turbulence field with self generated turbulence, it was necessary to extract the residual upstream turbulence field from these results. This is discussed in Section 6 and in consequence the modification of the upstream kinetic energy components by the screens is discussed there.

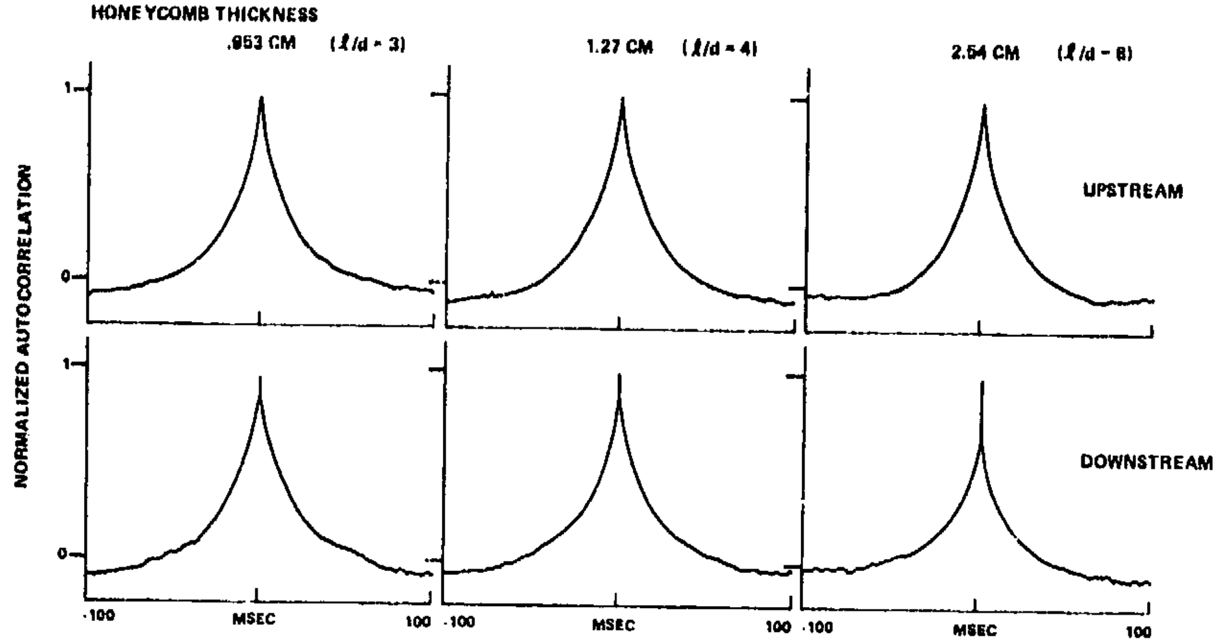

Figure 17 The Change in the Streamwise Component Autocorrelation Across the Honeycomb Screens. Duct Speed 76.2 m/s

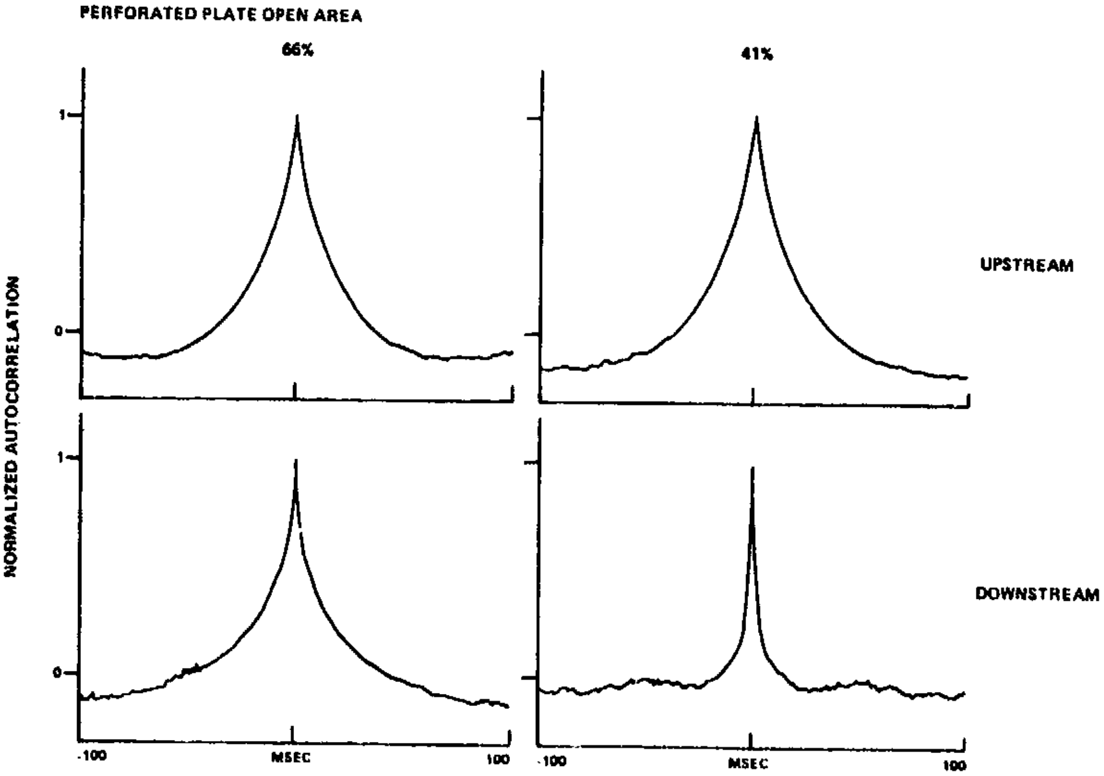

Figure 18 The Change in the Streamwise Component Autocorrelation Across Perforated Plate. Duct Speed 76.2 m/s

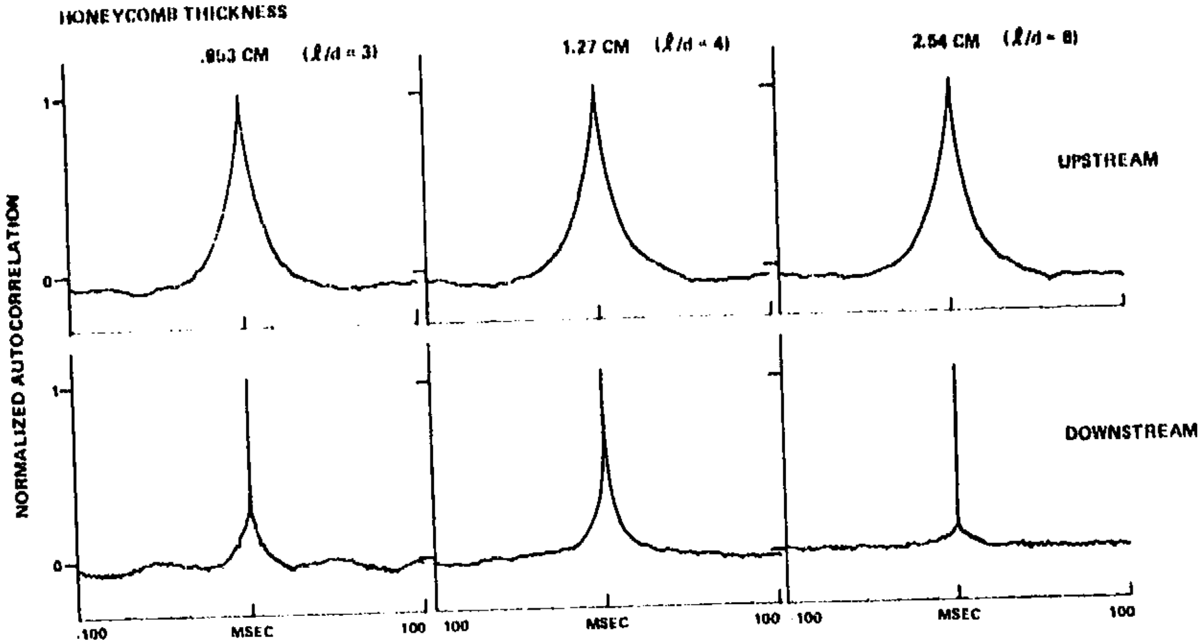

Figure 19 The Chang. in the Transverse Component Autocorrelation Across the Honeycomb Screens. Duct Speed 76.2 m/s

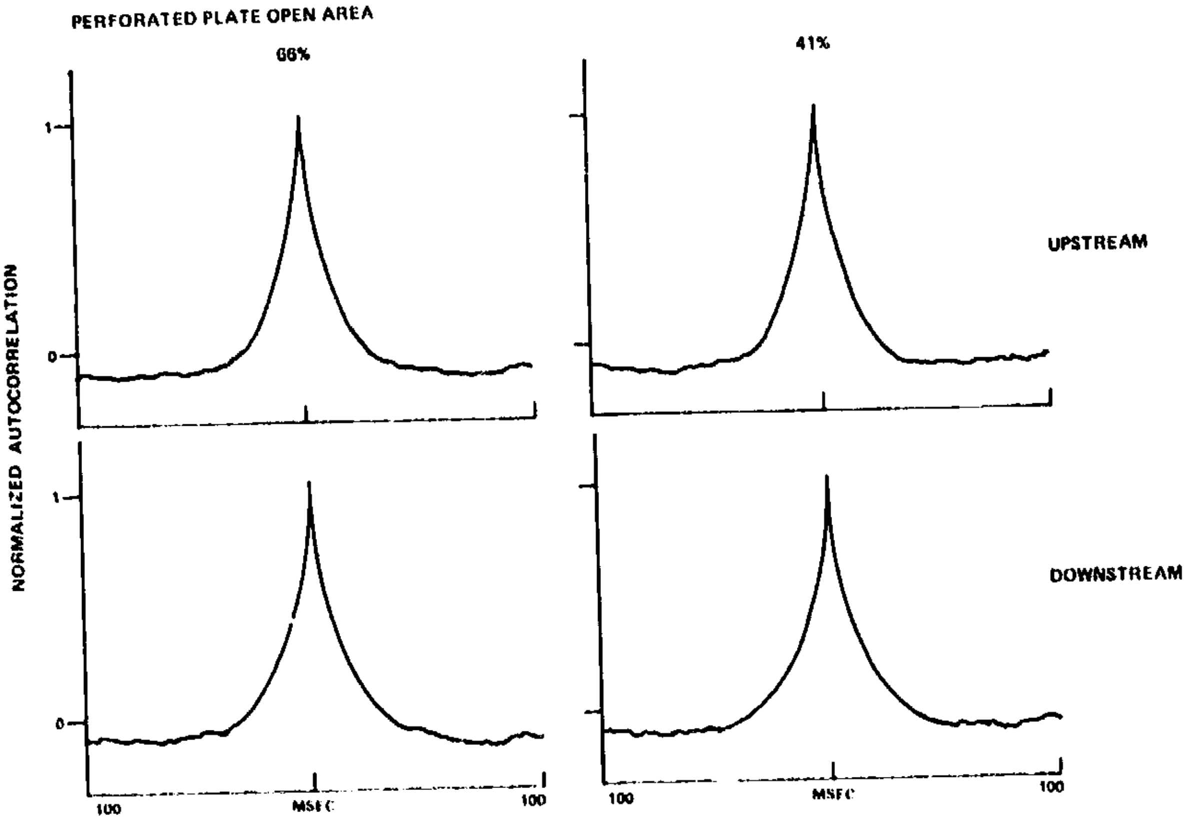

Figure 20 The Change in the Transverse Component Autocorrelation Across Perforated Plate. Duct Speed 76.2 m/s

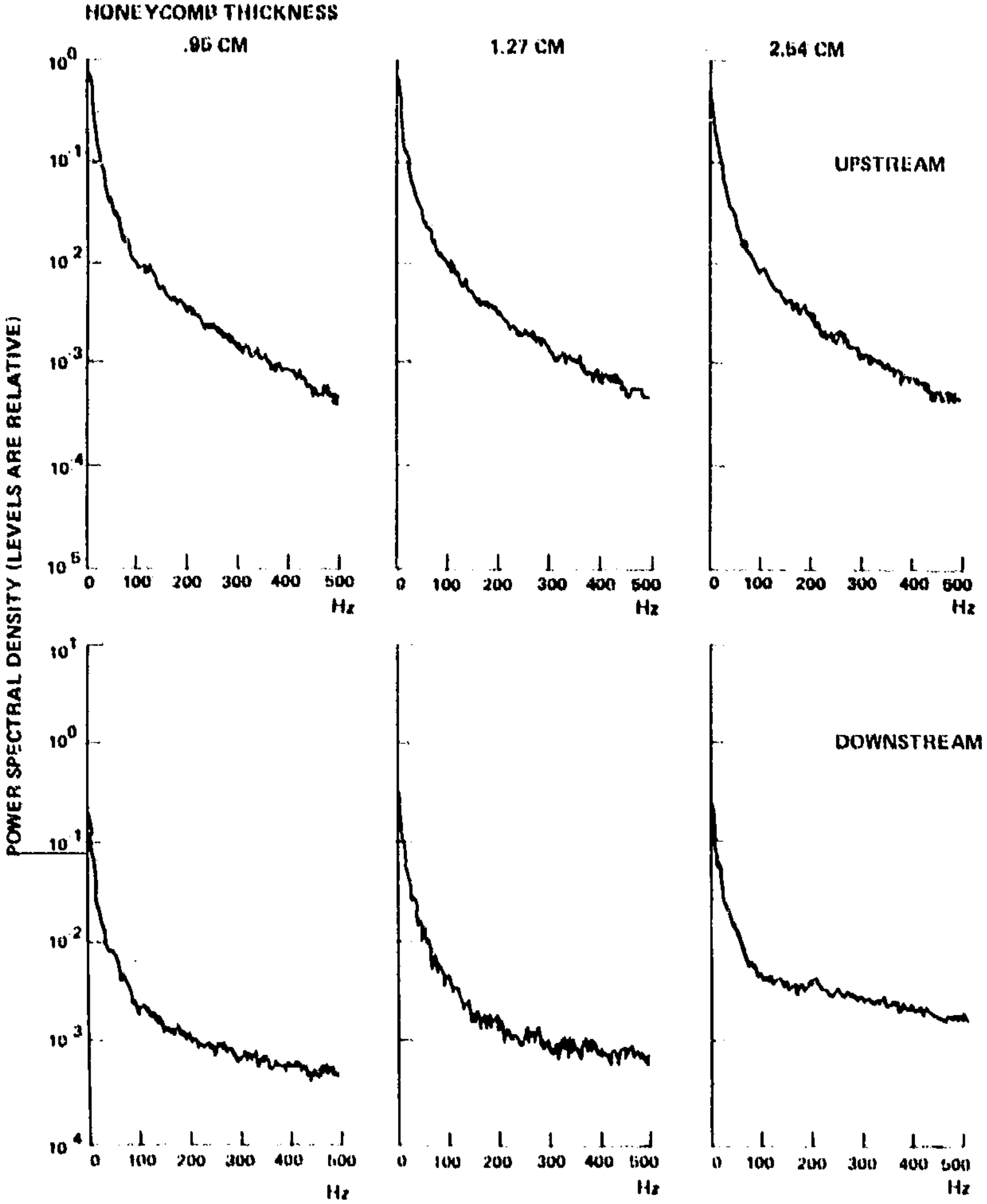

Figure 21 The Change in the Streamwise Component PSD Across the Honeycomb Screens. Duct Speed 26.2 m/s

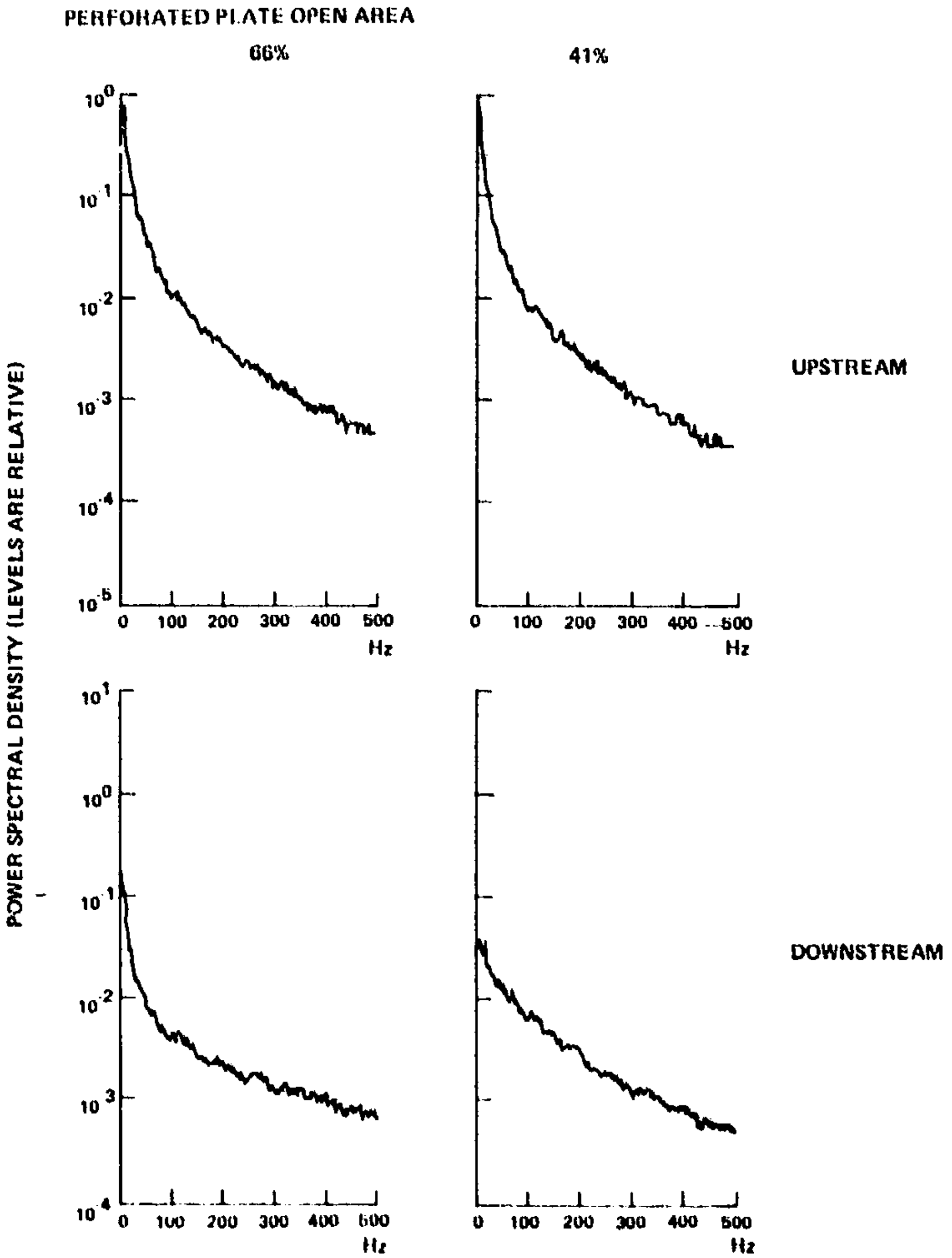

Figure 22 The Change in the Streamwise Component PSD Across Perforated Plate. Duct Speed 76.2 m/s

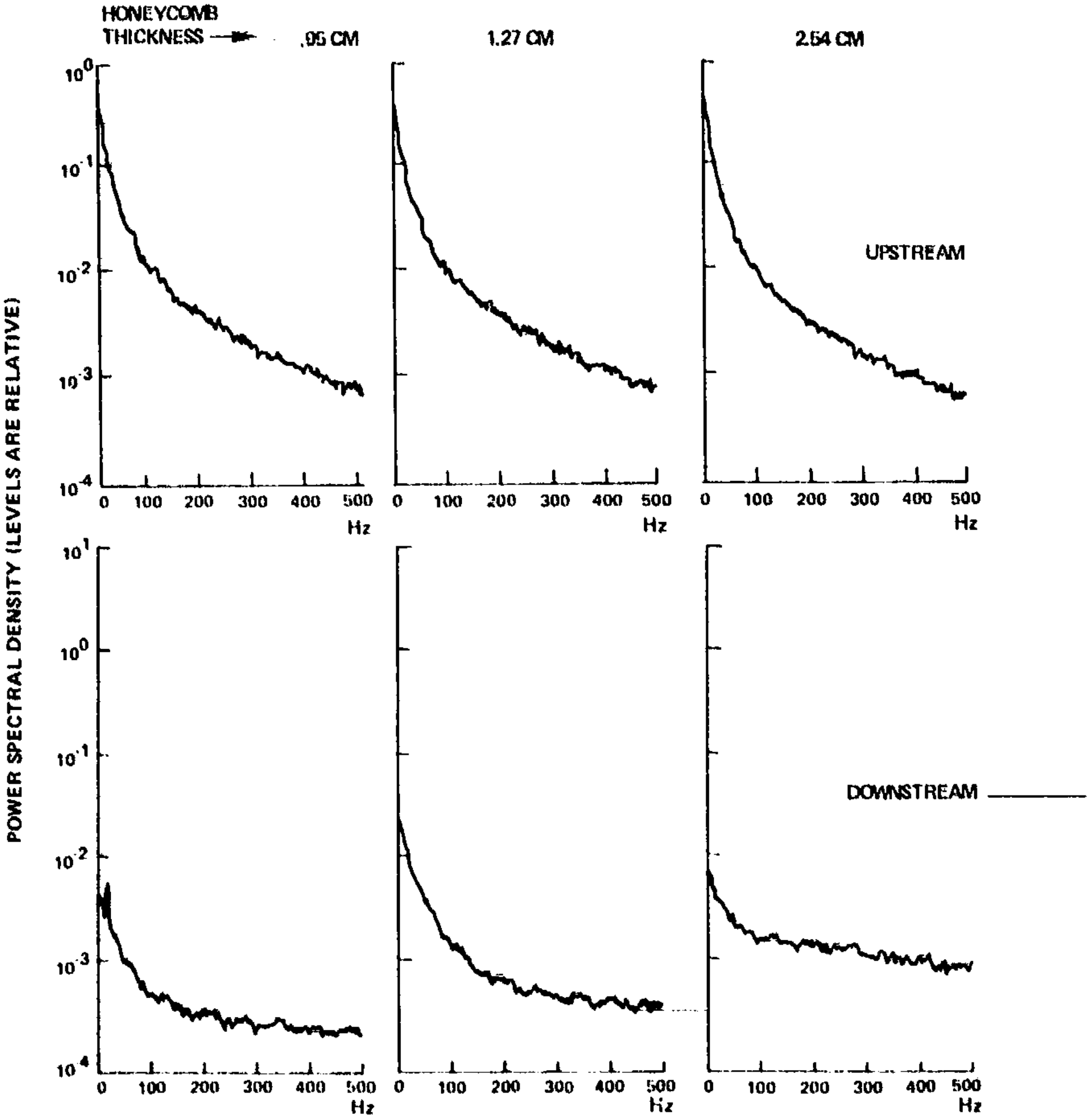

Figure 23 The Change in the Transverse Component PSD Across the Honeycomb Screens. Duct Speed 76.2 m/s

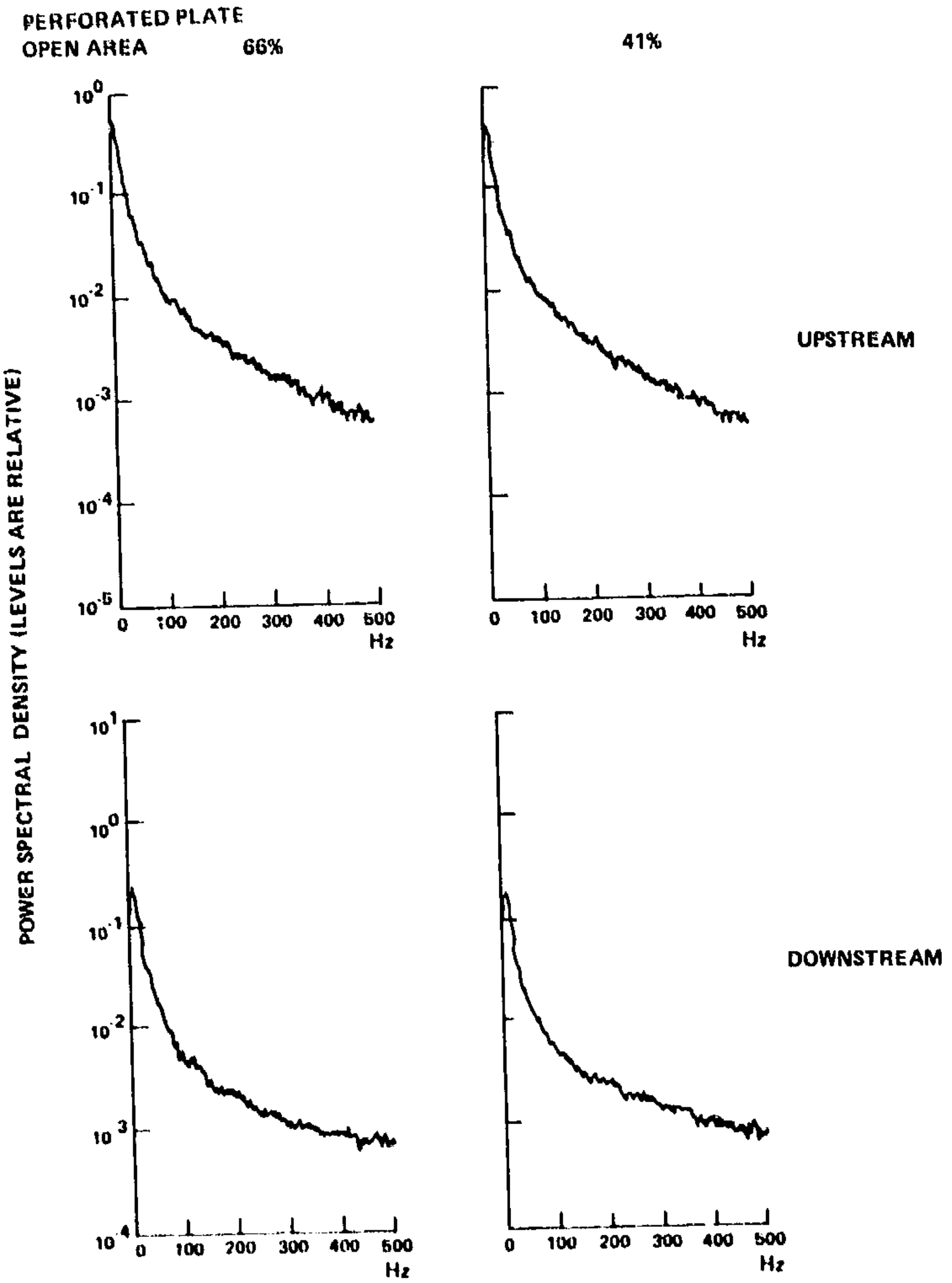

Figure 24 The Change in the Transverse Component PSD Across Perforated Plate. Duct Speed 76.2 m/s

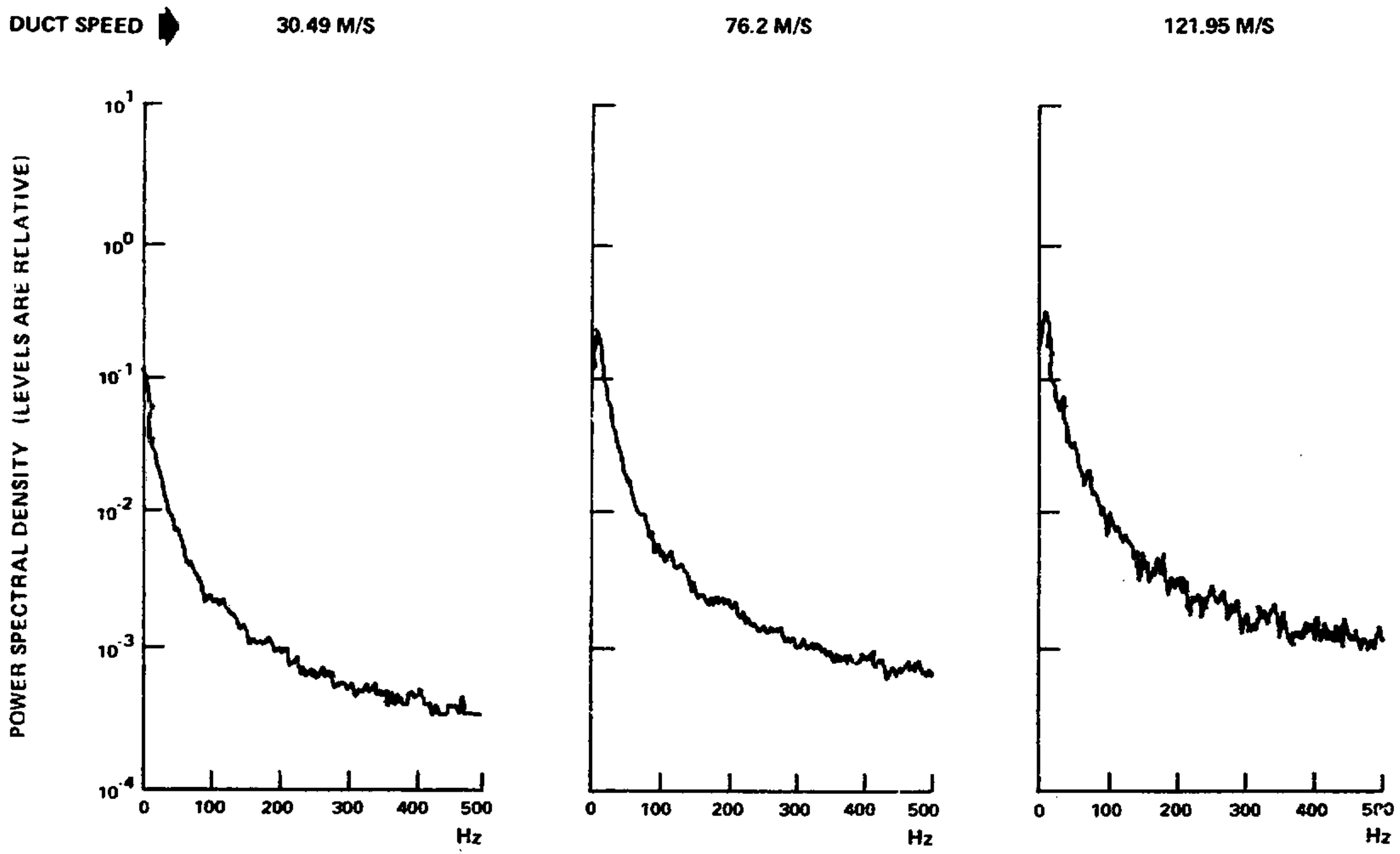

Figure 25 The Transverse Component PSDs Downstream of the 66% Open Area Perforated Plate (Increasing Throughflow Speed).

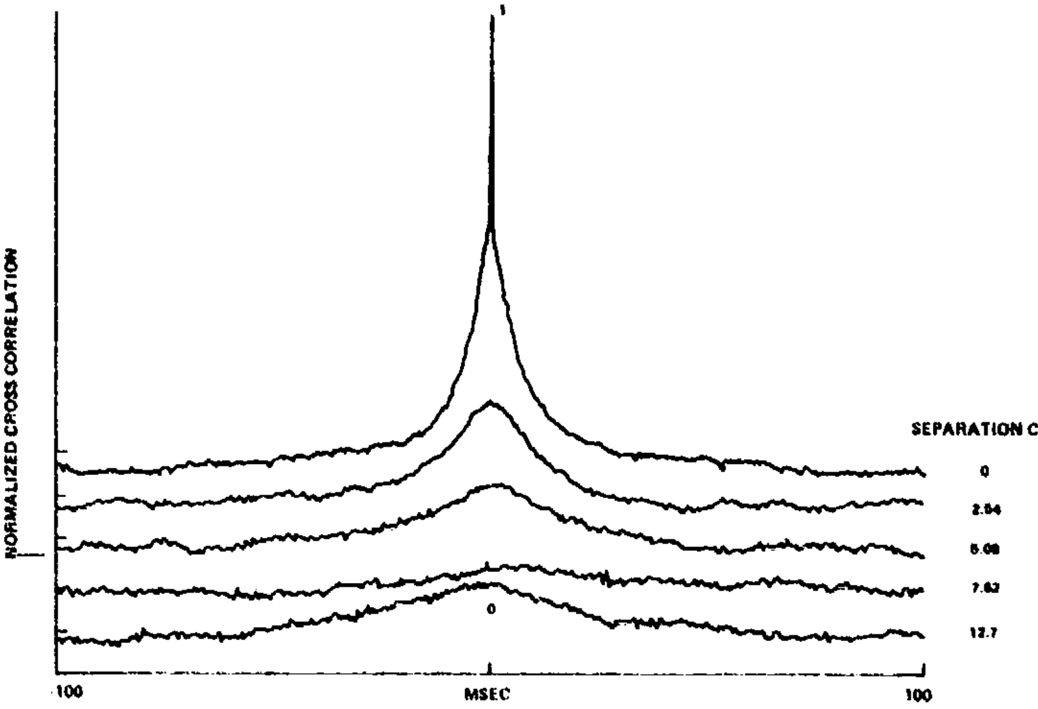

Figure 26 An Example of Cross Correlation of the Transverse Velocity Component in the Transverse Direction Downstream of 1.27 cm Honeycomb

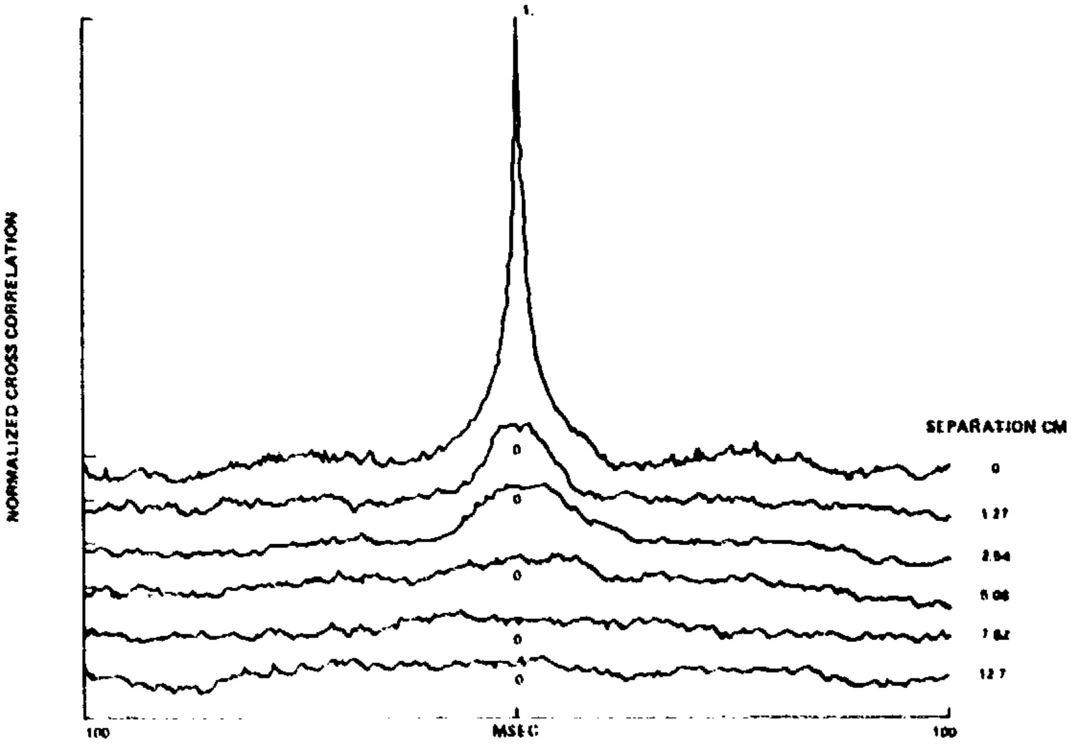

Figure 27 An Example of Cross Correlation of the Streamwise Velocity Component in the Transverse Direction Downstream of 41% Open Area Perforated Plate

For the steady distortion portion of this experiment, the generators used were a 3.81 cm square rod, a 5.08 cm x 7.62 cm rod and the afore mentioned NACA 0012 airfoil for making a tip vortex. The rods produced streamwise velocity deficits and the effect of the two screen types on them is shown in Figures 28 and 29. In general, the higher the resistance of the screen, the greater is the suppression of the deficit. The screen having the highest resistance, the 41 percent open area perforated plate produces a deficit inversion, changing the wake into a jet.

The tip vortex azimuthal velocity field was destroyed by all honeycomb tested, (Figure 30), however, the axial velocity distortion associated with the vortex increased across the honeycomb. It is interesting to observe that this distortion is almost cusp-like. The perforated plates were not effective as suppressors of the vortex, as can be seen in Figure 31. The core of the vortex becomes larger due to the plates, but outside of this region, little change is seen in the azimuthal velocity field. The axial velocity deficit change depended on the open area of perforated plate. The lower resistance plate increased it while the higher suppressed it. These contrary effects could be due to the previously mentioned deviation of the flow around the plate.

5.1.3 The Pressure Drop Coefficients of the Screens

Theoretical models of the pressure drop coefficients of perforated plate and honeycomb were presented in (29). Values of the pressure drop coefficients of the screens were used in the test program with a view to assessing these theoretical models. Briefly the theoretical models are for a honeycomb, Blasius' pipe flow coefficient formula,

$$K = \frac{.3164}{Re^{.25}} \cdot \frac{\ell}{d} \qquad 1$$

While the results of the work of Baines and Pearson, discussed in 29, was suggested for perforated plate

$$K = \left(\frac{1}{C_c\ (1-s)} - 1\right)^2 \qquad 2$$

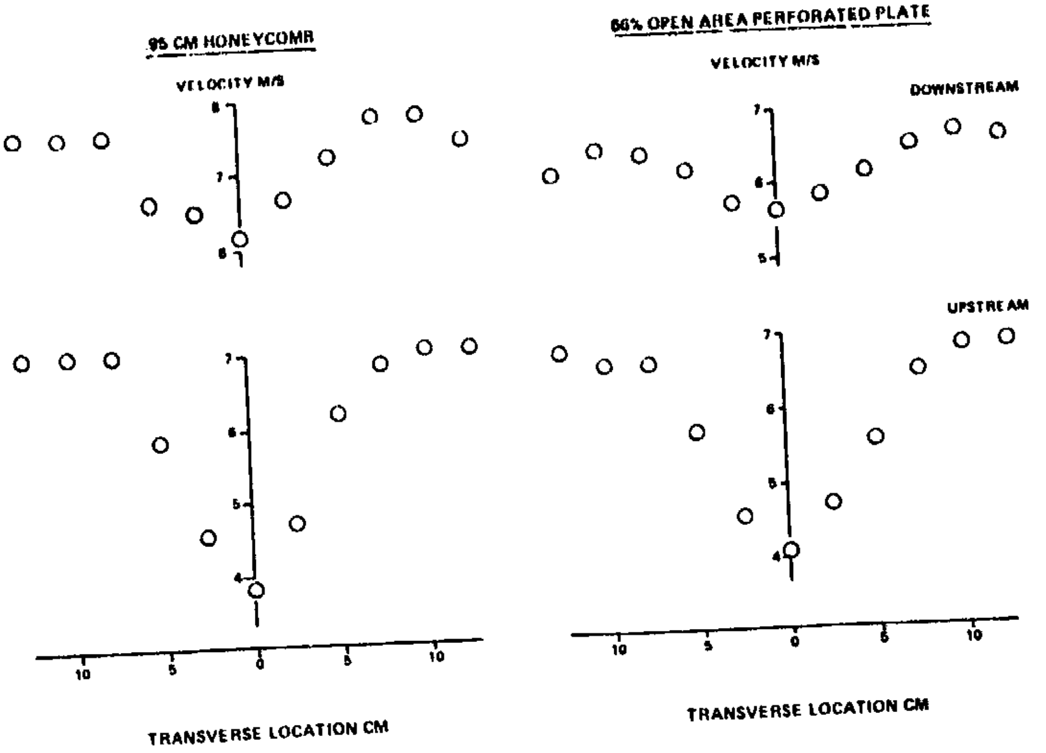

Figure 28 The Change in a Wake From a 3.81 cm Square Rod on Convection Through a Screen

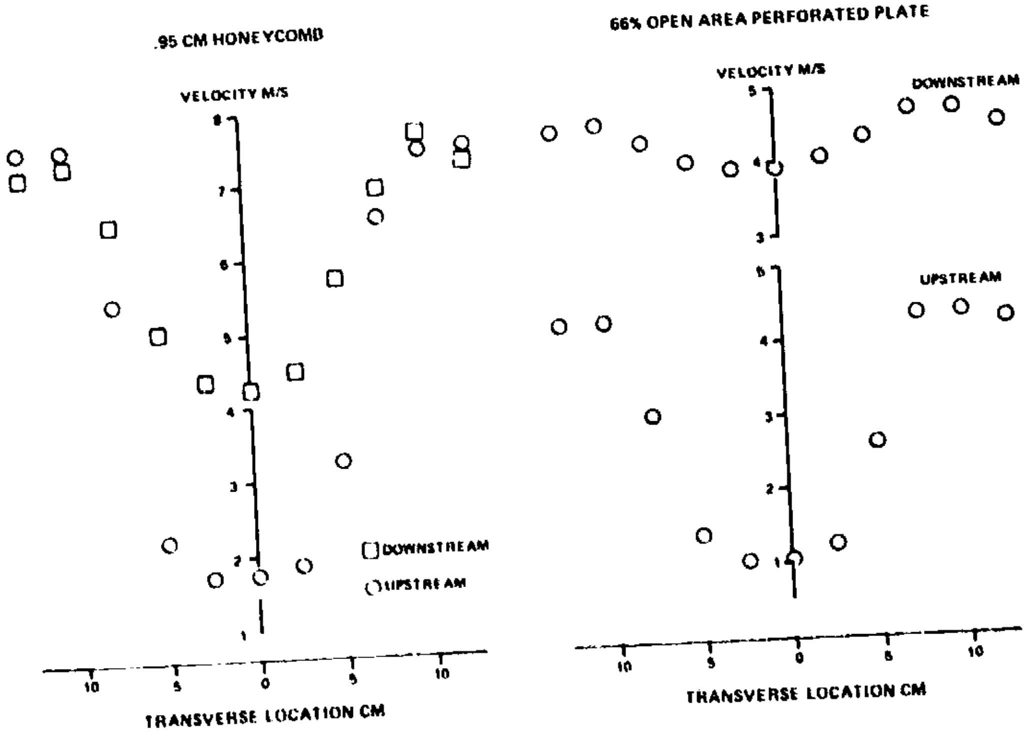

Figure 29 The Change in a Wake From a 5.08 cm x 7.62 cm Rod on Convection Through a Screen

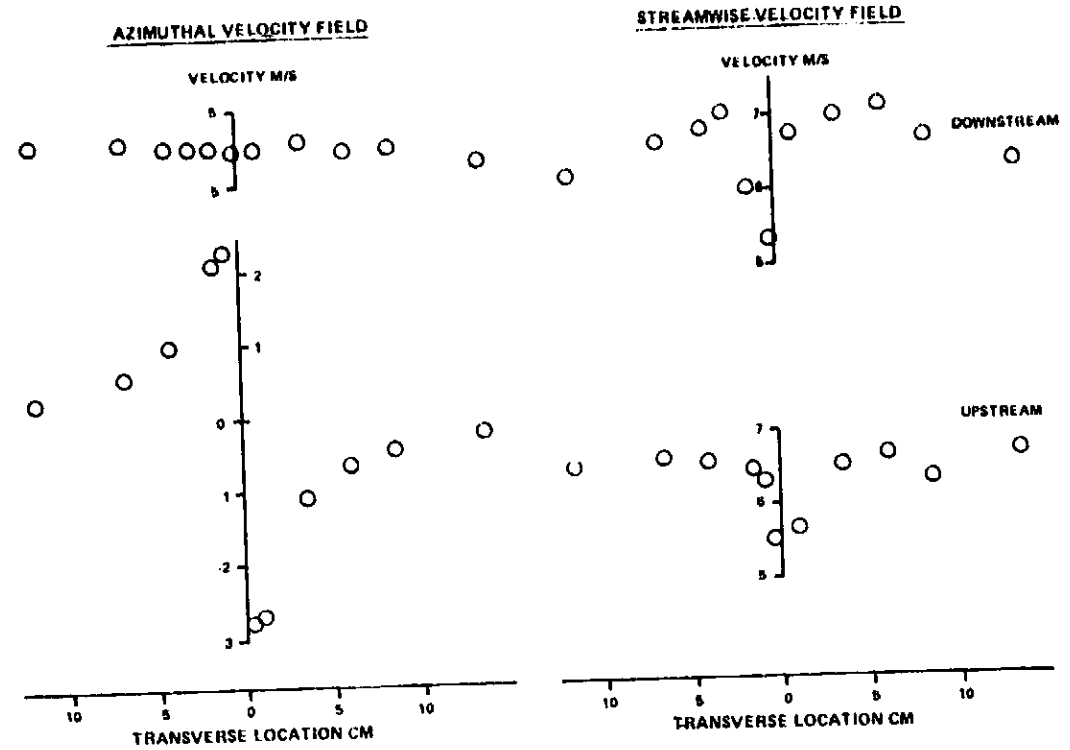

Figure 30 The Change in the Velocity Field of a Vortex on Convection Through 1.27 cm Thick Honeycomb

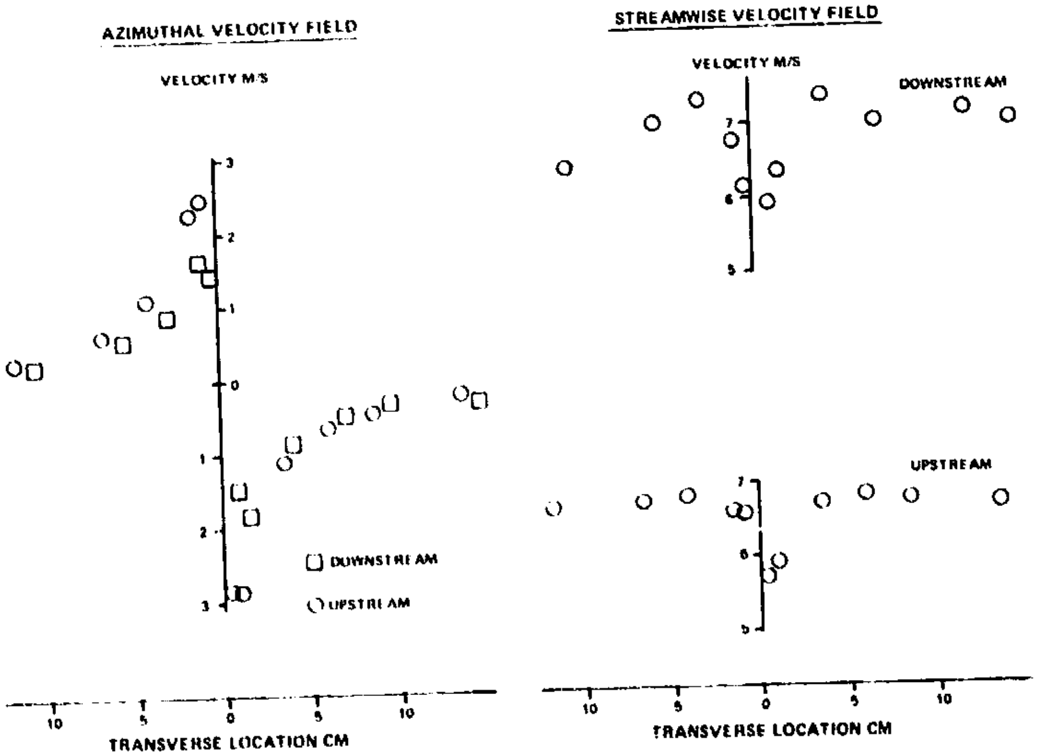

Figure 31 The Change in the Velocity Field of a Vortex on Convection Through 66% Open Area Perforated Plate

The screen pressure drop coefficients were obtained by placing the screens over a nozzle and measuring the static pressure drop across them. This information, together with the velocity at the screen (determined with a calibrated venturi) allowed the screen pressure drop coefficient to be calculated. A schematic diagram of the test arrangement is shown in Figure 32. A gauze was mounted upstream in the supply pipe to produce a uniform velocity profile at the test screen. The pressure drop coefficient is, by definition:

$$K = \frac{p_{TU} - p_{TD}}{q} \qquad 3$$

or in terms of the measured quantities,

$$K = \frac{p_{SU} - p_{AMB}}{\frac{1}{2}\rho U_1^2} \qquad 4$$

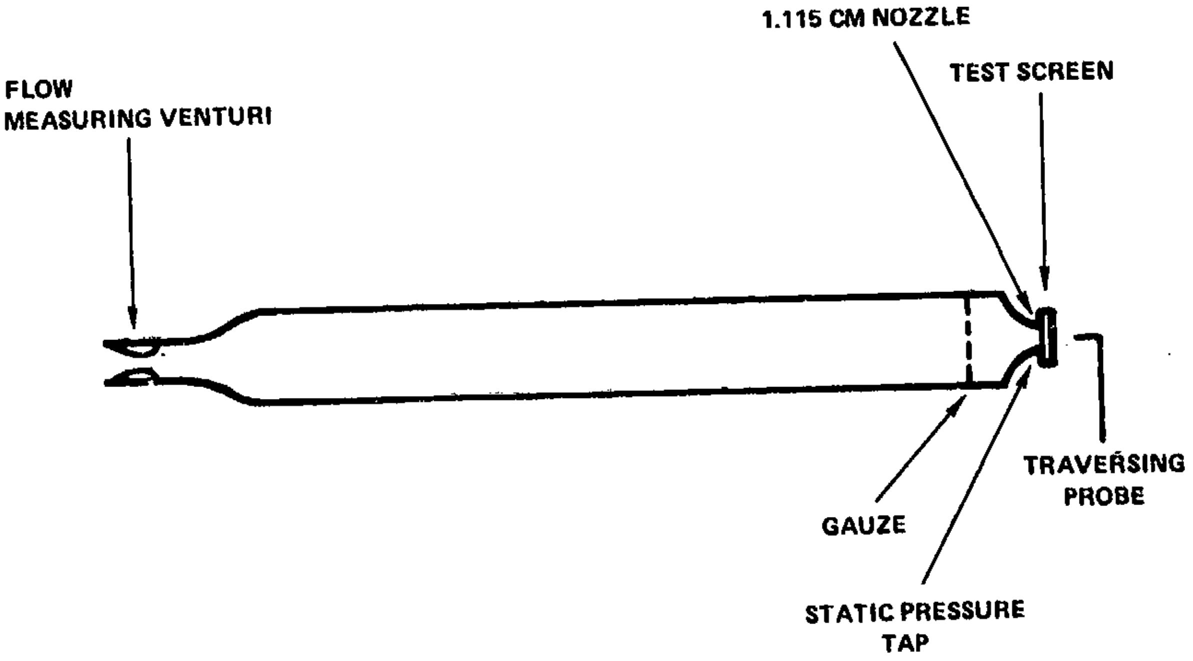

Figure 32 Schematic Diagram of Screen Pressure Drop Coefficient Measurement Arrangement

ORIGINAL PAGE IS
OF POOR QUALITY

These quantities were measured at several throughflow velocities and the results are shown in Figure 33. The loss coefficient of each screen is reasonably constant with throughflow velocity. The higher solidity perforated plate (41 percent open area) has a higher resistance than the 66 percent open area perforated plate. The resistances of the 0.95 cm and 1.27 cm thick honeycomb screens are apparently reversed; however, as was noted earlier in this section, the 1.27 cm honeycomb is made of a thinner material. This raised the possibility that there was a significant base drag contribution to the honeycomb pressure drop. This possibility, however, was discounted since the open area ratios of the screens were between 98 percent and 99 percent. On inspection of the 0.95 cm honeycomb under a microscope, it was seen that there was much more burring of this honeycomb than the other two and the inconsistency in the pressure drop coefficients was ascribed to this. In Figure 34 a table is shown comparing measurements and theoretical predictions of the pressure drop coefficient. As can be seen for the 1.27cm and 2.54 cm honeycombs, there was a ratio of about 2:1 between measured and predicted values. The burred 0.95 cm honeycomb had a corresponding ratio of 3.8:1. It seems, then, that entrance conditions to the honeycomb can be important in determining the pressure drop coefficient, K, and even with apparently smooth inlet conditions there is still sufficient roughness to raise the value of K above the smooth pipe value. It should be recalled that in (29) the pressure drop coefficient of a 0.95 cm diameter honeycomb was accurately predicted by Blasius' formula

$$K = \frac{.3164}{Re^{.25}} \cdot \frac{\ell}{d} \qquad 5$$

It is thus concluded that for any given honeycomb it is possible for its pressure drop coefficient to be up to four times the Blasius' coefficient and a typical value of two is suggested for design purposes.

$$K = \frac{.6328}{Re^{.25}} \cdot \frac{\ell}{d} \qquad 6$$

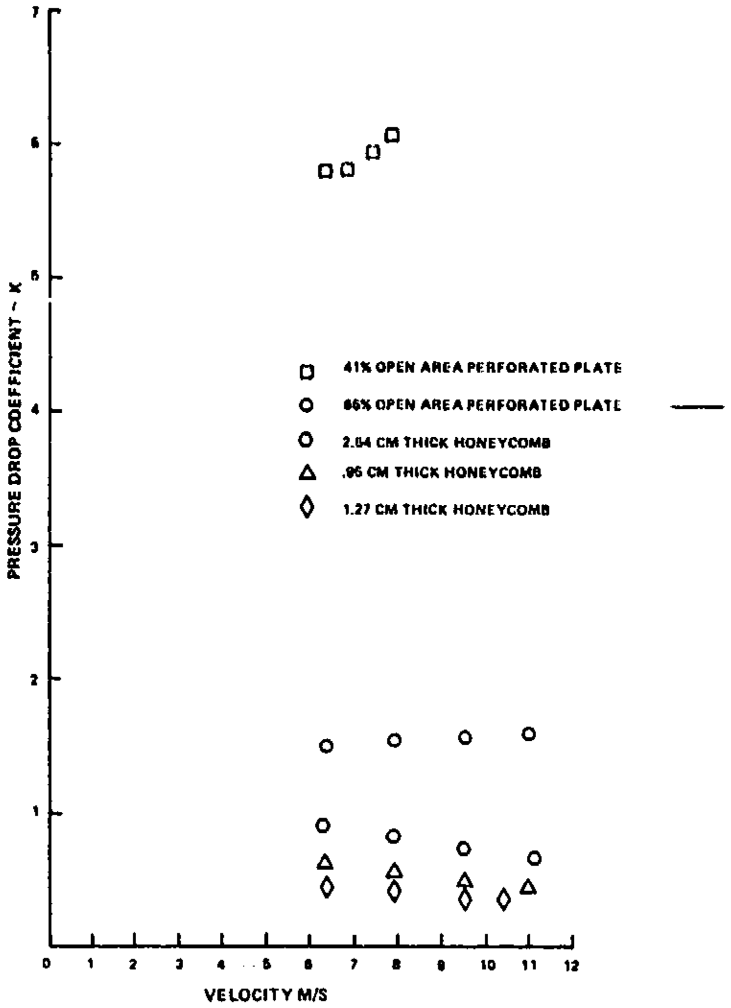

Figure 33 Measured Pressure Drop Coefficients of Screens

SCREEN	PRESSURE DROP COEFFICIENT		
	MEASURED	THEORY	MODIFIED THEORY
.95 CM HONEYCOMB	.46 → .63	.143	.286
1.27 CM HONEYCOMB	.36 → .45	.193 } B	.386 } 2xB
2.54 CM HONEYCOMB	.66 → .91	.381	.762
66% OPEN AREA PERFORATED PLATE	1.5 → 1.6	1.16 } B&P	
41% OPEN AREA PERFORATED PLATE	5.8 → 6.06	6.9	

B – BLASIUS

B&P – BAINES & PETERSON

Figure 34 Comparison of Measured and Predicted Screen Pressure Drop Coefficients

The measured values of the perforated plate pressure drop coefficients are consistent with the theoretical values, Figure 33, and thus lend confidence to the model.

5.2 The Transmission Loss and Directivity Effects of ICS Elements

In the acoustic part of the test program, the transmission loss of various screen materials in the presence of flow was measured. In addition, the effect on the radiation field of possible discontinuities in the ICS structure was examined.

5.2.1 The Acoustic Transmission Loss of The Screens

The screens tested in the aerodynamic part of the program were also used in the transmission loss measurements. In the ICS configuration to be encountered on the test stand the angle of incidence of the acoustic wave to the screen material will be approximately normal. In any event, for the perforated plate this represents a worst case, and the honeycomb transmission loss is very insensitive to incidence angle. (i.e. Transmission loss <1dB, for incidence angle $<51^0$)

The measurements were made at P&WA's dual reverberation chamber facility. The source of noise was a Nor-Aire generator and flow through the duct was provided by vacuum pumps. A schematic diagram of the test arrangement is shown in Figure 35. The test section lay between the reverberation chambers and the duct was 2.54 cm in diameter to ensure only plane wave propagation over most of the frequency range of interest. The screen samples are shown in Figure 36 and the method of mounting in the test section is shown in Figure 37. The nominal throughflow velocities for which the screen transmission loss was measured were 6.1 m/s, 9.15 m/s and 12.2 m/s. The noise generated by the Nor-Aire then propagates upstream through the screen. An array of three microphones was placed in each of the chambers, Figure 35. The signals from each microphone were recorded simultaneously for a no-screen configuration, in addition to the

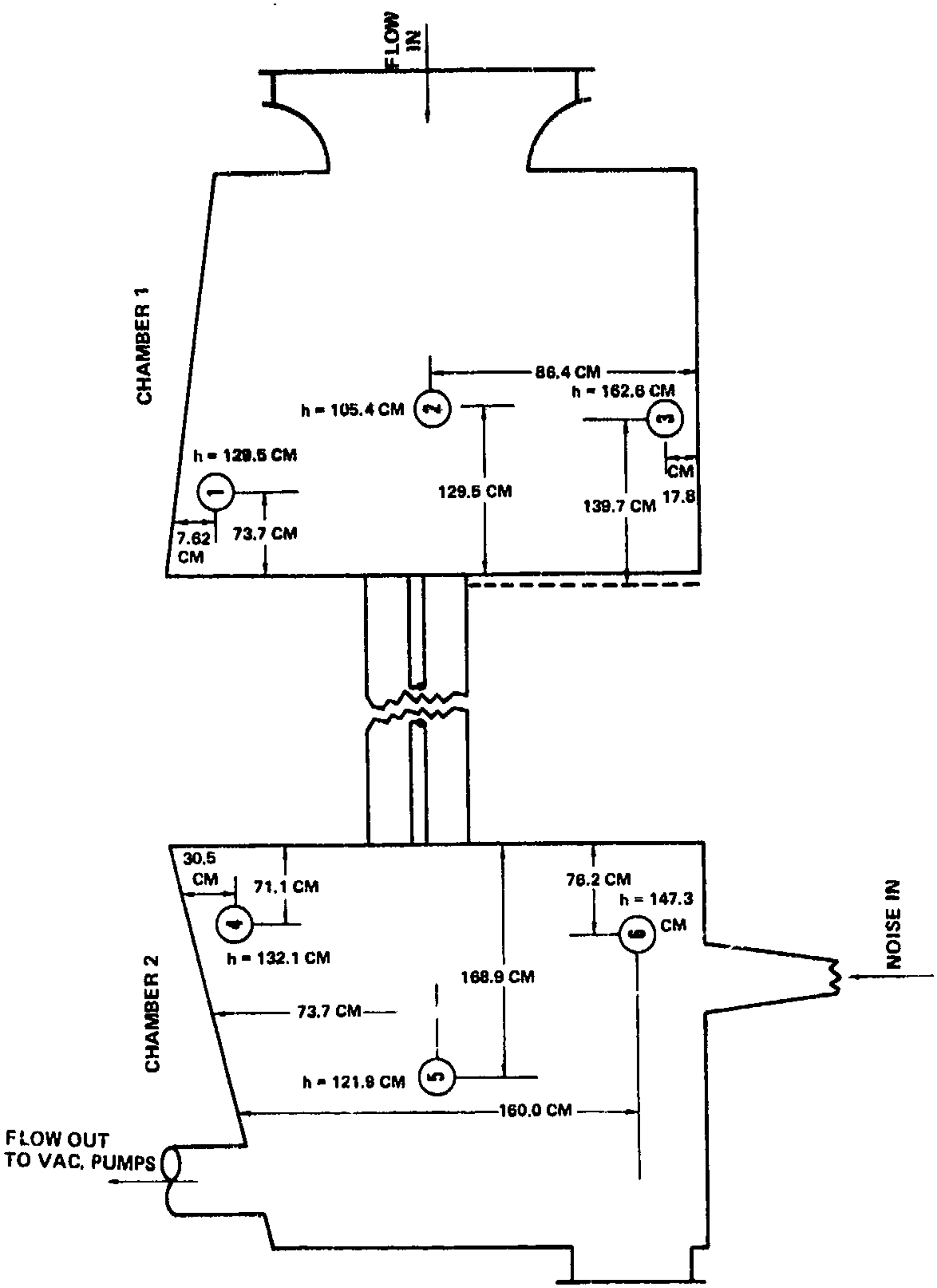

Figure 35 Microphone Locations for Transmission Loss Measurements

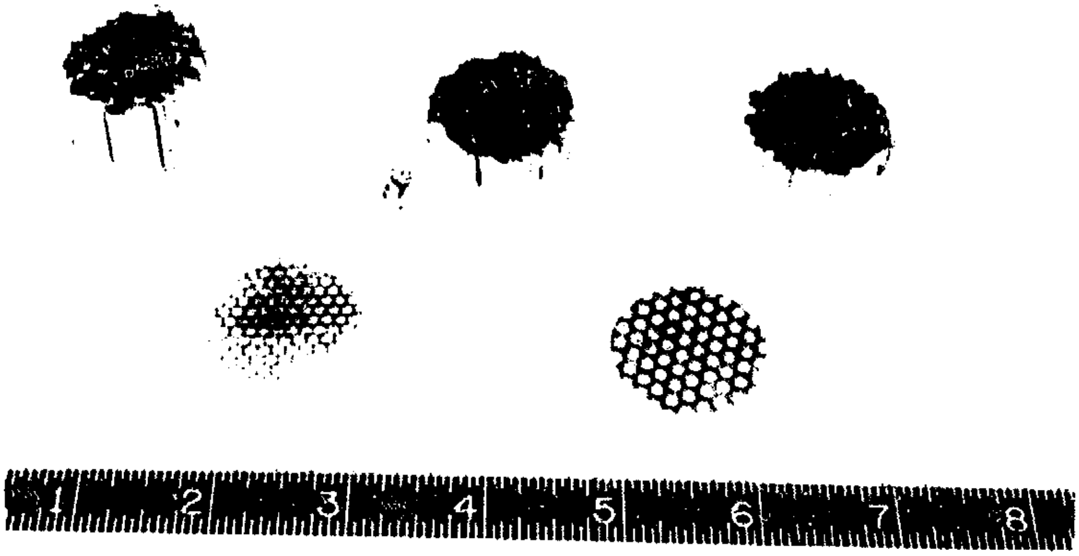

Figure 36 Screen Samples

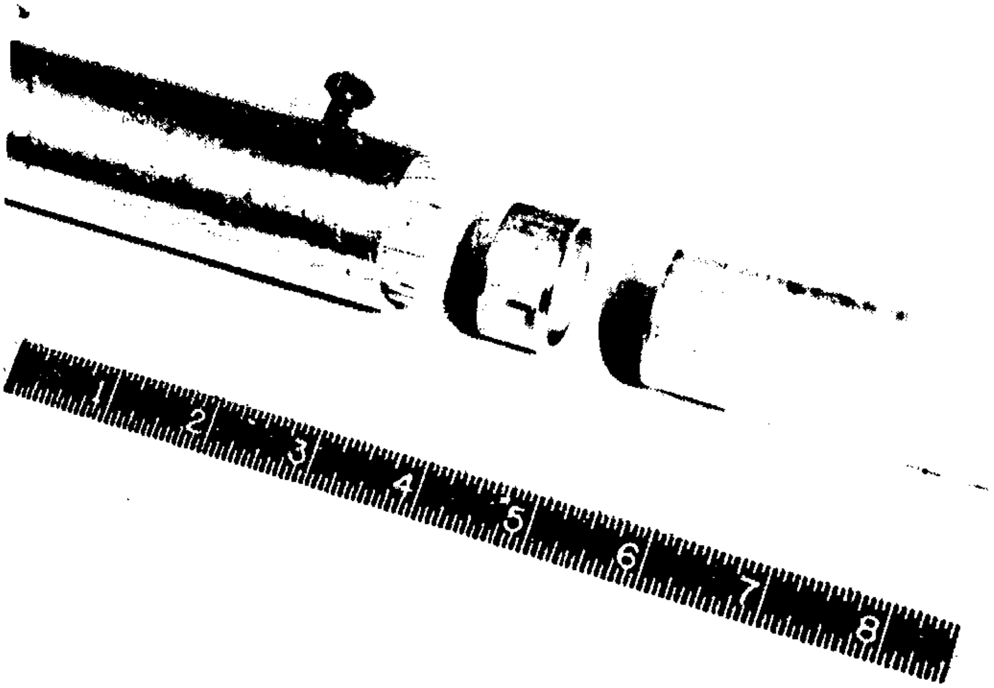

Figure 37 Method of Mounting Screen Samples

0.95 cm, 1.27 cm and 2.54 cm thick honeycombs and the 66 percent and 41 percent open area perforated plates. Subsequently, a one third octave band analysis was performed on the data from which estimates of the transmission loss were made.

To determine the transmission loss of the various screen samples the noise reduction between each chamber was first computed for each configuration. These noise reductions were obtained by subtracting the levels at each pair of microphones for each one third octave band, i.e.,

$$NR = SPL_S - SPL_R \qquad 7$$

Since there are three microphones in each chamber this operation produces nine estimates of the one third octave band noise reduction for each configuration. The transmission loss of each screen sample is then found by subtracting the no-screen (baseline) noise reduction from the noise reduction obtained for each screen sample.

$$TL_{SC} = NR_{SC} - NR_B = \left(SPL_S - SPL_R \right)_{SC} - \left(SPL_S - SPL_R \right)_B \qquad 8$$

Equation 8 produces, therefore, eighty one estimates of each one third octave band transmission loss for each screen sample, from which the average and standard deviation of the attenuation may be found.

For the ideal situation of truly reverberant source and receiver chambers, the computations described above would be redundant since all microphones in any chamber at a given condition would produce the same measurement and one calculation would be sufficient to define a screen transmission loss. However, this is not the case in practice and the forming of many transmission loss estimates enhances the confidence in the result.

The standard deviations of the one third octave band transmission losses for all screens and flows were, in general, of the order of the mean value. The majority of the values were then not significantly different from zero.

The average value of the 66 percent open area perforated plate transmission loss increases with throughflow speed. There is however, little variation in that quantity with frequency, as can be seen in Figure 38. where the 9.14 m/s flow case is shown. At 12.19 m/s there is a considerable increase in transmission loss, (Figure 39).The mean transmission loss of the 41 percent open area perforated plate however, decreases with increasing frequency at all speeds. With increasing speed there is small change in the average value, although at 12.19 m/s, Figure 40, the scatter of the data is higher than for the lower speed conditions. The reason for the difference in behavior of the two perforated plates in frequency is not understood. In addition, the higher transmission loss measured for the higher open area plate at the higher one third octave bands is intuitively questionable.

The transmission loss of the 0.95 cm honeycomb is unchanged by increasing throughflow speed. The mean value is approximately zero for all one third octave bands, except the highest where it increases to a maximum of about 1.5 dB. The transmission loss shown in Figure 41 for the 9.14 m/s flow is typical. The 1.27 cm honeycomb has similar characteristics. The 2.54 cm honeycomb has a mean transmission loss that is more uniform in frequency than the thinner honeycomb, see Figure 42. In addition, the mean increased with flow speed from about 0 dB at 6.1 m/s to 2 dB at 12.19 m/s. In spite of the large standard deviation of transmission loss values encountered here, there is an indication that the thickest honeycomb (2.54 cm) may attenuate a normally incident wave at the highest flow speed (12.19 m/s). This suggests that the resistive component of the honeycomb impedance is no longer insignificant in this case.

In summary, then, there is a possibility that at the higher flow speed (12.19 m/s) the perforated plate of 66 percent open area and the 2.54 cm honeycomb have non-zero transmission losses even though the standard deviations are large. In contrast, the thinner honeycombs (0.95 cm, 2.37 cm) present no significant obstacle to the incident sound field. The 41 percent open area perforated plate appears to attenuate the incident field in the lower one third octave bands. These results are compared with the theoretical predictions in Section 6.3 below.

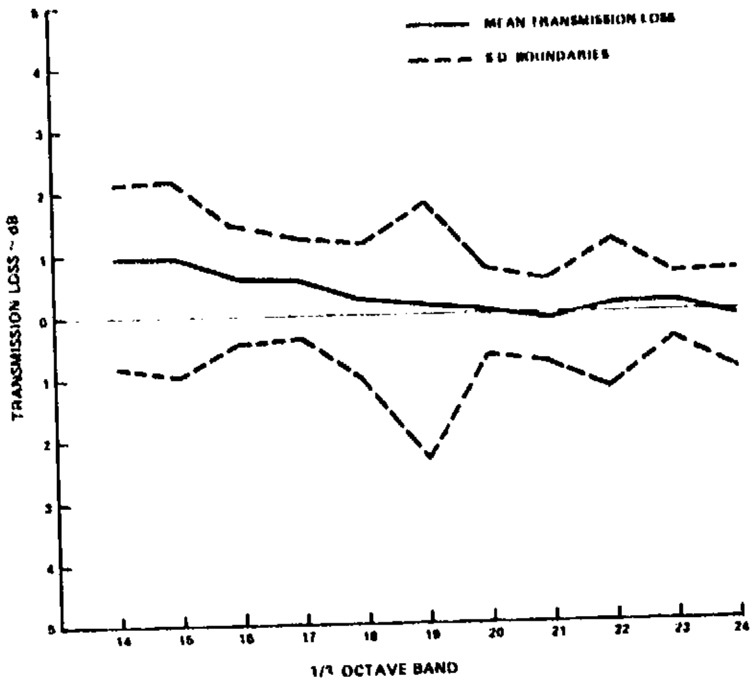

Figure 38 Transmission Loss of 66% Open Area Perforated Plate at 9.14 m/s

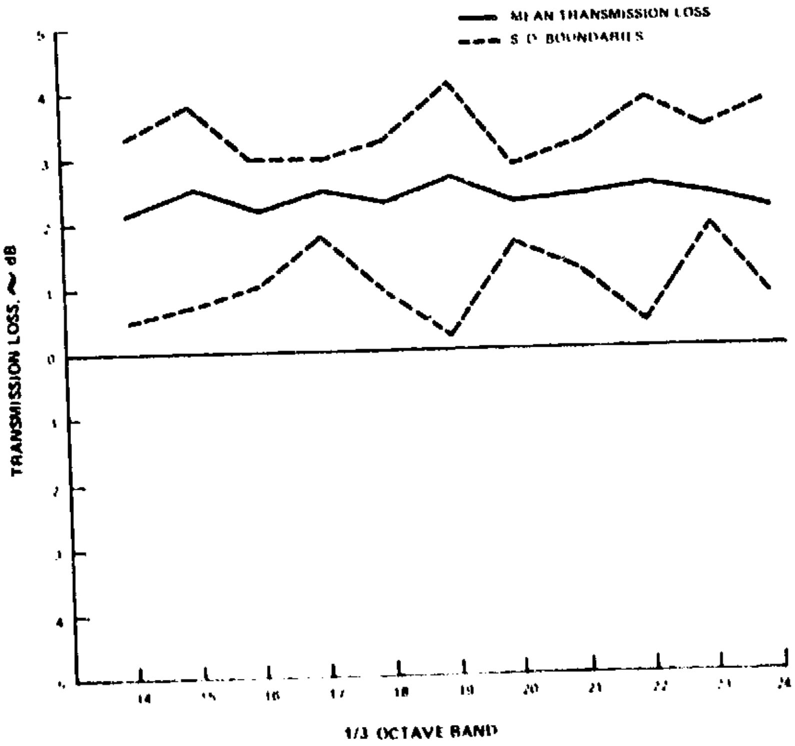

Figure 39 Transmission Loss of 66% Open Area Perforated Plate at 12.19 m/s

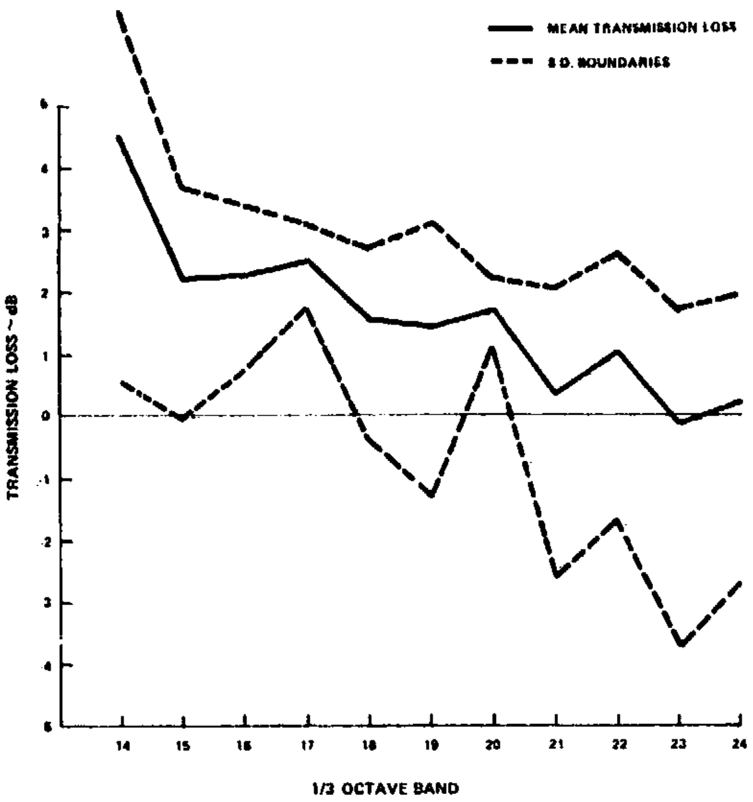

Figure 40 Transmission Loss of 41% Open Area Perforated Plate at 12.19 m/s

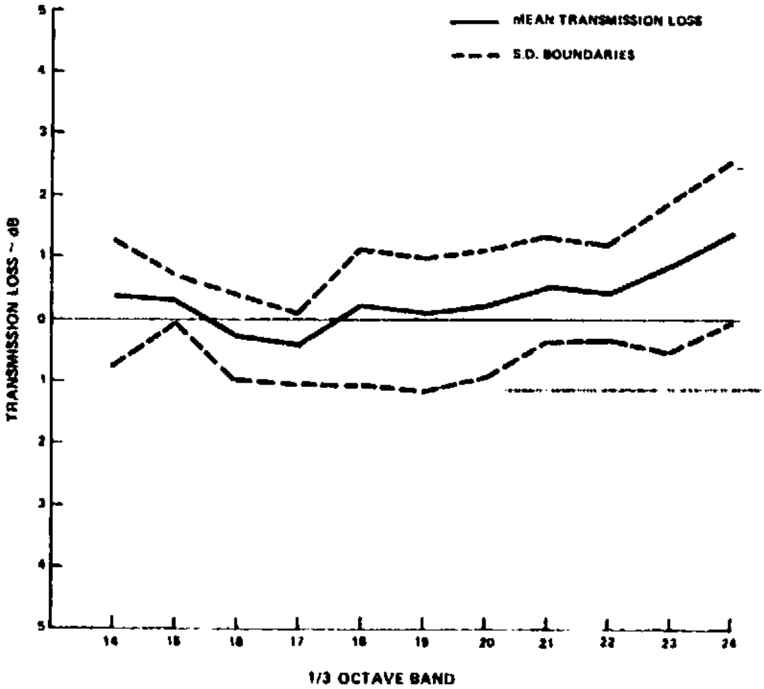

Figure 41 Transmission Loss of .95 cm Honeycomb at 9.14 m/s

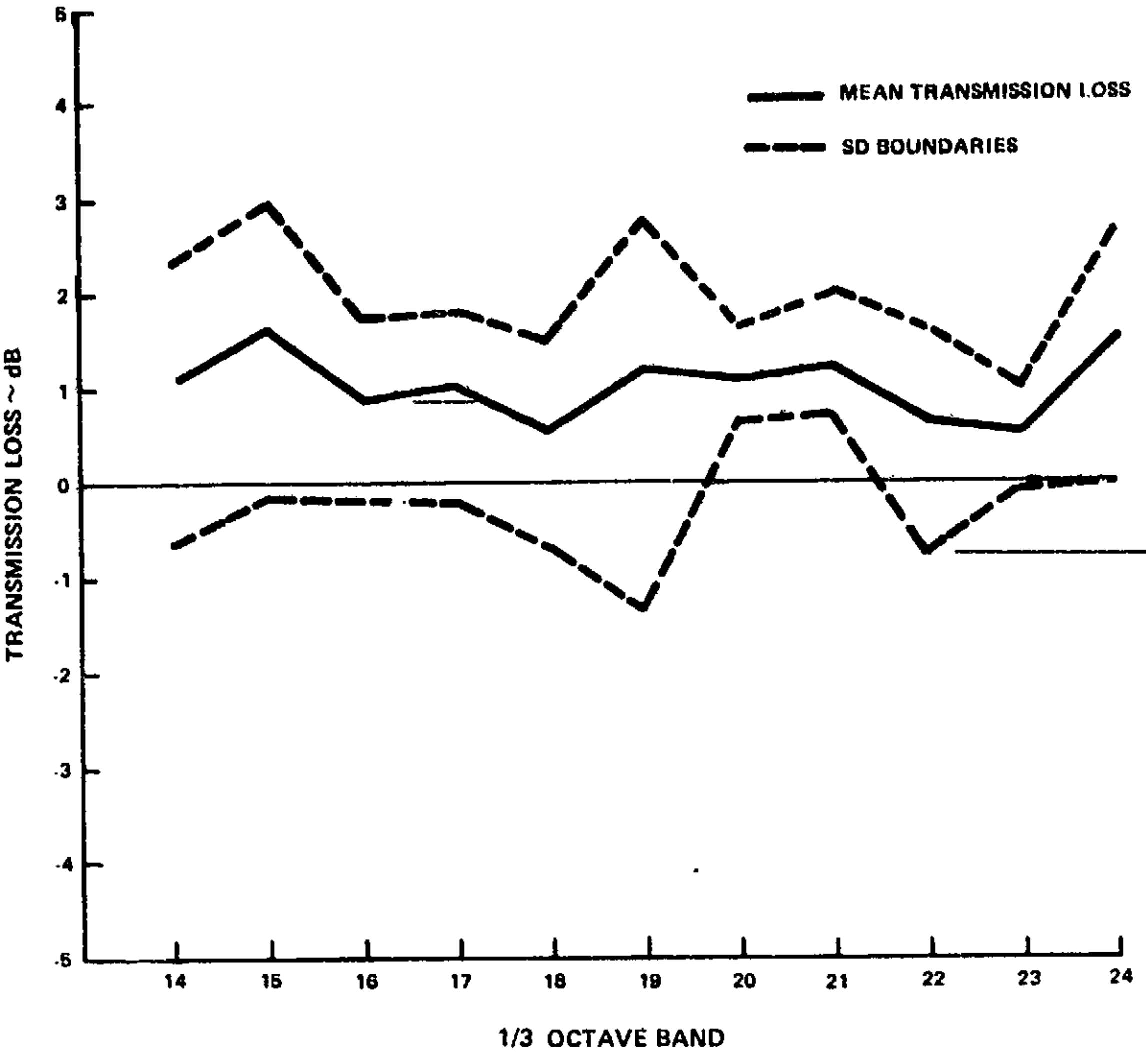

Figure 42 Transmission Loss of 2.54 cm Honeycomb at 9.14 m/s

5.2.2 The Effect on Acoustic Field Directivity of Honeycomb Corners and Structure

The test program was performed at Pratt & Whitney Aircraft's anechoic chamber, X-207 stand. The test setup is shown in the schematic diagram in Figure 43 and in Figure 44. The chamber has a volume of 340 m^3 and is lined on all surfaces with specially constructed anechoic wedges to provide an anechoic environment for frequencies above 150 Hz. The floor, designed to be acoustically transparent, is constructed of tensioned wire mesh located above the floor wedges.

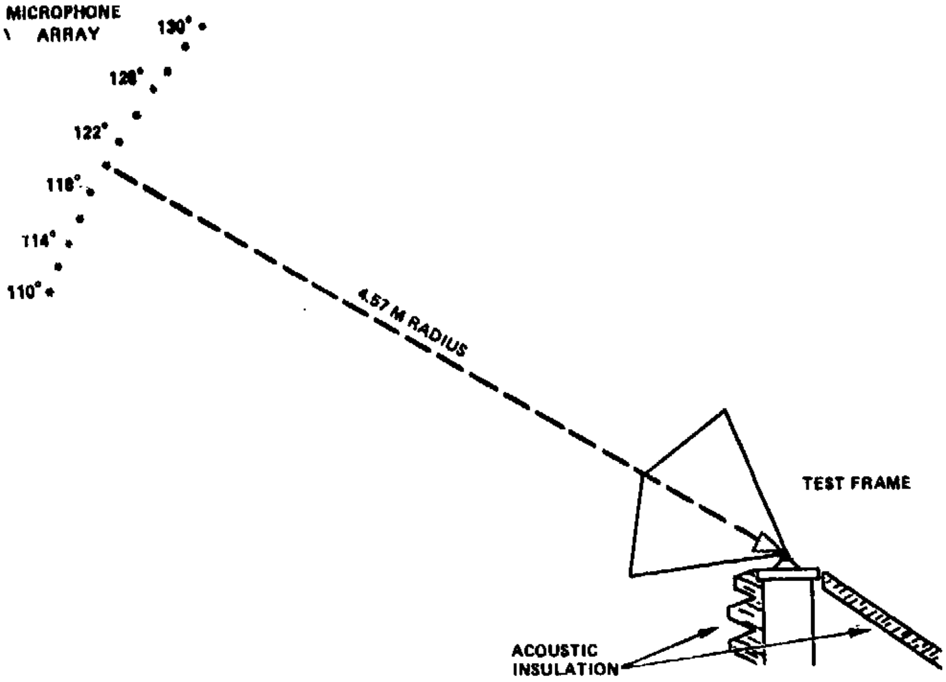

Figure 43 Schematic Diagram of Directivity Test Arrangement

Figure 44 The Panel Mounting Frame

A metal frame fabricated from angle iron was used to simulate one corner of the ICS, Figure 45. Meeting at an angle of 135^0, two .61m x .61m sheets of 7.62 cm thick .95 cm cell honeycomb were attached to the frame to form an angle of 135^0. The corner formed by the sheets of honeycomb was sealed with tape to prevent sound leakage. The honeycomb were removable to allow for testing of other corner structures, such as a 2.54 cm diameter round rod and a 2.54 cm square bar. Sound insulation material was added to all exposed metal structures (other than the test sections) to prevent spurious sound reflection patterns. The sound source used was a 2.54 cm diameter University Driver Model Number ID65X located in line with the corner of the frame and the 120^0 microphone as shown in Figure 45. A 12.7 cm diameter metal cone was installed on the driver to assure a smooth acoustic directivity pattern. The driver was installed on a rotating mount to allow for changes of sound incidences (0^0, 5^0, 10^0, incidence angles) with respect to the corner structure. The driver was activated by a General Radio Model 1310 oscillator used in conjunction with a McIntosh Model MC30 amplifier. The source was driven nominally at 2 KHz, 5 KHz and 9 KHz. Capability to reorient the frame structure with respect to the microphone array was also utilized.

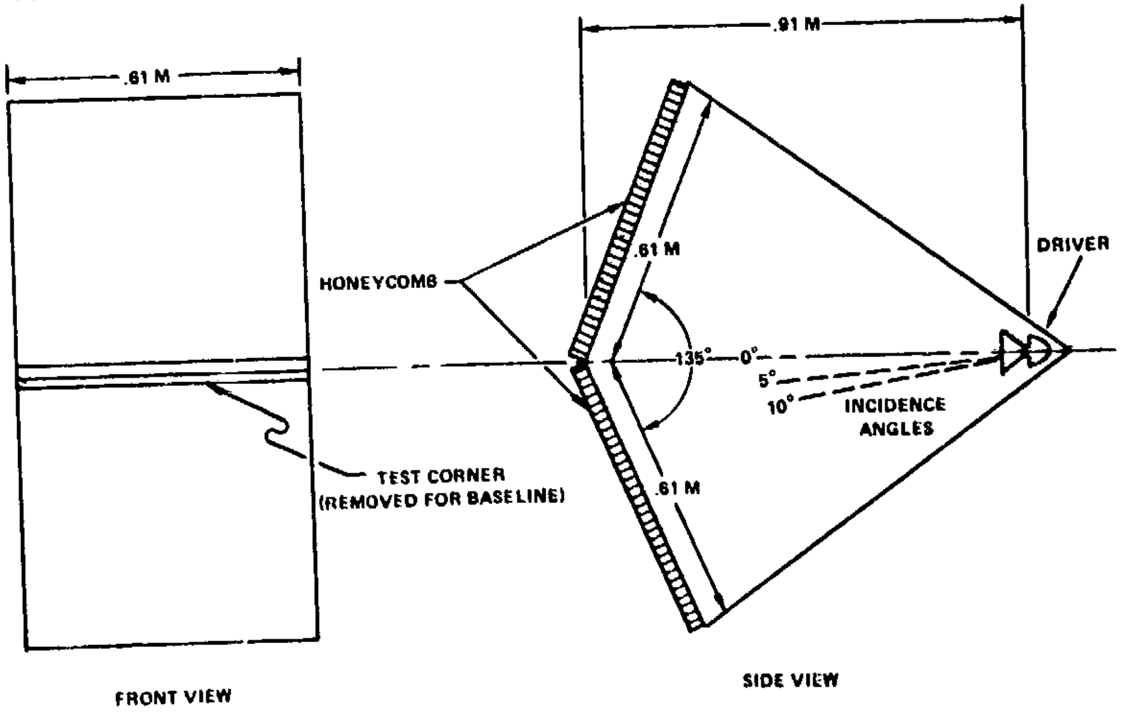

Figure 45 Geometry of Honeycomb Panel Mounting Frame

Acoustic signals were detected by a polar array of .635 cm diameter B&K microphones (Model 4135) positioned at normal incidences to the sound source at a distance of 4.57 m. Microphone measurements were taken at 2^0 increments with respect to the sound source. Two microphone positioning methods discussed below were used to obtain the data; however, only Method (B) proved satisfactory.

Method (A)

Six microphones were located at angles of 110^0, 115^0, 120^0, 125^0, 130^0 and 140^0 with respect to the test stand vertical axis. At each test condition the frame was repositioned angularly from 0^0 to 8^0, in 2^0 increments, effectively providing measurements every 2^0, from 102^0 to 140^0. This technique was curtailed during the test program when problems were encountered. The sound field within the chamber did not remain consistent for each position of the frame structure, resulting in a discontinuous directivity pattern (i.e. repositioning of the frame produced a different sound field in frame fixed coordinates).

Method (B)

Twelve microphones were located every 2^0 from 110^0 to 132^0 relative to the test stand vertical axis. The angular range was necessarily smaller than Method (A); however, the resultant directivity pattern remained consistent. Test time was also reduced since fewer configuration changes were required.

For each incidence angle tested a base line condition was obtained to define the directivity patterns of the driver and frame alone. To obtain the base line condition, sound levels were measured for each microphone at each of the nominal frequencies tested; 2000 Hz, 5000 Hz, and 9000 Hz. Several repeats of of the base line conditions were made to assure measurement consistency. The measurements were repeated with the various test items attached; i.e., honeycomb, 2.54 cm square bar and 2.54 cm round rod. For each of the microphones, the results were then subtracted from the base line data at the corresponding incidence angle and frequency to give the directivity modification due to the presence of the body. The honeycomb corner configuration was repeated at each incidence angle with an aluminum tape seal to determine whether sound leakage occurred with the screen cloth tape seal. The results indicate no noticeable differences in directivity patterns.

The directivity patterns obtained for the corner between honeycomb panels have been presented in (29) and discussed here. An example of these patterns is given in Figure 46 (The prediction shown is that obtained from the theory described in (29)). In general more disruption of the far acoustic field was observed with increasing frequency and incidence angle.

The two rods produced symmetric directivity patterns and the modification to the free field pattern was also greater in amplitude at the higher frequencies, as can be seen in Figure 47. The rod X-sectional shape does not affect the directivity pattern greatly.

5.3 Conclusion

The major observations from the test program were

- The flow contraction amplifies the transverse turbulent velocity component and at low contraction ratios, it suppresses the stream-wise velocity component. At high contraction ratios the streamwise turbulent velocity component increases, although it did not attain the starting value.
- Steady streamwise velocity deficits are suppressed rapidly by the flow contraction. The azimuthal velocity component of a streamwise aligned vortex was substantially unchanged by the flow contraction. The streamwise velocity distortion associated with the vortex increased in amplitude and extent.

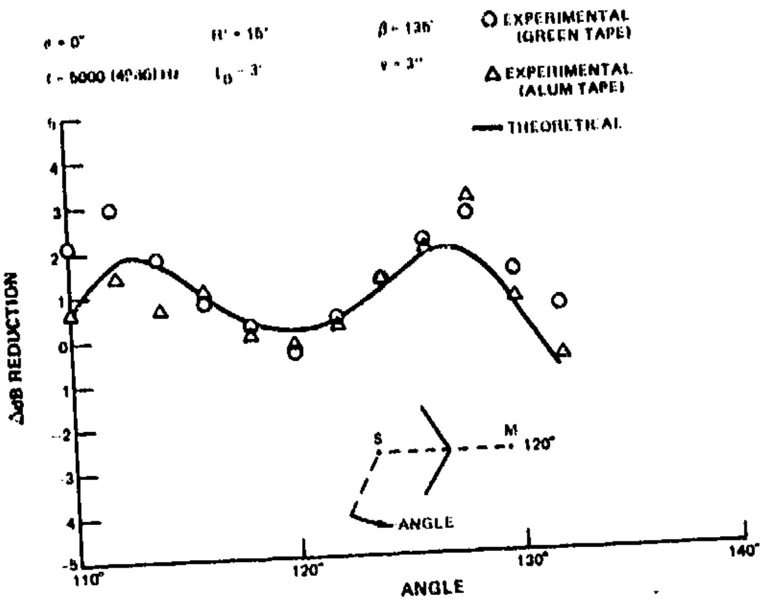

Figure 46 Directivity Effect of a Honeycomb Corner

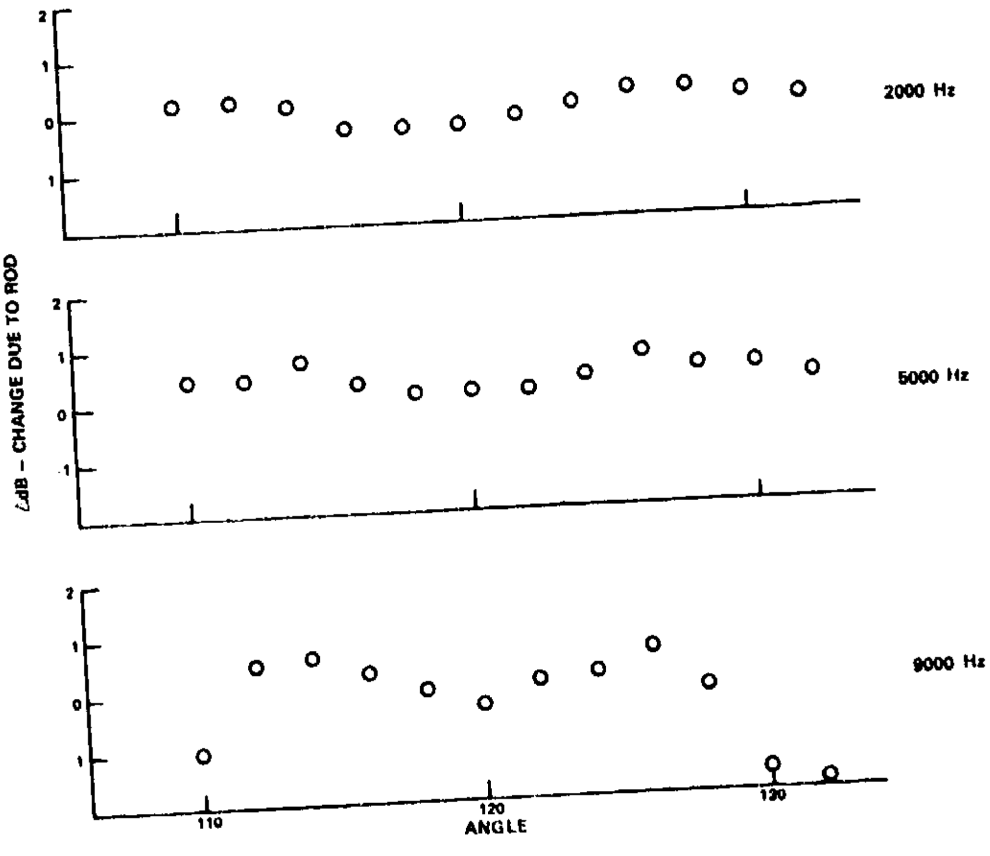

Figure 47 The Acoustic Directivity Change Due to the Presence of a 2.54 cm Diameter Rod in the Radiation Field

- The turbulence data gathered downstream of both honeycomb and perforated plate was contaminated with self generated turbulence. The honeycomb screen suppressed the transverse turbulent velocity field. (The effect of the screens on other turbulence parameters is discussed in the next section, where the residual upstream turbulence field is separated from the screen self generated field).

- Steady streamwise velocity deficits are suppressed according to the resistance of the screen. In the resistance range studied here, the higher the resistance the greater the suppression. The azimuthal velocity field of the vortex was totally suppressed by the honeycombs and somewhat reduced and dispersed by the perforated plates. The streamwise velocity distortion associated with the vortex increased on convection through the honeycomb and the 66 percent open area perforated plate.

- The resistance of perforated plate is adequately predicted by theory. The resistance of the honeycomb is dependent on the entrance conditions and this precludes accurate estimates of the resistance for an arbitrary honeycomb. However an estimate may be made, by doubling the value obtained from Blasius' expression (Equation 6).

- The transmission loss of the thinnest honeycombs (.95 cm and 1.27 cm) is negligible and invariant with throughflow speed. The thickest honeycomb (2.54 cm) has a transmission loss that increased with throughflow speed to 2dB at 12.19 m/s.

- The transmission loss of the 66% open area perforated plate is negligible at the lower speeds (9.14 m/s and 6.1 m/s) but increases to 2dB at 12.19 m/s. This attenuation is constant in 1/3 octave band. The 41% open area perforated plate transmission loss decreased with frequency and changes little with throughflow speed. The transmission loss is significant at the lower 1/3 octave bands.

- The presence of honeycomb panel corners and structure can disturb the radiation field of a simple discrete source by significant amounts. The higher the frequency the higher the disruption of the radiation field.

The data gathered during the test program was used to assess and, if necessary, modify the theoretical models presented in (29). The results of this comparison are discussed in the next section.

6.0 THE DEVELOPMENT OF THE ICS DESIGN SYSTEM (TASK G)

In this section the test results of Section 5 are used to assess and/or modify the analytical models described in (29). Then the design criteria for an ICS are examined and the criteria for ICS location and material selection are established. The process is presented as a step by step procedure and exercised for the JT9D and JT15D engines.

6.1 The Transfer Functions for the Effects of Contraction and Screening on Turbulence

Measured changes in a turbulence field due to convection through 1) a flow contraction and 2) various screens, were described in Section 5. Theoretical models of these phenomena were identified in the Interim Phase II Report (29). The aim of this section is to compare the theoretical and experimental results and thereby assess the models. If necessary the theoretical models will be modified.

6.1.1 Contraction

The comparison of measured with predicted characteristics as the turbulence is convected through a contraction begins at the coarsest level, the kinetic energy, and proceeds through increasingly detailed properties to the power spectral densities.

The measured kinetic energy ratio across the contractions, as a function of contraction ratio, is shown in Figure 48 together with the predictions using the simple models. The measured variation is approximately linear in contraction ratio and its gradient is approximately half that of the theoretical variation. This discrepancy is in part due to viscous dissipation not accounted for in the model. A correction for viscous decay was suggested by Ribner and Tucker (33) and applied by Tucker and Reynolds (34) to their data with some success (i.e. their corrected data was in closer agreement with Ribner and

Tucker's Theory). This correction is based on a linear decay of turbulent kinetic energy with distance in a uniform mean velocity field, and can be written as

$$KE \propto (X - X_o)^{-1} \qquad 9$$

where X_o in Equation 9 refers to the position of the virtual source of the turbulence. This correction was applied to the present data and the corrected values are shown in Figure 49. Also shown in this figure are data gathered by Uberoi (31) and Hussein and Ramjee (32). These data are also viscous decay corrected and as can be seen, the data are in good agreement with each other. Various contraction types were studied by these investigators; Uberoi examined contractions of square cross section, Hussein and Ramjee considered circular cross sections. The contraction rates were also varied. The agreement is quite close and thus the decay process through the contraction is not strongly dependent on the details of the contraction.

On comparing the viscous decay corrected data to the predictions of the Batchelor-Proudman, Ribner-Tucker theory, much closer agreement is observed (Figure 50). The simple theory predictions are not as close as the Batchelor-Proudman, Ribner-Tucker theory. The corrected data is still somewhat low at the higher contraction ratios, but this is attributable to error in estimating the location of the virtual turbulent source, i.e. X_o.

The next higher level of detail of the turbulence field is supplied by the RMS values of the component turbulent velocities. Two velocity components were measured in the test program and the resulting RMS velocity ratios through the contraction are shown in Figure 51. These data are not viscous decay corrected in this figure. The predictions using the simple theory of Prandtl discussed in (29) overestimate both the increase in the transverse velocity component and the suppression of the streamwise velocity component. The theory of Batchelor-Proudman, Ribner-Tucker produces predictions that are closer to the data but still err in the same way as the simple theory predictions. A reason for the departure from the linear theory (in addition to the viscous decay discussed earlier) was foretold in the Interim Phase II Report (29). There it

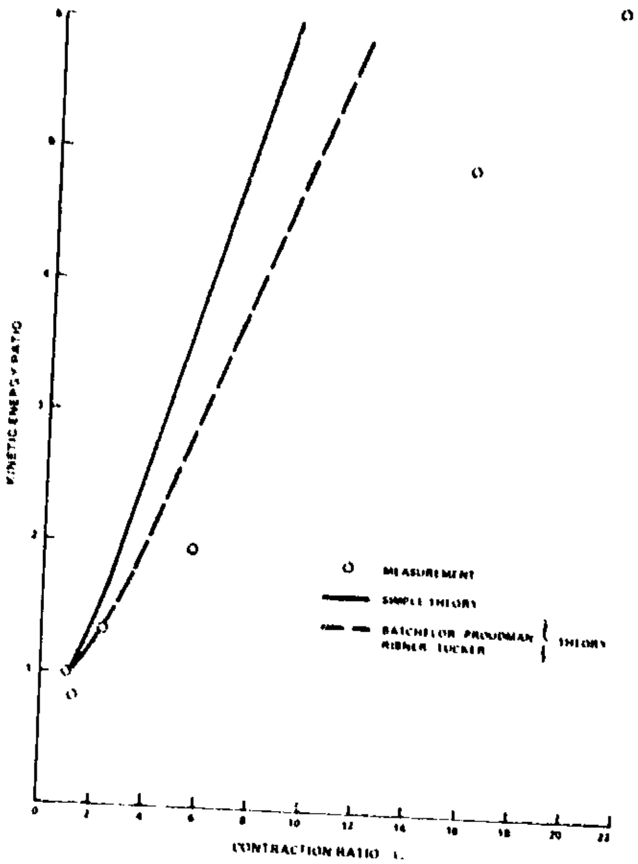

Figure 48 Kinetic Energy Ratio Through the Contraction

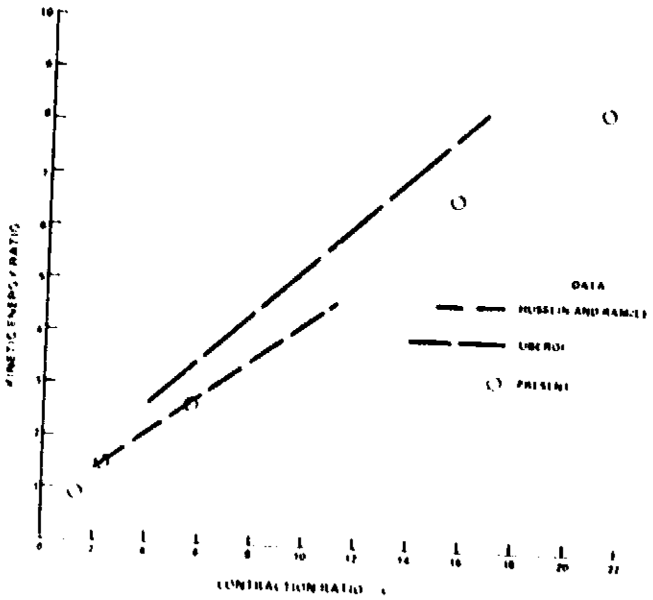

Figure 49 The Comparison of the Present Data With Other Data (Viscous Decay Corrected)

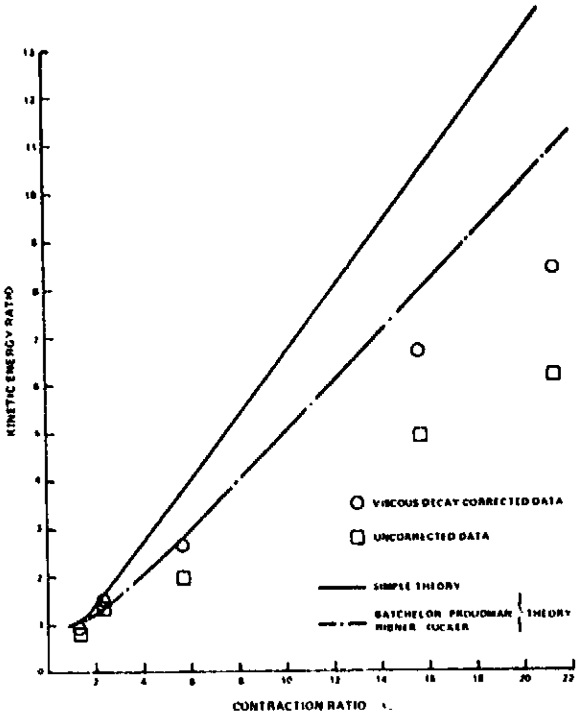

Figure 50 *The Kinetic Energy Ratio Through a Contraction Showing the Effect of Correcting for Viscous Decay*

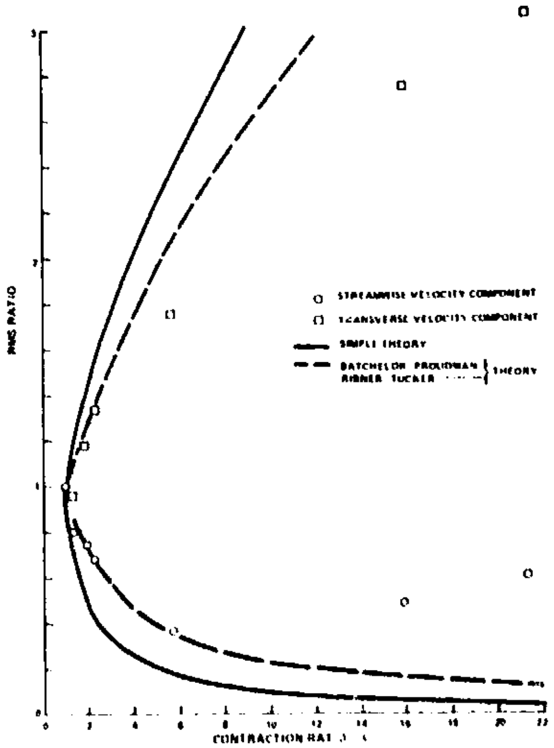

Figure 51 *The Effect of a Contraction on the Turbulent RMS Velocity Ratios*

was stated that for this configuration the turbulence inertial effects are not negligible and that consequently there would be a tendency to return to isotropy in the contraction (or perhaps more accurately, a tendency to equipartition of the kinetic energy between the three velocity components). This tendency is seen most apparently in the streamwise component (Figure 51) as it reaches a minimum and subsequently increases. This type of deviation from the linear theory is not explainable by viscous decay. The tendency to equipartition is shown more clearly in Figure 52 where the ratio of the RMS values of the transverse to streamwise velocity component is plotted as a function of contraction ratio. At the higher contraction ratios a maximum of this RMS ratio is reached and subsequently a tendency to equipartition of kinetic energy is seen. The predicted values are also shown on this figure. The anisotropy predicted by the linear theory is observed in the data only at low contraction ratios (< 2). In this regime for the present configuration this probably corresponds to the region where viscous decay and turbulence inertial effects are negligible. The data of Uberoi and Hussein and Ramjee will now be compared to the current data.

Figure 53 compares the data of Uberoi and, Hussein and Ramjee. The first thing to note is that the close agreement in kinetic energy ratio data of the three experiments, previously noted, is repeated when the transverse RMS velocity ratios are compared (i.e. The ratios obtained by dividing the RMS value at a contraction of ℓ_1 by the RMS value at a contraction ratio of unity). The transverse RMS velocity ratio data of Uberoi agrees very closely with the present data. The data of Hussein and Ramjee is somewhat lower than Uberoi's and the current data, but those authors note that the position at which their reference RMS values were determined was not the same as Uberoi's (who used the beginning of the contraction). Hussein and Ramjee assert that their transverse RMS velocity data agrees closer to that of Uberoi if the same reference position is used. Thus the variation of the RMS ratio of the turbulent transverse component is to a large extent independent of the contraction rates and shapes. The viscous decay correction for the three experiments is similar, so that the same statement can be made of the corrected transverse RMS ratio data.

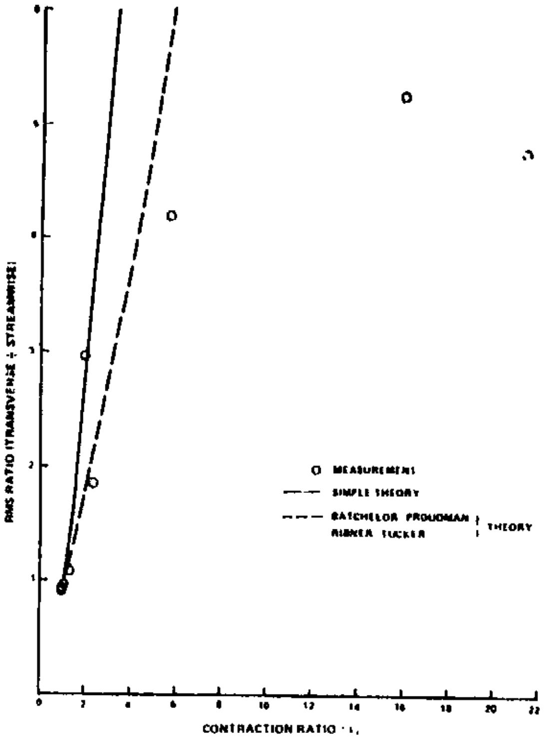

Figure 52 Ratio of Transverse To Streamwise RMS Values Through The Contraction

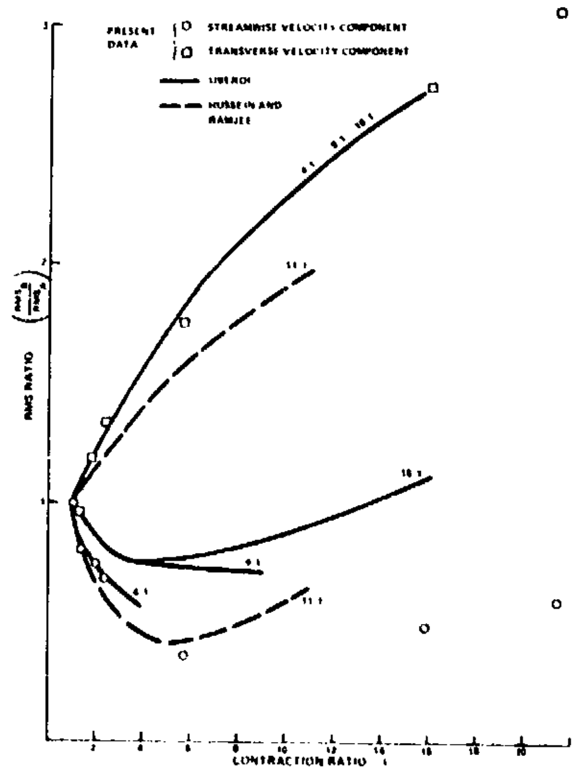

Figure 53 Comparison of Present RMS Ratios With The Data of Uberoi, And Hussein And Ramjee

In contrast, the RMS ratios (i.e. Ratio between the RMS value at contraction ratio ℓ_1 and at a unity contraction ratio) of the streamwise turbulent velocity component for the various contractions are quite different although the general trends are similar. This appears to be in conflict with the previous observation that the total kinetic energy ratio and the transverse velocity ratio variations are approximately the same, for the experiments of Uberoi, Hussein and Ramjee and the present data. For if the kinetic energy is the same and the transverse components are the same, one would expect the streamwise component variations to be the same for all three experiments. However, if the streamwise turbulent velocity contribution to the kinetic energy is small compared to that of the transverse components then variations in the streamwise velocity component level will not affect the magnitude of the kinetic energy significantly. This is the case for the contractions considered above, except at the lowest contraction ratios.

In view of the dominance of the energy in the transverse turbulent velocity components, it is important that the behavior of this component be properly modelled. Thus the viscous decay correction is applied to these components. A comparison of the corrected transverse RMS levels with theory is shown in Figure 54. There is close agreement with predictions using the Batchelor-Proudman (35), Ribner-Tucker theory. The simple theory is not as good. The Batchelor-Proudman, Ribner-Tucker theory when corrected for viscous decay then provided the best estimate for the transverse RMS ratio through a contraction.

$$\mu_2 = \mu_3 = \frac{3\ell_1}{4} \frac{(X - X_o)_A}{(X - X_o)_B} \qquad 10$$

Neither this theory nor the simple theory are close for the streamwise RMS ratio predictions although at the low contraction ratios (<6) before energy transfer is apparent, the Batchelor-Proudman, Ribner Tucker theory provides a reasonable estimate. The model for this component will be selected based on this and other considerations to be discussed in Section 6.4.

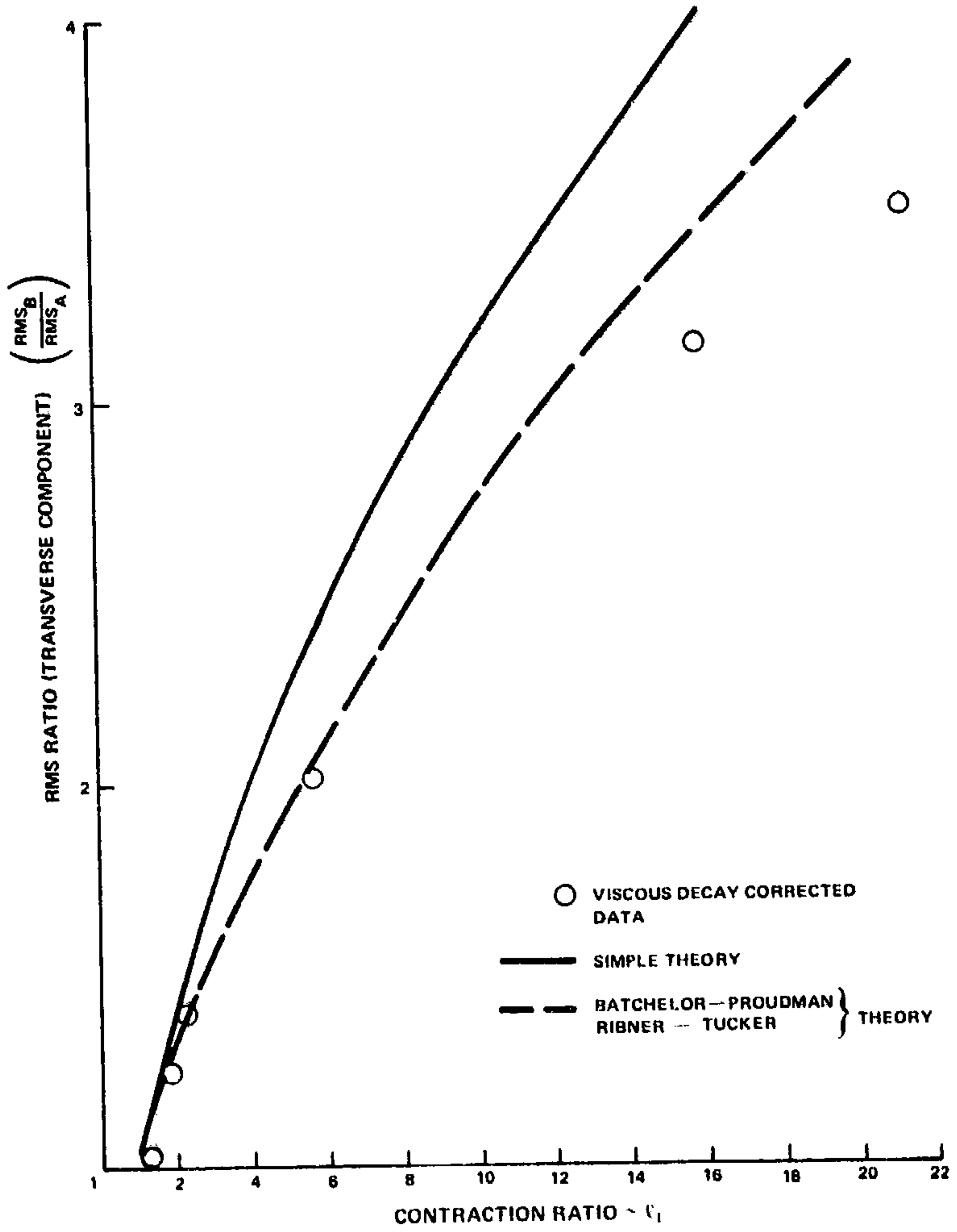

Figure 54 Viscous Decay Corrected Data Compared To Theoretical Prediction

The variations in length scale ratios (i.e. The ratio between the length scale at a contraction ratio of ℓ_1 and the value at a contraction ratio of unity) through the contraction are shown in Figures 55 and 56. Four integral length scales were computed from measurement (as described in Section 5), an axial and a transverse scale of the streamwise turbulent velocity component (L_{11}, L_{13}) and an axial and a transverse scale of a transverse turbulent velocity component (L_{21}, L_{23}). Considering the data first, it is interesting to note that the tendency to equipartition of energy observed between the turbulent velocity components is not reflected by a tendency to isotropy in the integral length scales. The axial scales increase and the transverse scales decrease almost monotonically. Both axial scales and transverse scale ratios of the streamwise turbulent velocity component, (i.e. $\frac{L_{11B}}{L_{11A}}, \frac{L_{13B}}{L_{13A}}$), are well predicted by the simple theory. The scale ratios of the transverse component, (i.e. $\frac{L_{21B}}{L_{21A}}, \frac{L_{23B}}{L_{23A}}$), however, are not well predicted at the higher contraction ratios. The measured component scale ratios, (i.e. $\frac{L_{13B}}{L_{13A}}, \frac{L_{23B}}{L_{23A}}$), are closer to the predictions of the viscous-decay corrected Ribner-Tucker theory (33), also shown in Figures 55 and 56. The length scale ratios were determined using this theory by U. Ganz (36). He found that for the transverse velocity components

$$\frac{(L_{21})_B}{(L_{21})_A} = \frac{(L_{31})_B}{(L_{31})_A} = \frac{\ell_1^{\,2}}{\mu_2} \qquad 11$$

$$\frac{(L_{22})_B}{(L_{22})_A} = \frac{(L_{33})_B}{(L_{33})_A} = \frac{\ell_1^{\,1/2}}{\mu_2} \qquad 12$$

$$\frac{(L_{23})_B}{(L_{23})_A} = \frac{(L_{32})_B}{(L_{32})_B} = \frac{1}{\ell_1 \, \mu_2} \qquad 13$$

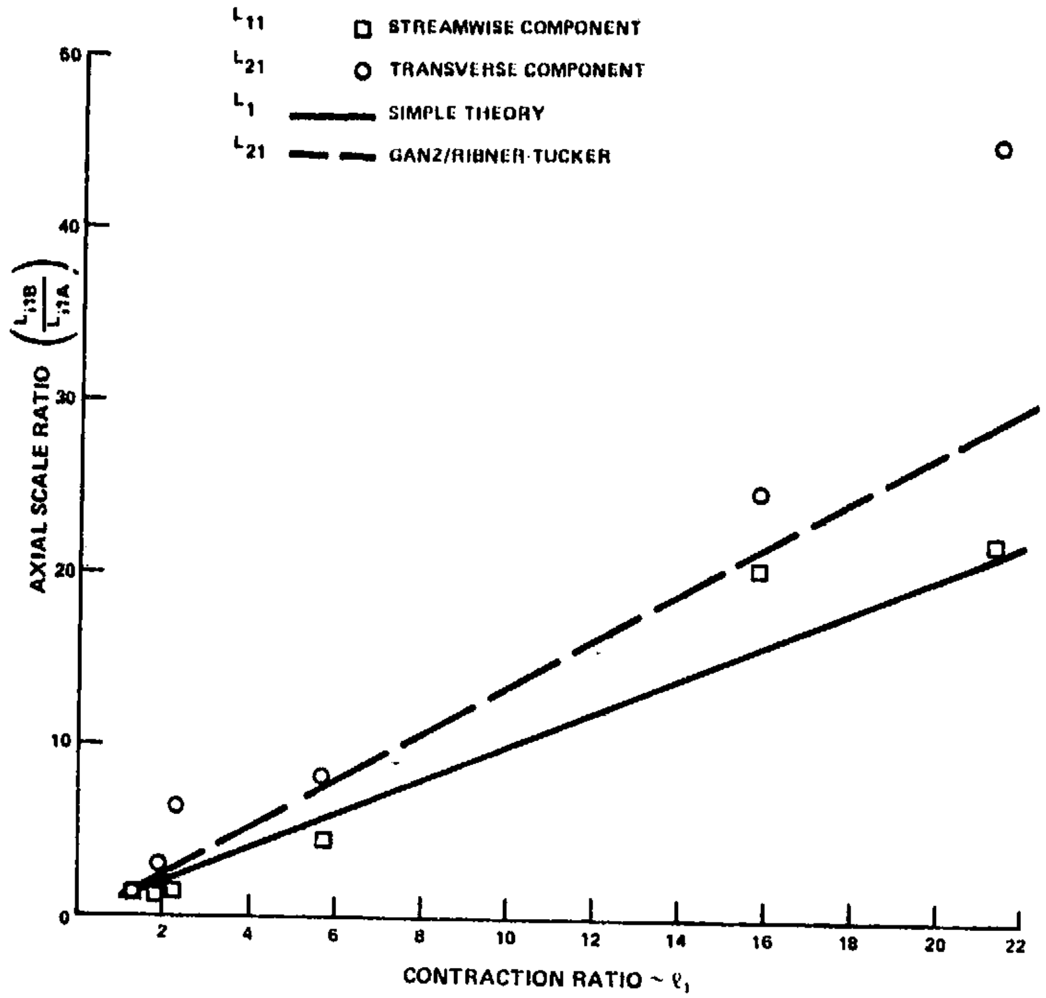

Figure 55 The Axial Length Scale Ratios Through A Contraction

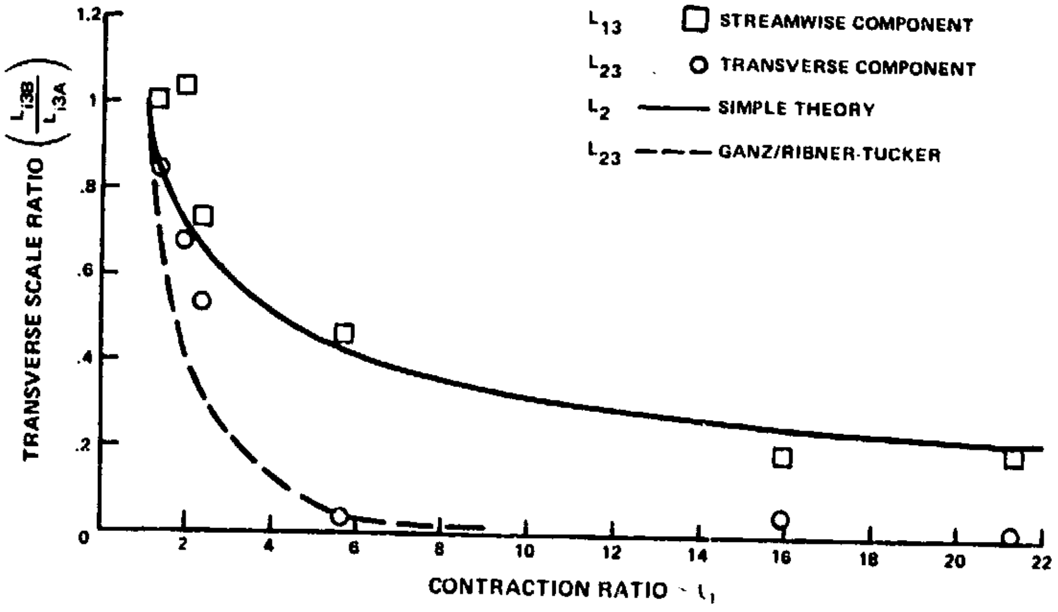

Figure 56 The Transverse Length Scale Ratios Through A Contraction

The predictions in Figures 55 and 56 used the expressions 11 and 12 with the viscous corrected mean square velocity ratio discussed earlier in this section. In consequence the ICS design system will use the simple models for the streamwise component length scales and Ganz's formulation (with the viscous corrected mean square velocity ratio) for the transverse velocity component length scale ratios.

Two types of PSDs of the turbulent velocity field were determined by measurement, (see Section 5), both in the frequency domain (which corresponds to the streamwise wave number under the frozen turbulence assumption) of the transverse and streamwise velocity components. The pre and post contraction PSDs are shown in Figure 57 for the transverse velocity component. There is very little change in this PSD over the contraction range examined. It should be noted that in this figure and Figure 58 only the spectral shapes are being compared (each PSD has been normalized by it's maximum value). This result, i.e., the constancy of the transverse component PSD, is inconsistent with the simple model since from the measurement

$$\tilde{F}_{2B}(\omega) \simeq \tilde{F}_{2A}(\omega) \qquad 14$$

where F denotes a normalized PSD and noting that

$$\omega = U_{1A}\, k_{1A} = U_{1B}\, k_{1B} \qquad 15$$

This is Taylor's frozen turbulence assumption, and the PSDs in this equation and in the subsequent section, show the frequency domain may be mapped into either the upstream or downstream axial wave number space using these transformations.

Then Equation 14 becomes

$$\tilde{F}_{2B}\left(k_{1A}\right) = \tilde{F}_{2A}\left(k_{1A}\right) \qquad 16$$

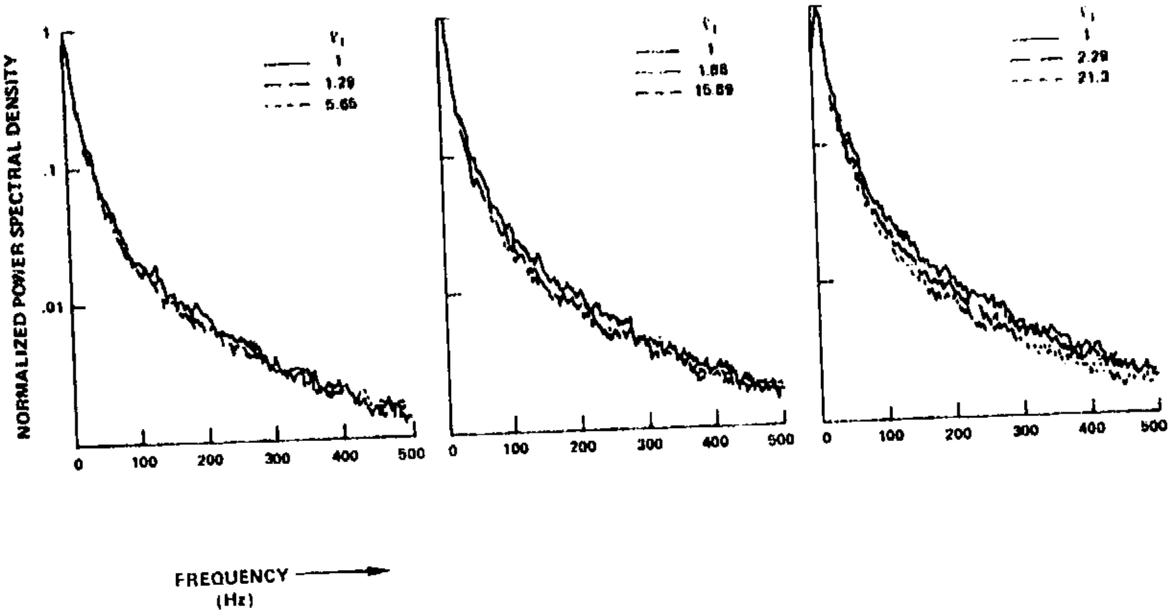

Figure 57 Normalized Transverse Velocity Component PSDs At Various Contraction Ratios

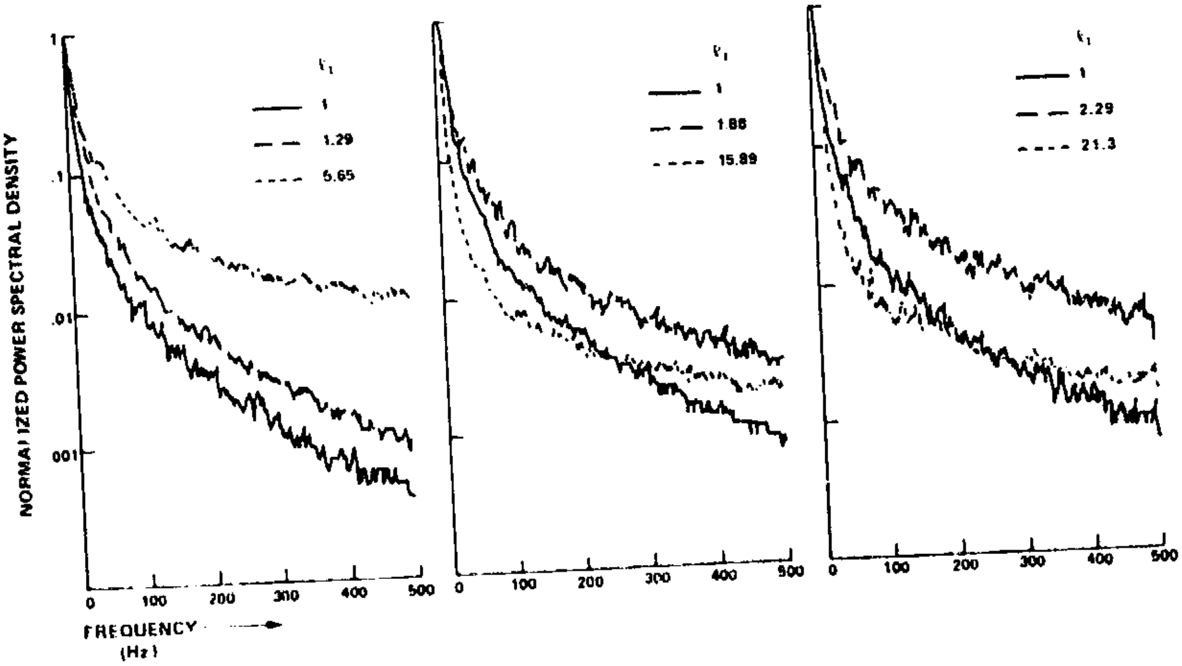

Figure 58 Normalized Streamwise Velocity Component PSDs At Various Contraction Ratios

This is in conflict with the simple model which would predict that

$$\tilde{F}_{2B}\left(k_{1B}\right) = \tilde{F}_{2A}\left(k_{1A}\right) \qquad 17$$

or

$$\tilde{F}_{2B}\left(\frac{k_{1A}}{\ell_1}\right) = \tilde{F}_{2A}\left(k_{1A}\right) \qquad 18$$

The approximation of Equation 16 is, however predicted by the Ribner-Tucker theory (33). In their report the comparison of the PSD, F_2 (k_1) before and after the contraction shows that the PSDs are very similar in shape when plotted as a function of the upstream streamwise wave number.

The streamwise velocity component PSDs are shown in Figure 58. Each PSD is denoted by the contraction ratio at which it occurs. Those marked with 1 are pre contraction PSDs. If this figure is viewed together with Figure 51 it is immediately apparent that as the streamwise component RMS value becomes lower its spectrum shape diverges from the pre contraction PSD. At a contraction ratio of 5.65, a minimum in the RMS value is reached corresponding to a PSD shape that is most different from the pre contraction PSD. Subsequently as energy is transferred into the streamwise component from the transverse component, the streamwise PSD becomes more similar to the pre contraction PSD. In the pre energy transfer region (i.e. contraction ratios ≤ 5.65), if the PSDs are plotted in terms of the local wave number, it is clear that they are very similar in shape. An example is shown in Figure 59 where the PSD at a contraction ratio of 2.29 is compared with the pre-contraction PSD. In short, for contraction ratios ≤ 5.65.

$$\tilde{F}_{1A}\left(k_{1A}\right) = \tilde{F}_{1B}\left(k_{1B}\right) \qquad 19$$

This is in accordance with the simple model. The characteristics of this PSD as predicted by the theory of Ribner and Tucker (33) and in the extension of U. Ganz (36) are not observed in the streamwise velocity component data.

From Equation 19 and the corresponding mean square velocity and integral length scale ratios, the relationship between the un-normalized PSDs may be determined as

$$F_{1B}\left(k_{1B}\right) = \mu_1 \frac{L_{11B}}{L_{11A}} F_{1A}\left(k_{1A}\right) \qquad 20$$

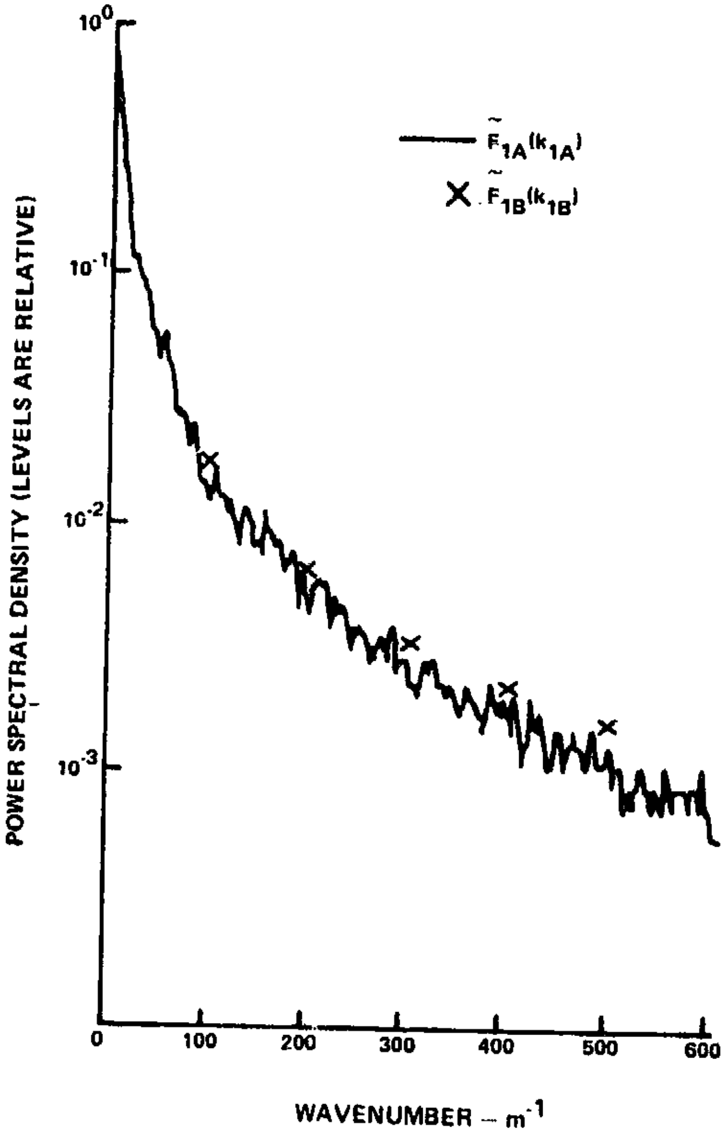

Figure 59 Comparison of Normalized Pre and Post Contraction Streamwise Wave Number PSDs ($\ell_1 = 2.29$)

For the other streamwise velocity component PSDs, it is reasonable, in view of the good agreement of the predicted length scale ratios with measurement, to assume that these PSDs will be related in a similar manner to Equation 20. In general then for the streamwise velocity component in the initial contraction region:

$$F_{1B}\left(k_{jB}\right) = \mu_1 \frac{L_{1jB}}{L_{1jA}} F_{1A}\left(k_{jA}\right) \qquad 21$$

At the higher contraction conditions the streamwise component spectra change radically. This is due to the transfer of energy from the transverse velocity components discussed earlier (recall that the energy transferred from the transverse velocity component is small initially compared with the total transverse velocity kinetic energy, but is large compared to the existing streamwise kinetic energy. Therefore while the effect of this transfer on the transverse spectra is small, the effect on the streamwise velocity component is large). Specifically the streamwise PSD receives energy in the low frequency regime and this is expected since the mechanism of transfer is inertial. Neither the simple model nor the linear theory of Ribner and Tucker predict the effect of energy transfer on the streamwise component of the turbulent velocity field. However, there is an alleviating condition that will be discussed below.

The comparisons of measured and predicted PSDs together with the scale and RMS velocity ratio comparisons point to the conclusion that the transverse characteristics are most accurately portrayed by the viscous decay corrected Ribner-Tucker, Batchelor-Proudman theory. Thus the 6 transverse velocity PSDs will be modelled in the ICS design system by the viscous decay corrected formulations of Ribner and Tucker and Ganz (33,36) who extended the work of Ribner and Tucker to complete the PSD matrix. The streamwise velocity scales and PSDs in the pre-energy transfer region, described above, are accurately modelled by the simple theory. Other characteristics, namely, the RMS velocity ratios and PSDs in the energy transfer region are not described well by either theory and it is appropriate to discuss at this time the alleviating condition mentioned above that lessens the importance of accurately predicting stream wise characteristics.

The component of the turbulent velocity field that is probably most important as regards noise generation is the upwash in the tip region of the fan rotor. As shown in (29) this is related to the transverse and streamwise turbulent velocity components by means of the relative blade inflow angle, γ_0,

$$F_n(\omega) = F_1(\omega)\cos^2\gamma_0 + F_2(\omega)\sin^2\gamma_0 \qquad 22$$

where F denotes a PSD and the subscripts 1 and 2 refer to the streamwise and transverse velocity components, respectively.

Integrating this equation over frequency yields,

$$\overline{u_n^{\,2}} = \overline{u_1^{\,2}}\cos^2\gamma_0 + \overline{u_2^{\,2}}\sin^2\gamma_0 \qquad 23$$

Now if it is assumed that the turbulence is initially isotropic then

and the ratio of the mean square values of the upwash component across a contraction may be written as

$$\frac{\left(\overline{u_n^{\,2}}\right)_B}{\left(\overline{u_n^{\,2}}\right)_A} = \frac{\left(\overline{u_1^{\,2}}\right)_B}{\left(\overline{u_1^{\,2}}\right)_A}\cos^2\gamma_o + \frac{\left(\overline{u_2^{\,2}}\right)_B}{\left(\overline{u_2^{\,2}}\right)_A}\sin^2\gamma_o \qquad 24$$

where B denotes the post contraction location and A, the pre-contraction, or upstream location. In the tip region of a JT9D, a typical value of γ_0 is 30^0. If this fact is used together with the measured data at a contraction ratio of 21.3 then an estimate of the mean square ratio of the upwash velocity component across the contraction can be made, and is

$$\frac{\left(\overline{u_n^{\,2}}\right)_B}{\left(\overline{u_n^{\,2}}\right)_A} = \underset{\substack{\uparrow \\ \text{STREAMWISE}}}{.2883} + \underset{\substack{\uparrow \\ \text{TRANSVERSE}}}{2.48} \qquad 25$$

The upwash velocity ratio thus appears to be dominated by the transverse turbulent velocity component and hence the prediction of the turbulent upwash velocity through the contraction is probably not strongly affected by errors in the streamwise component characteristics provided the energy transfer is not too far advanced. Consequently for the purposes of the ICS design system and in view of the tendency of the streamwise component energy to recover at the high contraction ratios encountered on the test stand (see Figure 53, where at a contraction ratio of 21 the streamwise RMS ratio $\simeq .6$), it is suggested that the streamwise component mean square velocity ratio be approximated by .5 in the higher contraction regime ($\ell_1 > 6$, say). With regard to the post contraction streamwise PSD, in this higher contraction region, there is some similarity between this PSD and the pre contraction PSD in the upstream wave number, k_{1A}. It is thus suggested that the PSD relationships be at the higher contraction ratios, for purposes for ICS design.

$$F_{1B}\left(k_{jA}\right) = \mu_1 \frac{L_{11B}}{L_{11A}} F_{1A}\left(k_{jA}\right) \qquad 26$$

In summary the contraction models to be used in the ICS design system are

Item	Source	Expression	
Kinetic Energy Ratio		$\frac{KE_B}{KE_A} = \frac{1}{3}\left\{\mu_1 + 2\mu_2\right\}$	27
Transverse Component Mean Square Velocity Ratio	Ribner-Tucker Batchelor-Proudman	$\mu_2 = \mu_3 = \frac{3\ell_1}{4} \frac{\left(X - X_o\right)_A}{\left(X - X_o\right)_B}$	28
Streamwise Component Mean Square Velocity Ratio	Prandtl	$\mu_1 = \ell_1^{-2} \quad \ell_1 < 6$	29
	Data	$\mu_1 \simeq .5 \quad \ell_1 \geq 6$	30

Item	Source	Expression	
Transverse Velocity Component Length Scales	Ribner-Tucker Ganz	$\frac{(L_{21})_B}{(L_{21})_A} = \frac{(L_{31})_B}{(L_{31})_A} = \frac{\ell_1^{2}}{\mu_2}$	31
		$\frac{(L_{22})_B}{(L_{22})_A} = \frac{(L_{33})_B}{(L_{33})_A} = \frac{\ell_1^{1/2}}{\mu_2}$	32
		$\frac{(L_{23})_B}{(L_{23})_A} = \frac{(L_{32})_B}{(L_{32})_B} = \frac{1}{\ell_1 \mu_2}$	33
Streamwise Velocity Component Length Scales	Simple Model	$\frac{(L_{11})_B}{(L_{11})_A} = \ell_1 .$	34
		$\frac{(L_{13})_B}{(L_{13})_A} = \frac{(L_{12})_B}{(L_{12})_A} = \ell_1^{-1/2}$	35

Item	Source	Expression
Transverse Velocity Component Length Scales	Ribner-Tucker Ganz	

$$F_{2B}\left(k_{1B}\right) = F_{3B}\left(k_{1B}\right) \simeq \frac{\pi N \ell_1}{2\gamma^2}\left\{\frac{1+\frac{2k_{1A}^2}{\gamma^2}}{\left(1+\frac{k_{1A}^2}{\gamma^2}\right)^2}\right\} \qquad 36$$

$$F_{2B}\left(k_{2B}\right) = F_{3B}\left(k_{3B}\right) \simeq \frac{\pi N \ell_1}{\gamma^2 s}\left\{1+\frac{p}{2}+\frac{s\sqrt{p}}{4}\left[\sin^{-1}\left(1-\frac{2}{s}\right)-\frac{\pi}{2}\right]\right\}$$

$$F_{2B}\left(k_{3B}\right) = F_{3B}\left(k_{2B}\right) \simeq \frac{\pi N \ell_1}{\gamma^2}\left\{\left(\frac{1}{s}-\frac{1}{2}\right)\frac{p}{s}-\frac{\sqrt{p}}{4}\sin^{-1}\left(1-\frac{2}{s}\right)-\frac{\pi}{2}\right\} \qquad 37$$

Item	Source	Expression
Streamwise Velocity Component PSDs	Data	

$$F_{1B}\left(k_{jB}\right) = \mu_1 \frac{\left(L_{1j}\right)_B}{\left(L_{1j}\right)_A} F_{1A}\left(k_{jA}\right) \qquad \ell_1 < 6 \qquad 38$$

$$F_{1B}\left(k_{jA}\right) = \mu_1 \frac{\left(L_{1j}\right)_B}{\left(L_{1j}\right)_A} F_{1A}\left(k_{jA}\right) \qquad \ell_1 > 6 \qquad 39$$

6.1.2 Screening

The experimental determination of the effect of a screen on a turbulence field convecting through it, is complicated by the turbulence generated by the screen itself. This screen-generated turbulence contaminates any downstream turbulence measurements as noted in Section 5. Furthermore since the energy lost from the mean flow is converted in part into turbulent kinetic energy by the screen, the greater the mean flow energy loss the greater will be the turbulent kinetic energy gain. Thus the screen generated turbulence intensity level can be expected to increase with increase in screen resistance and throughflow speed.

The contamination of the downstream turbulence field was particularly evident in the perforated plate configurations. This contamination is illustrated in Figure 60 where pre and post screen transverse velocity component PSDs are shown for various throughflow velocities for the 66% open area perforated plate. As the duct speed increases (this is the velocity in the suction rig duct, Figure 5), the throughflow speed increases and the self generated turbulence increases. It should be noted that the PSD level increases at all frequencies. The high frequency increase is due to turbulence generated at the perforated plate holes while the increase at lower frequencies is probably due to the large scale turbulence generated by the flow around the edge of the screen. This latter source of self generated turbulence will not be present in an ICS. The small scale hole-associated turbulence, however, will be present but will not contribute to the fan tones provided the perforated plate hole size is small.

In order to extract the characteristics of the residual upstream turbulence field, uncontaminated by screen generated turbulence, it was felt that since the downstream intensities and kinetic energy increased as the throughflow increased, if the data were extrapolated back to small throughflow velocities, a reasonable estimate of the residual turbulence characteristics would be obtainable. In Figure 61 the kinetic energy ratios across the perforated plates are shown as functions of duct velocity. On extrapolation back to zero duct

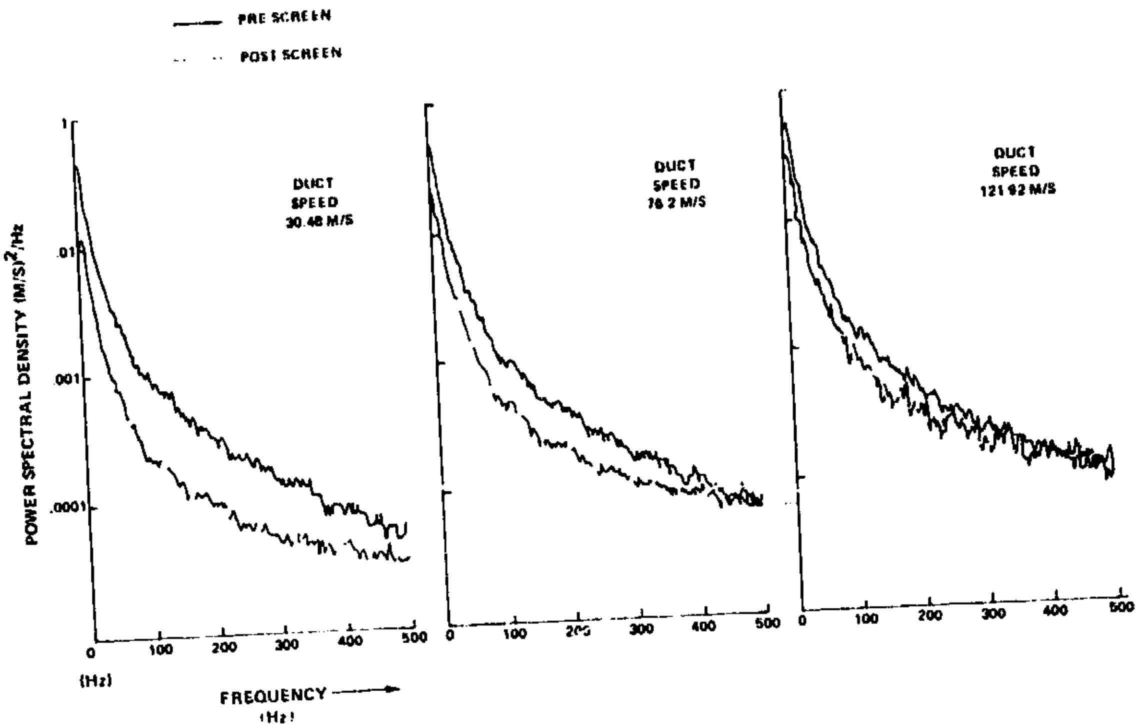

Figure 60 Transverse Velocity Component PSDs Across A 66% Open Area Perforated Plate

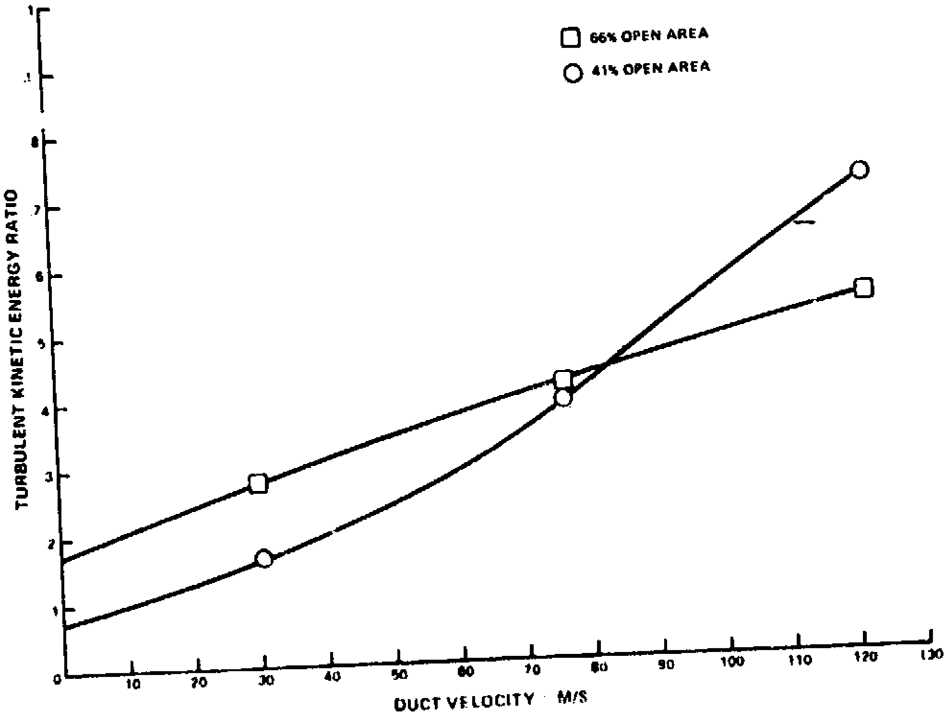

Figure 61 The Measured Turbulent Kinetic Energy Ratios Across Perforated Plate

speed (this corresponds to a low throughflow velocity), values of the kinetic energy ratio due primarily to the residual turbulence fields are obtained for the two perforated plates (66% open area, 41% open area). The extrapolation is performed using duct velocity since the screen throughflow velocity is not as accurately known. These data are compared with simple model predictions and Townsend's (37) data (obtained using gauzes) in Figure 62. The agreement is good.

This technique is also used to estimate the ratios of the mean square values of the turbulent velocity components across the perforated plates. The extrapolated values obtained are shown compared to theory and Townsend's data in Figure 63. As can be seen, the currently measured transverse and streamwise component ratios indicate a return to isotropy for each perforated plate (it should be noted that the turbulence upstream of each perforated plate appeared to be approximately isotropic) (The return to isotropy is at a more advanced stage in the present experimental data than in Townsend's data). Neither component ratio is, in consequence, predicted well by the theory of Taylor and Batchelor (29) or the simple theory, although the measured streamwise component ratio for the higher solidity perforated plate (41% open area) is not much different from the theoretical prediction. The values of the velocity component ratios predicted by theory do provide an upper bound to the extent of the unequal energy distribution due to the screen. The assumption of a return to isotropy provides the lower bound. The choice of a model for the mean square velocity ratio will be discussed in the context of the test stand situation in Section 6.4, below.

The integral length scale ratios were also determined by extrapolation and they are shown in Figure 64 where they are compared to the predicted values using Taylor and Batchelor's theory and the simple theory. Four length scale ratios were determined for each perforated plate. They are those of L_{11}, L_{21}, L_{13}, L_{23} where L_{21}, for instance, is the integral length scale of the u_2 velocity component in the x_1 direction.

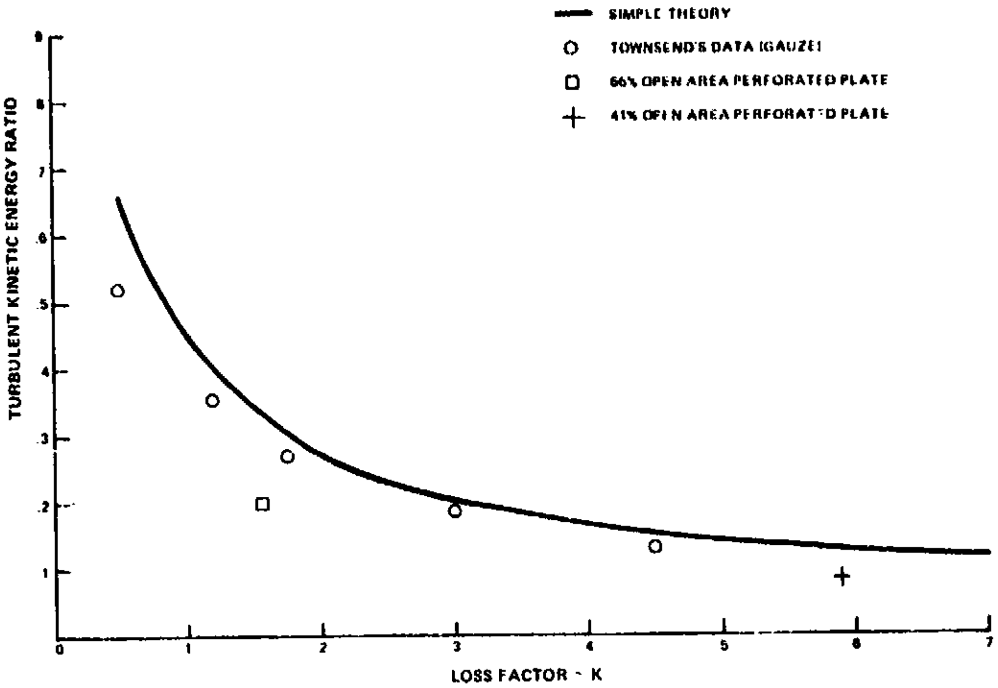

Figure 62 The Turbulent Kinetic Energy Ratio Across Perforated Plate

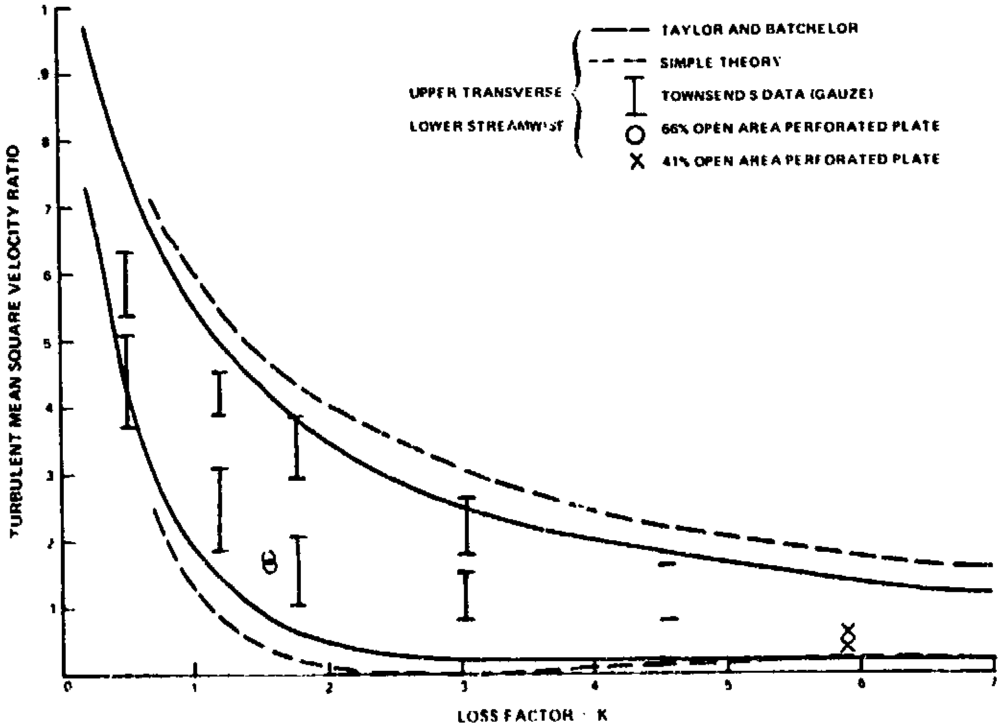

Figure 63 The Turbulent Velocity Ratios Across Perforated Plate

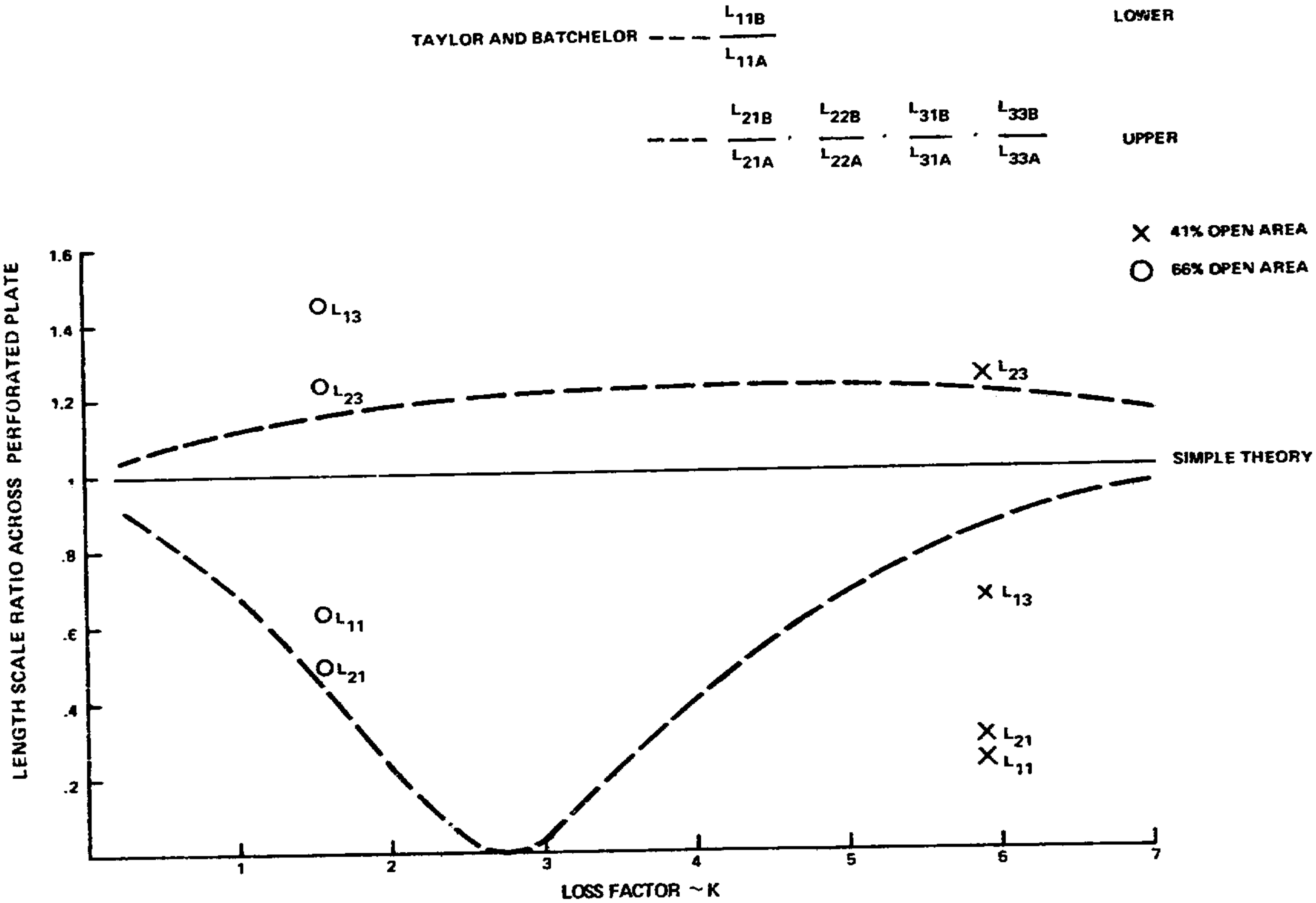

Figure 64 Turbulence Scale Ratios Across Perforated Plate

The measured scale ratios do not agree well with either theory. This is not unexpected in view of the lack of agreement at the mean square velocity ratio level. However, the discrepancy is not due to the returning of the turbulence to isotropy since this would require that the scale ratios be all of the same value. Thus, as observed in the contraction experiment, while the energy distribution tends to equipartition between components there is not a corresponding tendency for the length scales to attain their isotropic values. The scale data is, however, to some extent questionable due to the diffusion of the flow by the perforated plate. This diffusion has little effect on the kinetic energy ratio across the perforated plates. Consequently the scale model will be chosen as a result of other considerations discussed below in sub section 6.1.3. The shape of the PSD of the transverse velocity component downstream of the perforated plates is similar to that upstream at the lower frequencies (Figures 65 and 66). The higher frequencies are contaminated with self-generated turbulence. This agreement in spectral shape is in accordance with the simple theory. The streamwise component PSD's (Figures 67 and 68) tend to become similar in shape to the corresponding pre-screen PSD's as the plate throughflow velocity decreases. Thus these data tend to support the simple theory that, as a whole, the PSD shape of the upstream turbulence is unchanged by the perforated plate. This may be the result of the tendency to return to isotropy observed in the mean square velocity components.

In summary, both PSD's and mean square velocity ratio's indicate a tendency to return to isotropy. The integral length scales do not yield clear information. The kinetic energy change across the perforated plate is predicted fairly well by the simple theory as are the residual turbulence PSD shapes downstream of the perforated plate. The effect of the honeycomb on convected turbulence will now be considered.

The turbulence field downstream of all honeycombs examined was also contaminated by self-generated turbulence as noted in Section 5. It is seen in the PSDs (see Figure 74, for example) and is particularly noticeable in the auto correlations of the transverse velocity component, Figure 69. Here the increasing

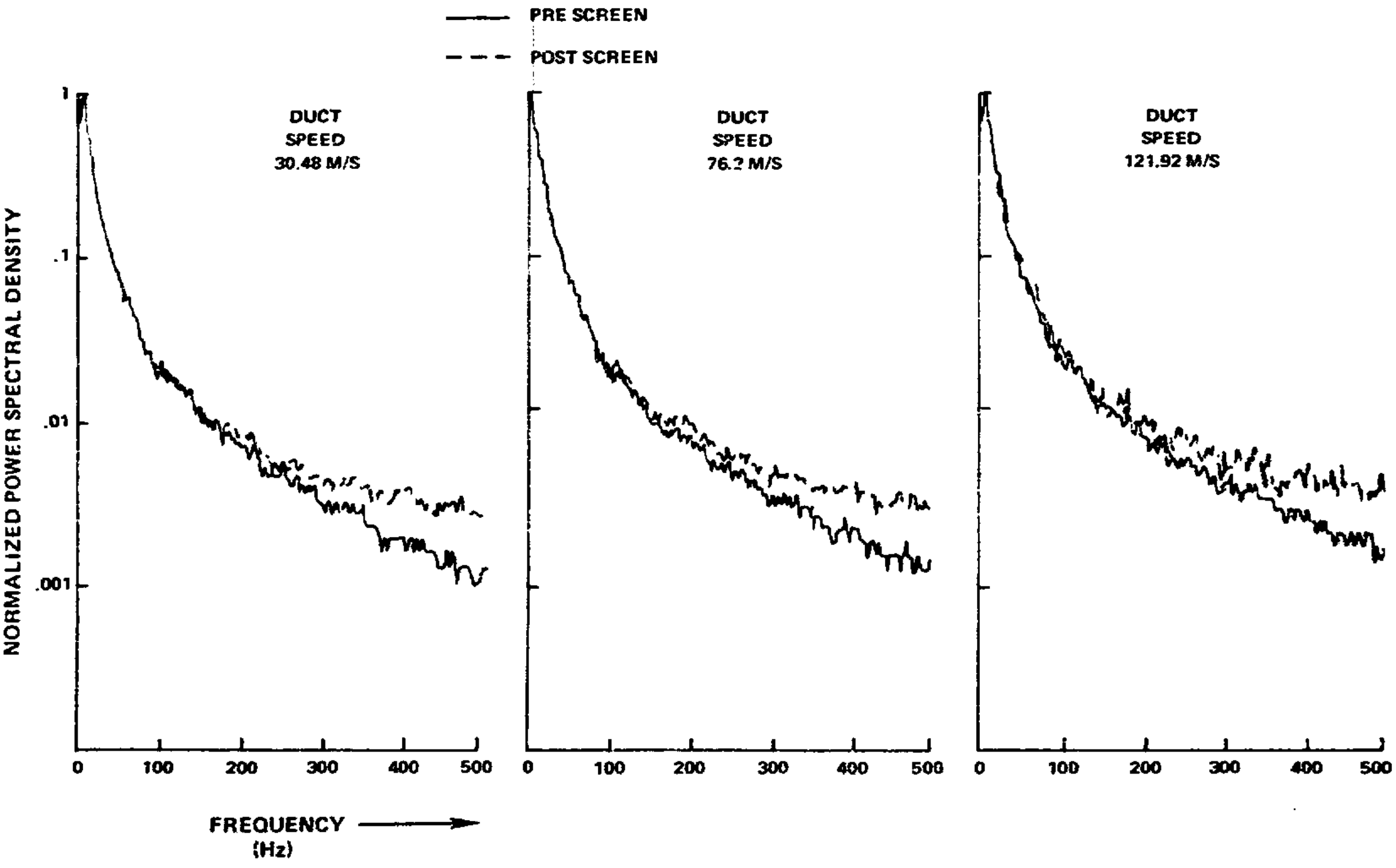

Figure 65 *Normalized Transverse Velocity Component PSDs Across 66% Open Area Perforated Plate*

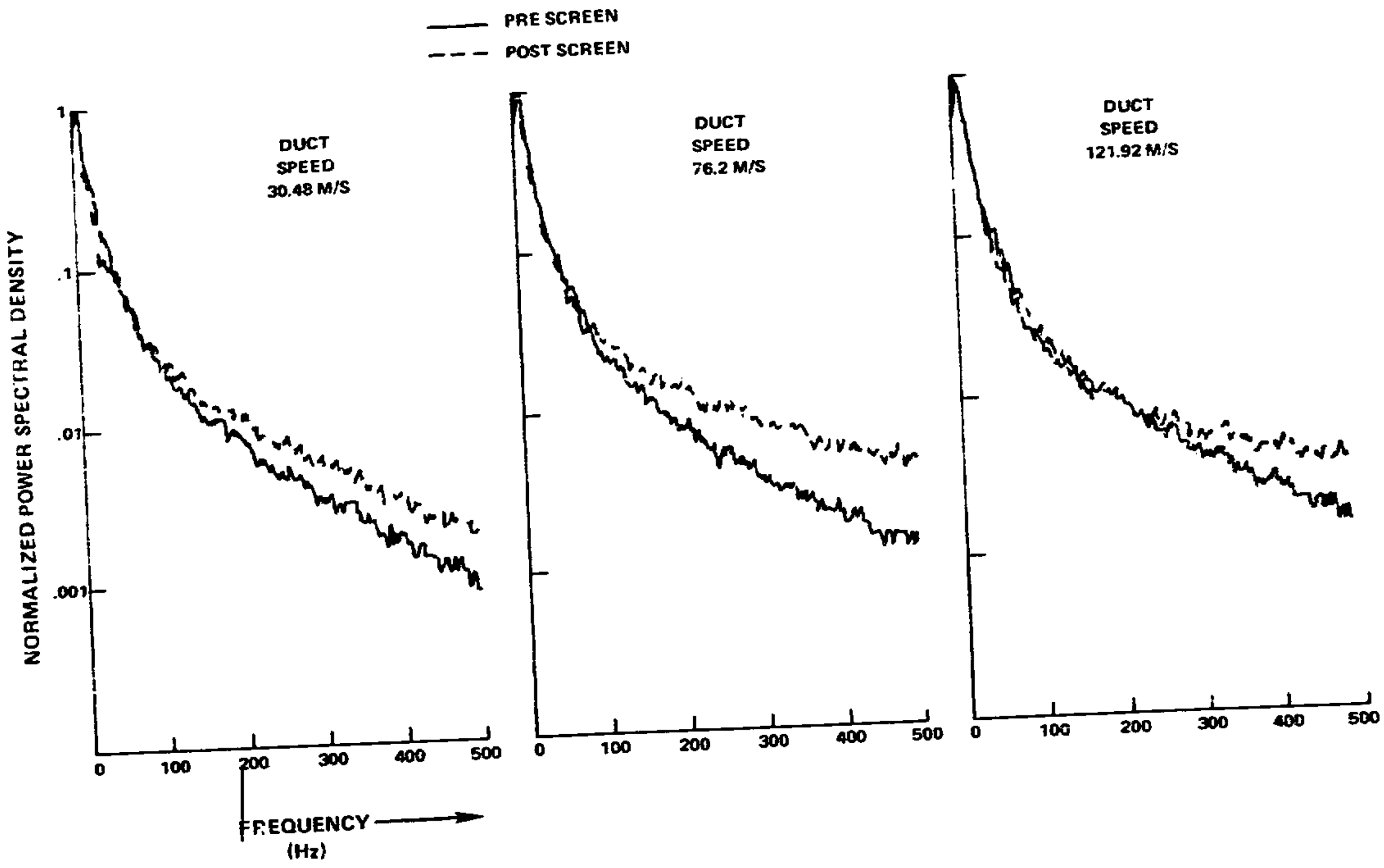

Figure 66 Normalized Transverse Velocity Component PSDs Across 41% Open Area Perforated Plate

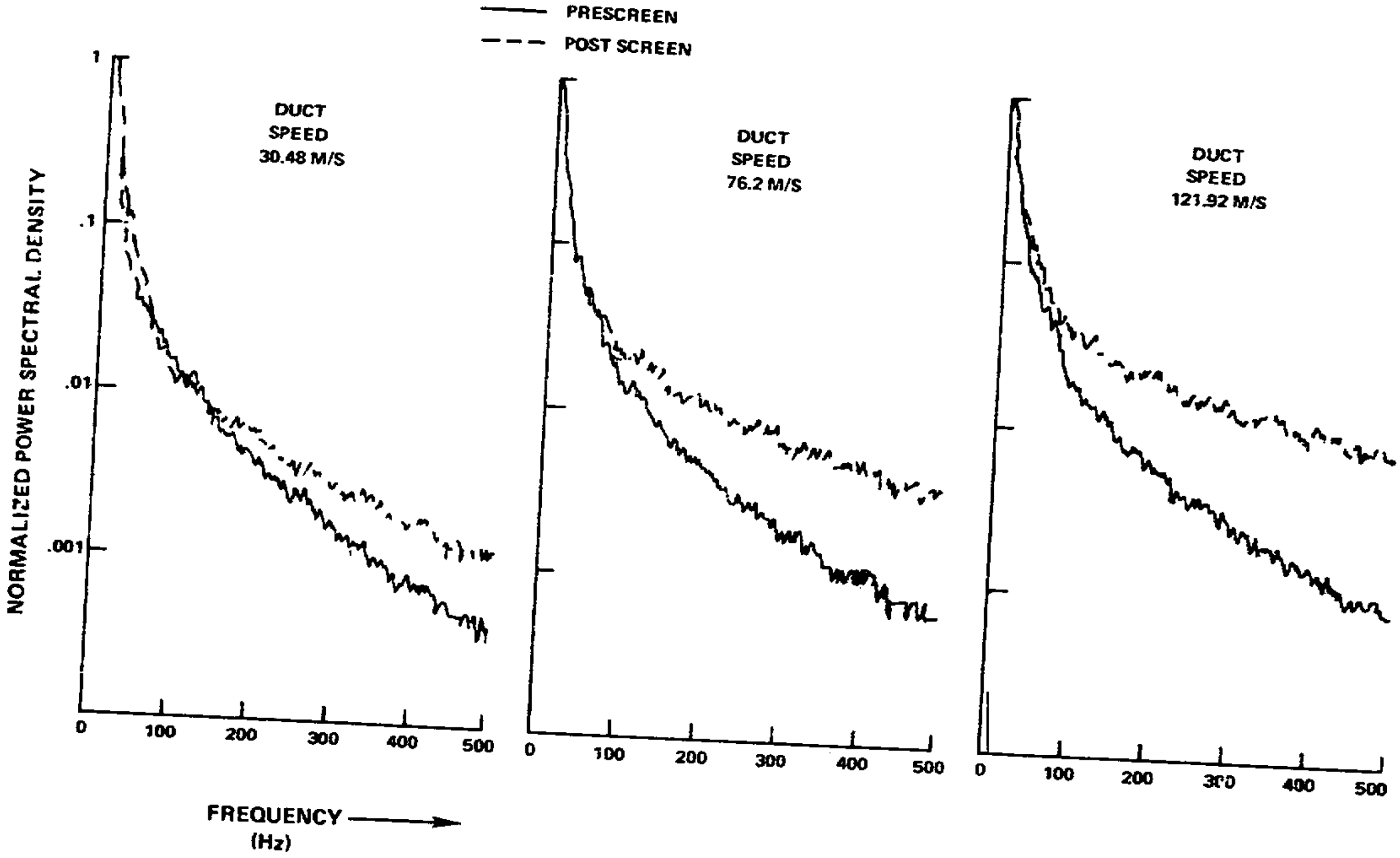

Figure 67 Normalized Streamwise Velocity Component PSDs Across 66% Open Area Perforated Plate

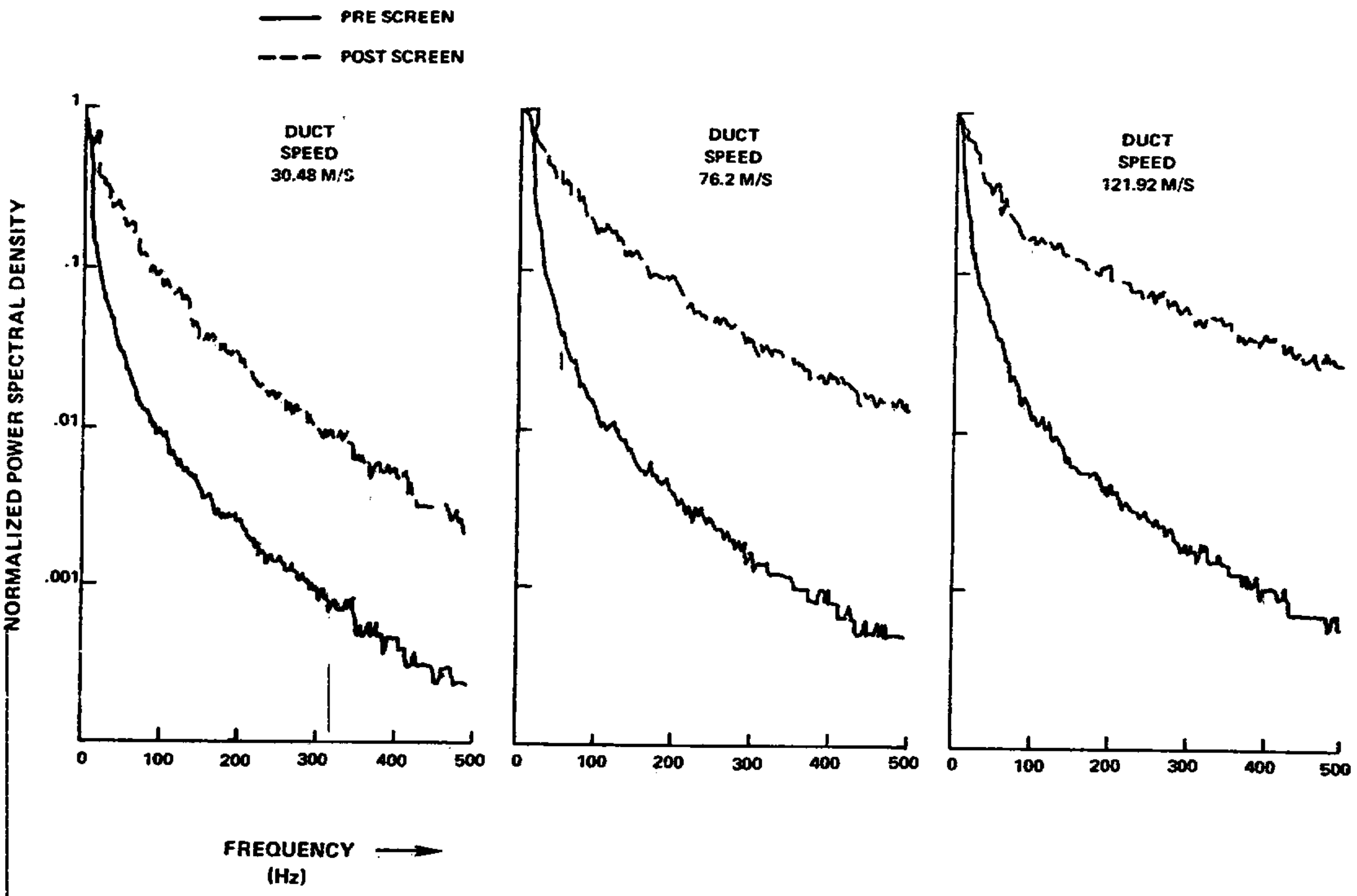

Figure 68 Normalized Streamwise Velocity Component PSDs Across 41% Open Area Perforated Plate

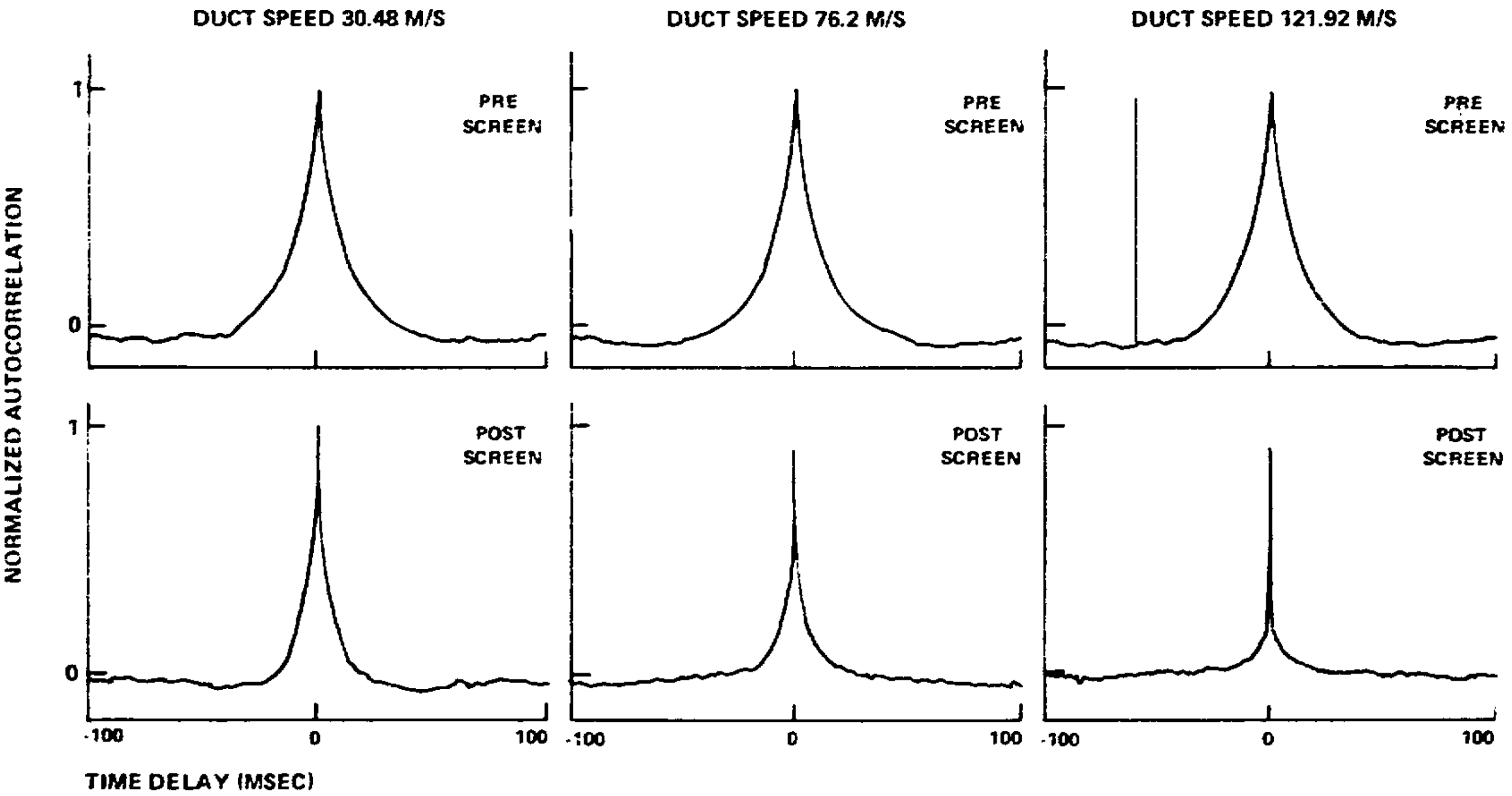

Figure 69 Auto Correlations of the Transverse Velocity Component Across 1.27 cm Honeycomb

level of high frequency turbulence is seen with increasing through flow velocity. This increasing level of high frequency energy is manifested in the autocorrelation as a progressively sharper spike. The upstream autocorrelations are also shown in the figure, and the higher frequency energy content of the downstream turbulence field is self-evident. The extraction of the residual turbulence levels and integral length scales is carried out by using the auto correlations, (see Figure 70). (This procedure is used rather than the extrapolation method described for the perforated plates because it produced more data points and also because the self generated turbulence was not clearly defined in the perforated plate auto-correlation.) Thus the turbulent kinetic energy ratio across the honeycomb could be found for the turbulence convected through the honeycomb, uncontaminated by self-generated turbulence. (It is unlikely in view of the small scale of the self generated turbulence that it will contribute to fan tone noise, however, there could be a contribution to fan broadband noise).

The ratios determined from the residual convected kinetic energy are shown in Figure 71. They are plotted as a function of the pressure loss coefficient. This parameter is chosen rather than the flow angle ratio (α) which is effectively zero for each honeycomb (see Section 5). The theoretical values of the kinetic energy ratio are also shown as a function of pressure loss coefficient for $\alpha = 0$.

$$\frac{KE_B}{KE_A} = \frac{1}{3}\left(\frac{1}{1+K}\right)^2 \qquad 40$$

The agreement with the prediction of the simple theory is good.

The mean square component velocity ratios (with the self generated contribution removed) are shown in Figure 72. The streamwise velocity component levels are higher than the transverse component levels. The equipartition of energy observed downstream of the perforated plate is not therefore, repeated in the case of the honeycomb, as might be expected, since honeycomb greatly attenuates the transverse velocity component. On comparison with predicted levels, however, it is noted that the measured transverse component levels are higher

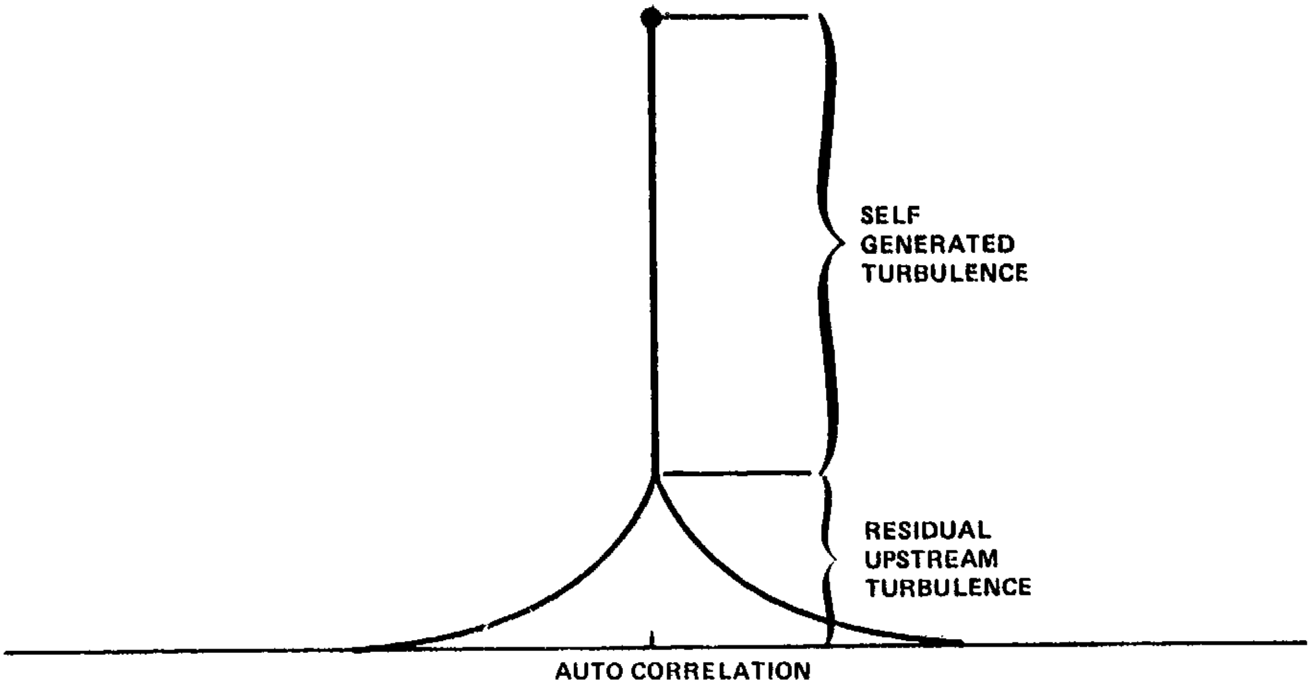

Figure 70 Extraction of Residual Upstream Turbulence Characteristics From the Downstream Autocorrelation

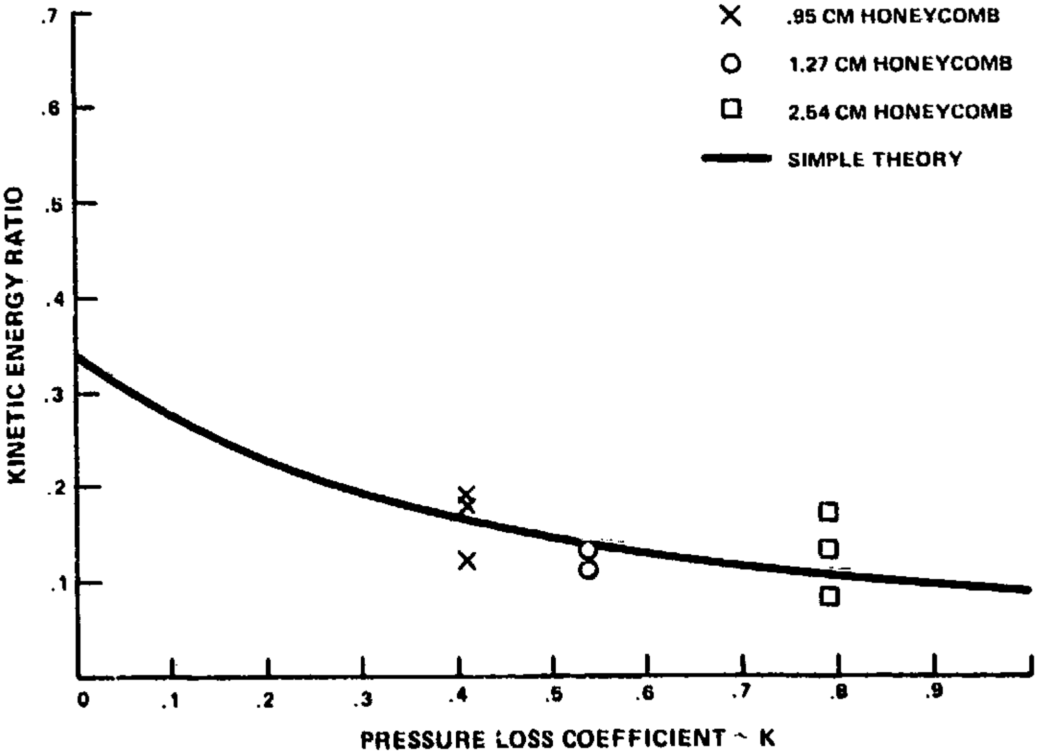

Figure 71 Comparison of Measured and Predicted Kinetic Energy Ratios Across Honeycomb

than the predicted values (of approximately zero) while the streamwise component values are for the most part, lower. A slight tendency to isotropy or equipartition of the turbulent kinetic energy relative to the theoretical prediction is thus indicated.

Again then, as in the case of the perforated plate, the data lie between values predicted assuming a return to isotropy and those predicted assuming no return. The situation likely to be encountered downstream of an actual ICS will be discussed in the following section.

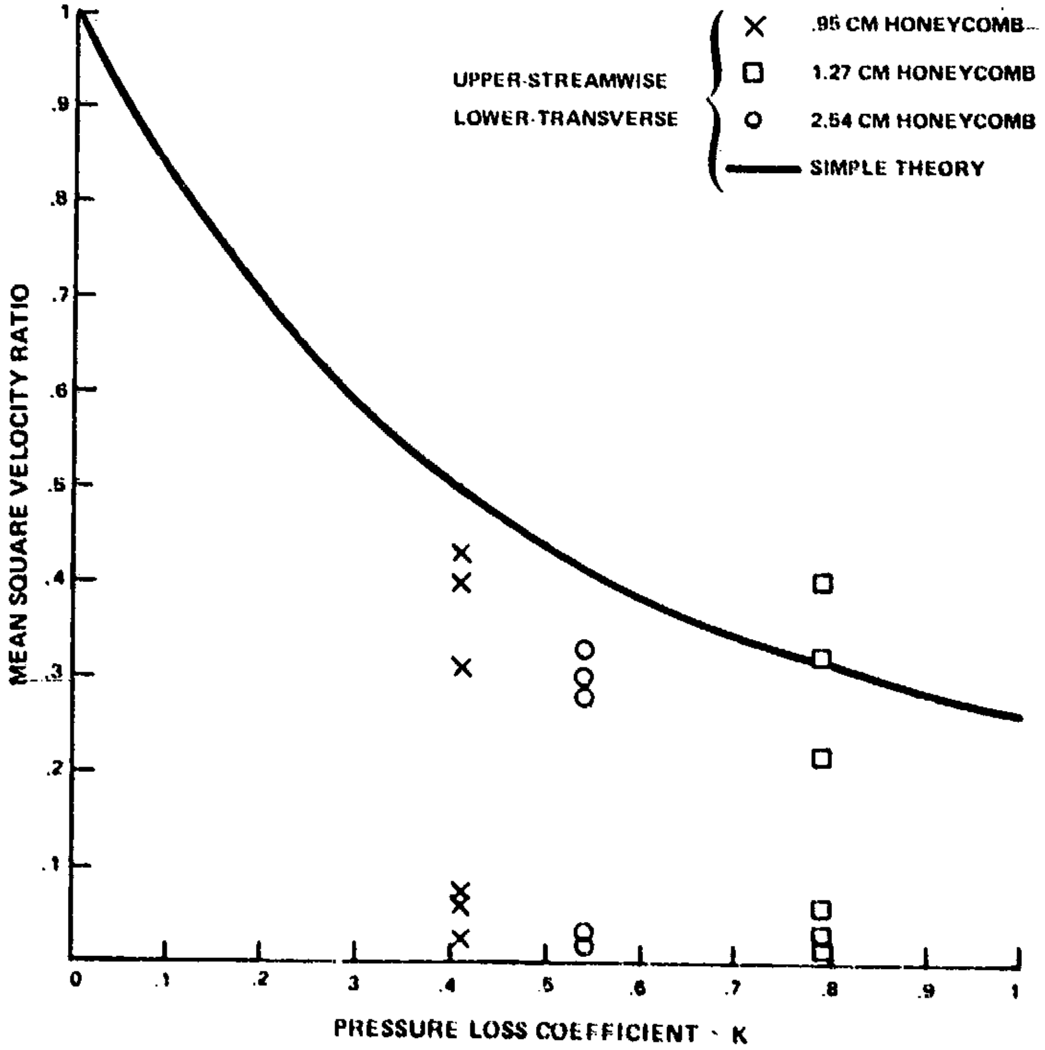

Figure 72 Comparison of Measured and Predicted Mean Square Velocity Ratios Across Honeycomb

The integral length scale ratios are shown in Figure 73. The transverse scale ratios tend to be close to the predicted value of unity, while the axial length scale ratios are on the whole somewhat higher. The 2.54 cm thick honeycomb (K = .79) yielded erratic values and this was due in part to the low level of the residual turbulence compared to the honeycomb generated level. The length scale ratios support the non-isotropy in the turbulence field observed in the energy distribution. The length scale ratios may be roughly approximated by unity and this value will be used in the ICS design system.

The change in shape of the PSDs of the two velocity components is shown in Figures 74 and 75. The 2.54 cm thick honeycomb configuration is shown here, but the comparisons are typical for the other honeycombs. Each PSD is normalized by its maximum value thus allowing a comparison of the shapes to be made. The comparisons of the streamwise velocity component PSDs, Figure 74, indicate that the honeycomb generated turbulence increases with increasing throughflow speed. This corresponds to the deductions made previously from the autocorrelations. In addition there is a tendency for the downstream PSD shape to approach the upstream PSD shape as the throughflow velocity decreases (i.e. at the 30.48 m/s duct velocity condition, corresponding to the lowest throughflow speed, the downstream streamwise velocity PSD is most similar to the upstream PSD shape). The transverse component PSD comparisons show a similar trend, however, because of the extreme suppression of the component, the downstream PSDs are dominated by the self-generated turbulence even at the lowest throughflow velocity. The current measurements then provide little information on the distribution of the residual energy in the transverse velocity component downstream of the honeycomb. The integral length scale ratios discussed above are roughly unity, which suggests that the residual energy distribution of the transverse velocity component could be similar to the prescreen distribution. These data then do provide some support for the simple model PSD relationship

$$\tilde{F}_{ijB} = \tilde{F}_{ijA} \qquad 41$$

where $\tilde{F}$ represents a PSD normalized with respect to its maximum value. This model will then be used in the ICS design system.

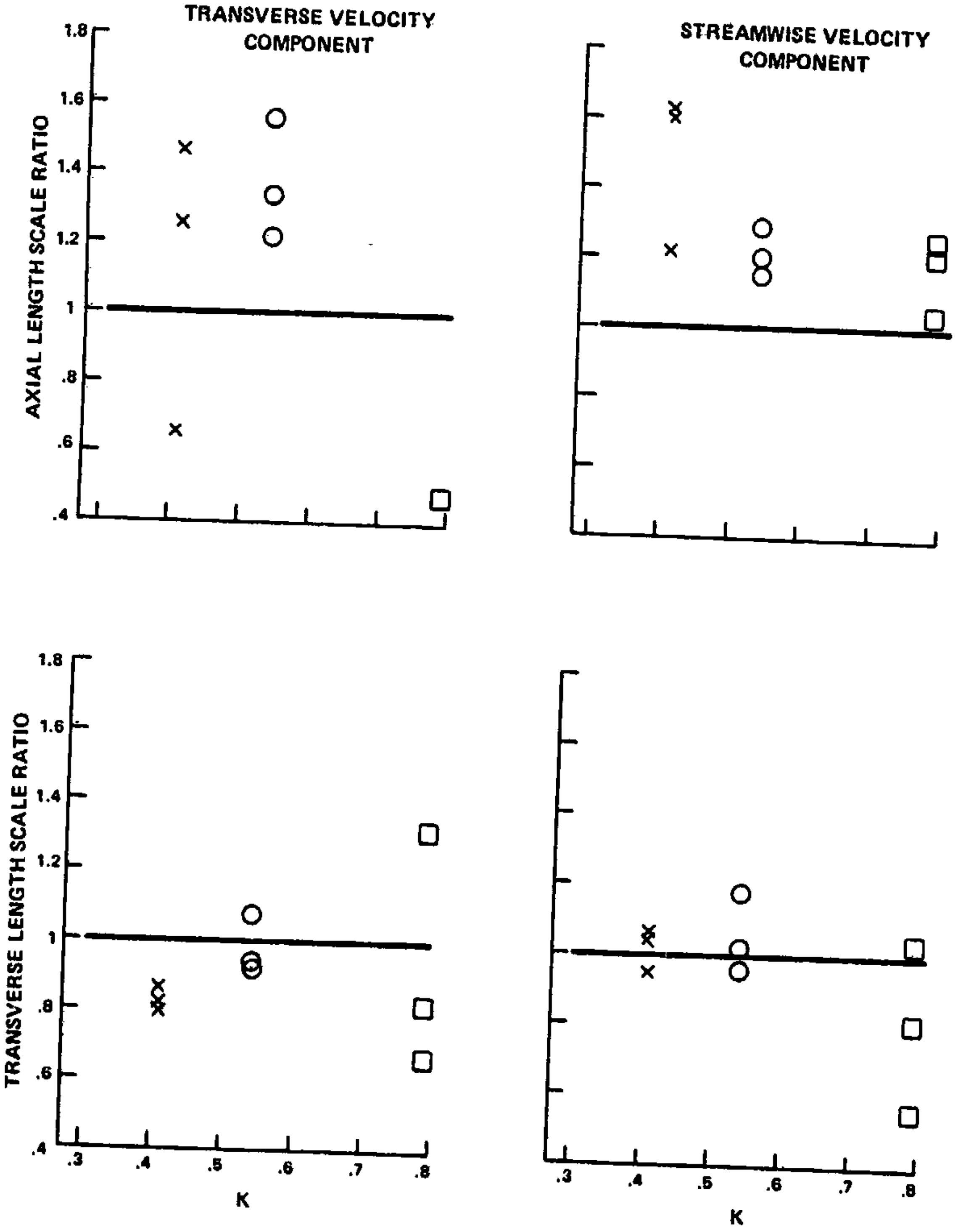

Figure 73 The Length Scale Ratios Across Honeycomb

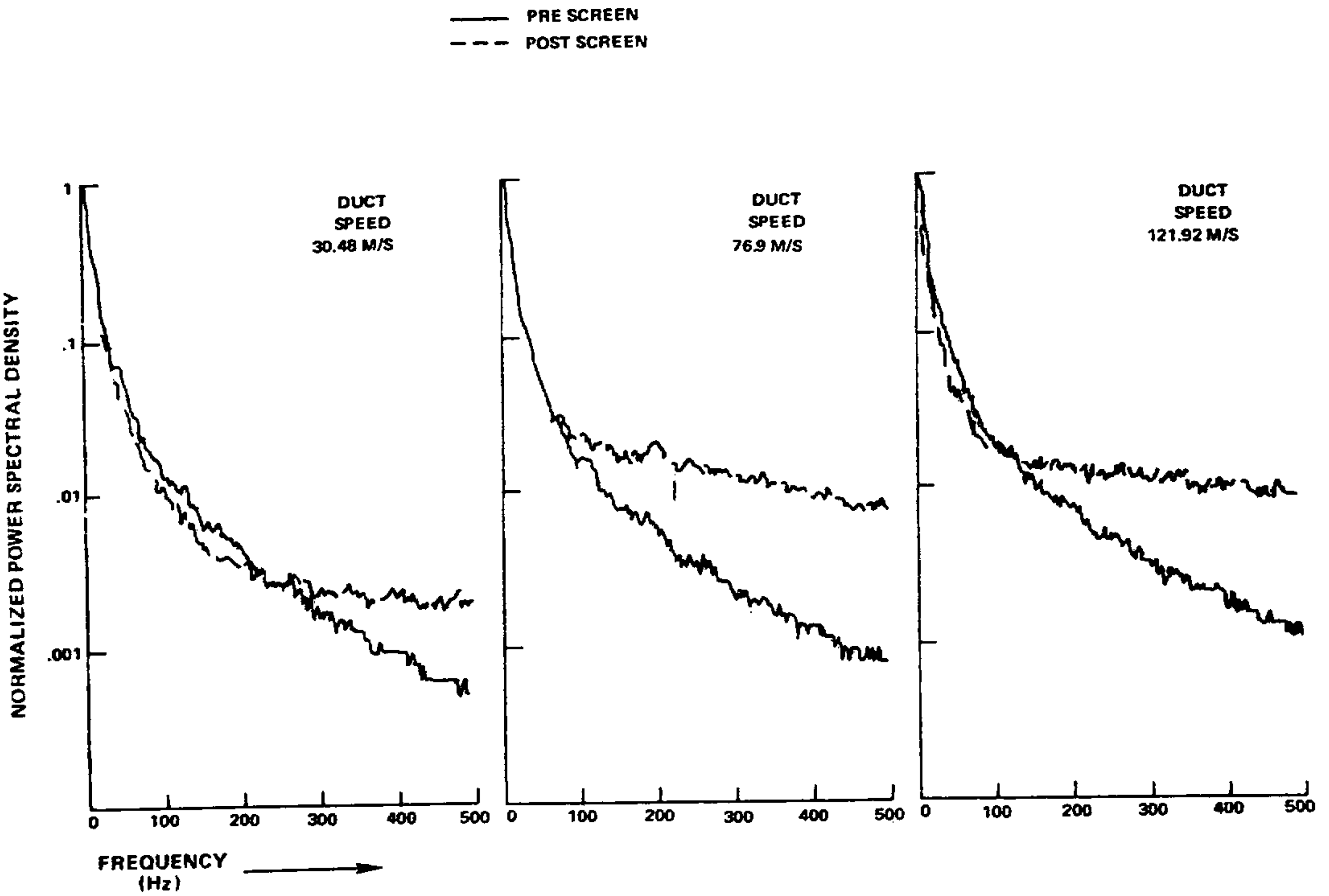

Figure 74 Normalized Streamwise Velocity Component PSDs Across 2.54 cm Honeycomb

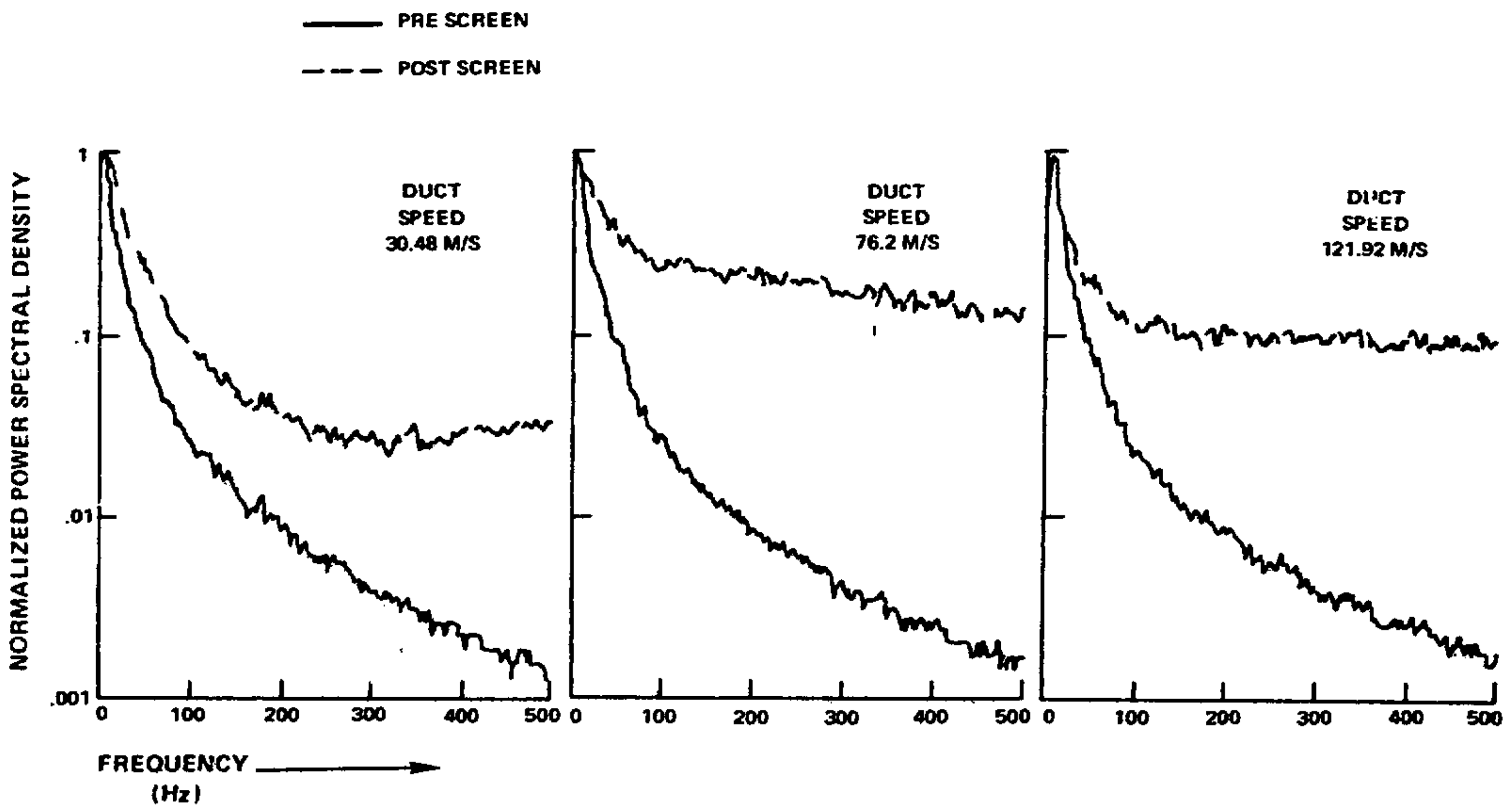

Figure 75 Normalized Transverse Velocity Component PSDs Across 2.54 cm Honeycomb

In summary, the turbulence kinetic energy ratio across both types of screen (perforated plate and honeycomb) with self generated turbulence corrected out is reasonably well predicted by the simple theory of Taylor and Batchelor. The corresponding values of the streamwise and transverse components and mean square velocity ratios are not well predicted for the perforated plate in view of an apparent return to isotropy. The theoretical predictions are closer for these ratios across honeycomb, probably because the honeycomb produces a much more uneven energy distribution between streamwise and transverse velocity components. The measured integral length scale ratios across the screens are scattered around unity, while the downstream PSDs are contaminated to a greater or lesser extent by self-generated turbulence. There is some evidence to suggest that the residual turbulent energy is distributed in wave number in a similar way to the pre-screen turbulence.

The models for the effect of perforated plate and honeycomb on turbulence to be used in the ICS design system are:

Item	Source	Expression	
Kinetic Energy Ratio		$\frac{KE_B}{KE_A} = \frac{1}{3}\left\{ \mu_1 + 2\mu_2 \right\}$	42
Mean Square Velocity Ratios	Taylor and Batchelor (Simple)	$\mu_1 = \left(\frac{1 + \alpha - \alpha K}{1 + \alpha + K} \right)^2$	43
		$\mu_2 = \alpha^2$	44
		On return to Isotropy $\mu_1 = \mu_2 = \frac{KE_B}{KE_A}$	45
Integral Length Scale	Simple Model	$L_{ijB} = L_{ijA}$	46
PSD	Simple Model	$F_{ijB} = \mu_i F_{ijA}$	47

6.2 The Transfer Functions for the Effects of Contraction and Screening on Steady Distortions.

As described previously (Section 5) three types of wake generators were tested to study the effects of contraction and screening on steady distortions. Two of these produced streamwise velocity deficits while the third, an airfoil, produced a vortex. For the contraction part of the program a 3.81 cm square rod and a symmetric airfoil, 1 cm thick, were used to produce the axial velocity deficits. For the screening part, a 3.81 cm square rod and a 5.08 cm X 7.62 cm rod were used to produce the axial velocity deficit. The data gathered in these experiments were used as described below, to validate or modify the theoretical transfer functions.

6.2.1 Contraction

The transfer function for the effect of contraction on a steady axial deficit is first considered. From the measurements using the 3.82 cm square rod, values of the wake deficit ratios and wake width ratios as a function of contraction ratio were obtained. The tabulation of these ratios is shown in Figure 76. The comparison with theory is shown in Figure 77. Only two values of the measured wake width ratio are shown in Figure 77, since at the other contraction ratios the velocity deficit ratio was zero and the corresponding wake width ratio was indeterminate.

The theoretical model for the contraction of a viscous wake was reported in the interim Phase II report (29) of this contract.

It is

Velocity Deficit Ratio

$$\frac{\Delta U_1(r)}{\Delta U_1(r_o)} = \ell_1^{-1/4} \left\{ \ell_1^{3/2} + \frac{2D}{X(r_o)} \frac{\ell_1}{\left(1 + \ell_1^{1/2}\right)} \right\}^{-\frac{1}{2}} \tag{48}$$

Wake Width Ratio

$$\frac{b(r)}{b(r_o)} = \ell_1^{-5/4} \left\{ \ell_1^{3/2} + \frac{2D}{X(r_o)} \frac{\ell_1}{\left(1 + \ell_1^{1/2}\right)} \right\}^{1/2} \tag{49}$$

RIG SPEED	STATIONS CM		CONTRACTION RATIO	VELOCITY DEFICIT RATIO	WAKE WIDTH RATIO
30.48 M/S	55.9	25.4	.963	.247	1.352
30.48 M/S	55.9	20.3	3.918	0	0
76.20 M/S	55.9	25.4	1.258	.147	1.611
76.20 M/S	55.9	20.3	9.346	0	0
121.92 M/S	55.9	25.4	1.413	0	0
121.92 M/S	55.9	20.3	14.167	0	0

Figure 76 Wake Ratios Through a Contraction (3.81 cm Square Rod)

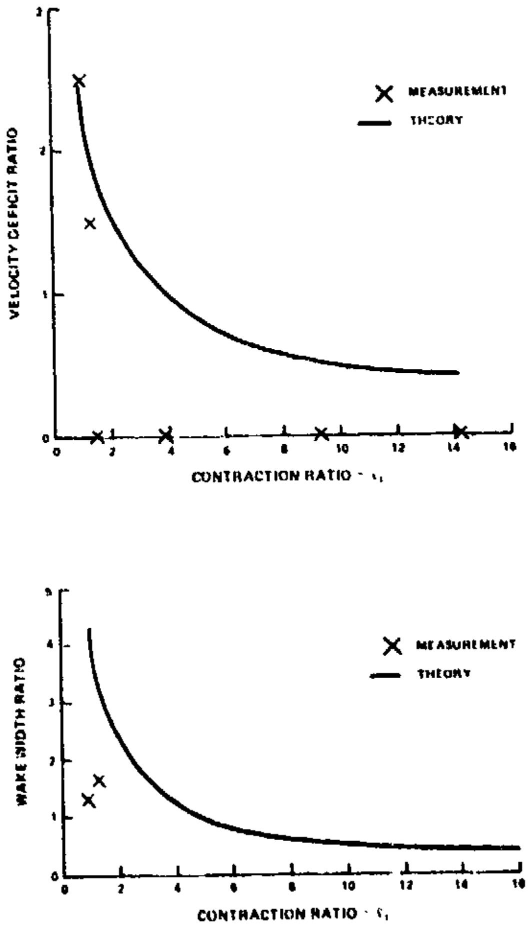

Figure 77 Comparison of Measurement and Theoretical Prediction (3.81 cm Square Rod)

The value of the virtual source distance $X(r_0)$ was, for a case with the contraction ratio equal to unity determined from the measured data and was found to be .29 cm. The model predictions in Figure 77 use this value.

The comparison of measured with predicted values shows that the trend of wake velocity deficit decay is duplicated by the model but the absolute velocity deficit ratios are overpredicted. At low contraction ratios, not unexpectedly, the agreement is close. The wake width ratio is not well predicted by the model. The two data points available indicate an increase in wake width ratio with contraction ratio. However, it is expected that at high contraction ratios the slope will be negative. A mechanism not accounted for by the theory is thus indicated.

The discrepancies between model predicted ratios and measured values could be due to an interaction between the contraction and viscous effects unaccounted for by the model. A possible explanation which would explain the data is that at low contraction ratios the viscous forces in the wake are more dominant than the inertia forces thus causing the wake width to increase. The velocity deficit correspondingly decreased more rapidly than would be predicted by a theory not accounting for this interaction. Subsequently as the contraction ratio increases, the inertial forces become increasingly dominant causing the wake width to contract.

To account for this contraction-viscous interaction the following procedure was adopted:

a) The distance between measuring stations D was adjusted to fit the measured velocity deficit ratios. With this approach the interaction effect manifests itself as an effective distance D which is a function of contraction ratio, ℓ_1. In normalized form, using the wake generator thickness, a, this function was determined to be

$$\frac{D_{EFF}}{a} = 30.12\ \ell_1 - 21.56 \qquad 50$$

and is shown in Figure 78.

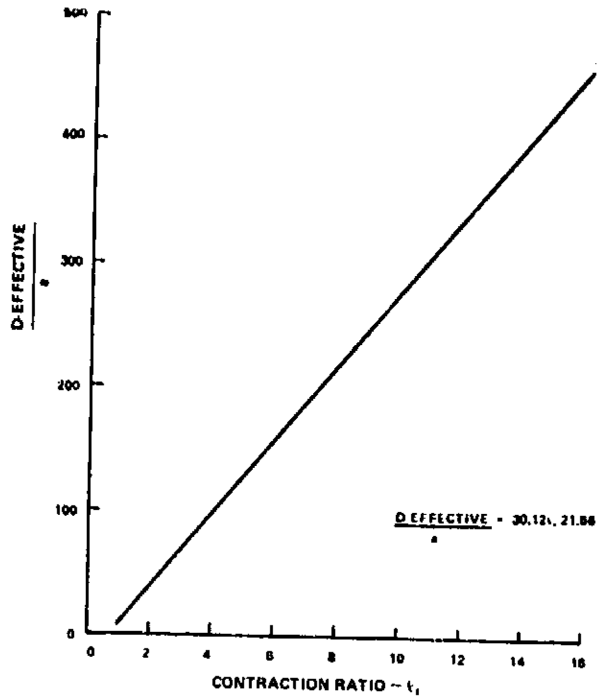

Figure 78 Normalized D-Effective as a Function of Contraction Ratio

The corresponding value of the virtual source distance $X(r_o)$, when normalized is

$$\frac{X(r_o)}{a} = .49 \qquad 51$$

b) A multiplicative constant was applied to the wake width ratio expression and evaluated using the measured data interpolated at $\ell_1 = 1$. This constant was determined to be .318.

The adjusted transfer functions thus become:

Velocity Deficit Ratio

$$\frac{\Delta U(r)}{\Delta U(r_o)} = \ell_1^{-1/4} \left\{ \ell_1^{3/2} + \frac{2a\left(30.12\ \ell_1 - 21.56\right)\ell_1}{X(r_o)\left(1 + \ell_1^{1/2}\right)} \right\} \qquad 52$$

Wake Width Ratio

$$\frac{b(r)}{b(r_o)} = .318\ \ell_1^{-5/4} \left\{ \ell_1^{3/2} + \frac{2a\left(30.12\ \ell_1 - 21.56\right)\ell_1}{X(r_o)\left(1 + \ell_1^{1/2}\right)} \right\} \qquad 53$$

The plots of these models are shown in Figure 79 together with the measured values.

From the measurements obtained using the symmetric airfoil, shown in Figure 80, it is apparent that the wake generated by this type of body recovers very rapidly. In fact at the 25.4 cm and -20.3 cm measuring stations at which data at contraction ratios ranging from 1 to 14 approximately were gathered, no wake was detected. In the plots of Figure 80 the predicted values of the velocity deficit and wake width ratios using Equations 52 and 53 are shown. Expression 51 above was used to determine the virtual source distance. A low value of the velocity deficit ratio is predicted using this model.

While the adjusted expressions fit the measured data well there is no guarantee that these expressions are universally applicable. However, these measurements have indicated that a viscous wake in a contracting flow is subject to an accelerated recovery in excess of that expected by a linear combination of viscous and contraction effects. With this in mind and considering the model predictions of the velocity deficit ratio at high contraction ratio, Figures 79 and 80, it seems that the velocity deficit as predicted by pure contraction $\frac{\Delta U(r)}{\Delta U(r_o)} = \ell_1^{-1}$ provides a valid upper bound. Similarly the prediction of the wake width $\frac{b(r)}{b(r_o)} = \ell_1^{1/2}$ provides a minimum estimate of that quantity.

The effect of contraction on a vortex will now be considered.

A vortex is comprised of two regions, an outer region where viscous forces are negligible and an inner core region where they are not. When a vortex is convected through an axisymmetric contraction, consideration of the conservation of circulation leads to the conclusion that the outer velocity field is unchanged, see Appendix B. In the vicinity of the core the theoretical model discussed in the Interim Phase II report (29) predicts that the maximum transverse velocity increases according to

$$\frac{U_{2B}}{U_{2A}} = \ell_1^{1/2} \qquad 54$$

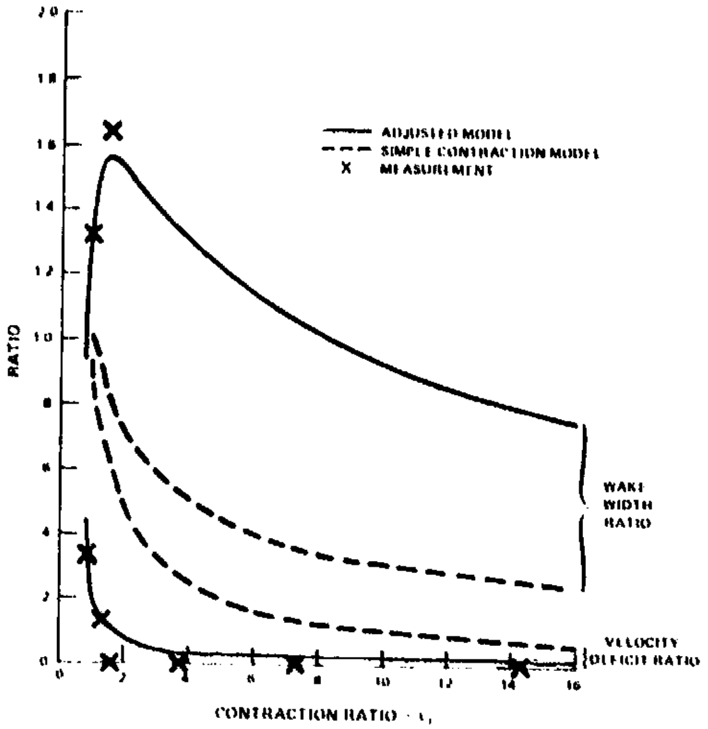

Figure 79 Comparison of Adjusted Model Predictions With Measurement (3.81 cm Square Rod)

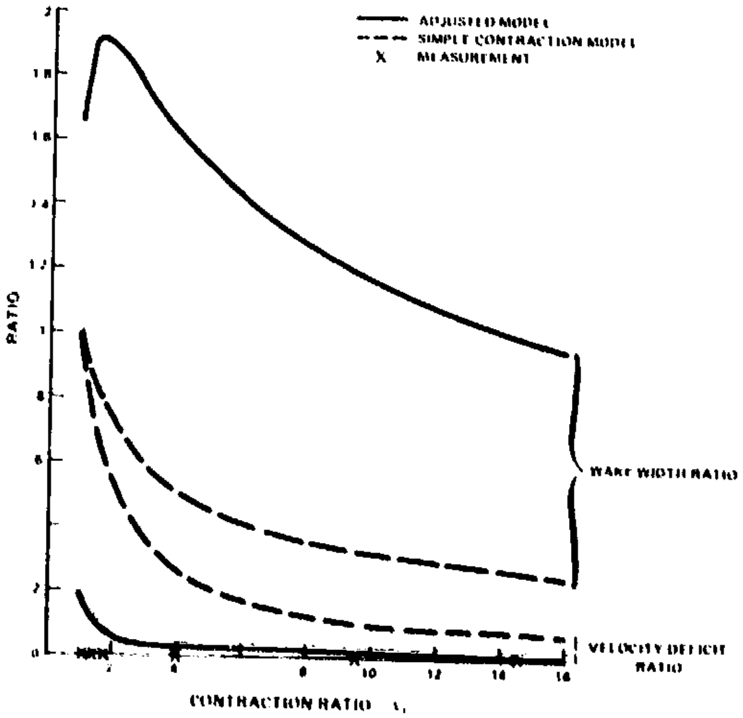

Figure 80 Comparison of Adjusted Model Predictions With Measurement (Symmetric Airfoil)

and the core radius reduces according to

$$\frac{r_B}{r_A} \doteq \ell_1^{-1/2} \qquad 55$$

The transverse velocities measured at the three axial locations 48.26 cm., 30.48 cm., and 20.32 cm. (referred to the bellmouth) through the contraction, support the invariance of the transverse velocity field in the outer region (Figure 13). The maximum velocity (at the core boundary) changes slightly.

In the light of these data it is concluded that the viscous inertial force equilibrium at the core boundary of the vortex is not significantly changed by convection through an axi-symmetric flow contraction up to a contraction ratio of about 15, for the contraction lengths examined here. In fact the core radius of the vortex remains relatively unchanged (Figure 81) as do the circulation and therefore the vortex transverse velocity field. Accordingly the analytically-derived functions are modified

Transverse Velocity Ratio	At any radius	$\frac{U_{2B}}{U_{2A}} = 1$	56
Core Radius Ratio		$\frac{r_B}{r_A} = 1$	57

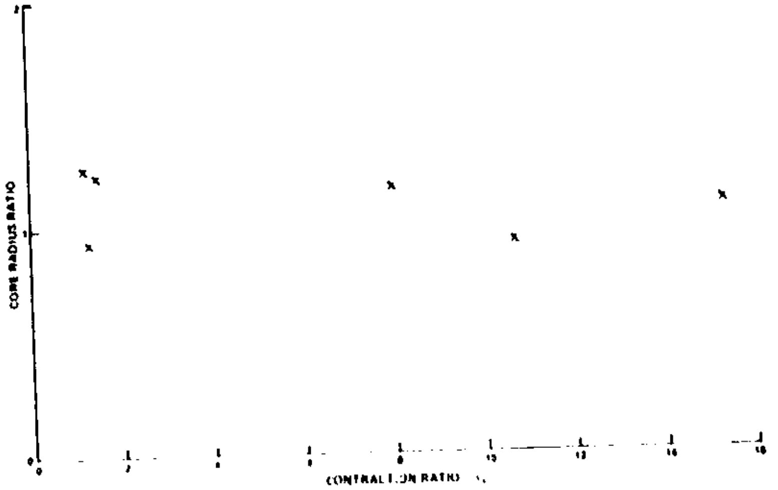

Figure 81 The Variation of Vortex Core Radius With Contraction Ratio

It was observed in Section 5, that there is an axial velocity distortion associated with the vortex. This distortion is roughly a deficit. There is evidence (Figure 15) that this axial velocity deficit is cusp shaped at the beginning of the contraction. Subsequently as it is convected into the contraction the deficit increases and becomes fuller and broader (Figure 15). This deficit does not then behave as a two dimensional wake. Figure 82 presents the variation of axial velocity deficit ratio with contraction ratio. It should be noted that at the initial part of the contraction it is difficult to determine the minimum of the axial velocity due to the cusp nature of the deficit. At the higher contraction condition measurement of the full recovered axial velocity component were impeded by the presence of the duct. All deficit estimates in this Figure (82) are therefore probably low. Also plotted in this figure is the theoretical axial velocity deficit ratio for an inviscid wake for reference. As can be seen initially (at low contraction ratios) the measured velocity deficit decreases (data follows approximately this curve), but as the contraction induced inertial forces increase, the deficit on an absolute basis tends to increase. The broadening of the deficit in this phase is probably due to viscous diffusion. Thus viscosity disperses the axial velocity distortion more rapidly than the transverse (vortical) velocity distortion.

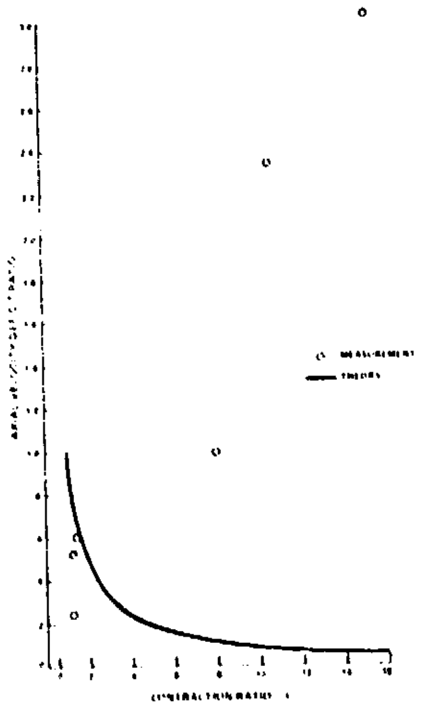

Figure 82 Variation of Axial Velocity Deficity Ratio in a Vortex With Contraction Ratio

From a noise generation standpoint the transverse velocity field of a vortex is invariant under the axisymmetric contraction of moderate length, while the axial velocity distortion associated with the vortex is amplified on an absolute basis by the contraction. This indicates that if a vortex exists in the contracting inflow to a fan on a static test stand, it should be suppressed (e.g. by use of an ICS) as far away from the fan face as possible.

In summary the steady distortion contraction models to be used in the ICS Design System are

1) Axial Velocity Distortion

Velocity Deficit Ratio

$$\frac{\Delta U_{1B}}{\Delta U_{1A}} = \ell_1^{-1} \tag{58}$$

Wake Width Ratio

$$\frac{b_B}{b_A} = \ell_1^{-1/2} \tag{59}$$

2) Vortex Velocity Distortion

Azimuthal Velocity Ratio

$$\frac{U_{2B}}{U_{2A}} = 1 \tag{60}$$

Core Radius Ratio

$$\frac{r_B}{r_A} = 1 \tag{61}$$

6.2.2 Screening

As in the previous discussion on contraction defects, the modification of an axial velocity distortion will first be examined. Five screens were used and as found in Section 5 the pressure drop coefficient, K, varied from .41 for the thin honeycomb to 5.9 for the 41% open area perforated plate (See Figure 33). The generators of the axial velocity deficits were the 3.81 cm square rod and the 5.08 cm X 7.62 cm rod. For each rod and screen combination, three duct conditions were set at 53.34, 76.2 and 121.92 m/s. The parameters that were used to characterize the wakes generated were again the velocity deficit and the wake width. As noted in Section 5 the flow across the screens is not uniform; in general, there exists either a diffusion or contraction of the flow due to the fact that it is unrestrained. To account for this effect the velocity deficit and wake width ratios are plotted as a function of contraction ratio and the value of the ratio taken at a contraction ratio of unity. An example of this process is shown in Figure 83 for the .95cm thick honeycomb. The characteristic ratios of wakes for the various screens are shown in Figures 84 and 85 with the screens listed along the abscissa in increasing K. In general, the higher the screen resistance, the higher the wake deficit suppression as predicted by the transfer functions shown in (29). In addition, the wake inversion predicted for high resistance screens was observed in the 41% open area perforated plate configuration. The wake width was reasonably constant, and equal to unity as predicted by the model, although large variations in this quantity were observed in the 41% open area perforated plate configuration. The accurate determination of the downstream wake width was particularly difficult in this case.

The model presented in the interim report (29) due to Taylor and Batchelor (38) is

Axial
Velocity
Deficit
Ratio

$$\frac{\Delta U_{1B}}{\Delta U_{1A}} = \frac{1 + \alpha - \alpha K}{1 + \alpha + K} \qquad 62$$

Wake
Width
Ratio

$$\frac{b_B}{b_A} = 1 \qquad 63$$

and was used to produce the predicted values of the ratios as shown in Figures 84 and 85. The measured value of the pressure drop coefficient, K, Figure 33 and theoretical values of the flow angle ratio, α, (See Equations 66 and 67 below) were used in these expressions. The flow angle ratio is the ratio between the outflow angle from a screen to the inflow angle, both being referenced to the normal to the plane of the screen.

Examining first the comparison of measured and predicted velocity deficit ratios, it is apparent that the trend is well reproduced by the model. In particular the contention that Taylor and Batchelor's gauze theory is applicable to honeycomb and perforated plate made in (29) receives support from these data. In terms of the absolute level of the velocity deficit ratio, the predictions are in reasonable agreement with the data.

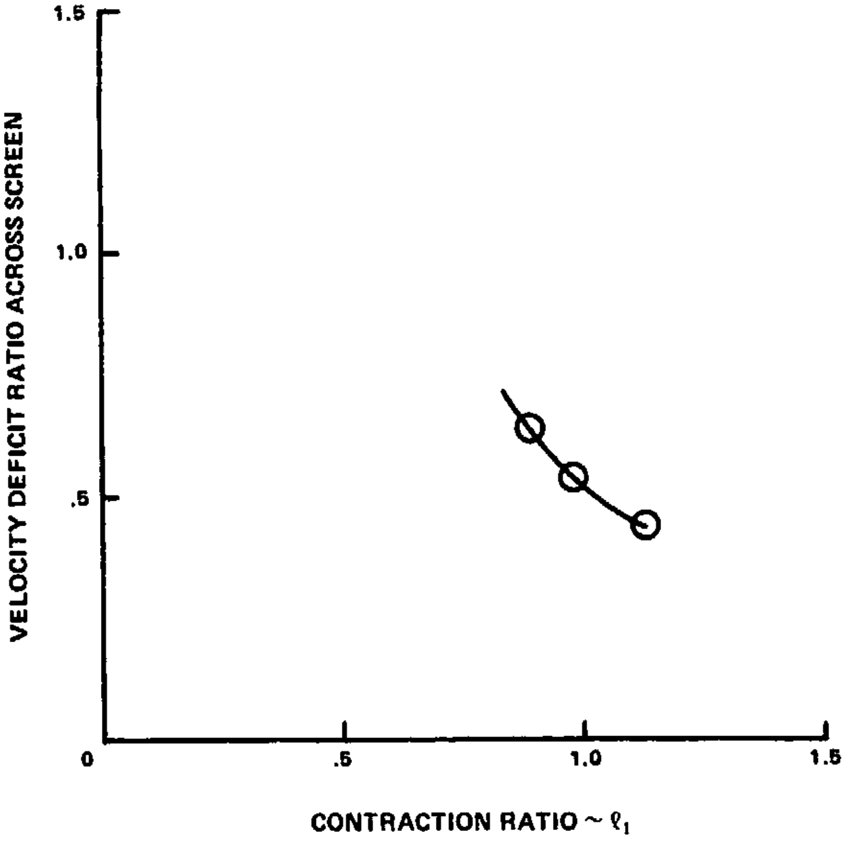

Figure 83 Variation of Velocity Deficit Ratio Across 0.95 cm Honeycomb With Contraction Ratio

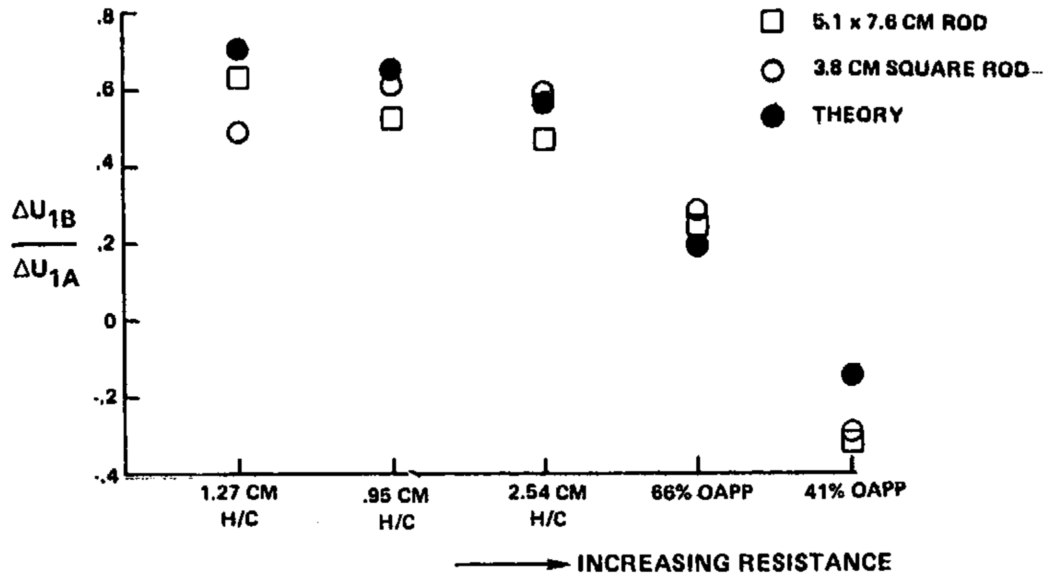

Figure 84 Velocity Deficit Ratio Across Screens

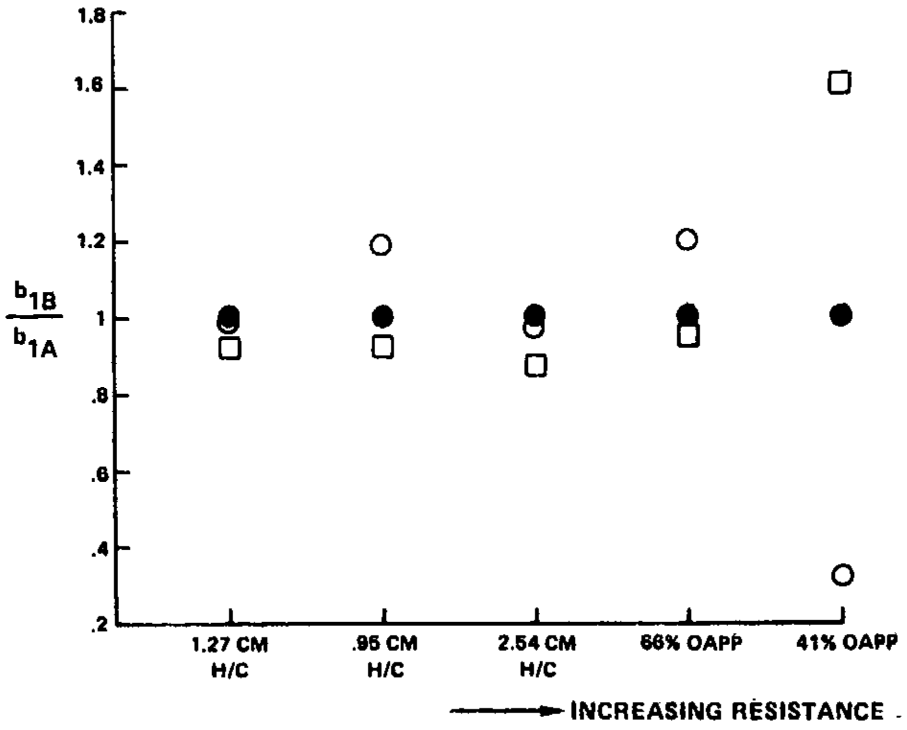

Figure 85 Wake Width Ratio Across Screens

In light of these comparisons the transfer functions to be used in the ICS design system are those given in Equations 62 and 63 above.

As observed in the contraction section, axial velocity wakes encountered on the test stand will invariably be effectively suppressed by the contraction and viscous diffusion, consequently screening solely for the purpose of axial velocity wake suppression is not necessary. It is, however, of paramount importance for the suppression of vortices since these are substantially unaffected by a contraction.

As in the contraction experiments, the vortex examined here was generated by a loaded NACA 0012 airfoil. The effect of the screens on the transverse velocity field of the vortex will be considered first.

As noted in Section 5 and illustrated by Figure 30, this velocity component is totally suppressed by all three honeycombs. It should be noted that the aspect ratios of these honeycombs were 3, 4, and 8. This is in agreement with the theoretical model of the interim report (29) and conclusively demonstrated that low aspect ratio honeycomb is a very powerful suppressant of transverse velocities. The expression for the flow angle ratio for honeycomb

$$\alpha = e^{-\pi \frac{\ell}{d}} \qquad 64$$

is thus substantiated in this aspect ratio range.

The perforated plate does not effectively change this velocity component. Both perforated plates reduce the strength of the vortex as noted in Section 5. Figure 31 which is representative of the data shows a reduction of the transverse velocity component over the vortex. This reduction is most apparent in the peak transverse velocity region near the core. At further distances from the core the reduction becomes increasingly smaller. In addition to this change in the transverse velocity magnitudes the core size increases across the perforated plate, indicating as mentioned in Section 5, that the viscous diffusion process is accelerated by the presence of the perforated plate. This characteristic is not modelled by the theory presented in the interim report.

The transfer function described there was

Transverse
Velocity
Component
Ratio

$$\frac{U_{2B}}{U_{2A}} = \alpha \qquad 65$$

According to this model the suppression of the transverse velocity component is solely due to the turning characteristic of the screen, which in turn is dependent on the pressure drop coefficient of the perforated plate.

$$\alpha = 1.1\ (1 + K)^{-1/2} \qquad 66$$

To account for the diffusion process (vortex broadening) across the perforated plates in order that the transfer function may be assessed, the upstream and downstream azimuthal velocity fields are plotted as a function of transverse dimension normalized by the core radius. An example of this is shown in Figure 86 for the 66% open area perforated plate. Subsequently the data is fitted, by minimizing the squares of the differences, to a potential vortex profile. The profile used was

$$U_2 = \frac{\Gamma}{\tilde{r}} + \beta,\ \tilde{r} = \frac{\tilde{r}}{r_c} \qquad 67$$

From this fit, an estimation of the circulation around the vortices upstream and downstream of the perforated plate is obtained. Now if the velocity field is corrected for any bias—β, then

$$\frac{U_{2B}\ (\tilde{r})}{U_{2A}\ (\tilde{r})} = \frac{\Gamma_B}{\Gamma_A} \qquad 68$$

Hence the ratio of the normalized azimuthal velocity fields across the perforated plate is the same as the circulation ratio. A comparison between measured and predicted values of this velocity ratio is shown in Figure 87. This comparison is shown plotted against the mean velocity ratio across the perforated plates.

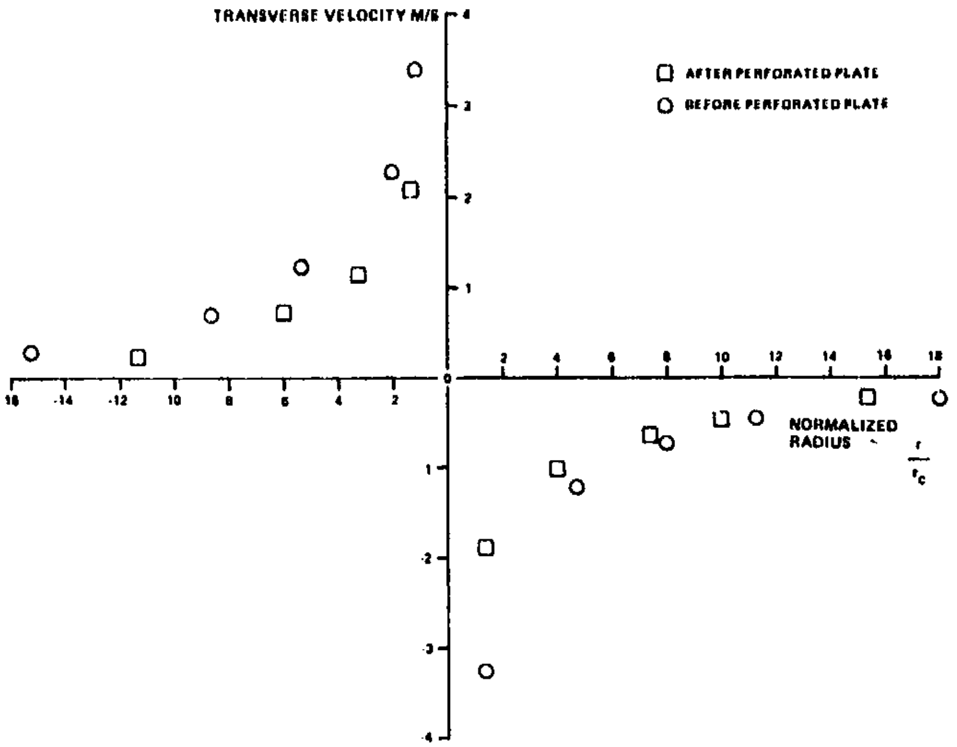

Figure 86 *The Vortex Transverse Velocity Field Each Side of the 66% Open Area Perforated Plate*

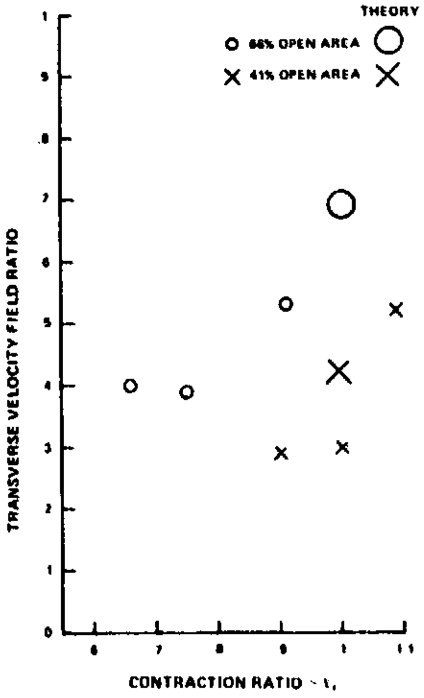

Figure 87 *Comparison of Measured and Predicted Transverse Velocity Field Ratios in a Vortex Across Perforated Plate*

Considering the difficulty in obtaining the true value of the core radius from the data the comparison is encouraging and provides some support for the model. The model is thus sufficiently accurate for use in the ICS design system. It remains to provide some estimation of the core radius change across the perforated plate.

The change in the core radius that is observed is shown graphically in Figure 88. The diffusion of the vortex, not unexpectedly, is higher, the greater the resistance of the perforated plate, and some indication is provided by the curve fit of the degree to which the vortex core would be modified by an arbitrary perforated plate.

The transfer function of Equation 65 does not describe all effects observed when a vortex is convected through perforated plate. It does provide, in conjunction with knowledge of the change in core radius, an estimate of the azimuthal velocity field change.

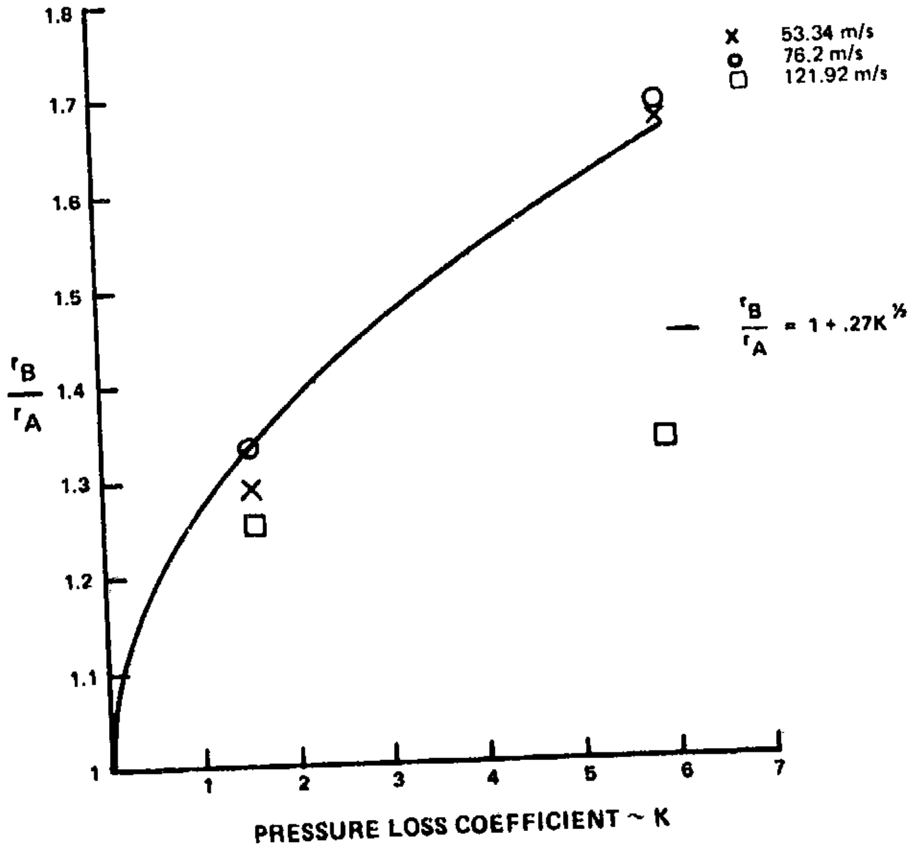

Figure 88 Vortex Core Radius Ratio Across Perforated Plate

Associated with the transverse velocity field of the vortex is an axial velocity distortion. It is cusp-like in shape and, as noted in Section 5, when the vortex is convected through honeycomb, the deficit is increased (see Figure 30). The cusp-like nature of this deficit is most apparent after the honeycomb.

The axial flow in the core of a vortex has been studied by, among others, Newman (39) and Batchelor (40). Various experiments, see Ramsey (41), have produced conflicting descriptions of the direction of this flow. The various results described by Ramsey can be explained qualitatively by considering Batchelor's work (40). A form of Batchelor's expression for the axial velocity field in a vortex is shown in Equation 69.

$$U_{1A}^{2} - U_{\infty}^{2} = \frac{2}{\rho} \left\{ p_{\infty} - p_{A} \right\} - U_{2A}^{2} - \frac{2}{\rho} \Delta H \qquad 69$$

The axial velocity profile in the vortex is a function of the static pressure distribution $p_{\infty} - p_{A}$, the azimuthal component of the dynamic head U_{2A}^{2} and the total pressure loss distribution ΔH due to passage of air over the generating body. Depending on the relative magnitude of these contributions, the axial profile in the vortex may be a deficit (wake), a surplus (jet) or even a combination of the two. In the present experiments the axial velocity profile was a deficit, indicating that the total pressure loss from the flow in the vicinity of the airfoil was the dominant term in Equation 69 since Batchelor has shown that the sum of the first two terms in Equation 69 is positive.

Equation 69 is now used as a starting point to determine the effect of a honeycomb on the vortex. The action of the honeycomb on this vortex is to totally suppress the circumferential velocity field and thus render the radial static pressure gradient unsupportable. The first two terms in Equation 69 are thus removed and the axial velocity deficit is increased accordingly.

The expression for the ratio of the maximum velocity deficits across the honeycomb is developed in Appendix C and is

$$\frac{\Delta U_{1B\ max}}{\Delta U_{1A\ max}} = 1 + \frac{U_{2A\ max}^{2}}{2U_{\infty}\ \Delta U_{1A\ max}} \qquad 70$$

Predictions using this expression are shown in Figure 89 together with the measured values of this ratio. The scatter of the measurements is possibly due to the error involved in estimating velocities at the critical points in the vortex. The shape of the axial velocity profile as predicted by the analysis in Appendix C is changed by the honeycomb (if the pressure loss across the honeycomb is uniform), but it is difficult to ascertain if the measured profiles support this (see for example Figure 30). The axial velocity field is also modified on convection through perforated plate.

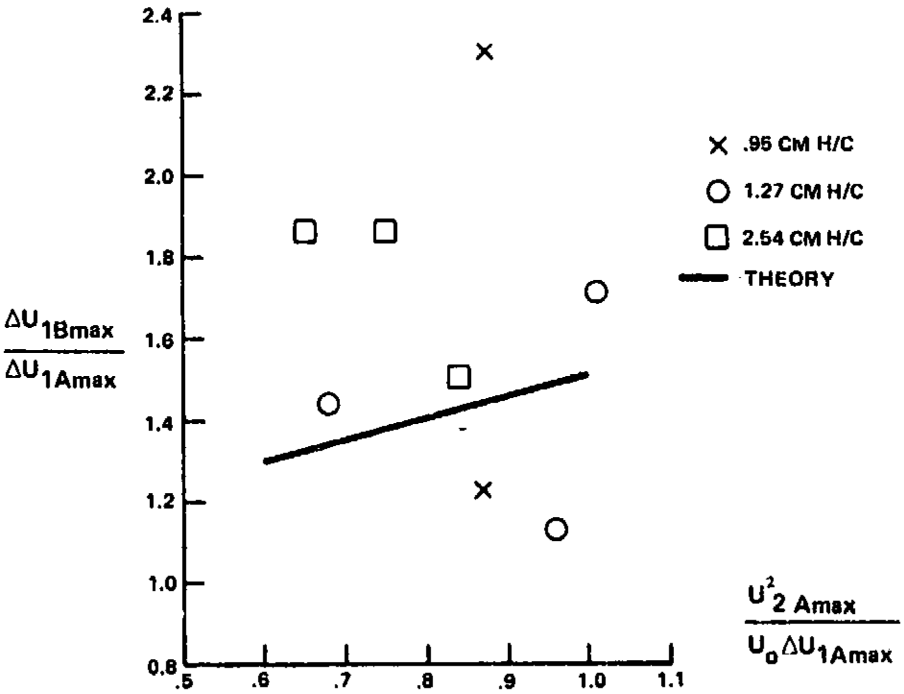

Figure 89 Vortex Axial Velocity Deficit Ratio Across Honeycomb

As recorded previously in Section 5, the 66% open area perforated plate caused an increase in the axial velocity deficit while the higher solidity (41% open area) plate suppressed the deficit. The measured values of the maximum axial velocity deficit ratio across perforated plate are shown in Figure 90. The theoretical predictions shown in this figure are derived using the model developed in Appendix C for perforated plate, namely

$$\frac{\Delta U_{1B\ \max}}{\Delta U_{1A\ \max}} = 1 + \frac{U_{2A\ \max}^{2}\ (1 - \alpha^{2})}{2U_{\infty}\ \Delta U_{1A\ \max}} \qquad 71$$

The data from the 66% open area perforated plate experiment is reasonably well predicted by this model, however, the ratio from the 41% open area case are of significantly lower value than the prediction. This difference is probably due to the higher resistance of this screen, which may cause the assumptions of the model to be violated.

The perforated plate has a dispersive effect on the vortex as seen from its action on the azimuthal velocity field and the axial velocity field will also feel the effect of this dispersion. The presence of the dispersion effect suggests that the pressure loss across the perforated plate is not (as assumed in the derivations in Appendix C) constant at every point in the vortex. It does apparently vary radially such that (at least for the high solidity perforated plate) variations in the pressure loss dominate the velocity deficit ratio (Equation A.10). This effect seems to suppress the axial flow distortion more than predicted, Figure 90 and thus the theory provides an estimate of the maximum value of the downstream axial distortion.

From the above experimental results, it is clear that the transverse velocity field in a vortex can be readily destroyed by use of honeycomb. Thus, since vortices are likely to exist in the vicinity of any test stand, an ICS should include honeycomb. In addition, because the axial velocity distortion in the vortex can be increased by passage through the honeycomb, it is important to put the honeycomb as far away from the fan inlet as possible. This then permits significant flow contraction downstream of the honeycomb to the fan face and as shown in the previous section 6.2.1., the contraction will eliminate the surviving axial velocity distortion.

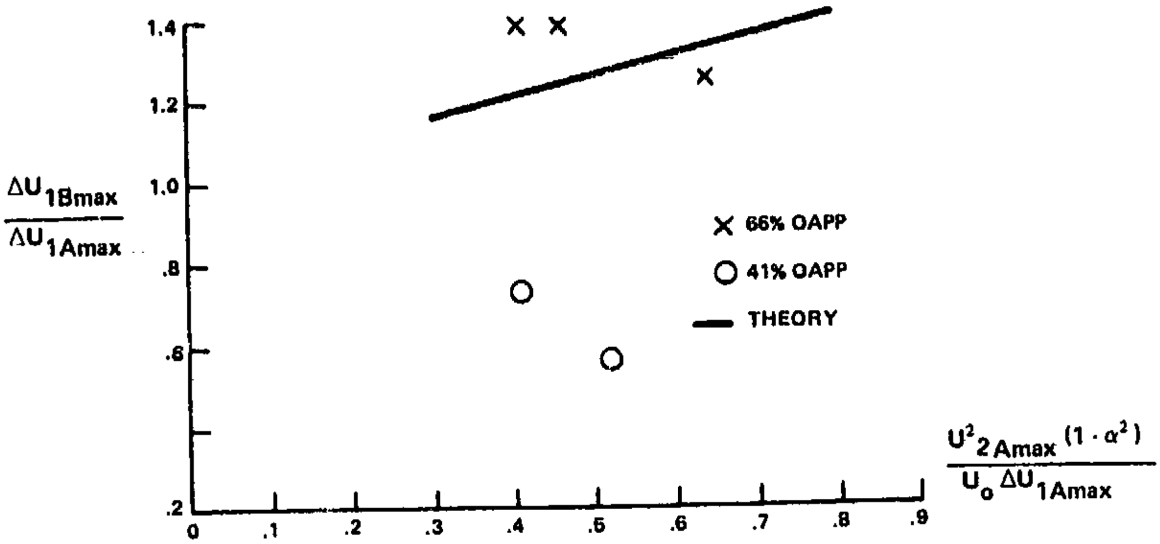

Figure 90 Vortex Axial Velocity Deficit Ratio Across Perforated Plate

In summary, the models for the screens to be used in the ICS design system are:

1) Axial Velocity Distortions

Velocity Deficit Ratio

$$\frac{\Delta U_{1B}}{\Delta U_{1A}} = \frac{1 + \alpha - \alpha K}{1 + \alpha + K} \tag{72}$$

Wake Width Ratio

$$\frac{b_B}{b_A} = 1 \tag{73}$$

2) Vortex Velocity Distortion

Azimuthal Velocity Ratio

$$\frac{U_{2B(\tilde{r})}}{U_{2A(\tilde{r})}} = \alpha \tag{74}$$

Core Radius Ratio

$$\frac{r_B}{r_A} = 1 \qquad \text{Honeycomb} \tag{75}$$

$$\frac{r_B}{r_A} = 1 + .27K^{1/2} \qquad \text{Perforated Plate} \tag{76}$$

Axial Velocity Ratio $$\frac{\Delta U_{1B\ max}}{\Delta U_{1A\ max}} = 1 + \frac{U_{2A\ max}^2}{2U_\infty\ \Delta U_{1A\ max}}$$ Honeycomb 77

$$\frac{\Delta U_{1B\ max}}{\Delta U_{1A\ max}} = 1 + \frac{U_{2A\ max}^2\ (1 - \alpha^2)}{2U_\infty\ \Delta U_{1A\ max}}$$ Perforated Plate 78

6.3 Models for the Acoustic Transmission Loss and Directivity Effects of Screens

In the Interim Phase II Report (29) models were presented that enabled the effect of the ICS on sound propagation to be determined. Specifically, expressions for the transmission loss of screen types (honeycomb and perforated plate) were shown. Also, a model of the effect of a corner made of honeycomb panels was developed and shown to agree closely with measured data. In this section the transmission loss model is assessed using the data gathered during experiments described in Section 5.2. The corner diffraction model was applied to a honeycomb corner in the Interim Phase II Report (29), and is here applied to structural members and the results are applied to measurements of the directivity effect of solid structure, described in Section 5.2. Finally, the impact of these effects on the measurements of farfield sound pressure due to an engine operating with an ICS is discussed.

6.3.1 The Acoustic Transmission Loss of Honeycomb Panels and Perforated Plate

The transmission loss of various screen materials was determined as described in Section 5.2. As noted there the large standard deviation of the measurements coupled with the small transmission loss of the material indicated that there is no significant transmission loss for many of the materials and flow conditions examined.

The model for the transmission loss of a sound wave normally incident to the honeycomb,

$$TL = 10 \log \left\{ 1 + \frac{\sin^4\theta\ \sin^2 k_1\ell}{4 \cos^2\theta} \right\} \qquad 79$$

predicts an effectively zero attenuation at all frequencies. The measured transmission loss mean for the .95 cm thick honeycomb at 12.19 m/s is shown in Figure 91. The standard deviation bounds are also shown and bracket the predicted value of zero. The large standard deviation coupled with the measured mean being close to zero confirm the predictions of the model, i.e., that the transmission loss is small. The results from this configuration are typical of those from the 1.27 cm honeycomb experiment. In Section 5.2.1, it was shown that there is an increase in mean transmission loss with flow speed for the thickest (2.54 cm) honeycomb. This is indicative of a non-zero resistive component in the honeycomb impedance. This characteristic is not accounted for by the honeycomb transmission loss model. Now since it is expected that the acoustic resistance is a function of the pressure drop coefficient, K, of the honeycomb, the range of applicability of the transmission loss model can be defined by K. From the measurements of K (Section 5), the thinnest honeycombs have pressure drop coefficients of .41 and .54. Thus a honeycomb having a pressure drop coefficient less than about .5 operating in a flow of less than 12.19 m/s will attenuate a sound field according to the model, Equation 79. This model could underpredict transmission losses at higher speeds and pressure drop coefficients. Equation 79 can be manipulated to provide a guide for honeycomb design that minimizes the transmission loss. If it is desired that the attenuation due to honeycomb be less than 1 dB, it is necessary that

$$\frac{\sin^4\theta \sin^2 k_1 \ell}{\cos^2\theta} < 1.03 \qquad 80$$

For $\sin^2 k_1 \ell = 1$, the worst case, this inequality shows that the incidence angle for the sound field can be as high as about 50^0 without resulting in an attenuation in excess of 1 dB. The implication for the ICS design system is that as far as honeycomb transmission loss is concerned, a spherical design will satisfy the condition of Equation 80 provided that the ICS radius is greater than about twice the fan diameter.

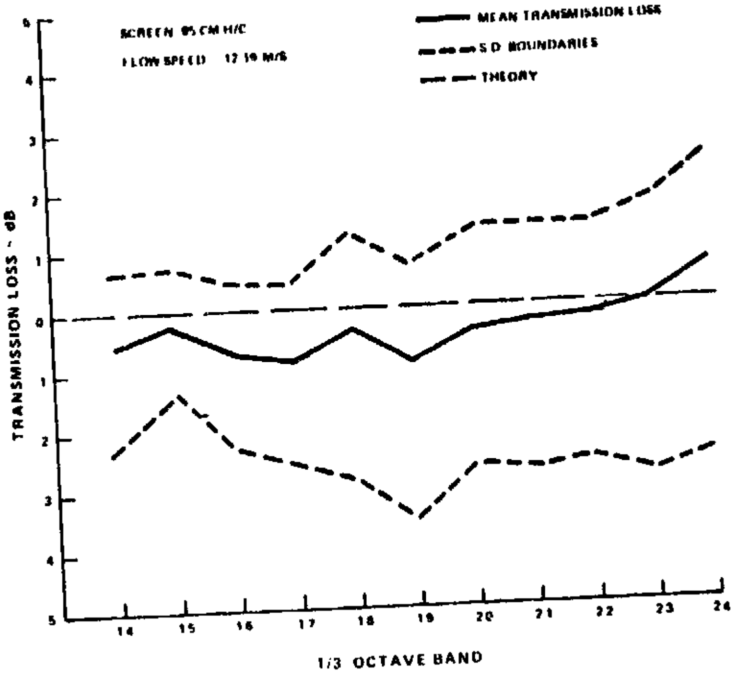

Figure 91 Transmission Loss of 0.95 cm Honeycomb

The model for the transmission loss of a sound wave normally incident to a perforated plate,

$$TL = 10 \log \left\{ \frac{(2 + KM)^2}{4} + \frac{\pi^2 f^2}{c^2 \sigma^2} \left[t + (1 - \sigma) d \right]^2 \right\} \qquad 81$$

predicts small values (< 1 dB) of the transmission loss of the 66% open area perforated plate. A comparison between measurement and prediction for this material is shown in Figure 92 for a flow speed of 9.14 m/s. The model predictions agree well at this flow speed and at 6.1 m/s. However, at the highest flow speed, 12.19 m/s, the average value of the transmission loss is higher than that predicted by the model. As noted in Section 5.2 the data at this speed is questionable. The model predictions for the 41% open area perforated plate at a flow speed of 9.14 m/s are shown in Figure 93. This plot is typical of the other speeds. The trend with frequency that is measured is somewhat different from the predicted trend. This difference is most apparent in the higher one-third octave bands where the model overpredicts the transmission loss. The model can therefore be used to indicate the maximum transmission losses likely to be encountered in these one-third octave bands.

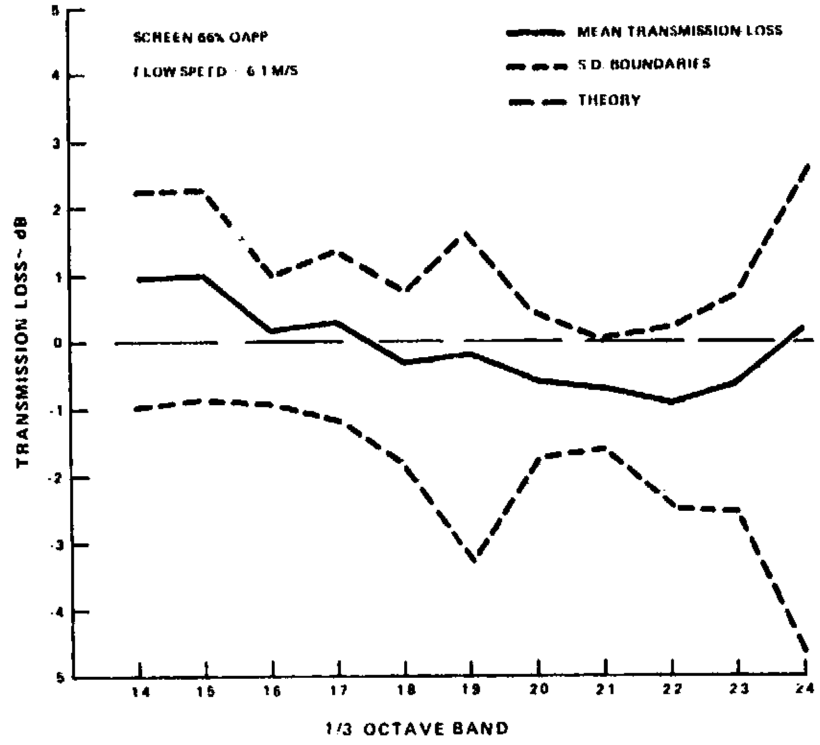

Figure 92 Transmission Loss of 66% Open Area Perforated Plate

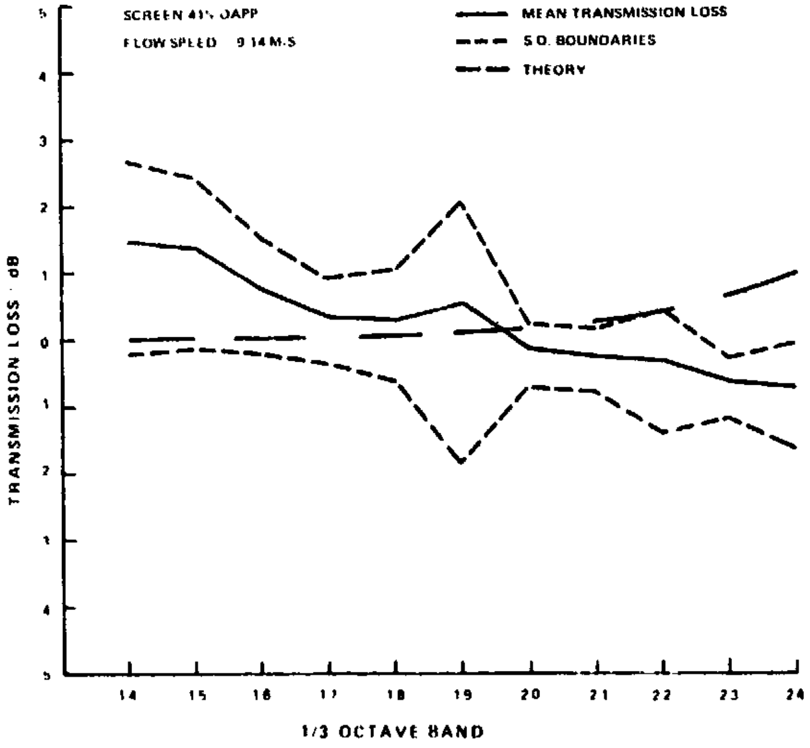

Figure 93 Transmission Loss of 41% Open Area Perforated Plate

The model indicates that it is possible for some perforated plates to significantly attenuate sound at the higher frequencies. This can be prevented by ensuring that the material satisfies the criterion,

$$\frac{(2 + KM)^2}{4} + \frac{\pi^2}{3 a_o^2 \sigma^2} \left[\ell + (1 - \sigma) d \right]^2 \left\{ \frac{f_2^3 - f_1^3}{f_2 - f_1} \right\} < 1.26 \qquad 82$$

which establishes a maximum transmission loss of 1 dB in a frequency band bounded by f_1 and f_2. Any deviation of the incident wave from normal will produce a lower transmission loss in the perforated plate.

The difference in behavior of the two perforated plates in frequency is not explainable in terms of the model. The higher transmission loss of the lower solidity plate is also confusing. However it should be noted that neither the screen of (15), (52% open area) nor the perforated plates of (22) exhibited any observable transmission loss.

While the honeycomb itself is acoustically transparent a corner formed by adjacent panels or structure can affect the directivity pattern in the far field.

6.3.2 Directivity Changes Due to a Honeycomb Corner and Structural Members

Measurements made of the sound field behind a honeycomb corner were shown in the Interim Phase II Report (29). A theoretical model of the phenomenon was also presented there and good agreement was observed between measurement and predictions. The experiment described in Section 5 also included the definition of the directivity changes due to structural members. The structures examined were a square rod and a circular rod. The diffraction model used to predict the honeycomb corner effect on the sound field was adapted to predict the effect of the rods on the field. Comparisons between measured values of the change in sound pressure level due to the presence of the rods are shown together with predictions in Figures 94 through 99. Both pattern shape and absolute level of the directivity change are well predicted. The prediction is at most about 1 dB different from the measured data. It is interesting that the shape of the rod cross-section does not affect the gross characteristics of the far field. The important parameter is the dimension of the obstruction normal to the incident wave number vector. The model then developed in the Interim Phase II Report (29) gives good estimates of directivity changes due to both corners in honeycomb panels and structural members.

There are two important differences between the idealized model and the actual situation at the test stand. Firstly, the source is not a point (as assumed in the model) and secondly the source does not radiate at a single frequency but over a wide band of frequencies. The actual source noise spectrum can, however, be considered to be made up of a combination of discrete tones and broadband noise.

The radiation field of the discrete tone component can be considered to be due to an array of point sources distributed over the engine inlet. Using the model and a distribution of sources along a line, the deviation from the free field radiation pattern due to the presence of a corner was computed. While the line source cannot be considered a simulation of the actual distributed source of the engine, the resulting directivity patterns of the two source types are qualitatively similar. In consequence, the distributed line source (and the two source models examined below) is useful in defining trends. The source amplitudes of the line source were uniform and an arbitrary source phase distribution was considered. The honeycomb corner simulated one found on the P&WA developed ICS. The schematic of this simulation is shown in Figure 100. The resulting directivity modification (i.e., the difference between the directivity patterns with and without the honeycomb corner) is shown in Figures 101 and 102 for frequencies of 1850 Hz and 3700 Hz, respectively. (These frequencies correspond to JT9D blade passing tone and harmonic frequencies at an approach condition.) For the purpose of comparison the directivity modifications due to the same corner with a single point source are also shown in these figures. The comparison indicates that the radiation field of the more realistic distributed source is disturbed more by the corner than that of a point source.

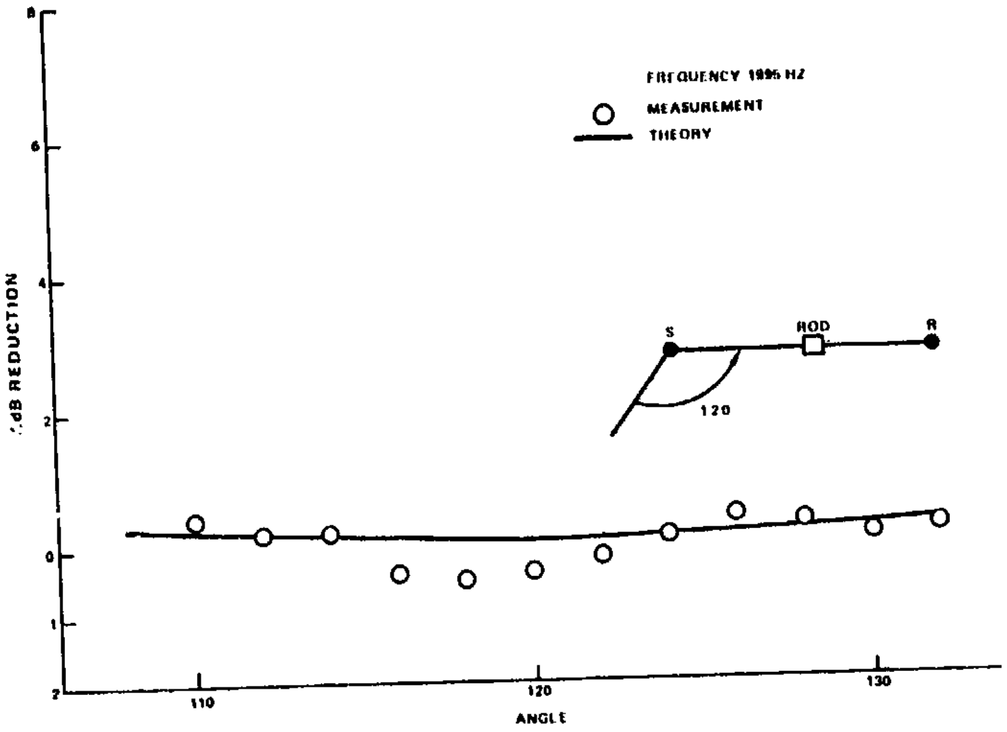

Figure 94 The Directivity Modification Due to a Square Bar

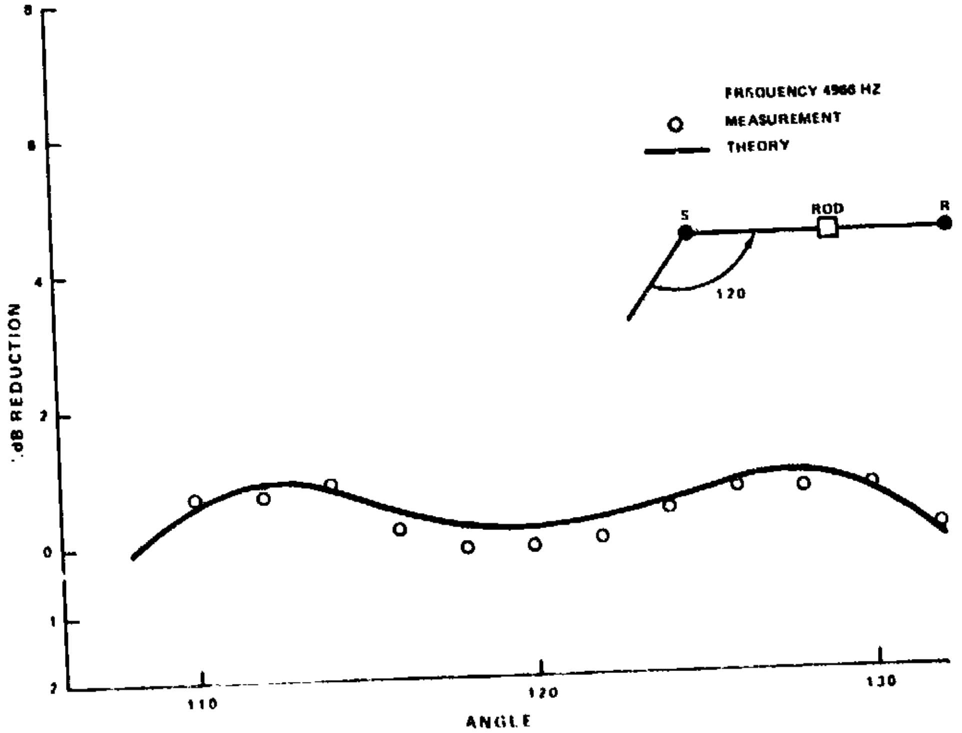

Figure 95 The Directivity Modification Due to a Square Bar

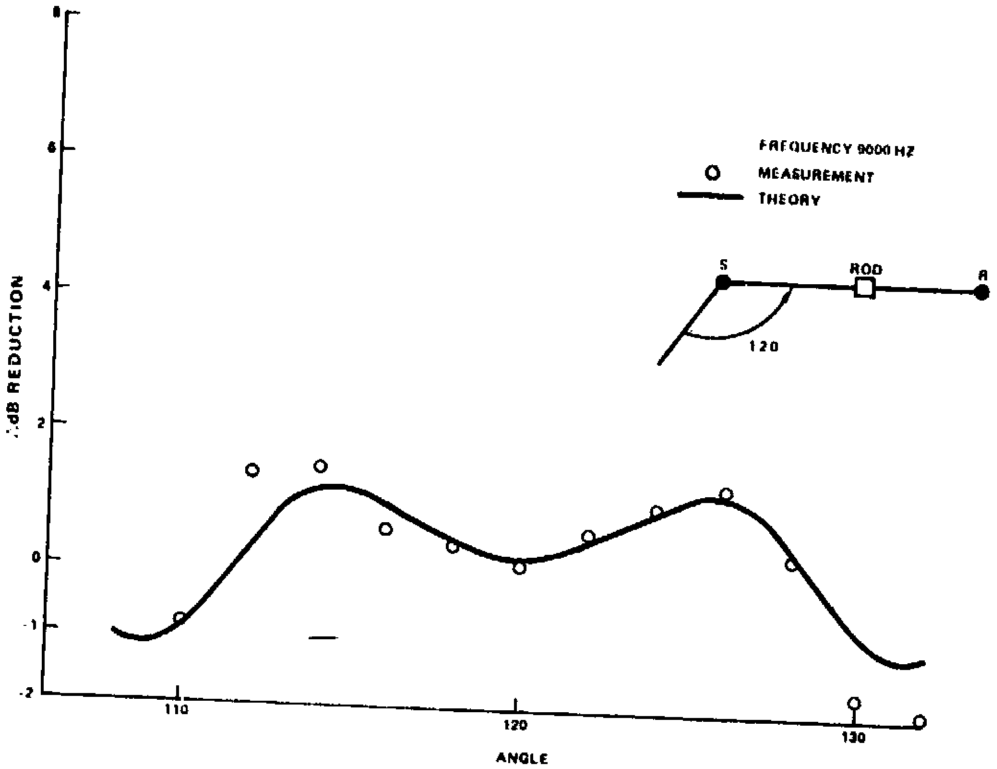

Figure 96 The Directivity Modification Due to a Square Bar

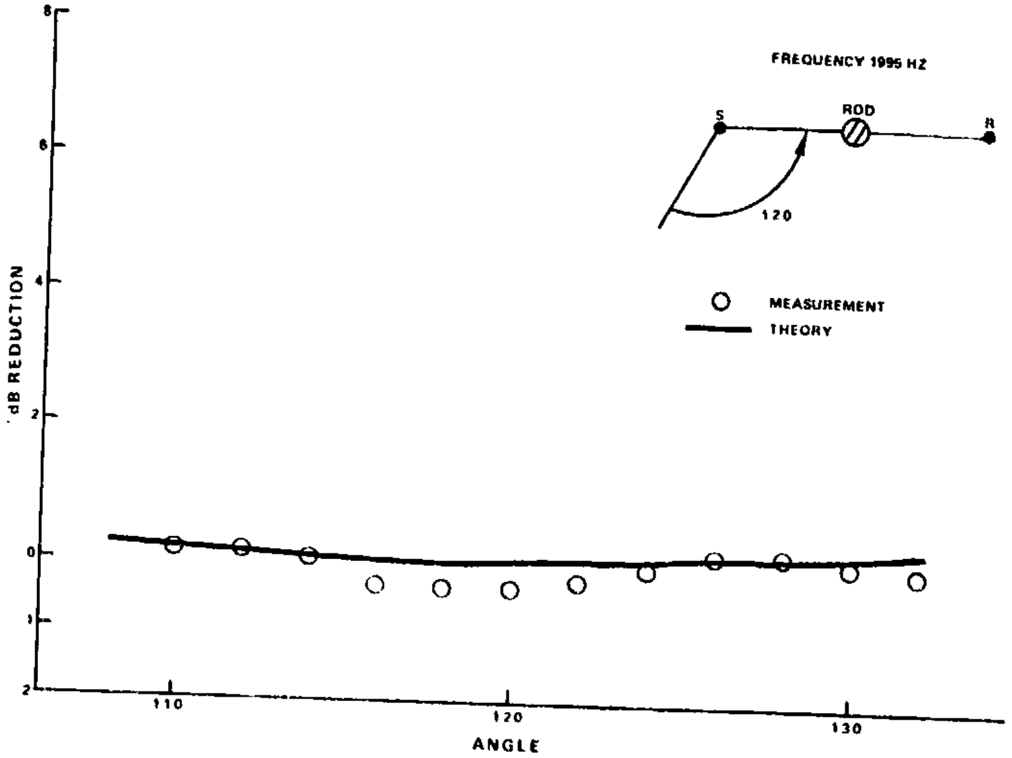

Figure 97 The Direction Modification Due to a Round Bar

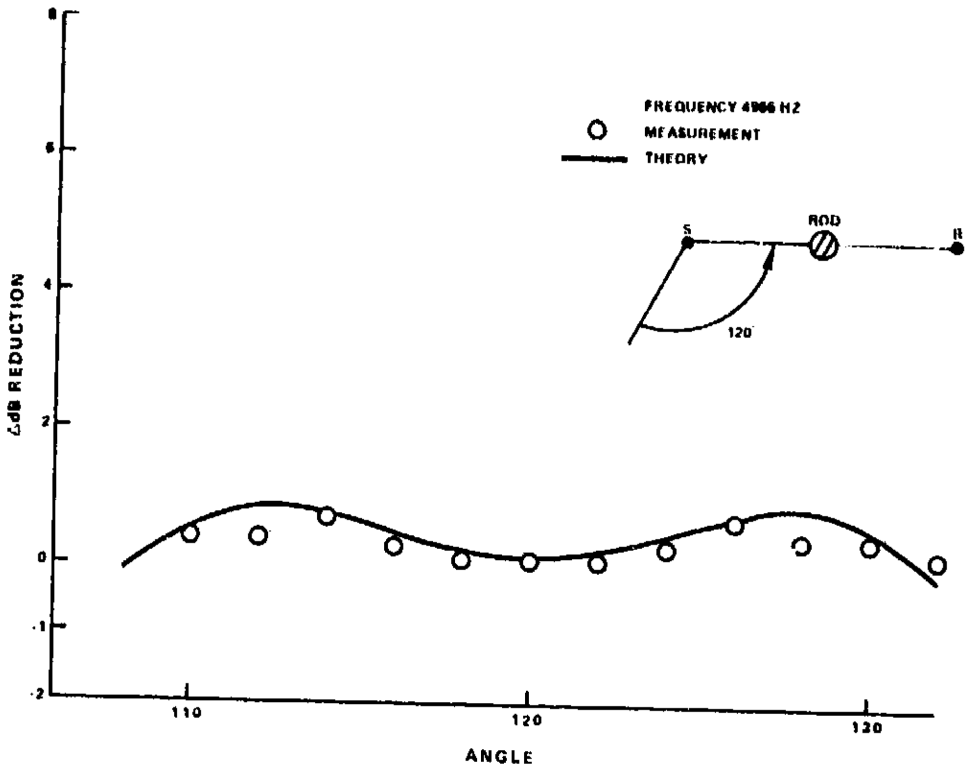

Figure 98 The Directivity Modification Due to a Round Bar

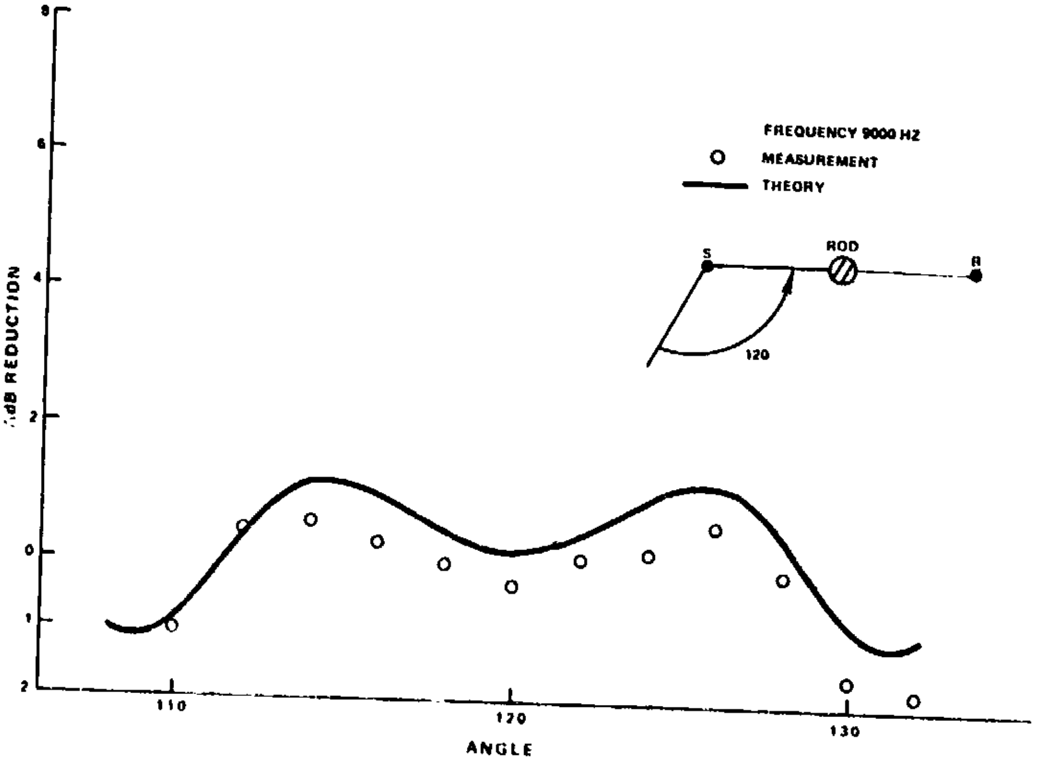

Figure 99 The Directivity Modification Due to a Round Bar

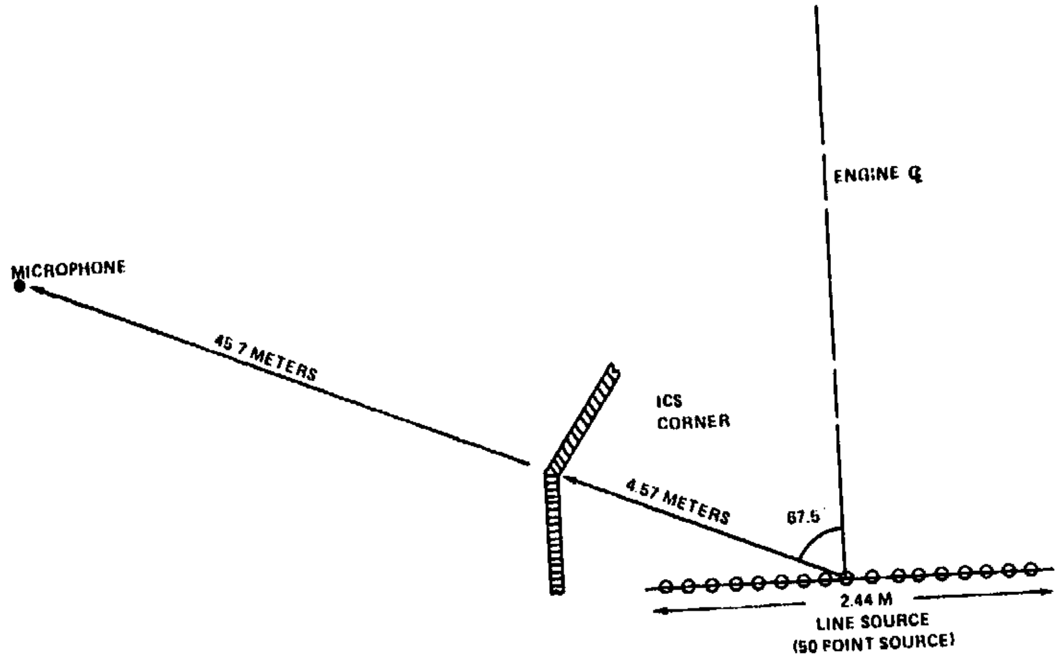

Figure 100 Diagram of Discrete Frequency Distribution Source Simulation

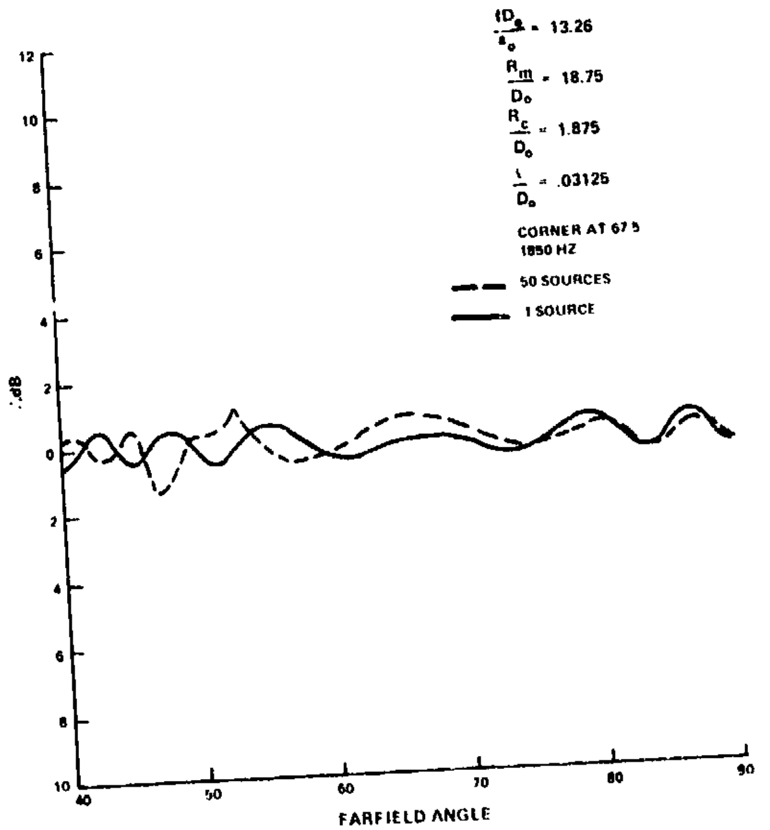

Figure 101 The Directivity Modification of a Honeycomb Corner at 1850 Hz

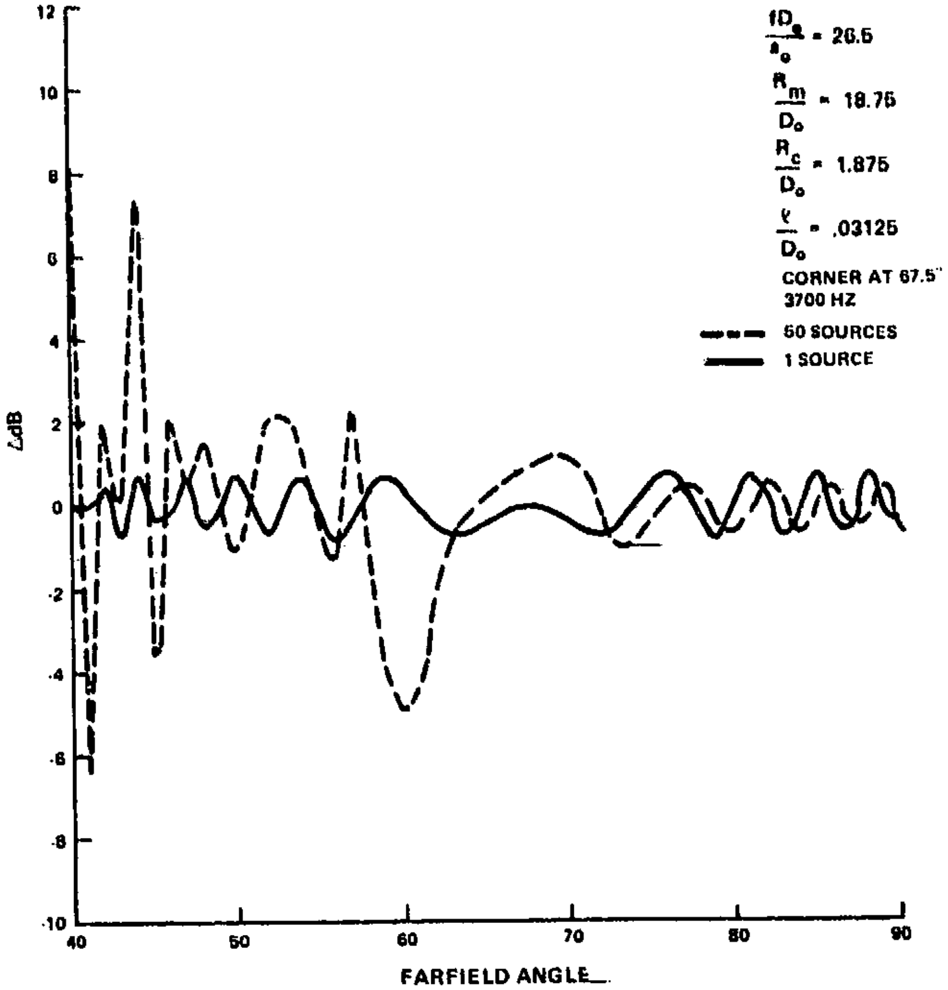

Figure 102 The Directivity Modification of a Honeycomb Corner at 3700 Hz

In contrast, if the source phases are allowed to vary, a different picture emerges. Consider, for illustrative purposes, a distributed source comprised of two sources, Figure 103. If the phase of one of these sources is varied with respect to the other and averages performed over the radiation patterns, an average directivity modification pattern can be computed (This changing of source phase relationships occurs in practice with variation of fan speed, and the averaging process over phase, described above, has a counterpart in averaging over engine speed in the test situation). This computation has been performed for several cases.

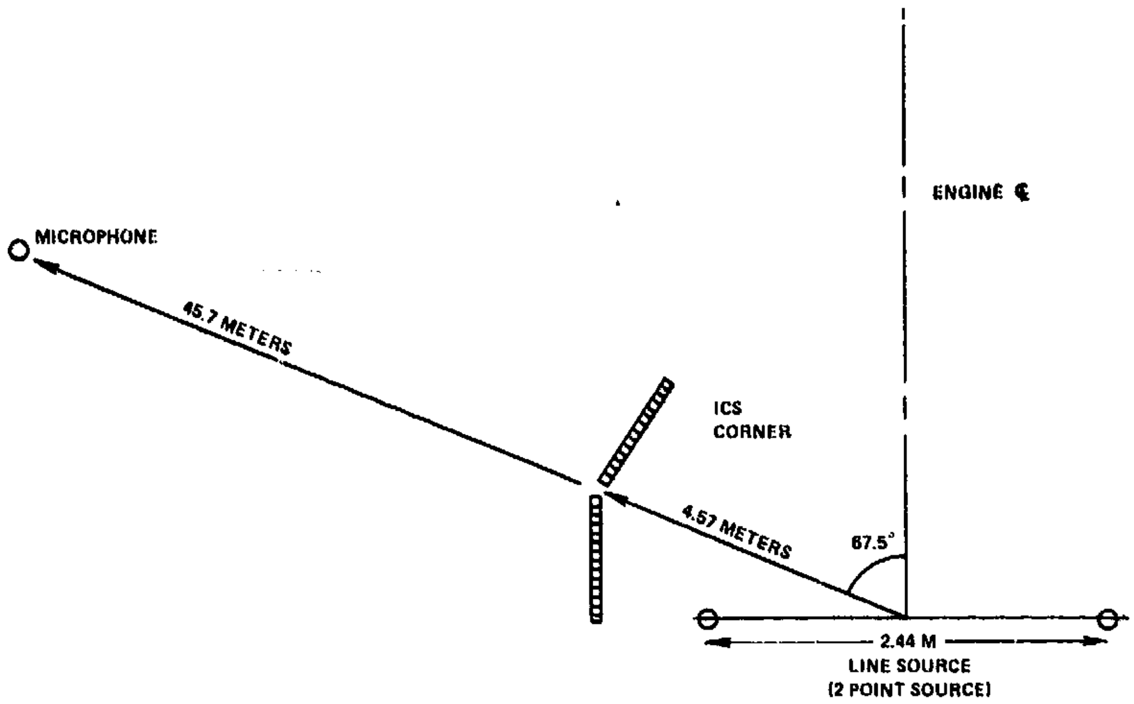

Figure 103 Diagram of Discrete Frequency Distribution Source Simulation

In Figure 104 the average directivity change has been computed for source variations over 1^0, 2^0 and 10^0 at a frequency of 1850 Hz due to a corner at 67.5^0. The averaging process produces a noticeable "washing out" of the corner effects for very small source phase variations. A similar plot is shown in Figure 105 for 3700 Hz and the same observation can be made at this frequency. The power of the "washing out" of corner effects by small source phase changes is apparent from this simple simulation. For the more accurate approximation of many sources distributed over the inlet disc, it is expected that small variations in the phase of the individual sources will suppress any corner effects even further. The impact of this observation on the ICS design system will be assessed in the following subsection 6.3.3.

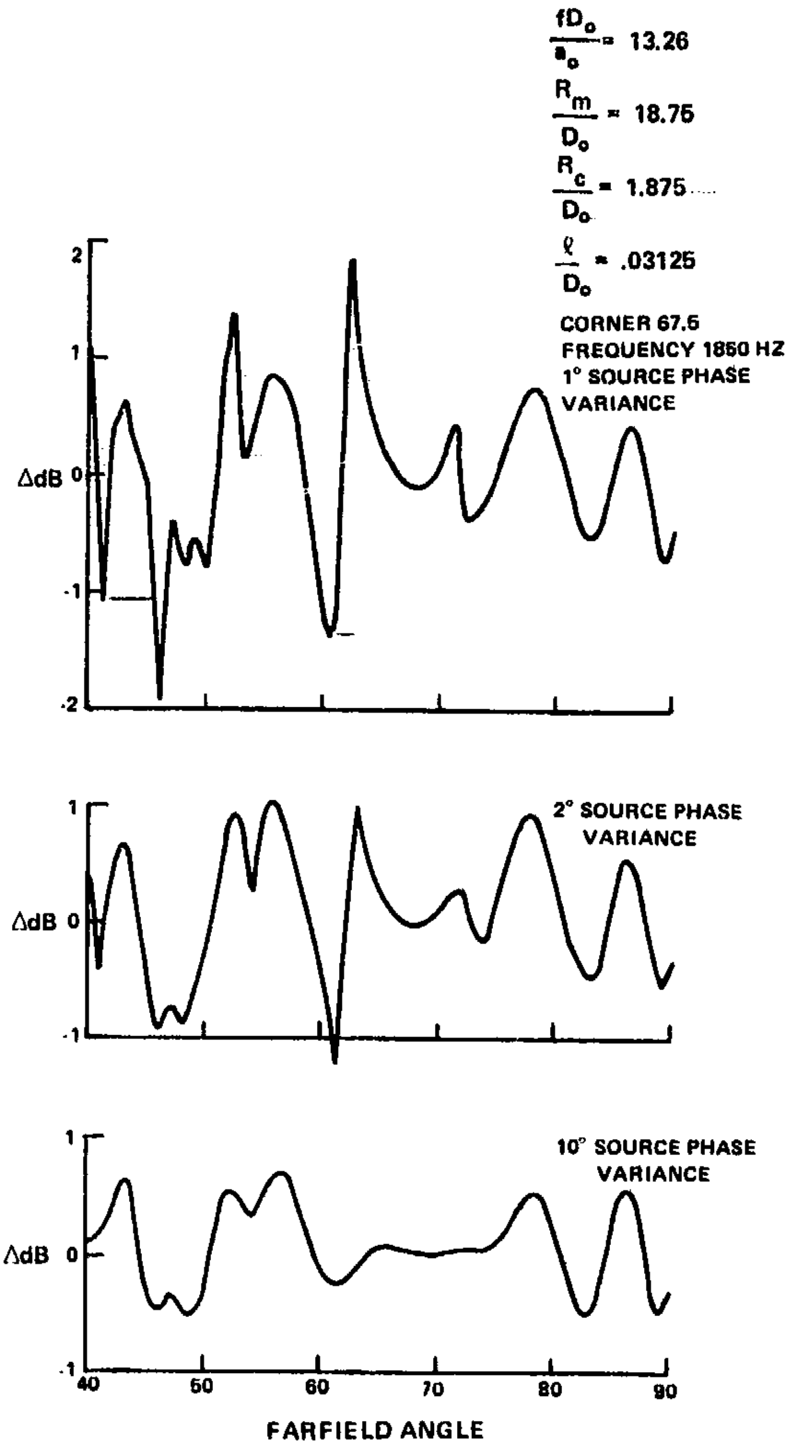

Figure 104 The Effect of Averaging Over Source Phase Differences on Corner Directivity Correction (2 Sources)

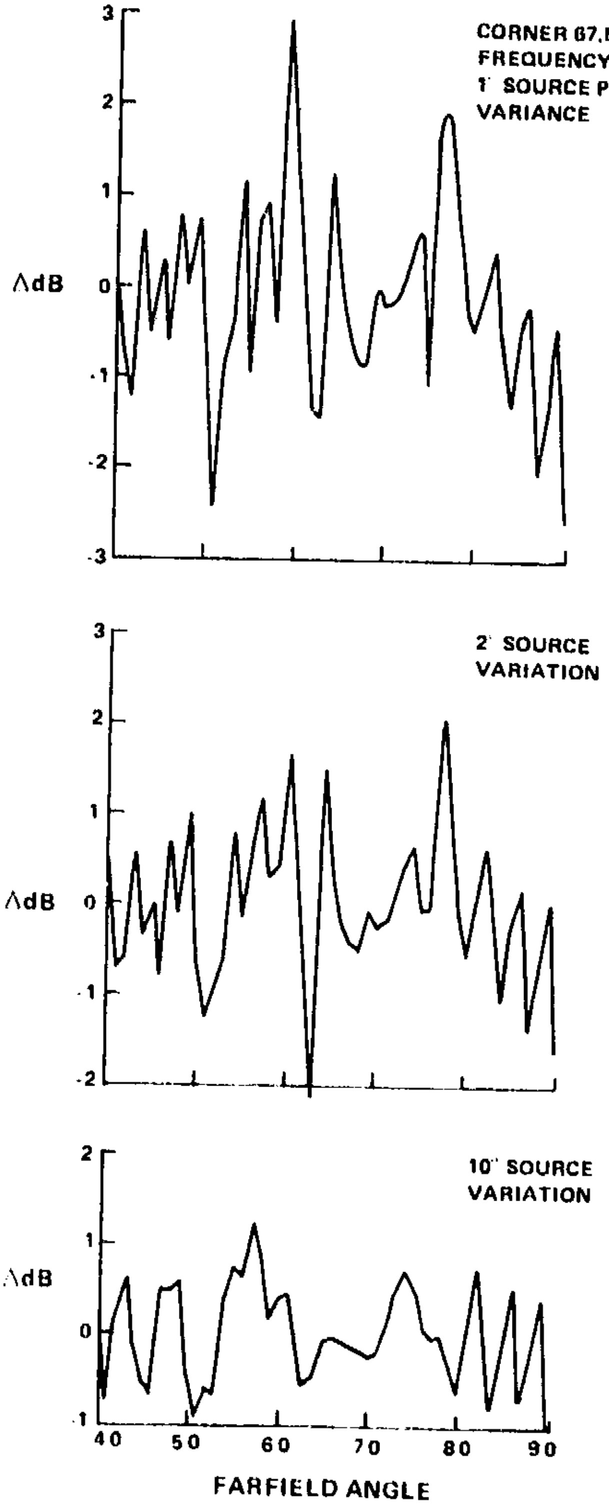

$$\frac{fD_o}{a_o} = 26.5$$

$$\frac{R_m}{D_o} = 18.75$$

$$\frac{R_c}{D_o} = 1.875$$

$$\frac{\ell}{D_o} = .03125$$

Figure 105 The Effect of Averaging Over Source Phase Differences on Corner Directivity Correction (2 Sources)

The acoustic similarity parameters $\frac{fD_o}{a_o}$, $\frac{R_m}{D_o}$, $\frac{R_c}{D_o}$ and $\frac{\ell}{D_o}$ are shown in Figures 101, 102, 104, and 105, evaluated for the JT9D approach condition and a static test configuration. For the JT15D these values of the parameters $\frac{R_m}{D_o}$ (normalized microphone radius), $\frac{R_c}{D_o}$ (normalized ICS corner radius) and $\frac{\ell}{D_o}$ (normalized honeycomb thickness) are typical. In particular the honeycomb thickness is quite realistic. The only variation from the JT9D case then is in $\frac{fD_o}{a_o}$. The values of this parameter for the JT15D at an approach condition and at blade passing frequency and its harmonic are 7.14 and 14.28 respectively. To digress slightly, the directivity modifications to the radiation field, in general, increase in magnitude, the higher the value of $\frac{fD_o}{a_o}$ all other parameters being held constant. Consequently since the JT15D values of $\frac{fD_o}{a_o}$, are less than the corresponding values for the JT9D, all of the previous comments addressed to the JT9D configuration are applicable to the JT15D configuration.

The second component of the fan source spectrum is the broadband component. For a random source, the amplitude and phase of the source at a given frequency are random variables. The consequence of this is that, at any given frequency, the directivity change due to the corner will tend to be washed out by the randomness of the source in a manner similar to that discussed previously for discrete tones. Another factor in determining broadband corrections is that they are defined on a one-third octave band basis. The third octave band correction is conceptually determined by integrating the intensity fields over each frequency range with and without a corner in place and evaluating the ratio of the resulting one-third octave band intensities at each angle. The simple simulation of Figure 103 was used to observe the effect on the directivity change due to summation over frequency. In Figure 106 a comparison is made between the directivity modification of the corner in the presence of source radiating in phase at a single frequency of 4000 Hz and that obtained when the sources are radiating in phase over the 20th one-third octave band (3565 Hz-4488 Hz). (The one-third octave band intensities were obtained by approximating the integral over frequency with a sum.) This comparison shows the great amount of suppression of corner effects that occurs when the modification of a broadband radiation field is examined on a one-third octave band basis.

The broadband directivity modification due to the honeycomb corner is minimal because of source randomness in phase and amplitude and the integration over one-third octave bands.

The consequences of these conclusions for the ICS design system and static testing procedures are discussed in the following section (6.3.3).

6.3.3 The Impact of the Acoustical Transmission Effects of an ICS on ICS Design and Static Testing Procedures

The transmission loss of typical possible ICS component materials (honeycomb and perforated plate) is negligible provided the design criterion presented in Section 6.3.1 are met. These criteria are for panels having low through-flow speeds. Corners between adjacent panels and ICS support structure can potentially modify the far radiation field.

It has been observed that an engine fitted with an ICS operates at a given fan speed with little, if any, variation from that speed. The stability of the engine operation is greatly enhanced by an ICS. Associated with this stability of engine operation is an increase in the stability of the discrete tone source. This is manifested in the far field by a much more peaked discrete tone field. However, even in this more stable operating condition, the tone level at a given angle varies greatly because the increased tone level gradients in the far field make the tone level very susceptable to any small variations in the source and/or the radiation field. The model is used to illustrate this point as shown in Figure 107. Here a part of the free radiation field of two sources radiating in phase is compared with that obtained when a 0.3^{0} phase difference exists between the sources. At some angles the level changes radically (10dB) while the general shape is unchanged. Inlet kulite data gathered during the Joint Noise Reduction Program (JNRP) also exhibit some unsteadiness in tone level with time, with an ICS in place, although the level of unsteadiness is lower than with no ICS in place. It is possible that this unsteadiness encountered when testing an engine with an ICS is sufficient to eliminate any corner effects on the radiation field, however, a more controlled and certain suppression is desirable.

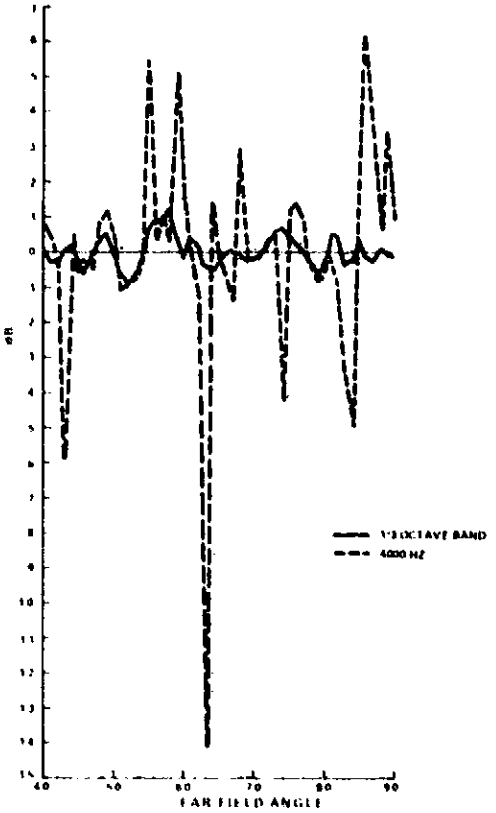

Figure 106 The Effect on Corner Directivity Modification of Averaging Over a 1/3 Octave Band (2 Sources)

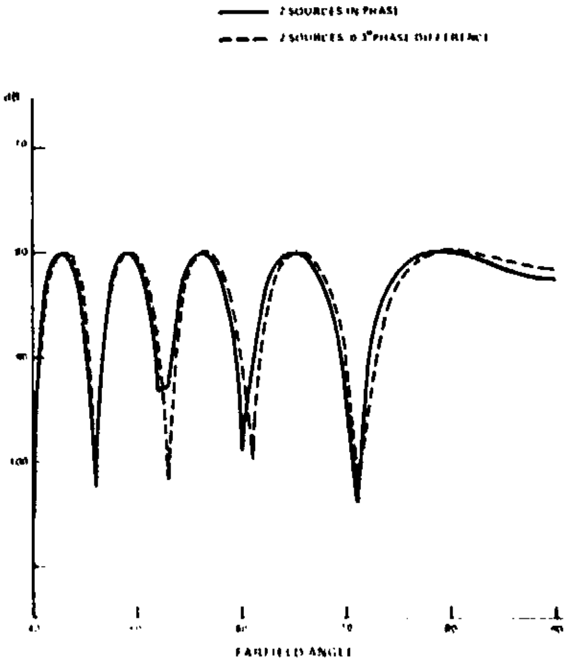

Figure 107 Variation of the Free Field Radiation Pattern of 2 Sources Due to a Small Phase Change

As demonstrated in Section 6.3.2 modifications to the discrete tone radiation field by a corner can be suppressed by averaging over source phase variations. The phase (and amplitude) relationships in the distributed source at the engine inlet may be varied by changing the fan speed. This has been performed for small increments in fan speed over a small speed range, on a JT9D fitted with an almost cornerless ICS (developed by The Boeing Company). Correlation techniques were used to determine the change in fan speed necessary to destroy any similarity between blade passing tone far field directivity patterns. It was found that a fan speed variation of the order of .5% produced uncorrelated far field patterns.

A similar analysis was performed on the patterns produced by the two source simulation examined in Section 6.3.2. A zero correlation between source radiation patterns was reached after a variation of the source phase difference of 2^{o}. As can be seen in Figures 104 and 105 the directivity modification to the radiation field by the corner when averaging over 2^{o} is significantly reduced to approximately a maximum of 1 dB. It is therefore suggested that directivity modifications to the discrete tone radiation field due to the presence of the corners and structural members of an ICS can be eliminated by varying the fan speed continuously during data acquisition by an amount in the order of .5% of the mean fan speed.

Directivity modifications to the broadband radiation field are probably negligible due to 1) source phase and amplitude randomness (even during stable engine operation), and 2) the practice of quantifying broadband noise levels over one-third octave bands. It is considered that either of these causes is sufficient to eliminate broadband directivity modifications due to panel corners and structural members.

It should be noted that the honeycomb corner used in the illustrative simulations of Section 6.2.3 has the characteristics of the P&WA developed ICS. The construction technique of this ICS resulted in discontinuities caused by corner structure and joints in honeycomb panels at these corners. Subsequent

ICS Designs (e.g. those of The Boeing Company and NASA Lewis) minimized the severity of these corners by using improved construction techniques. Consequently, the magnitudes of directivity modification due to a corner presented here, based on the P&WA ICS design, provide an indication of the upper bound of such change. Moreover, in spite of the severity of this ICS corner, no effect on the radiation field that could be attributed to the presence of a corner has been observed in P&WA experimental data. A possible explanation for this is the coarse measurement grid (every 10^0) used to define the radiation field. From the patterns generated using the directivity model, extreme directivity modifications occur over narrow far field angle ranges and the probability that a microphone in a coarse grid will appear at such an angle is not great. Coupled with this, any unsteadiness in the ambient conditions would contribute to the reduction of corner effects.

Therefore, it seems that even if severe discontinuities exist in the ICS construction, any directivity modifications resulting from them can be suppressed.

However, as discussed in the Interim Phase II Report (29), the problem is preferably eliminated at the design stage by minimizing all such discontinuities from the outset. The Boeing developed ICS is an excellent example for full scale engines as is the NASA Lewis produced ICS for the JT15D (23). Acoustically these designs are highly satisfactory.

6.4 The ICS Design System

In the Interim Phase II Report (29) the main elements of an ICS design were identified. They are:

- The criterion for material selection.
- The ICS self generated distortion constraint.
- The ICS acoustic transmission loss and directivity constraints.

The purpose of this section is to generate a design procedure, that incorporates these elements, in terms of parameters readily available to the ICS designer. The models detailed in the previous sections form the basis for the ICS design system.

6.4.1 The ICS Location and the Characteristic Dimension of the Screen Material

From considerations of acoustic transmission loss it is necessary that the ICS be placed such that it is subjected to a low throughflow velocity and to an approximately normal acoustic incidence angle. In addition the pressure loss across the ICS should be low enough so that engine operation is unaffected. This also requires a low throughflow velocity. These observations indicate that the in-duct ICS should be rejected in favor of the externally mounted ICS.

The external flowfield may be divided into three regimes; the first, in which the ambient conditions dominate the velocity field (i.e. Ambient wind speeds are an order of magnitude higher than engine induced flow speeds), the second, in which the engine induced flow dominates the field and the third in which both flow fields are comparable. In the first region, the airflow will vary from normal to grazing incidence with respect to the ICS surface. In consequence, the velocity field inside the ICS will be distorted and in part convected into the inlet. In contrast, an ICS placed in the engine dominated flowfield on an equipotential contour will not create any incidence induced distortion; however, since the incident flow velocity varies over this surface, a total pressure distortion is generated downstream of the ICS. This total pressure distortion manifests itself as a streamwise velocity distortion that is suppressed by the subsequent flow contraction. The equipotential contour placed in the engine dominated flow region thus appears preferable. However, the acoustic test window contains ambient wind speeds of 3 m/s and so the velocities at the ICS in an engine dominated region would be of the order of 30 m/s. This would violate the constraints discussed at the beginning of this section.

Consequently, it is suggested that the ICS be placed in the third region and be designed so that the engine induced velocity is 1.5 times the maximum ambient wind speed in the test window. This ensures that air flows into the ICS at all points and also that the pressure drop across the ICS is small. Correspondingly any total pressure or streamwise velocity distortion downstream of the ICS would be small and readily suppressed by the flow contraction. It is unlikely that the velocity distortion would generate significant turbulence. In view of the low distortions generated at such a surface in this region, the actual shape is probably not of great importance as long as it is roughly hemispherical. This insensitivity to shape is borne out by BMT measurements made with the P&WA, Boeing and NASA Lewis ICS's installed, where there was no evidence of distortions introduced due to the shape of these ICS's. The radius of the ICS can thus be determined from the engine inlet velocity at its lowest operating condition and the maximum ambient wind speed in the test window

$$R_{ICS} = R_o \sqrt{\frac{1}{2} \frac{U_o}{U_{ICS}}} \qquad 83$$

The characteristic dimension of the screen material can now be determined.

The minimum turbulence transverse scale to which the engine is sensitive will have a corresponding value at the ICS surface

$$\left(\lambda_{min} \right)_{ICS} = \ell_1^{1/2} \lambda_{min} \qquad 84$$

where the contraction ratio is that at the lowest engine speed and maximum ambient wind speed. Now in order for the ICS to act effectively, its characteristic dimension should be roughly an order of magnitude less than the minimum value of this scale at the ICS. This will ensure that turbulence scales likely to produce BPF tone noise will be suppressed by the screen.

Thus,

$$d_{ICS} = O\left[\frac{(\lambda_{min})_{ICS}}{10}\right] \qquad 85$$

This dimension refers to the solid material of the screen as well as the hole diameter of both honeycomb and perforated plate or gauze.

A flow chart of these calculation processes is shown in Figure 108.

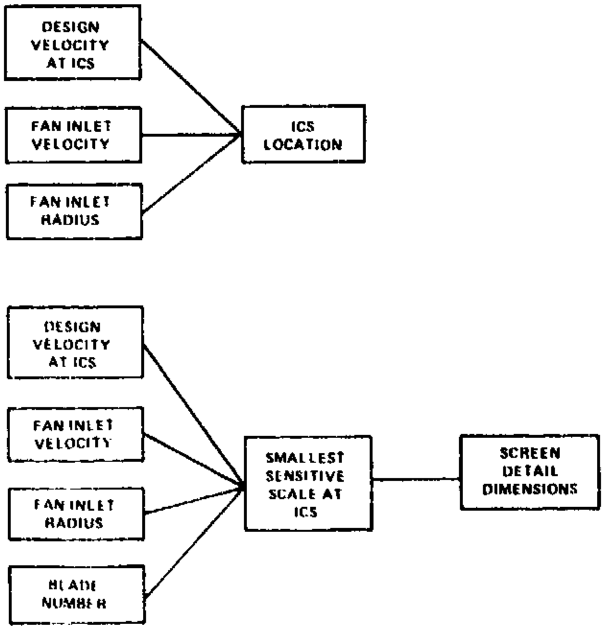

Figure 108 Flow Chart for Determining ICS Location and Detail Dimensions

6.4.2 The Criterion for ICS Material Selection

Two possible criteria for screen material selection were suggested in the Interim Phase II Report (29). One required that the material be chosen such that, in some sense, the inflight fan face flow distortion field was simulated. The other criterion suggested there was that the screen material be chosen such that all fan face inflow distortions generated upstream of, and by the ICS, be totally suppressed. Both of these criteria were confined to those elements of the distortion field outside of the nacelle boundary layer that would generate tone noise on interaction with the fan.

These criteria are, each for its own reason, difficult to attain. The simulation criterion, in addition, if attainable would strictly require a different material for each operating condition while the total suppression of fan face turbulence is probably impossible.

It is therefore suggested that a more attainable criterion be that the ICS material be chosen such that, in some sense, the fan face inflow distortion encountered statically be less than or equal to that expected in flight. The distortion field at the fan face has previously been considered in two parts a turbulent component and a steady (or quasi-steady) distortion. Following this division, the quantity that is best suited as a measure of the turbulence field at the fan face will now be examined in order to formulate the turbulence distortion criterion for ICS design; subsequently the steady (or quasi-steady) distortion component will be examined.

The detailed characteristics of a turbulent field are provided by the spectrum tensor, a quantity most easily explained as the Fourier transform of the correlation tensor. The diagonal elements of this tensor may be interpreted as the distribution of the energy associated with each velocity component in wave number space. If it is assumed that the rotor-turbulence source is primarily due to the fluctuating lift on the fan blades then the element of the spectrum tensor on which the source strength is most dependent is the upwash element,

$$\Gamma_{nn}\ (\underline{k})$$

This may be considered as a surface, infinite in extent. Now Pickett (42) and more recently Ganz (36) have implied that not all of this surface contributes significantly to the level of BPF tones (i.e. only the energy in certain wave number ranges contributes to BPF tones). This tone generating part of the spectrum surface may be defined by the inequalities,

$$k_1 < k_1{}^*$$

$$k_{2L} < k_2 < k_{2U}$$

$$k_{3L} < k_3 < k_{3U}$$

It should be noted that the three dimensional spectrum is discussed here in terms of Cartesian wave numbers, whereas in view of the inlet geometry, the polar versions are more appropriate; however, it is assumed that locally the field may be represented in the Cartesian frame. There are then only a block of wavenumbers at which turbulent energy produces BPF tone noise, Figure 109. (In this figure only two wave number components are represented, however the surfaces is in all three components). The characteristics of this block are dependent on engine size, fan blade number and engine speed. In terms of eddy sizes, this wavenumber block defines eddy geometries that can generate BPF tone noise upon interaction with the fan. A possible design criterion is, then, that the turbulence energy density in this wavenumber range be less statically than in flight. A simpler but approximate form of this criterion is that all three one dimensional PSDs based on the wavenumber range of interest be less statically than in flight in the appropriate wavenumber ranges. This would produce three designs in general. The differences in these ICS designs reflect the difference in shape between the flight and static fan face upwash spectra. If the shapes are similar the three screen designs would be similar and the design system could be based on one PSD alone.

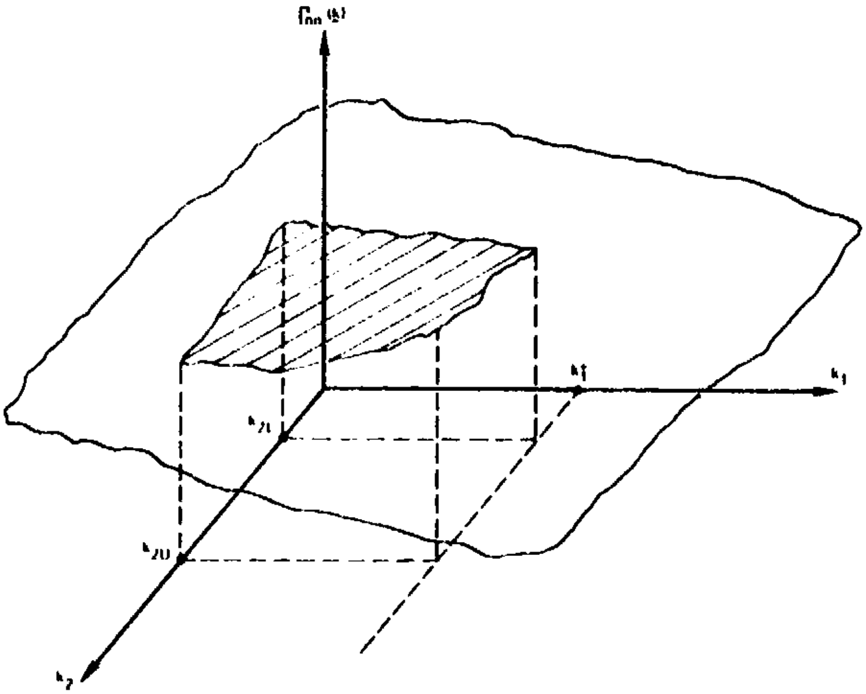

Figure 109 The Segment of $\Gamma_{nn}(\underline{k})$ *That Produces BPF Tone Noise On Interaction With a Rotor*

Assuming this to be the case, the one dimensional PSD $F_n(k_2)$ in the k_2 wave number range of interest will be used in the ICS design criterion. Thus, the criterion for turbulence suppression is

$$\begin{aligned} &F_n(k_2)_S \le F_n(k_2)_F \\ &k_1 < k_1^* \\ &k_{2L} < k_2 < k_{2U} \qquad (86) \\ &k_{3L} < k_3 < k_{3U} \quad . \end{aligned}$$

To determine the target value $F_n(k_2)_F$, the flight fan face upwash PSD, it will be assumed that the contraction in flight is negligible. Consequently, the fan face turbulence field will be assumed locally isotropic in the desired wavenumber range in the manner of the local flight atmospheric turbulence field. That field is best modelled on a one-dimensional PSD basis by the Von Karman spectrum (36). However, to evaluate $F_n(k_2)_F$ at the fan face, the wavenumber ranges of inequality in Equation 86 requires knowledge of the three dimensional spectrum $\Gamma_{nn}(\underline{k})$. For this manipulation the spectrum tensor that

produces the isotropic Dryden spectrum (36) is more suitable. The upwash element of this tensor is

$$\Gamma_{nn}(\underline{k}) = \Gamma_{11} \sin^2 \gamma_o + \Gamma_{22} \cos^2 \gamma_o + \text{CROSS TERM} \qquad (87)$$

or

$$\Gamma_{nn}(\underline{k}) = \frac{N_F}{\left(k^2 + \gamma_F{}^2\right)^3} \quad .$$

$$\left[k_1{}^2 \cos^2 \gamma_o + k_2{}^2 \sin^2 \gamma_o + k_3{}^2 \right] + \text{ODD TERM} \qquad (88)$$

This is derived in Appendix D.

The constants N_F and are chosen such that in the wavenumber range of interest the Dryden spectrum approximates the atmospheric Von Karman spectrum. The determination of N_F and γ_F is shown in (36). The relationship between N, γ and the variance and integral length scale of the turbulence are discussed in Appendix D.

From $\Gamma_{nn}(\underline{k})$, the desired one dimensional PSD $F_n(k_2)_F$ can be determined from,

$$F_n(k_2)_F = \int_{k_{3L}}^{k_{3U}} \int_{-k_1^*}^{k_1^*} \Gamma_{nn}(\underline{k})\; dk_1\; dk_3 \qquad 89$$

With the aid of suitable approximations this integration can be performed and is shown in Appendix D. The result is

$$F_n(k_2)_F = 64N_F \left(k_{3U} - k_{3L} \right) k_1^* \bullet$$

$$\bullet \frac{\left[4k_2^{\,2} \sin^2 \gamma_O + k_{3U} + k_{3L}\right]^2}{\left[4\left(k_2^{\,2} + \gamma_F^{\,2}\right) + \left(k_{3U} + k_{3L}\right)^2\right]^3} \qquad 90$$

The integration limits k_{3U}, k_{3L} and k_1^* are related to the range of

turbulence scales over which, upon interaction with the fan, blade passing tones are generated. Thus, if the turbulence scale ranges to which an engine is sensitive and the atmospheric turbulence parameters in flight, N_F and γ_F, are known, the target flight fan face upwash PSD $F_n(k_2)_F$ can be determined.

It is now necessary to formulate the second part of the inequality 86, the fan face upwash PSD $F_n(k_2)_S$ encountered statically with an ICS. To do this it is helpful to have a view of the operations and intermediate states that the atmospheric turbulence goes through, statically, on its way to the fan face. These are shown schematically in Figure 110. As in flight, the atmospheric spectrum tensor is approximated by the isotropic tensor Γ_{ij} in the wavenumber range of interest. This tensor is defined upon the appropriate choice of N_S and γ_S (See Appendix D). Subsequently this turbulence undergoes contraction to the ICS.

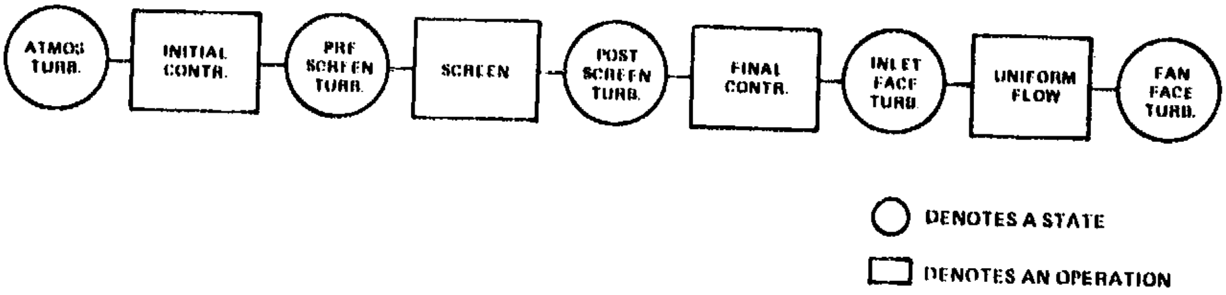

Figure 110 Flow Chart of the Processes to Which Atmospheric Turbulence is Subjected in Static Engine Operation

The nature of contraction from the atmosphere requires some discussion in view of the possibility of an infinite contraction ratio. Firstly, it is necessary to distinguish between turbulence present in the atmosphere independent of engine operation and that which relies upon the engine for its existence. It should be recalled that this section is concerned solely with the former type. On running an engine, then, this turbulence is ingested into the fan and for a given engine condition and ICS configuration the contraction ratio from the atmosphere to the ICS is determined by the local mean atmospheric wind speed. If an engine is run in the FAR-36 test window, this contraction ratio can vary from ∞ to small values (around 3). It is consequently necessary to choose the most appropriate value of the initial contraction ratio for the ICS design system.

For the identification of this contraction ratio consider the approximate one dimensional post-contraction PSDs presented in (36). An approximation is performed there by Ganz for $s \gg 1$, where $s = c_1^{-3}$.

This approximation is satisfied in the static test window. The post contraction PSD $F_2(k_2)$ in terms of the pre-contraction wavenumber is given there as

$$F_2(k_{2A}) = \frac{\pi N}{(k_2^{2})^2 s} \left\{ 1 + \frac{p}{2} + \frac{s\sqrt{p}}{4} \left[\sin^{-1}\left(1 - \frac{2}{s}\right) - \frac{\pi}{2} \right] \right\} \qquad 91$$

where β and ρ are functions of $\frac{k_{2A}}{\gamma}$.
Note that the shape is determined by β and ρ and thus by $\frac{k_{2A}}{\gamma}$ alone.
Now the pre-contraction wavenumber, $k_{2A} = \frac{k_{2B}}{\ell_1^{1/2}}$, where k_{2B} is the post contraction wavenumber and $\gamma = \frac{1}{L_{11A}}$, which from Ganz's model of the ingested atmosphere (36) is a function of the contraction ratio by virtue of the sampling of the atmosphere by the capture streamtube, so that

$$L_{11A} = .355\ R_o\ \ell_{1S}^{1/2} \qquad 92$$

Thus

$$\frac{k_{2A}}{\gamma} = k_{2B}\ .355\ R_o \qquad 93$$

i.e., $\frac{k_{2A}}{\gamma}$ is independent of contraction ratio. Correspondingly the shapes of the post contraction PSDs in the transverse wavenumbers are independent of contraction ratio. In addition, a small contraction is sufficient to transfer most of the energy in the streamwise wavenumber PSDs into the range where the blade passing tone level is independent of axial length scale. In short the tone generation capacity of the incoming turbulence is, above a low contraction ratio, independent of the distortion of the turbulence field and is greater or lesser solely according to the post-contraction upwash energy. The initial contraction ratio must therefore be chosen to account for the highest level of upwash energy encountered at the ICS in the test window.

The mean square value of the upwash velocity component at the ICS is

$$\overline{u_n^2} = \overline{u_1^2}\cos^2\gamma_o + \overline{u_2^2}\sin^2\gamma_o \qquad 94$$

which may be written in terms of the mean square value of the atmospheric turbulence velocity (isotropic initial conditions assumed)

$$\overline{u_n^2} = \left(\alpha_1\cos^2\gamma_o + \alpha_2\sin^2\gamma_o\right)\overline{u_{AS}^2} \qquad 95$$

where μ_1 and μ_2 are the mean square velocity component ratios across the initial contraction. Now using Prandtl's approximations

$$\mu_1 = \ell_1^{-2}, \; \mu_2 = \ell_1 \qquad 96$$

and Ganz's (36) expression for the initial variance of the atmospheric turbulance field sampled by the capture streamtube,

$$\overline{u_{AS}^2} \propto \ell_1^{-5/3} \qquad 97$$

in Equation 94 yields,

$$\overline{u_n^2} \propto \left(\cos^2 \gamma_o + \ell_1^3 \sin^2 \gamma_o \right) \ell_1^{-11/3} \qquad 98$$

Thus, the post-contraction upwash kinetic energy decreases monotonically with contraction ratio. In consequence, the contraction ratio in the test window that produces the most severe turbulence field at the ICS is the lowest value in that window. Knowing this contraction ratio, together with the initial atmospheric turbulence conditions, the model summarized in Section 6.1 can be used to determine the turbulence characteristics at the station upstream of the ICS, provided that the viscous dissipation factor can be quantified.

Since the lowest initial contraction ratio in the test window occurs at the design point, i.e., $\ell_1 = 1.5$, the contraction distance will be small compared to the distance from the origin of the turbulence. Consequently viscous decay effects are negligible.

At the entrance to the ICS then, from Equations 28 and 29

$$\overline{u_2^2} = \overline{u_3^2} = \frac{3}{4} \ell_{11} \overline{u_{AS}^2} \qquad 99$$

and

$$\overline{u_1^2} = \ell_{11}^{-2} \overline{u_{AS}^2}$$

since the initial contraction ratio will probably be less than 6.

Correspondingly, the integral length scales at the ICS from Equations 31, 32, 33, 34 and 35 are

$$L_{21} = L_{31} = \frac{2}{3} \ell_{11} L_{AS}$$

$$L_{23} = L_{32} = \frac{2}{3} \ell_{11}^{-2} L_{AS} \qquad 100$$

$$L_{13} = L_{12} = \frac{1}{2} \ell_{11}^{-2} L_{AS}$$

$$L_{22} = L_{33} = \frac{4}{3} \ell_{11}^{-1/2} L_{AS}$$

$$L_{11} = \ell_{11} L_{AS}$$

These are the turbulent field conditions at the entrance to the ICS.

The ICS material can be described, for distortion suppression, in terms of the parameters, α (the flow angle ratio) and K, (the pressure drop coefficient). These parameters have been discussed and defined in previous sections. If the screen model of Section 6.1 is applied to the upstream flow characteristics, the turbulent flow-field characteristics immediately behind the ICS (neglecting self generated turbulence) may be found. The mean square values of the turbulent velocity components there are

$$\overline{u_2^2} = \overline{u_3^2} = \frac{3}{4} \alpha^2 \ell_{11} \overline{u_{AS}^2} \qquad 101$$

$$\overline{u_1^2} = \left\{ \frac{1 + \alpha - \alpha K}{1 + \alpha + K} \right\}^2 \ell_{11}^{-2} \overline{u_{AS}^2}$$

While, according to the model, the integral length scales are unchanged and remain as in Equation 100 in order of magnitude. The turbulence field is, therefore, not isotropic downstream of the ICS although it is possible that there is equipartition of energy between the velocity components. This field is then contracted to the fan face.

At this point it is necessary to make some comments concerning the inflow control structure material. If the inflow control structure is composed solely of honeycomb, the transverse velocity components will be effectively suppressed while the streamwise turbulent velocity components will convect through the honeycomb largely unaffected. In consequence the turbulent energy distribution will be strongly weighted in favor of the streamwise velocity component, immediately downstream of the inflow control structure. However, due to a) the tendency to isotropy in turbulent flows and b) the amplification of the transverse velocity components of turbulent flows under contraction, there is probably a rapid increase in the amplitude of the transverse turbulent velocity component downstream of the inflow control structure. Now if the extraneous noise generating inflow distortion is a steady or quasi steady vortex then it is possible that a honeycomb may be sufficient, however it is probably not possible to a) make this assessment of the inflow distortion field aprior or b) if it can be made, ensure that this assessment remains valid under all conditions of use of the ICS. In this case, the use of a resistive element in the ICS would provide a conservative design. It is therefore, in general, necessary and/or conservative for an ICS to suppress both transverse and streamwise distortion velocity components i.e. the ICS should include both resistive and torque absorbing elements.

Now the contraction model of Section 6 requires isotropic turbulence as an initial condition and so to use this model, the design condition of isotropy is imposed on the ICS. Thus, while many ICS designs could satisfy the design criterion of producing an upwash field at the fan face in static operation less than or equal to that encountered in flight, the one that produces equipartition of the turbulent kinetic energy downstream of the ICS is chosen. In general, this will require a resistive element (gauze or perforated plate) and a torque absorbing element (honeycomb). Equipartition of the turbulent kinetic energy requires that downstream of the ICS

$$\overline{u_1^2} = \overline{u_2^2} = \overline{u_3^2}$$

If it is assumed that the two elements act independently and in series, then from Equation 101

$$\frac{3}{4}\,\alpha_P^{\,2}\;\alpha_H^{\,2}\;\ell_{11}^{\,3} = \left(\frac{1 + \alpha_P - \alpha_P K_P}{1 + \alpha_P + K_P}\right)^2 \left(\frac{1 + \alpha_H - \alpha_H K_H}{1 + \alpha_H + K_H}\right)^2 \qquad 102$$

In view of the small initial contraction the integral length scale relationships will exhibit roughly isotropic characteristics and a scale representative of this field is

$$L_{22} = \frac{4}{3}\,\ell_{1I}^{-1/2}\,L_{AS} \qquad 103$$

For the purposes of the final flow contraction the equipartitioned turbulence field downstream of the ICS is then, approximated by an isotropic field of characteristic length scale $L_{ii} = L_{22}$ As noted previously the upwash field resulting from the contraction of an isotropic field is dominated by the transverse (azimuthal) velocity component in the contraction range encountered on a test stand, hence

$$F_n(k_2)_S \simeq F_2(k_2)_S \qquad 104$$

and $F_2(k_2)_S$ can be obtained from Ganz's extension of the Ribner-Tucker theory (33), thus

$$F_n(k_2)_S \simeq \frac{\pi\, N_{ICS}\,\ell_{1F}}{\Lambda_{ICS}^{2}\, s}\left\{1 + \frac{p}{2} + \frac{s\sqrt{p}}{4}\left[\sin^{-1}\left(1 - \frac{2}{s}\right) - \frac{\pi}{2}\right]\right\} \qquad 105$$

$$N_{ICS} = \frac{2}{3}\,\frac{KE_{ICS}}{\Lambda^{2}\,L_{22}} \qquad \Lambda_{ICS} = L_{22}$$

where

$$p = \frac{k_2^{\,2}}{\ell_{1F}\,\Lambda_{ICS}^{\,2}} \qquad s = p + 1$$

The ICS subscript refers to the post-screen location and k_2 is the local post-final contraction wave number.

With the formulation of $F_n(k_2)_S$ it is now possible to expand the design criterion of Equation 86 with the help of Equations 90 and 105 so that the criterion becomes

$$\alpha_P^{\,2}\ \alpha_H^{\,2} \le \frac{32\pi\ N_F\ L_{AS}}{\ell_{1F}\ \ell_{1I}^{\,1/2}\ \overline{u_{AS}^{\,2}}} \bullet$$

$$\bullet \frac{s\left(k_{3U}-k_{3L}\right) k_1{}^{*}\left[4k_2^{\,2}\ \sin^2\gamma_O+\left(k_{3U}+k_{3L}\right)^2\right]}{\left\{4\left(k_2^{\,2}+\gamma_F^{\,2}\right)+\left(k_{3U}+k_{3L}\right)^2\right\}^3\left\{1+\frac{p}{2}+\frac{s\sqrt{p}}{4}\left[\sin^{-1}\left(1-\frac{2}{s}\right)-\frac{\pi}{2}\right]\right\}} \qquad 106$$

This criterion together with the honeycomb and perforated plate (or gauze) characteristics and the equipartition constraint of Equation 102 constitute a set of four equations in the four unknowns α_P, α_H, K_P, K_H (the characteristics of the two screen elements). The honeycomb characteristic does require knowledge of the cell diameter Reynolds number which can be found from Section 6.4.1.

The sensitive wavenumber ranges can be determined from the work of Ganz (36) and conservatively these are

$$k_1 < k_1^{\,*} = \frac{B}{R_O} \qquad 107$$

$$k_{2L} = \frac{B}{2R_O} < k_2 < k_{2U} = \frac{10B}{R_O} \qquad 108$$

$$k_{3L} = \frac{B}{2R_O} < k_3 < k_{3U} = \frac{10B}{R_O} \qquad 109$$

A summary of the process whereby the atmospheric turbulence encountered statically at the engine fan face is reduced to the flight level is shown in Figure 111 and a flow chart for determining the ICS material characteristics is shown in Figure 112. The step-by-step calculation procedure is presented in Section 6.4.4.

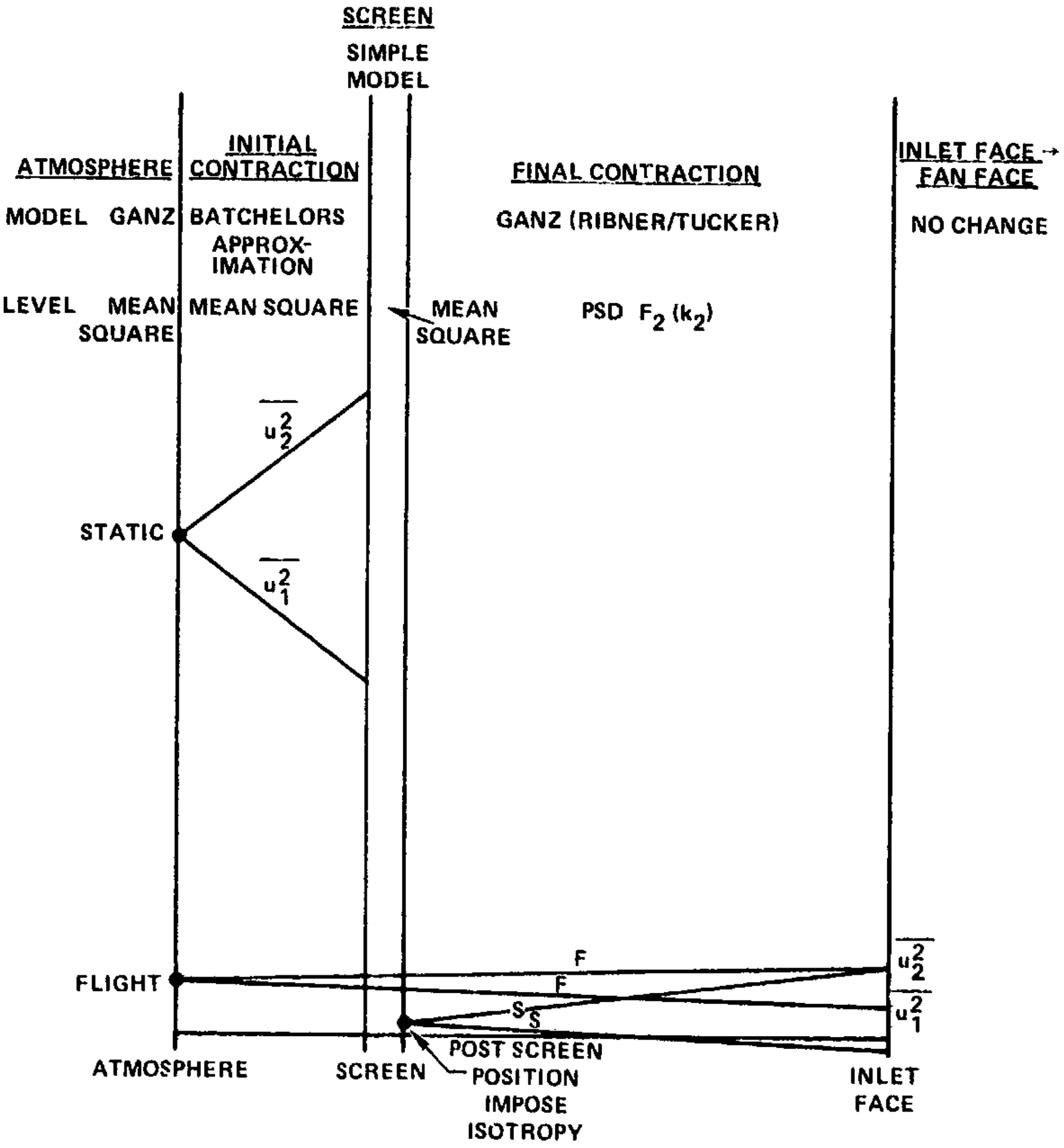

Figure 111 The Elements of the ICS Material Selection Criterion

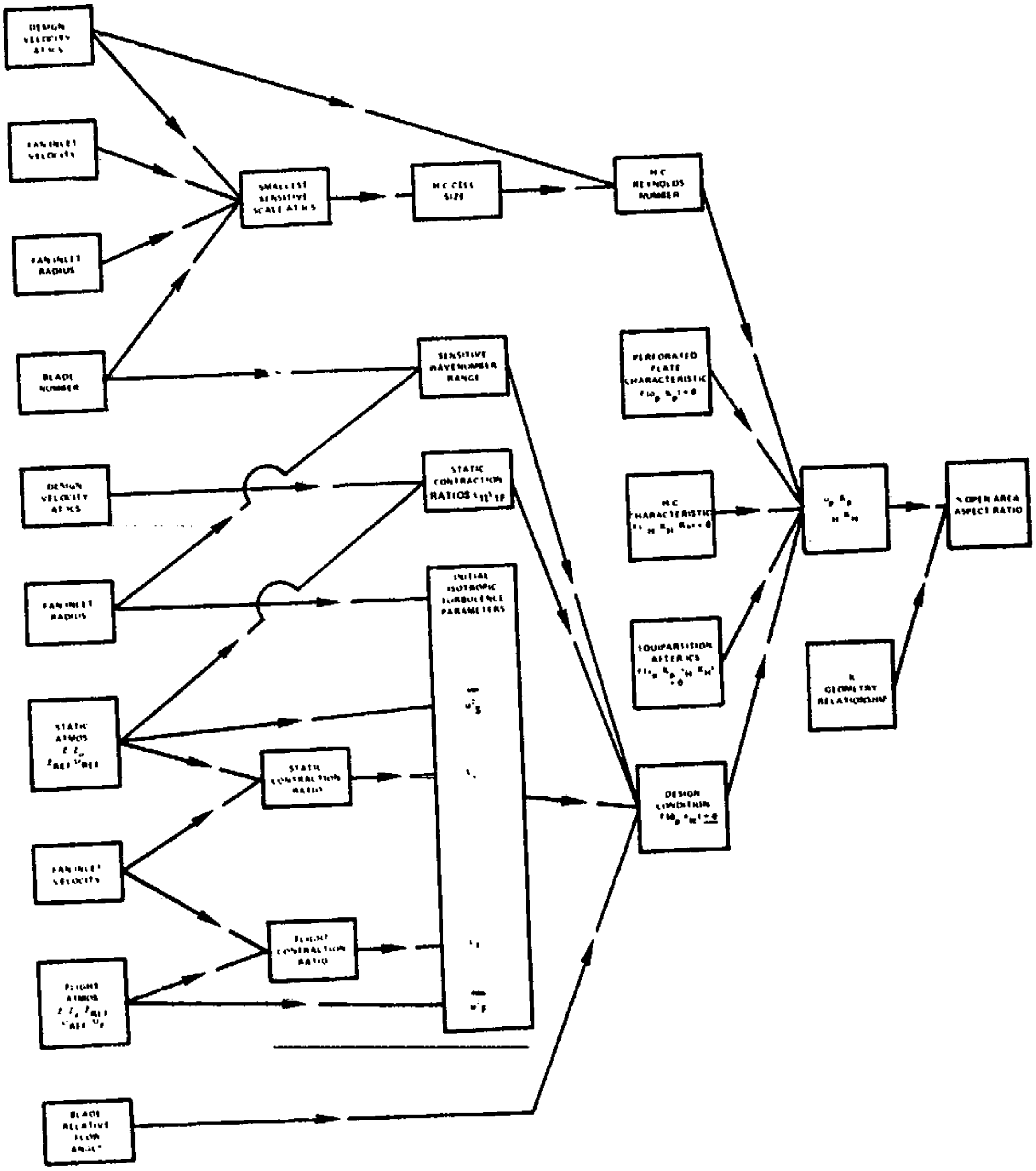

Figure 112 Flow Chart for Determining ICS Material (Turbulence Criterion)

The other element of the external field that must be considered is the steady or quasi steady velocity distortion. These can be in type either streamwise velocity deficits or vortices. Their origins can be surfaces over which the air travels on its way to the engine or mid-air stagnation points. Stand structure can be a source of both wakes and vortices, since variations in flow incidence angle over the structure can cause local separation over the body and subsequent vortex roll-up. This phenomenon has been observed in bluff bodies, for instance (43). The variation in loading over the support structure leads to the formation of potential vortex distributions. In addition, the ground plane can produce an ingested vortex and also the lesser known vortex originating at a mid-air stagnation point (44). Protuberances on the external nacelle have also been observed as sources of steady (quasi steady) inflow distortions.

The quantification of the initial conditions of these flow disturbances is difficult in view of the complexity of test stand geometries and more work needs to be performed in order to define them.

As with the atmospheric turbulence, a criterion for suppression of this type of disturbance must first be established. The steady inflow distortion in flight is ill-defined and is due if it exists for different reasons (e.g. aircraft angle of attack) from those encountered statically. It is therefore suggested that the amplitude velocity components of the steady inflow distortion field be reduced below the RMS value of the atmospheric turbulence field encountered in flight, or

$$\Delta U_{1S} \quad \sqrt{\overline{u_{AF}}^{2}} \qquad 110$$

$$\Delta U_{2S} \quad \sqrt{\overline{u_{AF}}^{2}} \qquad 111$$

where Δ indicates the amplitude of the distortion. The right hand side of these inequalities is readily determined as in the first part of this section. For the determination of the left hand side of the inequalities 110 and 111, it will be assumed that the streamwise velocity distortion is suppressed by the ICS independently of the suppression of the transverse velocity distortion.

If the initial condition of the streamwise distortion is ΔU_{1A} then after the initial contraction, using the model of section 6 (Equation 58) this deficit at the ICS entrance will be

$$\Delta U_1 = \ell_{1I}^{-1} \, \Delta U_{1A} \tag{112}$$

and assuming the honeycomb and perforated plate (gauze) act in series, the deficit downstream of the LCS is

$$\Delta U_1 = \ell_{1I}^{-1} \, \Delta U_{1A} \left\{ \frac{1 + \alpha_H - \alpha_H K_H}{1 + \alpha + K_H} \right\} \left\{ \frac{1 + \alpha_P - \alpha_P K_P}{1 + \alpha_P + K_P} \right\} \tag{113}$$

and after the final contraction at the fan face

$$\Delta U_1 = \ell_{1I}^{-1} \, \ell_{1F}^{-1} \, \Delta U_{1A} \left\{ \frac{1 + \alpha_H - \alpha_H K_H}{1 + \alpha_H + K_H} \right\} \bullet$$

$$\bullet \left\{ \frac{1 + \alpha_P - \alpha_P K_P}{1 + \alpha_P + K_P} \right\} \tag{114}$$

Again as in the case for atmospheric turbulence ingestion, the maximum streamwise velocity distortion will occur at the maximum ambient velocity in the test window, unless the wake generating structure lies in the region dominated by the engine inflow (which is unlikely).

The streamwise distortion criterion in Equation 110 is then

$$\left\{ \frac{1 + \alpha_H - \alpha_H K_H}{1 + \alpha_H + K_H} \right\} \left\{ \frac{1 + \alpha_P - \alpha_P K_P}{1 + \alpha_P + K_P} \right\} < \frac{\sqrt{\overline{u_{AF}^{2}}} \, \ell_{1I} \, \ell_{1F}}{\Delta U_{1A}} \tag{115}$$

On pursuing a similar course with the transverse (vortical) distortion, the inequality of Equation 111 becomes

$$\alpha_P \alpha_H > \frac{\sqrt{\overline{u_{AF}^2}}}{U_{2A\ max}} \qquad 116$$

Note here that the design criterion is independent of contraction ratio due to the invariance of a vortex under contraction. These two inequalities, together with the honeycomb and gauze (perforated plate) characteristics, form a set of four relationships in four unknowns which can be solved. A schematic of this aspect of the design system is shown in Figure 113 and the step by step procedure is given in Section 6.4.4.

6.4.3 Other Design Aspects of an ICS

Various observations on the general features that should be incorporated into an ICS have been made in this report and (29). In summary these are:

- Discontinuities whether of structure or profile should be minimized in order to minimize self-generated distortions and directivity modifications to the radiation field.

- The perforated plate (gauze) transmission loss criterion of Equation 82 should be applied to determine the allowable plate (gauze) thickness and hole diameter combinations.

- The construction of the ICS aft of the inlet plane is an open question. Both baffles and ICS screening material have been used in this region. The nacelle boundary layer is undoubtedly affected by the conditions here. However, evidence to date gathered under the JNRP has indicated that there is no significant difference in the noise fields of either configuration. In contrast, the work performed in (21) showed that the noise field was quite strongly dependent on the flow field in the boundary layer. The

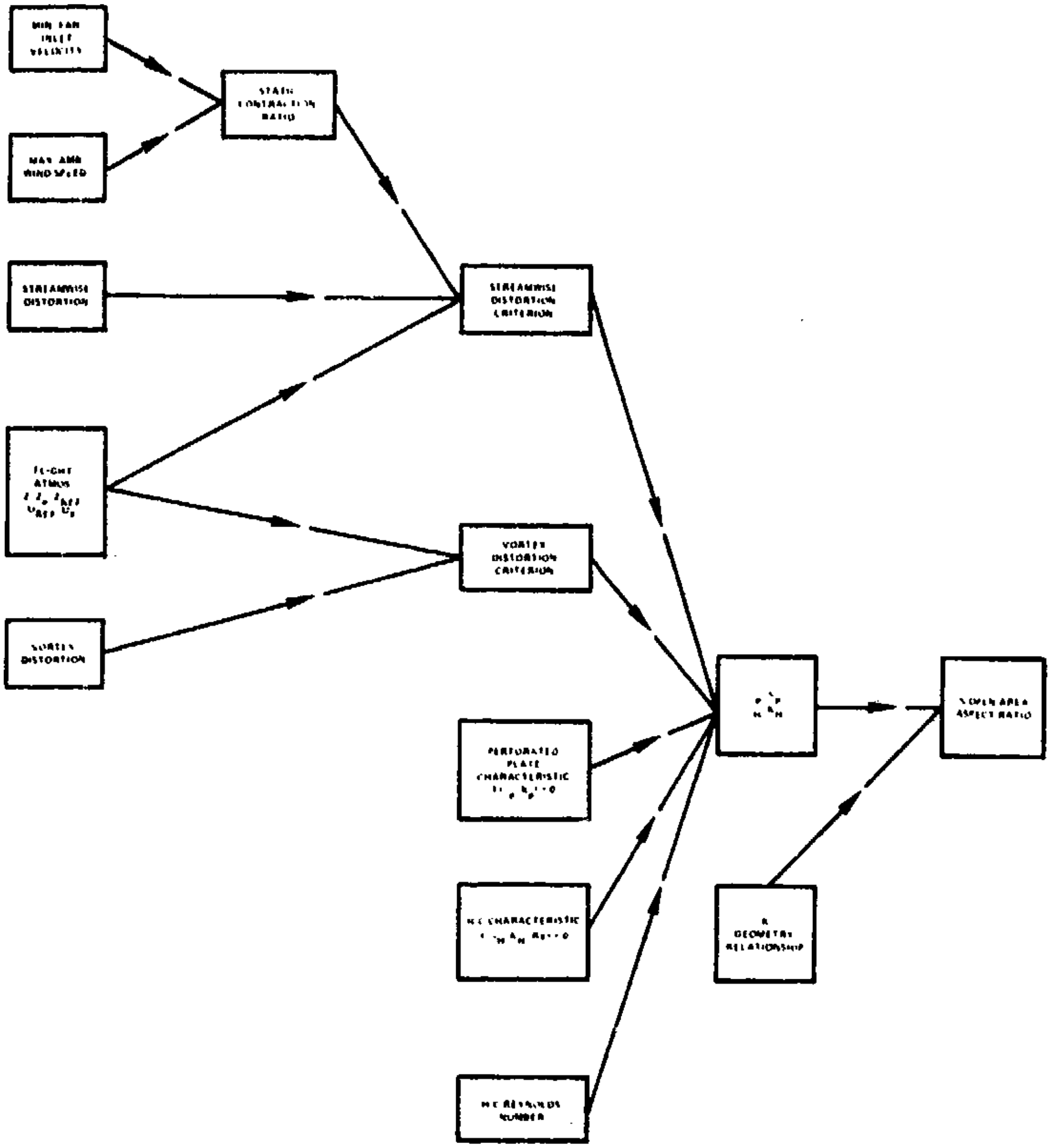

Figure 113 Flow Chart for Determining ICS Material (Steady Distortion Criterion)

sensitivity of the noise field to the nacelle boundary layer undoubtedly varies from fan to fan. It would be expected that an ICS open to the rear would allow more accurate noise measurements to be made at higher far field angles. Nevertheless, the whole question of simulation of the flight nacelle boundary layer, in static operation, needs more investigation.

- The use of two ICS materials in conjunction leads to the possibility of flow blockage when holes do not match up. This problem can be avoided by separating the two materials or alternately ensuring that the mesh size of one of the materials is significantly greater than the other. This latter solution is quite acceptable in view of the degree of latitude allowed to the detailed dimensions of the ICS material (Equation 85).

- The relative location of ICS materials, i.e., whether perforated plate should be placed upstream or downstream of the honeycomb is probably unimportant as regards the suppression of the noise generating elements of the inflow field. It may be that because of construction requirements one material may produce greater downstream distortion than the other. In this case, an indication of the best configuration is provided.

6.4.4 The Step By Step ICS Design Procedure

1. Determine inlet velocity at lowest operating condition - U_O
2. Determine maximum ambient wind velocity in test window - U_A
3. Compute design speed at ICS - U_{ICS}
4. Determine inlet radius - R_O
5. Compute nominal radius of ICS - R_{ICS}

$$R_{ICS} = R_O \sqrt{\frac{U_O}{2U_{ICS}}}$$

6. Determine blade number - B
7. Compute minimum sensitive transverse scale - λ_{min}

$$\lambda_{min} = \frac{\pi R_O}{5B}$$

8. Compute final contraction ratio (ICS to inlet) - ℓ_{1F}

$$\ell_{1F} = \frac{U_o}{U_{ICS}}$$

9. Compute minimum sensitive transverse scale at ICS - $(\lambda_{min})_{ICS}$

$$(\lambda_{min})_{ICS} = \ell_{1F}^{1/2}\,\lambda_{min}$$

10. Compute characteristic detail dimension of ICS material - d_{ICS}

$$d_{ICS} = o\left[\frac{(\lambda_{min})_{ICS}}{10}\right]$$

11. Compute Reynolds Number of honeycomb cell - Re

$$Re = \left[\frac{U_{ICS}\,d_{ICS}}{\nu}\right]$$

Atmospheric Turbulence Design

12. Determine engine height - z, roughness scale z_o, static reference height (engine height) z_{REF}, static reference wind speed (max, wind speed in test window) U_{REF}.

13. Compute RMS value of turbulent velocity in capture stream tube during static operation - $\sqrt{\overline{u_{AS}^{\,2}}}$

$$\sqrt{\overline{u_{AS}^{\,2}}} = \frac{.464\;R_o^{1/3}\;U_{REF}^{5/6}\;U_o^{1/6}\;z^{-1/3}}{\left(\ell n\,\frac{z}{z_o}\right)^{1/6}\left(\ell n\,\frac{z_{REF}}{z_o}\right)^{5/6}}$$

14. Compute static contraction ratio - ℓ_{1S}

$$\ell_{1S} = \frac{U_o}{U_A}$$

(Note initial contraction ratio, from atmosphere to ICS, $\ell_{1I} = 1.5$ by design)

15. Compute characteristic length scale of turbulence in capture streamtube during static operation - L_{AS}

$$L_{AS} = .355\, R_o\, \nu_{1S}^{1/2}$$

16. Determine, for flight operation, engine height z, roughness scale z_o, flight reference height - z_{REF}, flight reference wind speed - U_{REF}

17. Compute RMS value of turbulent velocity in capture stream tube in flight - $\sqrt{\overline{u_{AF}^{2}}}$

$$\sqrt{\overline{u_{AF}^{2}}} = \frac{.464\, R_o^{1/3}\, U_{REF}\, z^{-1/3}}{\left(\ln \frac{z}{z_o}\right)^{1/6} \left(\ln \frac{z_{REF}}{z_o}\right)^{5/6}}$$

18. Compute characteristic length scale of turbulence in capture streamtube in flight - L_{AF}

$$L_{AF} = .355\, R_o$$

19. Compute limits of sensitive wavenumber ranges - k_1^*, k_{2U}, k_{2L}, k_{3U}, k_{3L}

$$k_1^* = \frac{B}{R_o}, \quad k_{2U} = k_{3U} = \frac{10B}{R_o}, \quad k_{2L} = k_{3L} = \frac{B}{2R_o}$$

20. Compute in flight turbulence field characteristics - N_F, λ_F

$$N_F = \frac{2\,\overline{u_{AF}^{2}}}{2\, L_{AF}}, \quad \lambda_F = \frac{1}{L_{AF}}$$

21. Determine blade relative inflow angle at tip - β_o

22. Compute characteristic length scale of turbulence behind ICS - L_{ICS}

$$L_{ICS} = \frac{4}{3}\, \frac{L_{AS}}{\nu_{11}^{1/2}} \quad \text{if} > 1$$

$$= L_{AS} \quad \text{Otherwise}$$

23. Compute the parameters p and s

$$p = \frac{k_{2L}^{2}\,L_{TCS}^{2}}{\ell_{1F}} \qquad s = p + 1$$

24. Compute maximum value of flow angle ratio product - $\alpha_P\,\alpha_H$

$$\alpha_P\,\alpha_H = \left[\frac{32\pi\,N_F\,L_{AS}}{\ell_{1F}\,\ell_{1I}^{1/2}\,\overline{u_{AS}^{2}}}\cdot\frac{s\left(k_{3U}-k_{3L}\right)k_1^{*}}{\left\{4\left(k_{2L}^{2}+\gamma_F^{2}\right)+\left(k_{3U}+k_{3L}\right)^{2}\right\}^{3}}\right.$$

$$\left.\frac{\left(4k_{2L}^{2}\sin^{2}\gamma+\left[k_{3U}+k_{3L}\right]^{2}\right)}{\left\{1+\frac{p}{2}+\frac{s\sqrt{p}}{4}\left[\sin^{-1}\left(1-\frac{2}{s}\right)-\frac{\pi}{2}\right]\right\}}\right]^{1/2}$$

25. Solve the equation for perforated plate (gauze) flow angle ratio - α_P

$$\frac{2\alpha_P^{3}+\alpha_P^{2}-1.21\,\alpha_P}{\alpha_P^{3}+1.21} = .866\,\alpha_P\,\alpha_H\,\ell_{1I}^{2/3}$$

$$\left\{\frac{\alpha_P+\alpha_P\,\alpha_H-.201\,Re^{-1/4}\,\alpha_P\left[\ln\alpha_P\,\alpha_H-\ln\alpha_P\right]}{\alpha_P+\alpha_P\,\alpha_H\left(1+.201\,Re^{-1/4}\left[\ln\alpha_P\,\alpha_H-\ln\alpha_P\right]\right)}\right\}$$

26. Compute resistance of perforated plate (gauze) - K_P

$$K_P = 1.21\,\alpha_P^{-2} - 1$$

27. Compute flow angle ratio of honeycomb - α_H

$$\alpha_H = \frac{\alpha_P\,\alpha_H}{\alpha_P}$$

28. Compute resistance of honeycomb - K_H

$$K_H = -\,.201\,Re^{-1/4}\,\ln\alpha_H$$

Steady Distortion Design

29. Determine maximum azimuthal velocity in vortex - U_{2A}

30. Compute maximum value of flow angle ratio product - $\alpha_P \alpha_H$

$$\alpha_P \alpha_H = \frac{\sqrt{\overline{u_{AF}^{2}}}}{U_{2A}}$$

31. Determine maximum pre-contraction streamwise velocity deficit - ΔU_{1A}

32. Solve the equation for the perforated plate (gauze) flow angle ratio - α_P

$$\frac{2\alpha_P^{3} + \alpha_P^{2} - 1.21\ \alpha_P}{\alpha_P^{3} + 1.21} = \frac{\sqrt{\overline{u_{AF}^{2}}}}{\Delta U_{1A}}\ \epsilon_{1S}$$

$$\left\{ \frac{\alpha_P + \alpha_P\ \alpha_H - .201\ Re^{-1/4}\ \alpha_P \left[\ln \alpha_P\ \alpha_H - \ln\ \alpha_P \right]}{\alpha_P + \alpha_P\ \alpha_H \left(1 + .201\ Re^{-1/4} \left[\ln \alpha_P\ \alpha_H - \ln \alpha_P \right] \right)} \right\}$$

33. Compute resistance of perforated plate (gauze) - K_P

$$K_P = 1.21\ \alpha_P^{-2} - 1$$

34. Compute flow angle ratio of honeycomb - α_H

$$\alpha_H = \frac{\alpha_P\ \alpha_H}{\alpha_P}$$

35. Compute resistance of honeycomb - K_H

$$K_H = -\ .201\ Re^{-1/4}\ \ln\ \alpha_H$$

Conservative Design

36. Compare resistance of perforated plate (gauze) for atmospheric turbulence and steady distortion designs (Items 26 and 33). Choose the larger - K_P

37. Compare flow angle ratio of honeycomb for atmospheric turbulence and steady distortion designs. (Items 27 and 34). Choose smaller - α_H

38. Compute honeycomb length to diameter ratio - $\frac{\ell}{d}$

$$\frac{\ell}{d} = -\frac{1}{\ } \ln\ \alpha_H$$

39. Determine perforated plate open area ratio from Baines and Peterson plot Figure 114. -

Perforated Plate Transmission Loss

40. Determine the maximum mach number of flow incident on the ICS - M_{ICS}.

41. Plot perforated plate thickness, ℓ_p, against hole diameter d_p using the transmission loss criterion at the 24th one - third octave band.

$$\ell_p = 5.39.10^{-3}\left[5.04 - \left(2+K_p\,M_{ICS}\right)^2\right]^{1/2} \sigma_p - \left(1 - \sigma_p\right) d_p \text{ meters}$$

42. Select a perforated plate thickness and hole diameter consistent with the estimate of d_{ICS} in Item 10. __

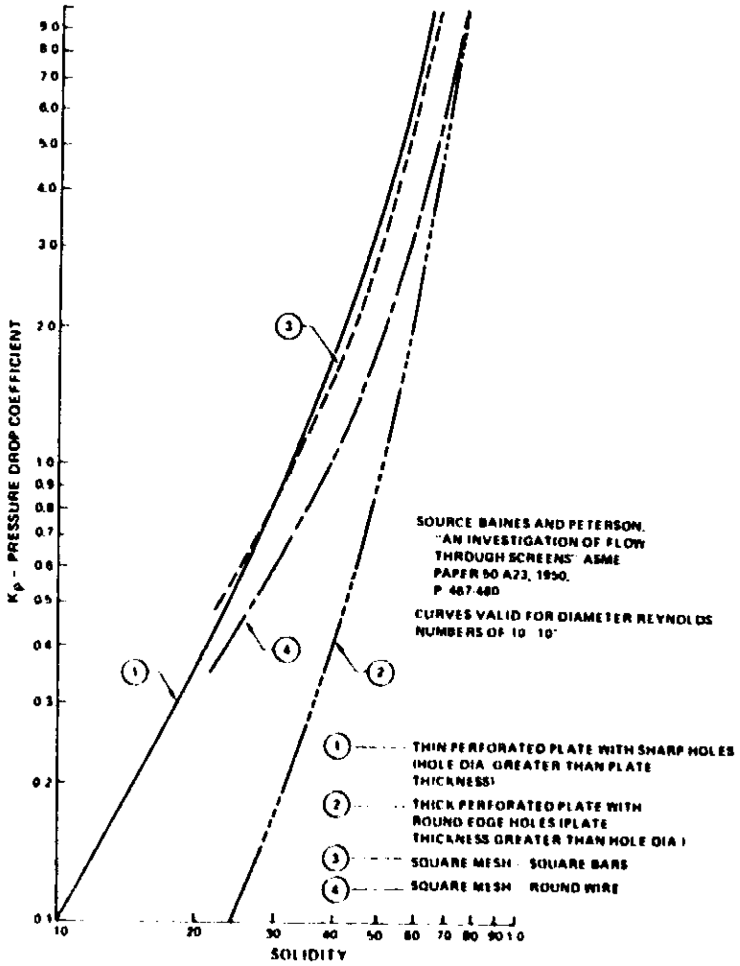

SOURCE BAINES AND PETERSON, "AN INVESTIGATION OF FLOW THROUGH SCREENS" ASME PAPER 50 A23, 1950, P 467-480

CURVES VALID FOR DIAMETER REYNOLDS NUMBERS OF 10 10

Figure 114 Perforated Plate and Gauze Pressure Drop Coefficients

6.4.5 The Application of the ICS Design System to the JT9D and JT15D

The step by step ICS design procedure is applied in Figures 115 and 116 for the JT9D and JT15D engines. A comparison between these designs and actual ICS's constructed for these engines is shown below

JT9D

Nominal Radius	Present Design 3.47m	P&WA 3.66m	Boeing 3.66m
Detail Dimension (Honeycomb)	.0067m	.0095m	.0032m
Detail Dimension (Perforated Plate or Gauze)	.003m	.0048m	.00157m
Thickness (Honeycomb)	.0117m	.0762m	.0381m
Thickness (Perforated Plate or Gauze)	.0009m	.0031m	.00079m
Open Area Ratio (Perforated Plate or Gauze	54%	51%	46%

The most noticeable difference between the present design and the P&WA and Boeing ICS designs is the much larger honeycomb length to diameter ratios in these designs - P&WA 8, Boeing 12, present 1.75. The P&WA and Boeing designs are very conservative in this respect. In other characteristics of the design the P&WA and Boeing designs are generally conservative.

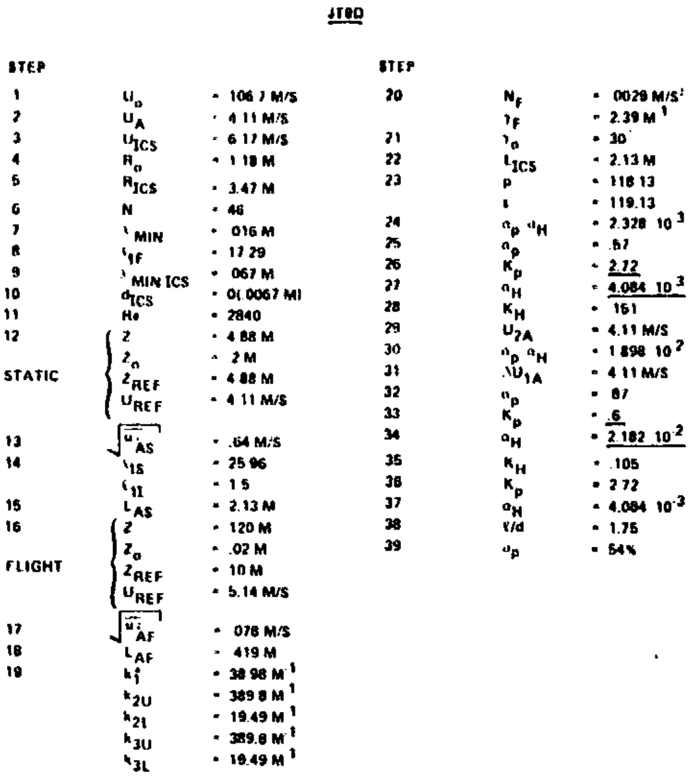

JT9D

STEP			
1		U_o	= 106.7 M/S
2		U_A	= 4.11 M/S
3		U_{ICS}	= 6.17 M/S
4		R_o	= 1.18 M
5		R_{ICS}	= 3.47 M
6		N	= 46
7		λ_{MIN}	= .016 M
8		λ_{1F}	= 17.29
9		$\lambda_{MIN\ ICS}$	= .067 M
10		d_{ICS}	= 0(.0067 M)
11		Re	= 2840
12	STATIC	Z	= 4.88 M
		Z_o	= .2 M
		Z_{REF}	= 4.88 M
		U_{REF}	= 4.11 M/S
13		$\sqrt{\overline{u'^2_{AS}}}$	= .64 M/S
14		λ_{1S}	= 25.96
		λ_{1I}	= 1.5
15		L_{AS}	= 2.13 M
16	FLIGHT	Z	= 120 M
		Z_o	= .02 M
		Z_{REF}	= 10 M
		U_{REF}	= 5.14 M/S
17		$\sqrt{\overline{u'^2_{AF}}}$	= .078 M/S
18		L_{AF}	= .419 M
19		k_1^*	= 38.98 M^{-1}
		k_{2U}	= 389.8 M^{-1}
		k_{2L}	= 19.49 M^{-1}
		k_{3U}	= 389.8 M^{-1}
		k_{3L}	= 19.49 M^{-1}

STEP		
20	N_F	= .0029 M/S^2
	λ_F	= 2.39 M^{-1}
21	λ_o	= 30
22	L_{ICS}	= 2.13 M
23	p	= 118.13
	t	= 119.13
24	$\alpha_p\ \alpha_H$	= 2.328 10^{3}
25	α_p	= .57
26	K_p	= 2.72
27	α_H	= 4.084 10^{3}
28	K_H	= .161
29	U_{2A}	= 4.11 M/S
30	$\alpha_p\ \alpha_H$	= 1.898 10^{2}
31	ΔU_{1A}	= 4.11 M/S
32	α_p	= .87
33	K_p	= .6
34	α_H	= 2.182 10^{-2}
35	K_H	= .105
36	K_p	= 2.72
37	α_H	= 4.084 10^{-3}
38	ℓ/d	= 1.75
39	α_p	= 54%

Figure 115 ICS Design Process for the JT9D

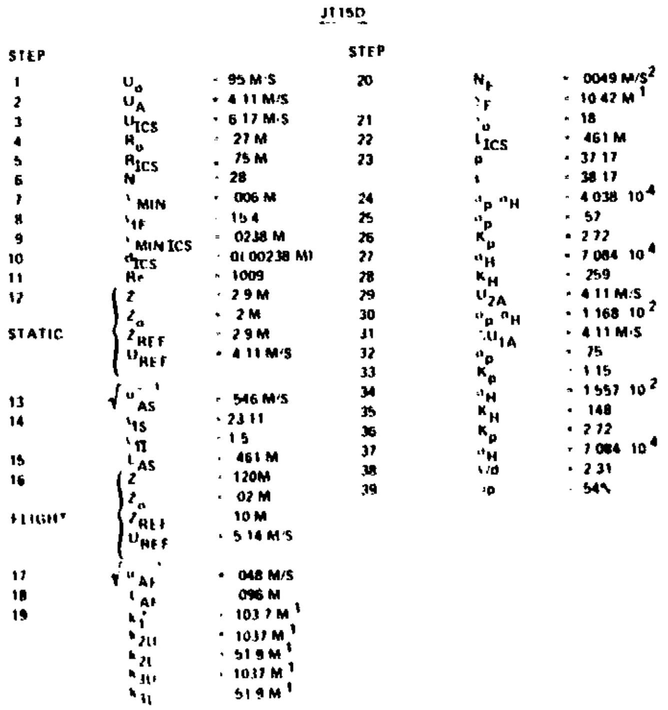

JT15D

STEP			
1		U_o	= 95 M/S
2		U_A	= 4.11 M/S
3		U_{ICS}	= 6.17 M/S
4		R_o	= .27 M
5		R_{ICS}	= .75 M
6		N	= 28
7		λ_{MIN}	= .006 M
8		λ_{1F}	= 15.4
9		$\lambda_{MIN\ ICS}$	= .0238 M
10		d_{ICS}	= 0(.00238 M)
11		Re	= 1009
12	STATIC	Z	= 2.9 M
		Z_o	= .2 M
		Z_{REF}	= 2.9 M
		U_{REF}	= 4.11 M/S
13		$\sqrt{\overline{u'^2_{AS}}}$	= .546 M/S
14		λ_{1S}	= 23.11
		λ_{1I}	= 1.5
15		L_{AS}	= .461 M
16	FLIGHT	Z	= 120M
		Z_o	= .02 M
		Z_{REF}	10 M
		U_{REF}	= 5.14 M/S
17		$\sqrt{\overline{u'^2_{AF}}}$	= .048 M/S
18		L_{AF}	.096 M
19		k_1^*	= 103.7 M^{-1}
		k_{2U}	= 1037 M^{-1}
		k_{2L}	= 51.9 M^{-1}
		k_{3U}	= 1037 M^{-1}
		k_{3L}	51.9 M^{-1}

STEP		
20	N_F	= .0049 M/S^2
	λ_F	= 10.42 M^{-1}
21	λ_o	= 18
22	L_{ICS}	= .461 M
23	p	= 37.17
	t	= 38.17
24	$\alpha_p\ \alpha_H$	= 4.038 10^{4}
25	α_p	= .57
26	K_p	= 2.72
27	α_H	= 7.084 10^{4}
28	K_H	= .259
29	U_{2A}	= 4.11 M/S
30	$\alpha_p\ \alpha_H$	= 1.168 10^{2}
31	ΔU_{1A}	= 4.11 M/S
32	α_p	= .75
33	K_p	= 1.15
34	α_H	= 1.557 10^{2}
35	K_H	= .148
36	K_p	= 2.72
37	α_H	= 7.084 10^{4}
38	ℓ/d	= 2.31
39	α_p	= 54%

Figure 116 ICS Design Process for the JT15D

	Present Design	NASA Lewis (ICD1)
Nominal Radius	.75m	1m
Detail Dimension (Honeycomb)	.00238m	.0063m
Detail Dimension (Perforated Plate or Gauze)	.003m	.0064m .0013m
Thickness (Honeycomb)	.0055m	.05m
Thickness (Perforated Plate or Gauze)	.0009m	.0006m
Open Area Ratio (Perforated Plate or Gauze)	54%	40%

Again this comparison shows a much greater honeycomb length to diameter ratio than would be required by the present design system - NASA Lewis 8, present, 2.31. The detailed dimensions of the screen material are also somewhat smaller for the present design than the NASA Lewis design. In addition, the open area ratio of the NASA Lewis gauze is more conservative than the present design. It should be noted that in both of these calculations estimates of the steady (quasi steady) distortion field were made. Both vortical and axial velocity distortions were assumed to be of the order of the maximum ambient wind speed.

6.4.6 Summary of the Main ICS Design Characteristics

o The ICS should be located external to the engine in a region where, within the ambient wind test window, the engine induced flow is somewhat greater than the maximum ambient windspeed. This location is probably the best compromise between the following requirements.

a) ICS generated flow distortions to be small enough that no additional extraneous BPF tone energy is generated.

b) Pressure drop across the ICS to be low enough so that the fan operating point is unaffected.

c) Flow through the ICS to be low enough so that acoustic transmission loss is negligible.

d) Steady or quasi-steady vortices to be suppressed sufficiently far upstream of the inlet so that the residual axial velocity distortion can be suppressed by the flow contraction.

o The shape of the ICS is to some degree flexible and while a basically hemispherical design is suggested in this report, any shape that does not create inflow distortions is acceptable.

o Whether to mount the ICS on an impervious backplate or continue the screen to the engine nacelle has not been resolved. This question must be addressed in conjunction with flight boundary layer simulation considerations.

o Discontinuities in the ICS should be minimized both for acoustic and flow distortion reasons.

o In view of the transfer of energy between transverse and streamwise velocity components in a turbulent field subject to contraction, it is necessary to suppress all three velocity components. Consequently, the ICS should contain both a resistive element (perforated plate, gauze) and a torque withstanding element (honeycomb). If the inflow distortion field is dominated by steady or quasi-steady vortical elements and inflow turbulence is not a significant noise generator, the resistive element may be redundant, however in general this situation cannot be identified a priori. However, if this situation exists the use of a resistive element produces a conservative design.

o The relative location of these two elements is probably not important as regards distortion suppression. However, other considerations, such as protection of the honeycomb, may suggest a preferred arrangement.

o The characteristics of the ICS elements are defined by the design system of Section 6.4.4.

7.0 THE ASSESSMENT OF THE ICS DESIGN SYSTEM (TASK H)

During the Boeing/Pratt & Whitney Aircraft Joint Noise Reduction Program, data were gathered using pressure transducers mounted on the blades of a JT9D fan, with an ICS in place. These transducers were discussed in (29) and there it was indicated that it is not apparent, in general, which particular stimulus a BMT is responding to. This is especially true when an ICS is in place. In view of this situation the capacity for assessment of the ICS design system using BMT data is reduced. It was however assumed that the BMT with an ICS in place was responding to the inflow velocity field and the assessment procedure was exercised. In addition, hot film data taken during the JNRP provided another and independent opportunity for assessment.

7.1 The Assessment Procedure

The assessment is made by comparing a theoretical prediction, using elements of the ICS design system, with an estimate obtained from measured data. The quantity that was compared was the one dimensional PSD of the upwash velocity component in the azimuthal, k_2, direction. A theoretical prediction of this PSD is directly obtainable from the ICS design system. The estimate of this PSD, $F_n(k_2)$, using BMT data requires some discussion.

The BMT samples the velocity and pressure fields along a spiral path, at an angle ϕ to the fan face, in the mean flow fixed coordinate system, Figure 117. It responds to duct fixed pressure and velocity fields and by averaging the signal on a once per revolution basis, this duct fixed or steady field may be determined. This and other operations were performed digitally. The steady contribution to the BMT signal is subtracted from the total signal to produce the duct unsteady field pressure signal. This duct unsteady signal is assumed to be due to perturbations in the incoming velocity field. The PSD of the unsteady pressure signal, P(f), may thus be determined.

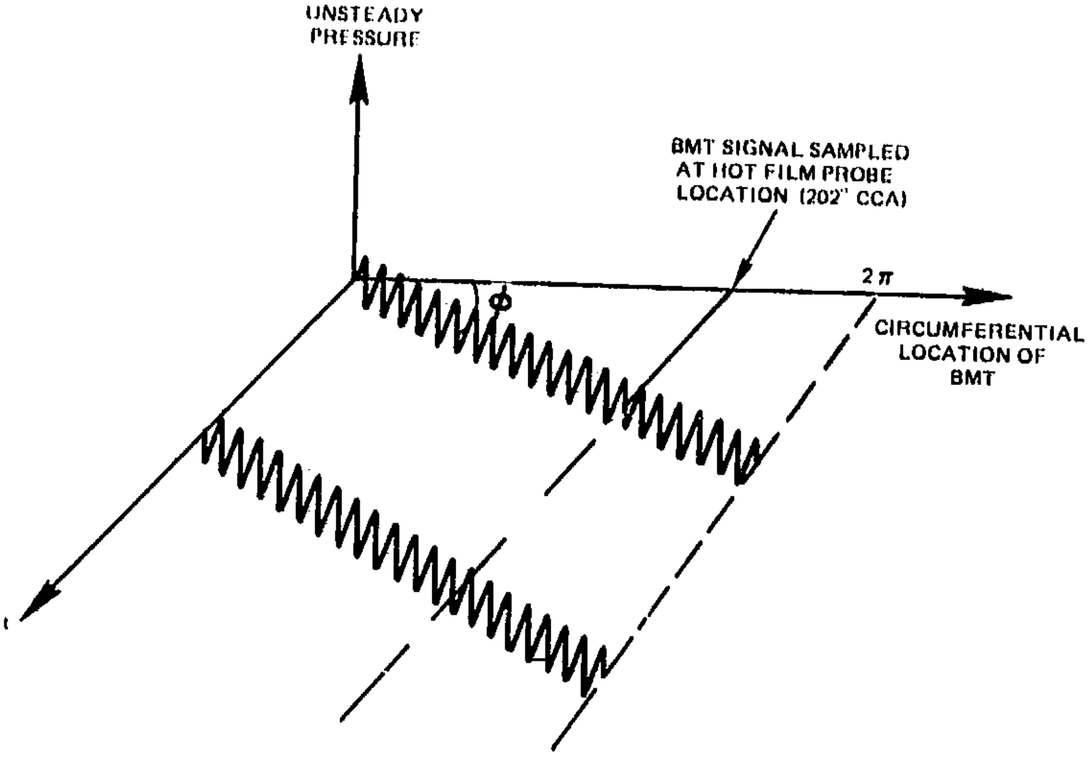

Figure 117 *Sampling of the BMT Pressure Signal*

Now as shown in (28) the response function of the BMT has been estimated by using hot film and BMT data gathered at the same circumferential location in the engine inlet. However, due to the sampling rate of the BMT, the upper frequency limit of the empirical part of the response function was about 20 Hz, and above this, a Sears function form was assumed. This is justified, for in the frequency range of interest, the angle of incidence of a given wave does not cause a significantly different response from the Sears function (see (45). It should be noted that while it is expected that the BMT response function will have a similar form to the Sears function, the two functions are not directly comparable. The BMT response function describes the surface pressure response while the Sears function is a measure of the lift response of the blade. With the response function and the pressure PSD, the upwash velocity PSD, $F_n(f)$ can be found.

The velocity of the blade at the BMT radial location is known and so the PSD, $F_n(f)$, may be transformed into wavenumber space, using the frozen turbulence assumption, so that

$$F_n\left(k_r = \frac{2\pi f}{M_r\ a_o} \right) = F_n(f)\ \frac{M_r a_o}{2\pi} \qquad 117$$

where k_r is the wavenumber component along the spiral path and M_r is the BMT flow relative Mach number. Finally if the turbulence field is made up of 'long eddies', due to the contraction, the wavenumber directions are substantially azimuthal and consequently, $F_n\left(k_2\right)$, can be determined

$$F_n\left(k_2 = \frac{k_r}{\cos\phi} \right) = F_n\ \left(k_r \right)\ \cos\phi \qquad 118$$

In this manner the required upwash velocity PSD was obtained from the measured BMT pressure signal. The prediction of this PSD from the ICS design system elements was performed using equation 86. The input variables were those prevailing at the time the BMT data were acquired. The computation was performed at several values of the wave number component k_2 in the range of interest.

The comparison between the theoretical prediction of the upwash velocity PSD, F_n (k_2) using Equation 105 and an estimate of the same PSD using BMT data, as described above, is shown in the tabulation below.

k_2	F_n (k_2)	
m^{-1}	N/m	
	Estimate From BMT Data	Predicted Using Equation 104
2.31	$1.56\ 10^{-2}$	$1.6\ 10^{-4}$
4.62	$1.71\ 10^{-2}$	$5.49\ 10^{-5}$
6.93	$3.45\ 10^{-2}$	$2.69\ 10^{-5}$
9.24	$6.17\ 10^{-2}$	$1.52\ 10^{-5}$
11.59	$8.45\ 10^{-2}$	$9.79\ 10^{-6}$

The predicted values are very much less than the values obtained from the BMT data and the shapes are different. This is also true for estimates obtained from other BMTs. Thus in view of the reservations expressed previously about the BMT response this comparison is inconclusive.

In addition to blade pressure data, unsteady inlet velocity field information was gathered from an array of split films mounted on a probe. This probe is described in (29). Both azimuthal and streamwise velocity measurements were made inside and outside of the nacelle boundary layer with an ICS in place. No information was acquired spatially in the azimuthal direction and hence these data could not be used to estimate F_n (k_2). However, the streamwise and azimuthal velocity component intensities were found and are shown in Figure 118 (this data was previously published in (13)), from which an estimate of the upwash velocity component intensity was obtained using Equation 23. Taking average values of the component intensities outside of the boundary layer, the upwash velocity component intensity was found to be approximately .5%.

A theoretical prediction of this quantity was made by using Equation 105 of the ICS design system. A numerical integration was performed over k_2 to give the theoretical value of the mean square value of the upwash velocity component, from which the intensity was computed and found to be approximately .25%.

7.2 Conclusions

- o Using BMT measurements to determine the upwash velocity PSD, F_n (k_2), there is a large discrepancy between this measured value and the value predicted using ICS design system elements. This indicates errors in the design system and/or a source of excitation of the BMT in addition to the inflow velocity field.

- o The agreement between predicted and measured values of the upwash turbulence intensity (obtained using hot films) is comparatively good. This provides support for the ICS design system.

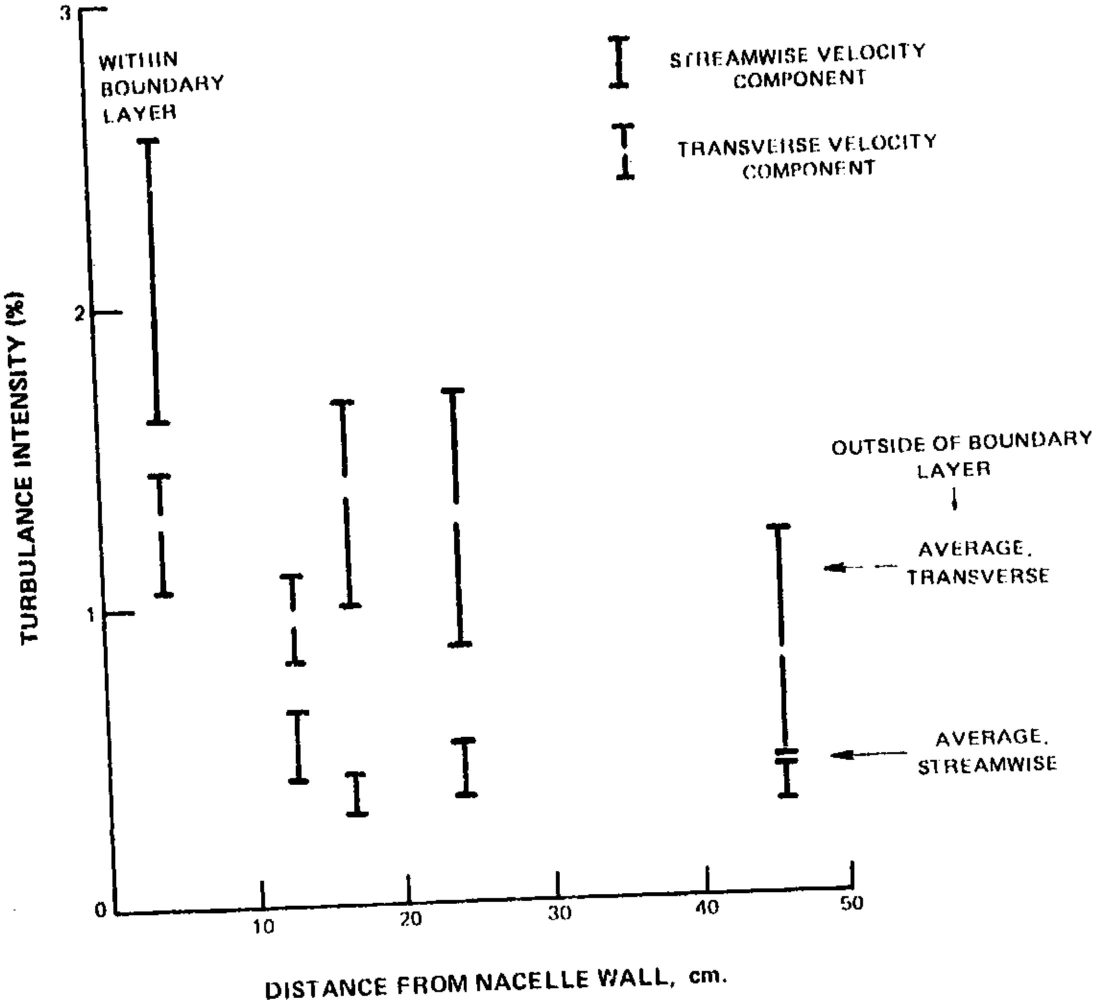

Figure 118 Component Turbulence Intensities Measured in the Inlet of a JT9D with ICS

8.0 CONCLUSIONS

A series of experiments have been conducted to evaluate the theoretical models to be used in the ICS design system. The major observations made during this test program were

- The flow contraction amplifies the transverse turbulent velocity component and at low contraction ratios, it suppresses the stream-wise velocity component. At high contraction ratios the streamwise turbulent velocity component increases, although it did not attain the starting value.

- Steady streamwise velocity deficits are suppressed rapidly by the flow contraction. The azimuthal velocity component of a streamwise aligned vortex was substantially unchanged by the flow contraction. The streamwise velocity distortion associated with the vortex increased in amplitude and extent.

- The turbulence data gathered downstream of both honeycomb and perforated plate was contaminated with self generated turbulence. The honeycomb screen suppressed the transverse turbulent velocity field.

- Steady streamwise velocity deficits are suppressed according to the resistance of the screen. In the resistance range studied here, the higher the resistance the greater the suppression. The azimuthal velocity field of the vortex was totally suppressed by the honeycombs and somewhat reduced and dispersed by the perforated plates. The streamwise velocity distortion associated with the vortex increased on convection through the honeycomb and the 66 percent open area perforated plate.

- The resistance of perforated plate is adequately predicted by theory. The resistance of the honeycomb is dependent on the entrance conditions and this precludes accurate estimates of the resistance for an arbitrary honeycomb. However an estimate may be made, by doubling Blasius' expression (Equation 6).

- The transmission loss of the thinnest honeycombs (.95 cm and 1.27 cm) is negligible and invariant with throughflow speed. The thickest honeycomb (2.54 cm) has a transmission loss that increased with throughflow speed to 2dB at 12.19 m/s.

- The transmission loss of the 66% open area perforated plate is negligible at the lower speeds (9.14 m/s and 6.1 m/s) but increases to 2dB at 12.19 m/s. This attenuation is constant in 1/3 octave band. The 41% open area perforated plate transmission loss decreased with frequency and changes little with throughflow speed. The transmission loss is significant at the lower 1/3 octave bands.

- The presence of honeycomb panel corners and structure can disturb the radiation field of a simple discrete source by significant amounts. The higher the frequency the higher the disruption of the radiation field.

Subsequently the ICS design system models were modified to account for the results of the test program where necessary and these modified models were shown in Section 6. A transmission loss design criterion was established for the ICS and the effect of discontinuities in the structure on the radiation field was examined. It was concluded that:

- Discontinuities in the ICS structure could affect the radiation field of discrete tones significantly but the broadband radiation field on a 1/3 octave band basis would be substantially unmodified.

- It was found that small source phase variations were sufficient to wash out the effect of the ICS discontinuities on the discrete tone radiation field, and it was suggested that controlled variations in engine speed of the order of 0.5 percent be made to accomplish this.

The ICS design procedure is described on a step by step basis in Section 6.4 and the procedure is exercised for the JT9D and JT15D. The designs produced by this procedure are similar to those already constructed for those engines by Pratt & Whitney Aircraft, Boeing and NASA Lewis. The most significant difference is in the honeycomb ℓ/d ratio where the physical ICSs have a substantial overkill. The assessment of the procedure was made in Section 7 using BMT and hot film data. It was concluded that:

- The hot film data provided some support for the validity of the ICS design system.

- The BMT data provided little support for the validity of the ICS design system. It was suspected however that the BMTs were responding to excitations in addition to the inflow velocity field which for the purpose of ICS design assessment were extraneous.

The similarity between the ICS design produced by this procedure and actual ICSs is also encouraging in view of the proven effectiveness of those designs.

APPENDIX A

FLOW MEASUREMENT INSTRUMENTATION AND ACCURACY

Measurement Type 1. (Mean Velocity in the Duct)

For mean velocity measurements in the duct (30.49 to 121.95 m/s), a wedge type 3 hole pressure probe was used. The probe has a 15^0 included angle, .292 cm width at the trailing edge and .051 cm diameter pressure tap. The probe has one total tap (P_{TP}) and two static taps (P_A & P_B located one on each side). Two certified pressure transducers, 2.54 and 101.6 cm H_2O F.S., were used to cover the full range of pressures.

A complete calibration included velocities of 34.45, 78.96 and 123.2 m/s. At each velocity, yaw angles of +.5% and $+1^0$. This accuracy applies to the whole system which includes the probe, transducer and voltmeter (the same system components were always used together throughout the tests). The system is shown in Figure 119.

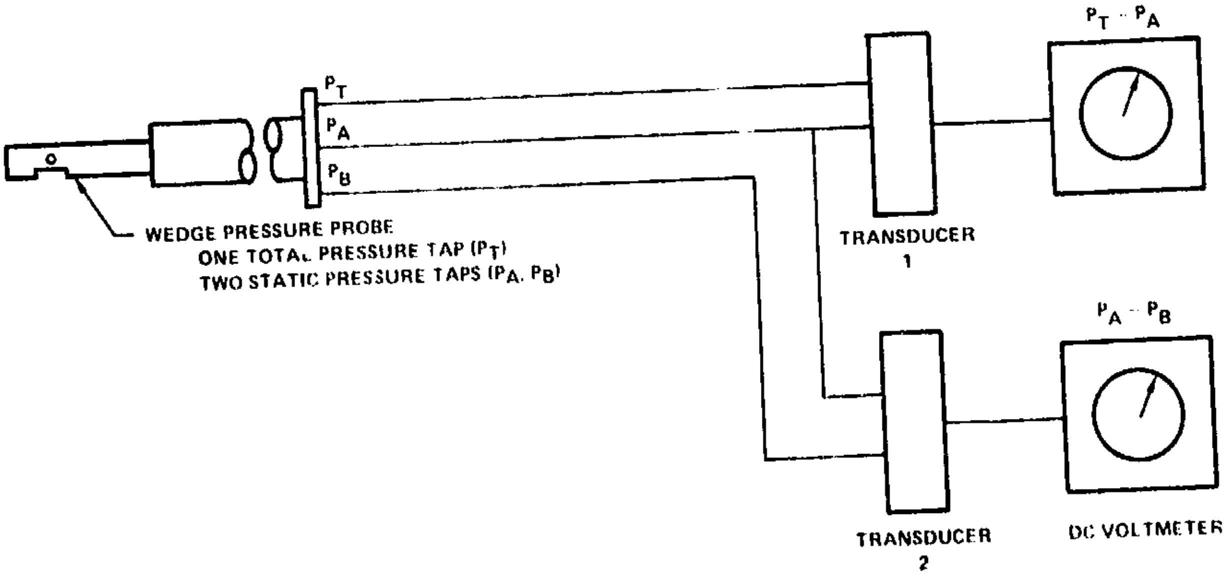

Figure 119 Wedge Probe System

The usual mode of operation of this type of probe is to rotate the probe until it is aligned with the flow stream (as determined by the two static tap readings being the same). Because of the small flow angle range expected in this test, the probe was operated in the fixed angle mode. The velocity (magnitude and angle) was determined from pressure readings (P_{TP}-P_A and P_A-P_B).

Measurement Type 2. (Turbulence in the Duct)

For turbulence measurements inside of the duct (24.39 to 121.95 m/s), X-array probes with hot-wire sensors were used. The probe tested was TSI model 1227 with a 9 um diameter, .279 cm long W wire sensor. The sensor was operated at 300°F overheat using a TSI model 1053A anemometer.

The system accuracy for X-array probes when used with linearizers and sum/difference amplifiers (to obtain turbulence components) is estimated to be +6.3%. The system is shown in Figure 120.

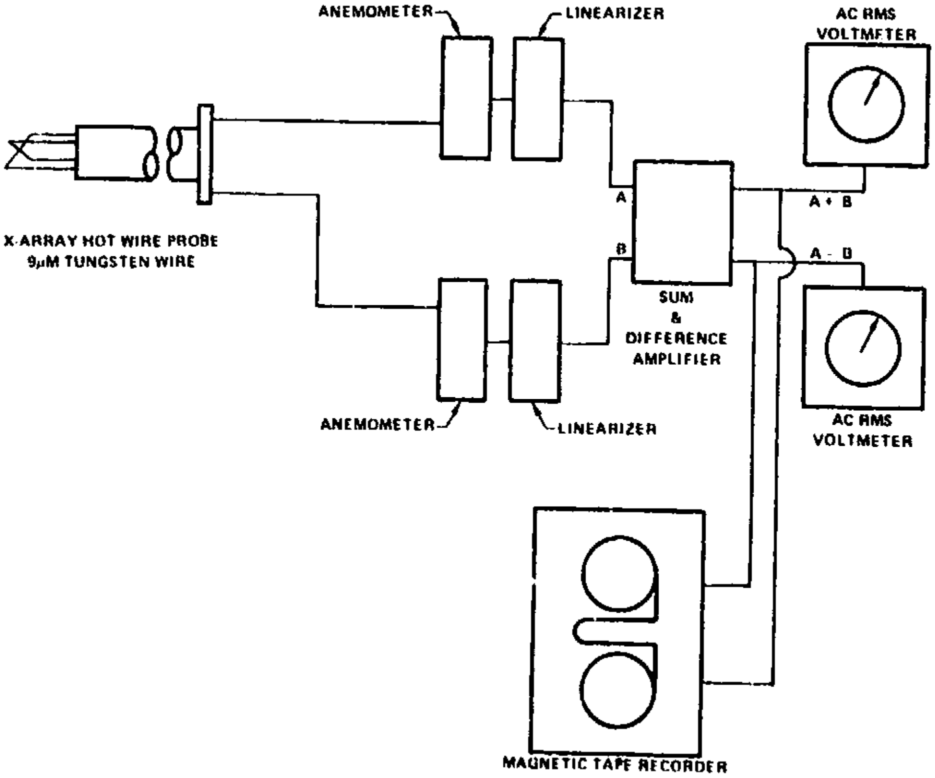

Figure 120 Hot Wire System

Measurement Type 3. (Mean Velocity Ahead of the Duct)

For mean velocity measurements ahead of the duct (2.44 to 12.2 m/s), a single element hot-wire sensor was used. The probe tested was a TSI model 1210 with a 9 um diameter, .559 cm long W wire sensor. The sensor was operated at 300°F overheat using a TSI model 1053A anemometer.

To determine the accuracy, three pre-test and one post test calibrations were performed. The calibration velocity range was 1.83 to 20.12 m/s and three probes were involved. Based on 12 sample comparisons, the accuracy was found to be +2.8%. The post test and pre-test calibrations agreed within 2.7%. This accuracy applies to the probe, anemometer and voltmeter. The system accuracy for X-array probes when used with linearizers and sum/difference amplifiers for mean velocity (magnitude and angle) measurements is +5.0% and +3°. The system is shown in Figure 121.

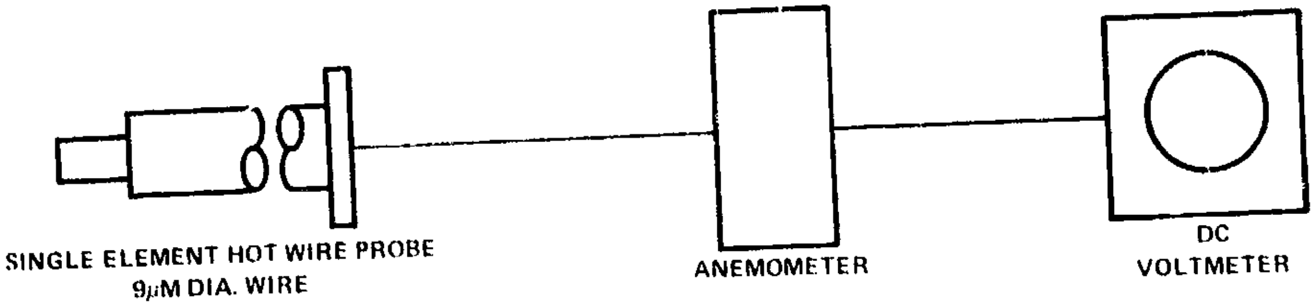

Figure 121 Single Hot Wire System

Measurement Type 4. (Turbulence Ahead of the Duct)

For turbulence measurements ahead of the duct (2.44 to 12.2 m/s), X-array probes with hot-wire sensors were used. The probe tested was a TSI model 1240 with a 9 um diameter, .110" long W wire sensor. The sensor was operated at 300°F overheat using a TSI model 1053A anemometer.

The system accuracy for X-array probes when used with linearizers and sum/difference amplifiers (to obtain turbulence components) is estimated to be +6.3%. The system is shown in Figure 120.

A summary of measurement accuracies is given in Table AI.

TABLE A-I

	Measurement Type	Instruments	Accuracy (2 s.d.)
1.	Mean Velocity in the Duct	Wedge pressure probe, transducer,	.5%, 1°
2.	Turbulence in the Duct	Same as type 4. Correlation factor of 1.36 must be applied for scale effect.	Same as type 4
3.	Mean Velocity Ahead of the Duct	9 µm x .220" Hot-wire probe, anemometer, voltmeter	2.8%
		Linearizer	2%
		Sum/Difference Amplifier	1%
		System:	5.0%, 3°
4.	Turbulence Ahead of the Duct	9 m x .110" Hot-wire probe, anemometer, voltmeter	3.9%*
		Linearizer	2%
		Sum/Difference Amplifier	1%
		System:	6.3%

*Estimate based on steady state calibration data and user experience

Post test calibration agre with pre test within 1.7%

APPENDIX B

THE INVARIANCE OF THE POTENTIAL VORTEX VELOCITY FIELD UNDER AXISYMMETRIC CONTRACTION

Applying the conservation of circulation to particles in a vortex subject to a circular axisymmetric contraction (Figure 122) produces

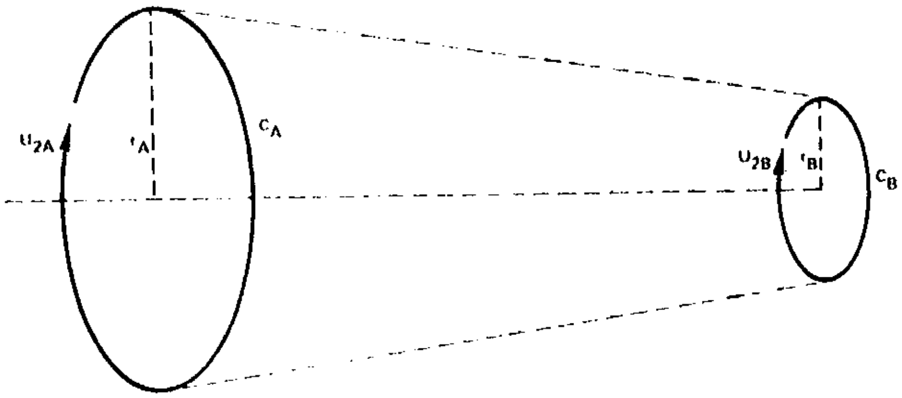

Figure 122 The Axisymmetric Contraction of a Vortex

$$\oint_{C_B} u_{2A}\, dS_A = \oint_{C_B} u_{2B}\, dS_B \tag{119}$$

$$u_{2A}(r_A)\, r_A = u_{2B}(r_B)\, r_B \tag{120}$$

but for a potential vortex circulation is constant at any radius

$$u_{2B}(r_B)\, r_B = u_{2B}(r_A)\, r_A \tag{121}$$

Thus substituting for $u_{2B}(r_B)\, r_B$ in 120

$$u_{2A}(r_A) = u_{2B}(r_A) \tag{122}$$

i.e., the azimuthal velocity field is invariant.

APPENDIX C

THE MODIFICATION OF THE VORTEX STREAMWISE VELOCITY ON CONVECTION THROUGH HONEYCOMB AND PERFORATED PLATE

a) Honeycomb

Applying Bernoulli's equation across the airfoil (following Batchelor) yields (Figure 123):

$$p_\infty + \frac{1}{2} \rho U_\infty^2 - \Delta H = p_A + \frac{1}{2} \rho \left(U_{1A}^2 + U_{2A}^2 + U_{3A}^2 \right) \qquad 123$$

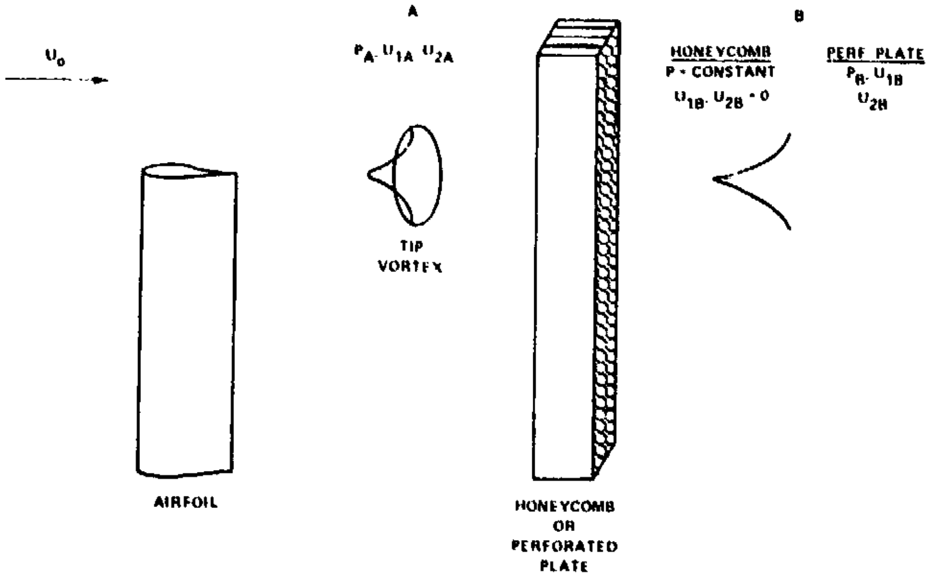

Figure 123 The Convection of a Vortex Through Honeycomb

If the radial velocity component is neglected then

$$U_{1A}^2 = \frac{2}{\rho} \left(p_\infty - p_A \right) + U_\infty^2 - U_{2A}^2 - \frac{2}{\rho} \Delta H \qquad 124$$

throughout the vortex. ΔH is the total pressure loss due to viscous effects at the airfoil surface. The static pressure distribution in the vortex, p_A , is a function of the azimuthal velocity field. Equation C2 illustrates the point made in the text that the axial velocity field depends on the relative magnitudes of the pressure loss across the airfoil and the azimuthal velocity field.

Now

$$U_{1A}^{2} = U_{\infty}^{2} \tag{125}$$

Then if $\Delta U_{1A} = U_{\infty} - U_{1A}$, Equation 124 becomes

$$\left(U_{1A} + U_{\infty} \right) \Delta U_{1A} = - \frac{2}{\rho} \left(P_{\infty} - P_{A} \right) + U_{2A}^{2} + \frac{2}{\rho} \Delta H \tag{126}$$

and if $U_{1A} \simeq U_{\infty}$

Then

$$\Delta U_{1A} = \frac{1}{2U_{\infty}} \left\{ - \frac{2}{\rho} \left(P_{\infty} - P_{A} \right) + U_{2A}^{2} + \frac{2}{\rho} \Delta H \right\} \tag{127}$$

Considering now the flow across both airfoil and honeycomb (see Figure 122) and again applying Bernoulli's equation gives

$$P_{\infty} + \frac{1}{2} \rho U_{\infty}^{2} - \Delta H - \Delta H_{S} = P_{B} + \frac{1}{2} \rho U_{2B}^{2} \tag{128}$$

where ΔH_S is the pressure loss through the honeycomb.

Solving for U_{2B}^{2},

$$U_{2B}^{2} = \frac{2}{\rho} \left(P_{\infty} - P_{B} \right) + U_{\infty}^{2} - \frac{2}{\rho} \left(\Delta H + \Delta H_{S} \right) \tag{129}$$

If again the deficit is assumed small

$$\Delta U_{1B} = \frac{1}{2U_{\infty}} \left\{ - \frac{2}{\rho} \left(P_{\infty} - P_{B} \right) + \frac{2}{\rho} \left(\Delta H + \Delta H_{S} \right) \right\} \tag{130}$$

Now if Equation 127 is subtracted from 130,

$$\Delta U_{1B} - \Delta U_{1A} = \frac{1}{2U_{\infty}} \left\{ -\frac{2}{\rho} \left(p_A - p_B \right) - U_{2A}^2 + \frac{2}{\rho} \Delta H_S \right\} \qquad 131$$

or

$$\frac{\Delta U_{1B}}{\Delta U_{1A}} = 1 + \frac{1}{\rho U_{\infty} \Delta U_{1A}} \left\{ p_B - p_A + \Delta H_S \right\} - \frac{U_{2A}^2}{2U_{\infty} \Delta U_{1A}} \qquad 132$$

Assuming that the total pressure loss across the honeycomb is constant and equal to the loss at ∞ .

Then $$\Delta H_S = \left(p_A - p_{\infty} \right)_{\infty} \qquad 133$$

Downstream of the honeycomb, the azimuthal velocity component is zero and consequently the static pressure gradient cannot be maintained and the static pressure will become uniform so that

$$p_B = p_{B\infty} \qquad 134$$

Substituting Equations 133 and 134 into Equation 132 gives

$$\frac{\Delta U_{1B}}{\Delta U_{1A}} = 1 + \frac{1}{\rho U_{\infty} \Delta U_{1A}} \left\{ p_{A\infty} - p_A \right\} - \frac{U_{2A}^2}{2U_{\infty} \Delta U_{1A}} \qquad 135$$

Now in a vortex

$$\frac{dp}{dr} = \frac{\rho U_{2A}^2}{r} \qquad 136$$

so that

$$p_{A\infty} - p_A = \rho \int_r^{\infty} \frac{U_{2A}^2}{r} dr \qquad 137$$

Substituting this expression in Equation 135

$$\frac{\Delta U_{1B}}{\Delta U_{1A}} = 1 + \frac{1}{U_\infty \; \Delta U_{1A}} \left\{ \int_r^\infty \frac{U_{2A}{}^2}{r} \, dr - \frac{U_{2A}{}^2}{2} \right\} \qquad 138$$

The integral is always positive, the initial deficit ΔU_{1A} may be positive (wake) or negative (jet). The honeycomb thus amplifies a vortex wake deficit and suppresses or inverts a vortex jet. In both cases the distortion shape is changed.

For the maximum axial deficit (excess) ratio across the honeycomb, assume a Rankine vortex (the measured azimuthal velocity fields can be approximated by a Rankine Vortex) so that

$$\int_0^\infty \frac{U_{2A}{}^2}{r} \, dr = U_{2A}{}^2{}_{\max} \qquad 139$$

and the ratio becomes

$$\frac{\Delta U_{1B\ \max}}{\Delta U_{1A\ \max}} = 1 + \frac{U_{2A\ \max}{}^2}{2U_\infty \; \Delta U_{1A\ \max}} \qquad 140$$

b) Perforated Plate

If the azimuthal velocity field is not destroyed as in the case of the perforated plate Equation 128 is replaced by

$$P_\infty + \frac{1}{2} \rho \, U_\infty{}^2 - \Delta H - \Delta H_S = P_B + \frac{1}{2} \rho \left(U_{1B}{}^2 + U_{2B}{}^2 \right) \qquad 141$$

and so for a small deficit,

$$\Delta U_{1B} = \frac{1}{\rho \, U_\infty} \left\{ P_B - P_\infty + \Delta H + \Delta H_S \right\} + \frac{U_{2B}{}^2}{2U_\infty} \qquad 142$$

Recalling Equation 127 and subtracting it from Equation 142,

$$\Delta U_{1B} - \Delta U_{1A} = \frac{1}{\rho U_\infty} \left\{ p_B - p_A + \Delta H_S \right\} + \frac{\left(U_{2B}^2 - U_{2A}^2 \right)}{2U_\infty} \qquad 143$$

now

$$U_{2B} = \alpha U_{2A} \qquad 144$$

Thus

$$\frac{\Delta U_{1B}}{\Delta U_{1A}} = 1 + \frac{1}{\rho U_\infty \Delta U_{1A}} \left\{ p_B - p_A + \Delta H_S \right\} + \frac{U_{2A}^2 \left(\alpha^2 - 1 \right)}{2U_\infty \Delta U_{1A}} \qquad 145$$

Again assuming $\Delta H_S = \left(p_A - p_B \right)_\infty$

$$\frac{\Delta U_{1B}}{\Delta U_{1A}} = 1 + \frac{1}{\rho U_\infty \Delta U_{1A}} \left\{ \left(p_{A\infty} - p_A \right) - \left(p_{B\infty} - p_B \right) \right\} + \frac{U_{2A}^2 \left(\alpha^2 - 1 \right)}{2U_\infty \Delta U_{2A}} \qquad 146$$

If further a Rankine vortex is assumed on both sides of the perforated plate, then

$$\frac{\Delta U_{1B\ \max}}{\Delta U_{1A\ \max}} = 1 + \frac{U_{2A\ \max}^2 \left(1 - \alpha^2 \right)}{2U_\infty \Delta U_{1A\ \max}} \qquad 147$$

APPENDIX D

THE UPWASH VELOCITY ELEMENT OF THE SPECTRUM TENSOR AND THE TARGET (FLIGHT) ONE DIMENSIONAL PSD AT THE FAN FACE.

The upwash velocity, assuming a frozen turbulence field, may be determined from a simple rotation of the Cartesian coordinates, Figure 124, and written as

$$u_n\ (\underline{x}) = -\ u_1\ (\underline{x})\ \sin \gamma_o + u_2\ (\underline{x})\ \cos \gamma_o \qquad 148$$

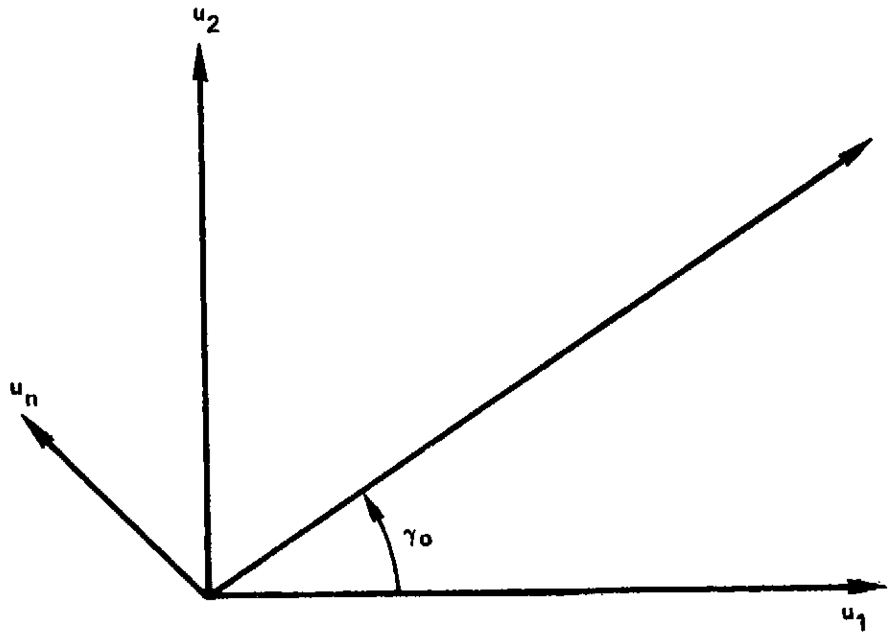

Figure 124 The Turbulence Upwash Velocity Component

If the three dimensional correlation is computed and Fourier transformed, the relationship between the spectrum tensors is found to be

$$\Phi_{nn}\ (\underline{k}) = \Phi_{11}\ (\underline{k})\ \sin^2 \gamma_o + \Phi_{22}\ (\underline{k})\ \cos^2 \gamma_o + \text{cross terms} \qquad 149$$

Now for an isotropic field of the Dryden type

$$\Phi_{11} = \frac{N\left(k_2^2 + k_3^2\right)}{\left(k^2 + \gamma^2\right)^3} \quad , \quad \Phi_{22} = \frac{N\left(k_1^2 + k_3^2\right)}{\left(k^2 + \gamma^2\right)} \qquad 150$$

and the cross terms are odd

$$\Phi_{nn} = \frac{N}{\left(k^2 + \gamma^2\right)^3}\left[k_1^2 \cos^2 \gamma_o + k_2^2 \cos^2 \gamma_o + k_3^2\right] \qquad 151$$

+ odd terms

where $N = \frac{2\,\overline{u^2}}{\pi^2 L}$ $\qquad \gamma = \frac{1}{L}$

Now the one sided one dimensional PSD over the ranges $k_1 < k_1^*$, $k_{2L} < k_2 < k_{2U}$, and $k_{3L} < k_3 < k_{3U}$ is

$$F_n\left(k_2\right) = 2\int_{k_1^*}^{k_1^*}\int_{k_{3L}}^{k_{3U}} \Phi_{nn}\left(\underline{k}\right)\, dk_3\, dk_1 \qquad 152$$

The k_3 integration is first performed by approximating the integrand with its value at the mid point in the k_3 wave number range, so that

$$2\int_{k_{3L}}^{k_{3U}} \Phi_{nn}\left(\underline{k}\right) dk_3 \simeq \qquad 153$$

$$\frac{2N\left[k_1^2 \cos^2 \gamma_o + k_2^2 \sin^2 \gamma_o + \left(\frac{k_{3U} + k_{3L}}{2}\right)^2\right]\left(k_{3U} - k_{3L}\right)}{\left[k_1^2 + k_2^2 + \left(\frac{k_{3U} + k_{3L}}{2}\right)^2\right]^3}$$

substituting this in Equation 152 yields

$$F_n\left(k_2\right) \simeq 32N\left(k_{3U} - k_{3L}\right) \int_{-k_1^*}^{k_1^*} \frac{4k_2^2 \sin^2 \gamma_o + \left(k_{3U} + k_{3L}\right)^2 + 4k_1^2 \cos^2 \gamma_o}{\left[4\left(k_2^2 + \gamma^2\right) + \left(k_{3U} + k_{3L}\right)^2 + 4k_1^2\right]^3} \, dk_1 \qquad 154$$

But over the integration range

$$4\left(k_2^2 + \gamma^2\right) + \left(k_{3U} + k_{3L}\right)^2 \gg 4k_1^2 \qquad 155$$

and $4k_2^2 \sin^2 \gamma_o + \left(k_{3U} + k_{3L}\right)^2 \gg 4k_1^2 \cos^2 \gamma_o$ 156

The integral in Equation 154 can then be approximated so that

$$F_n\left(k_2\right) \simeq \frac{64N\left(k_{3U} - k_{3L}\right) k_1^* \left[4k_2^2 \sin^2 \gamma_o + \left(k_{3U} + k_{3L}\right)^2\right]}{\left[4\left(k_2^2 + \gamma^2\right) + \left(k_{3U} + k_{3L}\right)^2\right]^3} \qquad 157$$

in the ranges $k_1 < k_1^*$, $k_{2L} < k_2 < k_{2U}$, $k_{3L} < k_3 < k_{3U}$ Equation 158 is then the target (flight) PSD that is to be aimed for on the static test stand with an ICS.

REFERENCES

1. Sofrin, T. G., McCann, J. C., "Pratt and Whitney Aircraft Experience in Compressor Noise Reduction", Paper presented at 72nd Meeting of Acoustical Society of America, 1966.

2. Cumpsty, N. A., Lowrie, B. W., "The Cause of Tone Generation by Aero-Engine Fans at High Subsonic Tip Speeds and the Effect of Forward Speed", Paper 73-Wa/GT-4 ASME, 1973.

3. Hodder, B. K., "The Effects of Forward Speed on Fan Inlet Turbulence and its Relation to Tone Noise Generation", NASA TMX 62, 381, 1974.

4. Roundhill, J. P. and Schaut, L. A., "Model and Full Scale Test Results Relating to Fan Noise Inflight Effects", AIAA Paper 75-465, 1975.

5. Feiler, C. E. and Merriman, J. E., "Effects of Forward Velocity and Acoustic Treatment on Inlet Fan Noise", NASA TMX-71591, 1974.

6. Plucinsky, J. C., "Quiet Aspects of the Pratt and Whitney Aircraft JT15D Turbofan", SAE Paper 730289, 1973.

7. Hanson, D. B., "Spectrum of Rotor Noise Caused by Atmospheric Turbulence", NASA Volume 56 No. 1, 1974.

8. Hanson, D. B., "Study of Noise Sources in a Subsonic Fan Using Measured Blade Pressures and Acoustic Theory", NASA CR-2574, 1975.

9. Hanson, D. B., "Study of Noise and Inflow Distortion Sources in the NASA QF-1B Fan Using Measured Blade and Vane Pressures", NASA CR-2899, 1977.

10. Bekofske, K. L., Sheer, R. E. Wang, J. F. C., "Fan Inlet Disturbances and Their Effect on Static Acoustic Data", ASME Paper No. 77-GT-63, 1977.

11. Povinelli, F. P., Dittmar, J. H., Woodward, R. P., "Effects of Installation Caused Flow Distortion on Noise from a Fan Designed for Turbofan Engines", NASA TN D-7076, 1972.

12. Hodder, B. K., "An Investigation of Possible Causes for the Reduction of Fan Noise Inflight", AIAA Paper 78-585, 1978.

13. Rogers, D. F., Ganz, U. W., "Aerodynamic Assessment of Methods to Simulate Flight Inflow Characteristics During Static Engine Testing", AIAA Paper 80-1023, 1980.

14. Leggat, L. J., Siddon, T. E., "Experimental Study of the Aeroacoustic Mechanism of Rotor-Vortex Interactions", JASA 64 (4), 1978.

15. Jones, W. L., McArdle, J. G., Homyak, L., "Evaluation of Two Inflow Control Devices for Flight Simulation of Fan Noise Using a JT15D Engine", AIAA Paper 79-0654, 1979.

16. Lowrie, B. W., Newby, D. R., "The Design and Calibration of a Distortion-Reducing Screen for Fan Noise Testing", AIAA Paper 77-1323, 1977.

17. Shaw, L. M., Woodward, R. P., Glaser, F. W. Dastoli, B. J., "Inlet and Fan Noise Measured in an Anechoic Wind Tunnel and Statically with an Inflow Control Device", NASA TM-73723, 1977.

18. Lowrie, B. W., "Simulation of Flight Effects on Aero Engine Noise, "AIAA Paper 75-463, 1975.

19. Woodward, R. P., Wazyniak, J. A. Shaw, L. M., MacKinnon, M. J., Effectiveness of an Inlet Flow Turbulence Control Device to Simulate Flight Fan Noise in an Anechoic Chamber", NASA-TM-73855, 1977.

20. Cocking, B. J., Ginder, R. B., "The Effect of an Inflow Conditioner on Fan Distortion Tones", AIAA Paper 77-1324, 1977.

21. Kantola, R. A., Warren, R. E., "Reduction of Rotor-Turbulence Interaction Noise in Static Fan Noise Testing", AIAA Paper 79-0656, 1979.

22. Atvars, Y., Rogers, D. F., "The Development of Inflow Control Devices for Improved Simulation of Flight Noise Levels During Static Testing of a HBPR Turbofan Engine", AIAA Paper 80-1024, 1980.

23. McArdle, J. G., Jones, W. L., Heidelberg, L. J., Homyak' L., "Comparison of Several Inflow Control Devices for Flight Simulation of Fan Tone Noise Using a JT15D-1 Engine" AIAA Paper 80-1025, 1980.

24. Woodward, R. P., Glaser, F. W., "Effect of Inflow Control on Inlet Noise of a Cut-on Fan", AIAA Paper 80-1049, 1980.

25. Ho, P. Y., Smith, E. B., Kantola, R. A., "An Inflow Turbulence Reduction Structure for Scale Model Fan Testing", AIAA Paper 79-0655, 1979.

26. Ginder, R. B., Kenison, R. C., Smith, A. D., "Considerations for the Design of Inlet Flow Conditioners for Static Fan Noise Testing", AIAA Paper 79-0657, 1979.

27. Prandtl, L., "Attaining a Steady Airstream in Wind Tunnels", NASA TM 726, 1933.

28. Loehrke, R. I., Nagib, H. M., "Control of Free Stream Turbulence by Means of Honeycombs: A Balance Between Suppression and Generation", ASME Paper No. 76-FE-2, 1976.

29. Gedge, M. R., "Analytical Models for Use in Fan Inflow Control Structure Design", NASA CR-159189, 1980.

30. Betchov, R., Lorenzen, C., Phys. Fluids Volume 17, 1503 (1974).

31. Uberoi, M. S., "Effect of Wind-Tunnel Contraction on Free-Stream Turbulence", J. Aero. Sci. 23, 8, 1956.

32. Hussein, A. K. M. F., Ramjee, V., "Effects of the Axisymmetric Contraction Shape on Incompressible Turbulent Flow". Journal of Fluids Eng., March 1976.

33. Ribner, H. S., Tucker, M., "Spectrum of Turbulence in a Contracting Stream", NACA 1113, 1953.

34. Tucker, H. J., Reynolds, A. J., "The Distortion of Turbulence by Irrotational Plane Strain", J. F. M., Volume 32, Pt. 4, 1968.

35. Batchelor, G. K., Proudman, I., "The Effect of Rapid Distortion of a Fluid in Turbulent Motion", Quart. Journ. Mech. and App. Math. Vol. VII, Pt. 1, 1954.

36. Ganz, U., "Analytical Investigation of Fan Tone Noise Due to Ingested Atmospheric Turbulence", NASA CR 3302, 1980.

37. Townsend, A. A., "The Uniform Distortion of Homogeneous Turbulence", Quart. Journ. Mech. and App. Math., Volume VII, Pt. 1, 1954.

38. Taylor, G. I., and Batchelor, G. K., "The Effect of Wire Gauze on Small Disturbances in a Uniform Stream", Quart. Journ. Mech. and Applied Math., Vol. II, Part 1, 1949.

39. Newman, B. G., "Flow in a Viscous Trailing Vortex", Aero. Quart. Vol. 10, May 1959.

40. Batchelor, G. K., "Axial Flow in Trailing Line Vortices", J. F. M. Vol. 20, Pt. 4, 1964.

41. Ramsey, V., "Acoustic Scattering from an Aircraft Trailing Vortex", University Microfilms 73-30, 463, 1973.

42. Pickett, G. F., "Effects of Non-Uniform Inflow on Fan Noise", Presented at the Spring Meeting, Acoustical Society of America, New York City, April 23-26, 1974.

43. Morel, T., "Effort of Base Slant on Flow in the Near Wake of an Ansymmetric Cylinder", Aero. Quart., May 1980.

44. Bissinger, N. C., Braun, G. W., "On the Inlet Vortex System", NGK-43-001-086 Tenn. Univ. Space Inst. 1974.

45. Filotas, L.T. "Reponse of an Infinite Wing to an Oblique Sinusoidal Gust: A Generalization of the Sears' Problem," NASA SP-207, 1969.